

UNIVERSIDADE DE SÃO PAULO  
ESCOLA POLITÉCNICA

THIAGO FERREIRA DE ABREU

**The CO hydrogenation on Co/SBA-15 and Co/Al<sub>2</sub>O<sub>3</sub> catalysts**

São Paulo  
2022



THIAGO FERREIRA DE ABREU

**The CO hydrogenation on Co/SBA-15 and Co/Al<sub>2</sub>O<sub>3</sub> catalysts**

**Revised Version**

Ph. D. Thesis presented to the Graduate Program in Chemical Engineering at the Escola Politécnica da Universidade de São Paulo to obtain the degree of Doctor of Science.

Concentration Area: Chemical Engineering

Advisor: Profa. Dra. Rita M. de B. Alves

Co-advisor: Prof. Dr. Ing. Martin Schmal

São Paulo

2022



Autorizo a reprodução e divulgação total ou parcial deste trabalho, por qualquer meio convencional ou eletrônico, para fins de estudo e pesquisa, desde que citada a fonte.

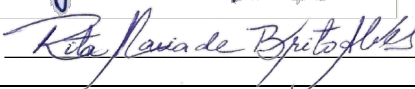
Este exemplar foi revisado e corrigido em relação à versão original, sob responsabilidade única do autor e com anuência de seu orientador.

São Paulo, 25 de abril de 2022

Assinatura do autor:



Assinatura do orientador:



#### Catálogo-na-publicação

Abreu, Thiago Ferreira de

The CO hydrogenation on Co/SBA-15 and Co/Al<sub>2</sub>O<sub>3</sub> / T. F. de Abreu  
-- versão corr. -- São Paulo, 2022.

186 p.

Tese (Doutorado) - Escola Politécnica da Universidade de São Paulo.  
Departamento de Engenharia Química.

1. Síntese de Fischer-Tropsch 2. Catalisadores à base de cobalto.  
3. Suportes óxidos. 4. Olefinas leves. 5 Combustíveis líquidos  
I.Universidade de São Paulo. Escola Politécnica. Departamento de  
Engenharia Química II. t.

Name: ABREU, Thiago Ferreira de

Title: The CO hydrogenation on Co/SBA-15 and Co/Al<sub>2</sub>O<sub>3</sub> catalysts

Ph. D. Thesis presented to the Graduate Program in Chemical Engineering at the Escola Politécnica da Universidade de São Paulo to obtain the degree of Doctor of Science.

Concentration Area: Chemical Engineering

Approved at: 24/02/2022.

#### Examination Board

Prof. Dr. Rita Maria de Brito Alves

Institution: POLI-USP

Judgement: Approved

Prof. Dr. Pedro Henrique Cury Camargo

Institution: Helsinki University

Judgement: Approved

Prof. Dr. José Mansur Assaf

Institution: UFSCAR

Judgement: Approved

Prof. Dr. Thamiris Franckini Paiva

Institution: SENAI Cetiq

Judgement: Approved

Prof. Dr. Thiago Lewis Reis Hower

Institution: POLI-USP

Judgement: Approved

*Ao meu amor Isabella G. Z., minha família e amigos, pela inesgotável fonte de motivação, apoio e palavras certas. Espero em algum momento poder retribuir tamanho apoio.*

*Aos meus pais, Pedro e Edna, por todo sacrifício que tiveram para que eu pudesse chegar até este momento. Pai, obrigado pelo exemplo de ética profissional, independente das dificuldades. Mãe, obrigado pelo amor, cuidado, dedicação e orações.*

*De repeteco, dedico às forças fundamentais da natureza que regem o universo. 42!*



## ACKNOWLEDGMENTS

First, to my advisors, Professors **Rita Maria de Brito Alves** and **Martin Schmal**, thank you for the almost six years spent together, the advisement, the criticizing and necessary words.

I would like to show my appreciation to my colleagues. I immensely appreciate all the learning that I had from you, both as individuals and as professionals, especially to **Thiago Hewer**, **Tamara Ramalho**, **Kelvin Pacheco**, **Jonas Laedson**, **Higor Azevedo**, **Camila Emilia** and **Fabio Cavalcanti**. For the technical supervision, for the teaching, the work meetings, the coffees, lunches, desserts and laughs. The profound conversations. For all the support. I would not be able to develop this work without it, keep that in mind. I do admire you. Specially, thank you, **Paulo Moreira**, for the technical support that must always be acknowledged. Thank you for being such an incredible person, both technically and personally.

Mom, dad and brothers (**Edna**, **Pedro**, **Diego**, **Rodrigo** and **Letícia**), I would like to thank you for the inspiration, the incentives and right words, from the beginning to the end. I would not be here, in this position, if it wasn't for you. **Isabella Grando Zamboni**, thank you, my love, for being such an admirable person and providing me strength and inspiration at the end of this journey. I want you to know that the source of inspiration and admiration to move forward and finish this work is you.

My friends, thank you for the support. **Giovana Morales**, **Anderson Okada**, **Leonardo Moura**, **Marina Artigas**, **Bruno Sakemi**, **Audrey Kalinouski**, **Daniel Eli Torres** and more. For my friends from the lab, thank you **Higor Azevedo Garona**, **Thiago Lewis Reis Hewer**, **Gabriel Machado**, **Paulo Moreira**, **Paul Sato** and more. You are very important to me. Thank you all for the laughs, the games, the profound conversations. For showing me when I was wrong, over and over again.

I would like to thank NUCAT-COPPE/UFRJ (Núcleo de Catálise - Instituto Alberto Luiz Coimbra de Pós-Graduação e Pesquisa de Engenharia of the Universidade Federal do Rio de Janeiro), especially **Marcos Anacleto**, **Sidnei Joaquim**, **Evelyn Muguet**, **Célio Carlos** and **Rodrigo Bonfim** for the technical support. Thank you for having me at the laboratory. **Sidnei**, I run short of words to honor you and to talk about the admiration I will always have for you and your abilities – anyway, I will always remember of you as the “Paulão from NUCAT, but with enhanced skills”.

I would also like to thank Prof. **Elisabete Assaf** and **Alessandra Lucredio** from Instituto de Química – Universidade de São Paulo, São Carlos campus, **Alfredo Duarte** from Central Analítica IQ-USP and also Prof. **Igor Bresolin**, from Universidade Federal de São Paulo, for the technical support.

I gratefully acknowledge the support of the RCGI – Research Centre for Gas Innovation, hosted by the University of São Paulo (USP) and sponsored by FAPESP – São Paulo Research Foundation (2014/50279-4) and Shell Brasil.

Finally, this study was financed in part by the Coordenação de Aperfeiçoamento de Pessoal de Nível Superior - Brasil (CAPES) - Finance Code 001.

*“Do not let your fire go out, spark by irreplaceable spark in the hopeless swamps of the not-quite, the not-yet, and the not-at-all. Do not let the hero in your soul perish in lonely frustration for the life you deserved and have never been able to reach. The world you desire can be won. It exists... it is real... it is possible... it's yours.”*

(RAND, 2005)

*“Be not disgusted, nor discouraged, nor dissatisfied, if thou dost not succeed in doing everything according to right principles; but when thou hast failed, return back again, and be content if the greater part of what thou doest is consistent with man's nature, and love this to which thou returnest”*

(AURELIUS, 2013, Book 5)

*“Live and act within the limit of your knowledge and keep expanding it to the limit of your life.”*

(RAND, 1963, p. 178)



## RESUMO

ABREU, Thiago Ferreira de. **Hidrogenação de CO em catalisadores de Co/SBA-15 e Co/Al<sub>2</sub>O<sub>3</sub>**. 2021. 188 p. Tese (Doutorado em Ciências)–Departamento de Engenharia Química da Escola Politécnica, Universidade de São Paulo, São Paulo, 2021.

Em todo o mundo, há demanda crescente por fontes de energia primária (FEP). O cenário atual sugere lenta transição de FEPs para combustíveis fósseis limpos, particularmente para gás natural (GN) e fontes de energia renováveis, com impactos também na indústria química. Nesse contexto, o processo *gas-to-liquids* (GTL) pode ter um papel estratégico nessa transição. A reação de hidrogenação do CO, o núcleo dessa tecnologia, leva à produção de produtos diversos, como parafinas e olefinas, a partir do gás de síntese ( $H_2 + CO$ ). A síntese de Fischer-Tropsch (SFT) é limitada por muitos fatores críticos e melhorias de eficiência por meio do *design* e da vida útil do catalisador são mandatórias para fornecer maior competitividade à tecnologia. Neste estudo foi avaliado o desempenho de catalisadores à base de cobalto para a reação de hidrogenação do CO utilizando suportes de  $\gamma$ -alumina e SBA-15 visando compreender os efeitos de condições operacionais sobre o desempenho dos catalisadores. Os suportes e catalisadores avaliados foram sintetizados e caracterizados para avaliação de propriedades texturais, morfológicas e estruturais. Os efeitos da temperatura e velocidade espacial sobre a atividade e seletividade para olefinas leves ( $C_2-C_4$ ) e hidrocarbonetos pesados ( $C_{5+}$ ) dos catalisadores 15% Co/SBA-15 e 15% Co/ $\gamma$ -Al<sub>2</sub>O<sub>3</sub> foram avaliados. A desativação do catalisador com o tempo em fluxo (TEF) também foi avaliada em termos de formação de carbono por técnicas de espectroscopia TGA/DTA e Raman. De maneira geral, os resultados mostram que ambos os catalisadores produzem parafinas como produto principal e apresentaram maior atividade em velocidade espacial mais baixa e temperatura mais alta e maior seletividade para hidrocarbonetos (HC) pesados e olefinas leves em velocidade espacial mais baixa e temperatura mais baixa. Dentre os catalisadores, o 15% Co/SBA-15 apresentou maior atividade e seletividade para HC leves até a faixa da gasolina, com seletividade para olefinas leves ligeiramente mais alta, enquanto o 15% Co/ $\gamma$ -Al<sub>2</sub>O<sub>3</sub> produziu HC mais pesados de acordo com a seletividade para  $C_{5+}$ . Dois estágios de desativação com deposição de carbono foram detectados para ambos os catalisadores. Diferenças na perda de rendimento com o TEF pode ser explicada pelo fenômeno de migração de carbono.

Palavras-chave: Síntese de Fischer-Tropsch. Catalisadores à base de cobalto. Suportes óxidos. Olefinas leves. Combustíveis líquidos.



## ABSTRACT

ABREU, T. F. **The CO hydrogenation on Co/SBA-15 and Co/Al<sub>2</sub>O<sub>3</sub> catalysts**. 2021. Thesis (Doctor of Science in Chemical Engineering). - Escola Politécnica, Universidade de São Paulo, São Paulo, 2021.

Worldwide there is an increasing demand for primary energy sources (PES). The current scenario suggests a low-rate shift of PES using clean fossil fuels, in particular natural gas (NG) and renewable energy sources, which also impacts the chemical industry. In this context, the gas-to-liquids (GTL) process may play a strategic role on this transition. The CO hydrogenation reaction, which is the core of this technology, leads to the production of many products, such as paraffins and olefins, from syngas (H<sub>2</sub>+CO). The Fischer-Tropsch Synthesis (FTS) is limited by many critical factors, so efficiency improvements through catalyst design and lifetime is mandatory to provide higher competitiveness to the technology. In this study, the performance of cobalt-based catalyst for the CO hydrogenation reaction was evaluated, using  $\gamma$ -alumina and SBA-15 supports, aiming at understanding the operating condition effects. The evaluated supports and catalysts were synthesized and characterized for textural, morphological and structural properties assessment. The effects of temperature and space velocity over the 15% Co/SBA-15 and 15% Co/ $\gamma$ -Al<sub>2</sub>O<sub>3</sub> catalysts were evaluated in terms of activity, selectivity to lower olefins (C<sub>2</sub>-C<sub>4</sub>) and C<sub>5</sub>+ selectivity. The catalyst deactivation with time-on-stream (TOS) was also evaluated in terms of carbon formation by TGA/DTA and Raman spectroscopy techniques. Overall, results show that both catalysts produced paraffins as main product and presented a higher activity at lower space velocity and higher temperature and higher selectivity to higher hydrocarbons (HC) and lower olefins at lower space velocity and lower temperature. From the tested catalysts, the 15% Co/SBA-15 presented higher activity and selectivity to lower HC up to the gasoline range, with a slightly higher selectivity to lower olefins, whereas the 15% Co/ $\gamma$ -Al<sub>2</sub>O<sub>3</sub> produced higher HC according to the C<sub>5</sub>+ selectivity. Two deactivation stages with similar carbon depositions were detected for both catalysts. Differences in yield loss with TOS can be explained by the carbon migration phenomenon.

Keywords: Fischer-Tropsch synthesis. Cobalt-based catalysts. Oxide supports. Light olefins. Liquid fuels.



## ILUSTRATION INDEX

Figure 1 – High-Temperature Fischer-Tropsch Synthesis (HTFT) and Low-Temperature Fischer-Tropsch Synthesis (LTFT) processes summarization .....	31
Figure 2 – Anderson-Schulz-Flory distribution of Fischer-Tropsch Synthesis products .....	34
Figure 3 – Routes for carbon deposition in cobalt-based catalysts for Fischer-Tropsch Synthesis .....	44
Figure 4 – Catalytic tests summary for 15% Co/SBA-15 and 15% Co/ $\gamma$ -Al <sub>2</sub> O <sub>3</sub> catalysts. ....	56
Figure 5 – SBA-15 support Infrared Spectroscopy analysis (FTIR) in the 4000-400 cm <sup>-1</sup> wavenumber range .....	60
Figure 6 – Thermogravimetric Analyses (TGA/DrTGA) for (A) SBA-15 (in black) and catalyst (15% Co/SBA-15, in red) and (B) alumina-supported catalysts (5, 10 and 15 wt. % Co/ $\gamma$ -Al <sub>2</sub> O <sub>3</sub> catalysts in black, red and blue, respectively) .....	61
Figure 7 – Nitrogen adsorption/desorption isotherms of the fresh, calcined SBA-15 (a) and 15%Co/SBA-15 (b) catalyst and the pore size distribution (c) and (d) .....	63
Figure 8 – Nitrogen adsorption/desorption isotherm of fresh, calcined (a) $\gamma$ -Al <sub>2</sub> O <sub>3</sub> , (b) 5%Co/ $\gamma$ -Al <sub>2</sub> O <sub>3</sub> , (c) 10%Co/ $\gamma$ -Al <sub>2</sub> O <sub>3</sub> and (d) 15%Co/ $\gamma$ -Al <sub>2</sub> O <sub>3</sub> .....	66
Figure 9 – Nitrogen adsorption/desorption isotherm of the fresh, calcined (a) $\gamma$ -Al <sub>2</sub> O <sub>3</sub> , (b) 5%Co/ $\gamma$ -Al <sub>2</sub> O <sub>3</sub> , (c) 10%Co/ $\gamma$ -Al <sub>2</sub> O <sub>3</sub> and (d) 15%Co/ $\gamma$ -Al <sub>2</sub> O <sub>3</sub> .....	67
Figure 10 – (a) SBA-15 support and (b) 15% Co/SBA-15 catalyst X-ray diffractograms in the 10° ≤ 2 θ ≤ 90° Bragg angle range .....	70
Figure 11 – X-Ray diffractograms of $\gamma$ -Al <sub>2</sub> O <sub>3</sub> support and of the Co/ $\gamma$ -Al <sub>2</sub> O <sub>3</sub> catalysts in the 10° ≤ 2 θ ≤ 90° Bragg angle range .....	71
Figure 12 – SEM images of SBA-15 support in different magnifications .....	74
Figure 13 – SEM images of 15 wt.% Co/SBA-15 catalyst in different magnifications .....	75
Figure 14 – SEM images of (a) $\gamma$ -Al <sub>2</sub> O <sub>3</sub> support, (b) 5 % Co/ $\gamma$ -Al <sub>2</sub> O <sub>3</sub> , (c) 10 % Co/ $\gamma$ -Al <sub>2</sub> O <sub>3</sub> , and (d) 15 % Co/ $\gamma$ -Al <sub>2</sub> O <sub>3</sub> catalysts in the same magnification (500x) .....	76

Figure 15 – Transmission Electron Microscopy (TEM) of the prepared SBA-15 with a resolution of (a) 500 nm (lateral view); (b) 50 nm (cross-section view) displaying parallel channels of the ordered silica and the hexagonal structure of the channels .....	78
Figure 16 – Transmission Electron Microscopy (TEM) of the prepared 15%Co/SBA-15 with a resolution of (a) 500 nm; (b) 100 nm; (c) 20 nm; and (d) 5 nm displaying parallel channels of the ordered silica and successful cobalt impregnation (contrast) .....	79
Figure 17 – Transmission Electron Microscopy (TEM) of the prepared 5%Co/ $\gamma$ -Al <sub>2</sub> O <sub>3</sub> with a resolution of (a) 500 nm; (b) 100 nm; (c) 50 nm; and (d) 20 nm along with EDS analyses of two selected spots (a and b). Detected copper (Cu) is due to the grid composition .....	83
Figure 18 – Transmission Electron Microscopy (TEM) of the prepared 10 % Co/ $\gamma$ -Al <sub>2</sub> O <sub>3</sub> with a resolution of (a) 100 nm; and (b) 10 nm, presenting one identified crystallographic orientation .....	84
Figure 19 – Transmission Electron Microscopy (TEM) of the prepared 15 % Co/ $\gamma$ -Al <sub>2</sub> O <sub>3</sub> with a resolution of (a) 100 nm; and (b) 20 nm .....	85
Figure 20 – Raman spectra of prepared catalysts: 5% Co/ $\gamma$ -Al <sub>2</sub> O <sub>3</sub> (a), 10% Co/ $\gamma$ -Al <sub>2</sub> O <sub>3</sub> (b), 15% Co/ $\gamma$ -Al <sub>2</sub> O <sub>3</sub> (c) and 15% Co/SBA-15 (d) .....	86
Figure 21 – Hydrogen-Temperature Programmed Reduction (H <sub>2</sub> -TPR) analyses for (a) 15% Co/SBA-15 and (b) 5, 10 and 15 wt.% Co/ $\gamma$ -Al <sub>2</sub> O <sub>3</sub> catalysts (y-offset plots) .....	89
Figure 22 – Temperature Programmed Desorption (H <sub>2</sub> -TPD) profiles .....	92
Figure 23 – Temperature Programmed Desorption (CO-TPD) profile using mass spectrometry as detector for 15%Co/SBA-15 .....	95
Figure 24 – Temperature Programmed Desorption (CO-TPD) profile using mass spectrometry as detector for 15%Co/SBA-15 .....	96
Figure 25 – Catalytic test of (a) 15% Co/SBA-15 at 543 K, H <sub>2</sub> /CO molar ratio of 2:1, 20 bar and (b) 15% Co/ $\gamma$ -Al <sub>2</sub> O <sub>3</sub> at 543 K, H <sub>2</sub> /CO molar ratio of 2:1, 20 bar. ....	98
Figure 26 – Relationship between WHSV and P <sub>CO</sub> for the (a) 15% Co/SBA-15 and (b) 15% Co/ $\gamma$ -Al <sub>2</sub> O <sub>3</sub> experiments. ....	100

Figure 27 – Effects of (a) WHSV and (b) $P_{CO}$ over 15% Co/SBA-15 and (c) WHSV and (d) $P_{CO}$ over 15% Co/ $\gamma$ -Al <sub>2</sub> O <sub>3</sub> conversion and CO <sub>2</sub> and CH <sub>4</sub> selectivities at 543 K, H <sub>2</sub> /CO molar ratio of 2:1 and 20 bar. ....	101
Figure 28 – (a) 15% Co/SBA-15 and (b) 15% Co/ $\gamma$ -Al <sub>2</sub> O <sub>3</sub> catalyst performance as function of Time-on-Stream (TOS) at 20 bar, 543.15 K, H <sub>2</sub> /CO = 2:1 and WHSV = 7.7 L.g <sup>-1</sup> .h <sup>-1</sup> . ....	103
Figure 29 – Temperature effect over (a) 15% Co/SBA-15 and (b) 15% Co/ $\gamma$ -Al <sub>2</sub> O <sub>3</sub> performance. ....	105
Figure 30 – WHSV effect over (a) 15% Co/SBA-15 and (b) 15% Co/ $\gamma$ -Al <sub>2</sub> O <sub>3</sub> performances. ....	106
Figure 31 – Olefin-to-Paraffin ratio and selectivity to paraffins and olefins with varying operating conditions (Temperature and WHSV) for (a) 15% Co/SBA-15 and (b) 15% Co/ $\gamma$ -Al <sub>2</sub> O <sub>3</sub> .....	108
Figure 32 – Anderson-Schulz-Flory distribution for (a) to (d) 15% Co/SBA-15 and (e) to (h) 15% Co/ $\gamma$ -Al <sub>2</sub> O <sub>3</sub> at each operational conditions: (a) and (e) 543 K at the beginning of the run (WHSV of 17.11 L.g <sub>cat</sub> <sup>-1</sup> .h <sup>-1</sup> ); (b) and (f) 523 K; (c) and (g) 493 K; (d) and (h) 543 K at the end of run (WHSV of 7.67 L.g <sub>cat</sub> <sup>-1</sup> .h <sup>-1</sup> ). ....	110
Figure 33 – CO and CO <sub>2</sub> effective reaction rates with $P_{CO}$ (bar) for each condition for (a) 15% Co/SBA-15 and (b) 15% Co/ $\gamma$ -Al <sub>2</sub> O <sub>3</sub> .....	113
Figure 34 – Thermogravimetric analysis, performed in air, organized as TGA/DTG and TGA/DTA (a) and (b) for 15% Co/SBA-15 and as (c) and (d) for 15% Co/ $\gamma$ -Al <sub>2</sub> O <sub>3</sub> , respectively .....	115
Figure 35 – Raman analysis performed for 15 wt.% Co/SBA-15 and 15 wt.% Co/ $\gamma$ -Al <sub>2</sub> O <sub>3</sub> catalysts after reaction .....	117
Figure 36 – Raman scattering analysis depicting the laser power effect over the post-reaction 15% Co/SBA-15 (a) and 15% Co/ $\gamma$ -Al <sub>2</sub> O <sub>3</sub> (b) catalyst samples .....	120



## TABLE INDEX

Table 1 – Main products from the FTS process and the respective chemical reactions .....	32
Table 2 – Effect of operational factors over the reaction performance .....	40
Table 3 – Characterizations performed for each sample developed in this study .....	50
Table 4 – Catalyst and Total Active Phase Mass (mg) used for Catalytic Tests .....	54
Table 5 – Conditions used for 15 % Co/SBA-15 catalytic test .....	57
Table 6 – Conditions used for 15 % Co/ $\gamma$ -Al <sub>2</sub> O <sub>3</sub> catalytic test .....	58
Table 7 – Thermogravimetric Analysis (TGA) for SBA-15 and cobalt catalysts (SBA-15 and alumina-based catalysts) .....	62
Table 8 – Surface area, pore volume and mean pore diameter of the SBA-15 support and 15% Co/SBA-15 catalyst from different methods .....	64
Table 9 – Surface area, pore volume and mean pore diameter of the $\gamma$ -Al <sub>2</sub> O <sub>3</sub> support and catalysts from BET and BJH methods .....	68
Table 10 – Crystallite sizes and parameters for the catalysts .....	71
Table 11 – Mean Crystallite size determination and the different parameters used for each catalyst .....	72
Table 12 – Inductively coupled plasma optical emission spectrometry (ICP-OES) analysis results for Co quantification .....	73
Table 13 – Densities of catalysts' compounds .....	82
Table 14 – Bands identified in Raman spectrum of each prepared catalyst .....	87
Table 15 – H <sub>2</sub> -uptake and degree of reduction (DR, %) for the prepared catalysts .....	90
Table 16 – Key Fragment Ion data for Mass Spectrometry .....	91
Table 17 – Particle size, Dispersion and Metallic Superficial Area measured by H <sub>2</sub> -TPD using TCD and MS detectors .....	94

Table 18 – Calculated Chain Growth Probability ( $\alpha$ ) for each reaction conditions. ....	111
Table 19 – Comparison between catalyst performance the 15% Co/ $\gamma$ -Al <sub>2</sub> O <sub>3</sub> , 15% Co/SBA-15 and the 15% Co/ $\gamma$ -Al <sub>2</sub> O <sub>3</sub> from Park <i>et al.</i> (2017). ....	114
Table 20 – Thermogravimetric Analysis (TGA) for spent cobalt catalysts and mass loss ...	116
Table 21 – Bands identified in Raman spectrum for spent catalyst at lower Raman wavenumber values .....	118

## ABBREVIATIONS AND ACRONYMS INDEX

<i>(hkl)</i>	Miller Indexes of a crystalline plane
<b>BET</b>	Brunauer-Emmett-Teller
<b>BJH</b>	Barrett-Joyner-Halenda
<b>C</b>	Conversion Factor for the Mass Flowmeter
$\bar{C}$	Mean Conversion Factor for Mass Flowmeter
<b>CO</b>	Carbon Monoxide Molecule
<b>Co</b>	Cobalt Element
<b>CO<sub>2</sub></b>	Carbon Dioxide Molecule (Formula)
<b>COPPE/UFRJ</b>	Instituto Alberto Luiz Coimbra de Pós-Graduação e Pesquisa de Engenharia of the Universidade Federal do Rio de Janeiro
<b>CTY</b>	Cobalt-Time-Yield
<b>D(%)</b>	Dispersion
<b>D<sub>cor</sub> (%)</b>	Corrected Dispersion (by degree of reduction)
<b>deg</b>	Degree
<b>DFT</b>	Density Functional Theory
<b>d<sub>hkl</sub></b>	Interplanar distance or space
<b>d<sub>p</sub></b>	Particle Diameter
<b>DR</b>	Degree of Reduction (%)
<b>FBR</b>	Fixed Bed Reactor
<b>fcc</b>	Face-Centered Cubic Lattice Cell
<b>FT-IR</b>	Fourier Transform Infrared Spectroscopy
<b>FTS</b>	Fischer-Tropsch Synthesis
<b>GHSV</b>	Gas Hourly Space Velocity
<b>H<sub>2</sub></b>	Hydrogen Molecule (Formula)
<b>H<sub>2</sub>-TPD</b>	Hydrogen Temperature Programmed Desorption
<b>H<sub>2</sub>-TPR</b>	Hydrogen Temperature Programmed Reduction
<b>ICDD</b>	International Centre for Diffraction Data
<b>ICP-OES</b>	Inductively Coupled Plasma Optical Emission Spectrometry
<b>IUPAC</b>	International Union of Pure and Applied Chemistry
<b>K</b>	Scherrer Equation's Dimensionless Shape Factor
<b>L/W</b>	Length-to-Width particle ratio
<b>L<sub>hkl</sub></b>	Crystallite Size
<b>MA</b>	Mesoporous Alumina

<b>MLR</b>	Monolithic Loop Reactor
<b>MS</b>	Mass Spectrometry
<b>MSC</b>	Metal-Support Compounds
<b>MSE</b>	Modified Scherrer Equation
<b>N<sub>2</sub></b>	Nitrogen Molecule (Formula)
<b>NLDFT</b>	Non-local density functional theory
<b>OMS</b>	Ordered Mesoporous Silica
<b>P</b>	Pressure
<b>P/P<sub>0</sub></b>	Pressure of the Adsorbate Relative to its Saturation Pressure, or Relative Pressure
<b>P<sub>0</sub></b>	Saturation Pressure/ Vapor Pressure of N <sub>2</sub> at 77 K
<b>PDF</b>	Powder Diffraction File
<b>PSD</b>	Pore Size Distribution
<b>R<sup>2</sup></b>	Squared Pearson Correlation or Coefficient of Determination
<b>rad</b>	Radian
<b>RMR</b>	Relative Molar Response
<b>RT</b>	Retention Time
<b>SBA-15</b>	Santa Barbara Amorphous-15 type material
<b>SEM</b>	Scanning Electron Microscopy
<b>SMSI</b>	Strong Metal-Support Interaction
<b>S<sub>SP</sub></b>	Metallic Superficial Area (m <sup>2</sup> /gcat)
<b>TCD</b>	Thermal Conductivity Detector
<b>TEM</b>	Transmission Electron Microscopy
<b>TGA</b>	Thermogravimetric Analysis
<b>TOF</b>	Turnover Frequency (s <sup>-1</sup> )
<b>TPD</b>	Temperature Programmed Desorption
<b>TPR</b>	Temperature Programmed Reduction
<b>VLE</b>	Vapor-Liquid Equilibrium
<b>WHSV</b>	Weight Hourly Space Velocity
<b>XPS</b>	X-Ray Photoelectron Spectroscopy
<b>XRD</b>	X-Ray Diffractometry
<b>Y.L.</b>	Yield Loss
<b>B</b>	Scherrer Equation's Line Broadening at Half the Maximum Intensity (FWHM)
<b>γ-Al<sub>2</sub>O<sub>3</sub></b>	gamma-Phase Alumina (Aluminum Oxide) (Formula)

- ⊖ Scherrer Equation's Bragg Angle
- Λ Scherrer Equation's X-Ray Wavelength



## SUMMARY

<b>1</b>	<b>INTRODUCTION .....</b>	<b>27</b>
<b>2</b>	<b>OBJECTIVES .....</b>	<b>29</b>
<b>3</b>	<b>BACKGROUND .....</b>	<b>31</b>
<b>3.1</b>	<b>FISCHER-TROPSCH SYNTHESIS .....</b>	<b>31</b>
<b>4</b>	<b>LITERATURE REVIEW .....</b>	<b>35</b>
<b>4.1</b>	<b>GENERAL ASPECTS OF FISCHER-TROPSCH PROCESSES .....</b>	<b>35</b>
<b>4.1.1</b>	<b>CATALYST DESIGN FOR FISCHER-TROPSCH SYNTHESIS .....</b>	<b>35</b>
<b>4.1.2</b>	<b>REACTOR TECHNOLOGY FOR FISCHER-TROPSCH SYNTHESIS .....</b>	<b>37</b>
<b>4.2</b>	<b>COBALT-BASED CATALYSTS DEVELOPMENT FOR FISCHER-TROPSCH SYNTHESIS .....</b>	<b>38</b>
<b>4.3</b>	<b>SBA-15 AS SUPPORT FOR FISCHER-TROPSCH SYNTHESIS .....</b>	<b>40</b>
<b>4.4</b>	<b>COBALT CATALYST DEACTIVATION UNDER FISCHER-TROPSCH SYNTHESIS CONDITIONS .....</b>	<b>43</b>
<b>4.5</b>	<b>FINAL CONSIDERATIONS .....</b>	<b>45</b>
<b>5</b>	<b>MATERIALS AND METHODS.....</b>	<b>47</b>
<b>5.1</b>	<b>MATERIALS .....</b>	<b>47</b>
<b>5.2</b>	<b>METHODS .....</b>	<b>47</b>
<b>5.2.1</b>	<b>SUPPORT PREPARATION .....</b>	<b>47</b>
<b>5.2.1.1</b>	<b>SBA-15 Synthesis .....</b>	<b>47</b>
<b>5.2.1.2</b>	<b><math>\gamma</math>-Al<sub>2</sub>O<sub>3</sub> Synthesis .....</b>	<b>48</b>
<b>5.2.2</b>	<b>CATALYST PREPARATION .....</b>	<b>48</b>
<b>5.2.2.1</b>	<b>Co/<math>\gamma</math>-Al<sub>2</sub>O<sub>3</sub> Preparation .....</b>	<b>48</b>
<b>5.2.2.2</b>	<b>Co/SBA-15 Preparation .....</b>	<b>49</b>
<b>5.3</b>	<b>CHARACTERIZATION METHODS .....</b>	<b>49</b>
<b>5.3.1</b>	<b>NITROGEN SORPTION ISOTHERMS .....</b>	<b>50</b>
<b>5.3.2</b>	<b>X-RAY DIFFRACTION (XRD) .....</b>	<b>51</b>
<b>5.3.3</b>	<b>FOURIER TRANSFORM INFRARED SPECTROSCOPY (FT-IR) .....</b>	<b>51</b>
<b>5.3.4</b>	<b>SCANNING ELECTRON MICROSCOPY (SEM) .....</b>	<b>52</b>
<b>5.3.5</b>	<b>TRANSMISSION ELECTRON MICROSCOPY (TEM) .....</b>	<b>52</b>
<b>5.3.6</b>	<b>THERMOGRAVIMETRIC ANALYSIS (TGA) .....</b>	<b>52</b>
<b>5.3.7</b>	<b>INDUCTIVELY COUPLED PLASMA OPTICAL EMISSION SPECTROMETRY (ICP-OES) .....</b>	<b>52</b>
<b>5.3.8</b>	<b>HYDROGEN TEMPERATURE PROGRAMMED REDUCTION (H<sub>2</sub>-TPR) .....</b>	<b>53</b>

5.3.9	TEMPERATURE PROGRAMMED DESORPTION (H <sub>2</sub> -TPD AND CO-TPD)	53
5.3.10	RAMAN MICROSCOPY	53
5.3.11	CATALYTIC TESTS	54
6	RESULTS AND DISCUSSION	59
6.1	CHARACTERIZATION	59
6.1.1	FOURIER TRANSFORM INFRARED SPECTROSCOPY (FT-IR) ANALYSIS	59
6.1.2	THERMOGRAVIMETRIC ANALYSIS (TGA)	60
6.1.3	N <sub>2</sub> -SORPTION ISOTHERM ANALYSIS	63
6.1.4	X-RAY DIFFRACTION (XRD) ANALYSIS	69
6.1.5	INDUCTIVELY COUPLED PLASMA OPTICAL EMISSION SPECTROMETRY (ICP-OES) ANALYSIS	72
6.1.6	SCANNING ELECTRON MICROSCOPY (SEM) ANALYSIS	73
6.1.7	TRANSMISSION ELECTRON MICROSCOPY (TEM) ANALYSIS	77
6.1.8	RAMAN SPECTROSCOPY ANALYSIS	85
6.1.9	HYDROGEN-TEMPERATURE PROGRAMMED REDUCTION ANALYSIS (H <sub>2</sub> -TPR)	88
6.1.10	TEMPERATURE PROGRAMMED DESORPTION ANALYSIS (H <sub>2</sub> -TPD AND CO-TPD)	90
6.2	CO HYDROGENATION TESTS	97
6.2.1	CO CONVERSION AND TOS	98
6.2.2	PRODUCT SELECTIVITY	104
6.2.2.1	The Anderson-Schulz-Flory distribution	109
6.2.3	REACTION RATES	112
6.3	POST-REACTION ANALYSIS	114
6.3.1	THERMOGRAVIMETRIC ANALYSIS (TGA)	115
6.3.2	RAMAN SPECTROSCOPY	117
6.3.2.1	The effect of Raman Scattering Laser Power	119
7	CONCLUSIONS AND SUGGESTIONS	123
7.1	CONCLUSIONS	123
7.2	SUGGESTIONS FOR FURTHER STUDIES	124
	REFERENCES	125
	APPENDIX A – FORMULAS AND DEFINITIONS	141
	APPENDIX B – N <sub>2</sub> -SORPTION ISOTHERMS	155
	APPENDIX C – CATALYST XRD ANALYSIS	162
	APPENDIX D – TEMPERATURE PROGRAMMED METHODS	169
	APPENDIX E – CATALYTIC TESTS	179

<b>APPENDIX F – BLANK REACTOR TEST .....</b>	<b>183</b>
<b>APPENDIX G – RAMAN ANALYSIS .....</b>	<b>185</b>



# 1 INTRODUCTION

Energy is one of the top ten global concerns nowadays. Its use has driven humankind advances since the ancient times and led to today's lifestyle. Nowadays, there is an obvious evidence of the negative impact of its usage worldwide, with an increased concern over the climate change, such as in global warming and local air pollution.

The countries involved in the Paris Agreement from December 2015 targeted at developing renewable energy sources and/or in energy efficiency improvements at three major segments: electricity, transportation and heating and cooling. The transportation sector is one of the most challenging in transitioning to a renewable energy future (FIGUERES et al., 2017; SAWIN; SEYBOTH; SVERRISSON, 2017).

Concomitantly, the chemical industry is also facing a challenge. Ethylene and propylene are the major building blocks for the production of chemicals, such as polymers, alcohols, acids, among others (LE VAN MAO et al., 2013). Overall, traditional processes for its production are limited by a rapid growth of demand (mainly of propylene) and a high consumption of energy (TORRES GALVIS; DE JONG, 2013), requiring more usage of crude oil as raw material.

Data from International Energy Agency (2017) show a worldwide energy source transition trend. The rate of this transition is not yet satisfactory, but this trend settles an opportunity for using alternative, cleaner fossil fuel energy sources, at least as a mid-term solution. The current target is natural gas, due to the large availability of reserves and improvements in extraction technologies (SAHA et al., 2016). Unfortunately, most of the gas is either being flared or its production sites are too far from the market.

Natural gas (NG) is a versatile gas composed mainly by methane, which can be used as a primary energy source or as raw material to obtain high value-added products. The gas-to-liquids (GTL) technology transforms NG to synthesis gas (a mixture of carbon monoxide (CO) and hydrogen (H<sub>2</sub>)) by reforming process prior to its transformation to high quality hydrocarbons by the Fischer-Tropsch Synthesis (FTS). FTS products are in a broad range of hydrocarbons, including olefins and paraffins. Hence, this places FTS as a strategic technology in this transitional scenario.

The FTS is an exothermic reaction that requires a catalyst to take place. The development of a FTS process requires a previous consideration of the reactor technology, catalyst size, shape

and formulation (PEREGO; BORTOLO; ZENNARO, 2009). There are two industrially employed FTS processes: Low-Temperature FTS (LTFTS) and High-Temperature FTS (HTFTS). Most industrial FTS processes use cobalt-based catalysts and most researches are mainly focused in improving LTFTS process.

To enable process feasibility, some approaches are enhancing the efficiency of the catalyst, which, at its best, means operating the reactor at conditions to produce the desired products, along with better understanding of the effects in which the catalyst deactivates; overall improving of the product yield, while mitigating deactivation effects; and improving the catalyst lifetime. Most studies in the literature were developed focusing on the optimization of C<sub>5+</sub> products, not always in a comprehensive way.

In this context, this study focused on obtaining a comprehensive understanding of Cobalt-based catalysts performance and deactivation for the CO hydrogenation reaction. The catalysts were supported over two high area supports – SBA-15 and  $\gamma$ -Al<sub>2</sub>O<sub>3</sub> and the effect of space velocity and temperature over the CO conversion and selectivity to lower olefins and paraffins was evaluated. Post-reaction characterizations provided insights about the deactivation mechanism, especially by carbon deposition.

This thesis is concisely structured in 7 chapters. From Chapter 1 to 4, the study proposal is given, with an Introduction, Objectives, Background and Literature Review, which provide basis for the comprehension of the following chapters. Chapter 5, Materials and Methods, succinctly provides the materials and procedures applied for the development of the study. Chapter 6, Results and Discussion, presents the results and concomitant discussion of each analysis. Conclusions are provided in Chapter 7. Finally, the References used for the development of the present study is also given. Further details, such as in the methods, or supplementary information are provided in APPENDICES A to G, as signalized in the text.

## 2 OBJECTIVES

The main objectives of this study are the development of cobalt-based catalysts supported on ordered mesoporous silica (SBA-15) and  $\gamma$ -Al<sub>2</sub>O<sub>3</sub> and its performance in the CO hydrogenation evaluation.

The specific objectives are:

- Synthesize the supports (SBA-15 and  $\gamma$ -Al<sub>2</sub>O<sub>3</sub>) and active phase impregnation;
- Characterize the structure, texture and superficial sites of the supports and catalysts;
- Carry out catalytic tests varying temperature and space velocity for a selected temperature to understand their effects over the production of lower olefins and high chain hydrocarbons;
- Carry out post-reaction analyses to evaluate catalyst stability and deactivation.



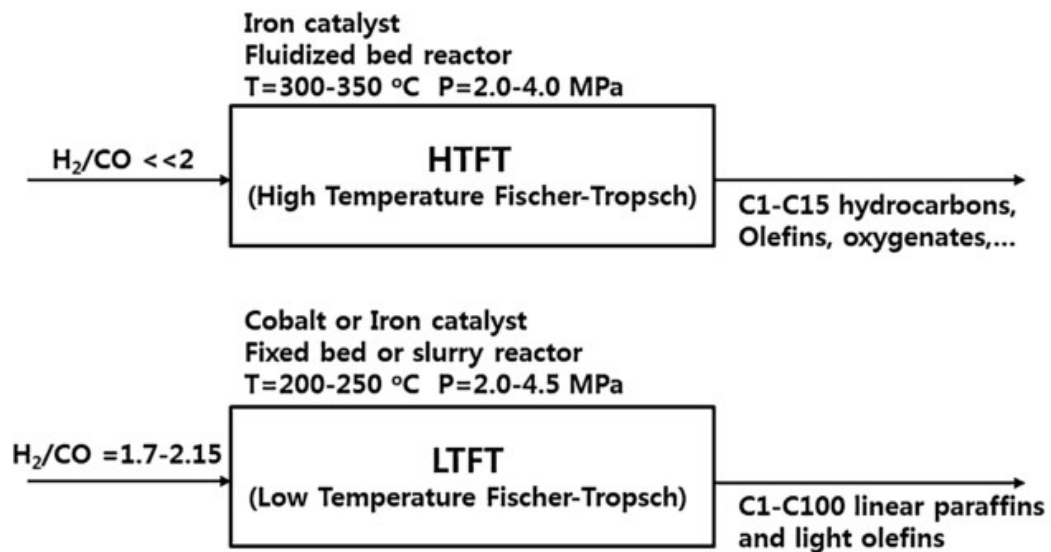
### 3 BACKGROUND

Here, a succinct background over Fischer-Tropsch Synthesis, main products and Anderson-Schulz-Flory (ASF) distribution is presented.

#### 3.1 FISCHER-TROPSCH SYNTHESIS

Fischer-Tropsch Synthesis (FTS), as aforementioned, is a process developed for the syngas conversion technology to produce syncrude. The FTS process can operate in two different conditions (Figure 1). The HTFTS is a two-phase reaction that operates at 300-350 °C and 18-30 bar ranges, using iron as the active phase, and aims to produce olefins and gasoline as main products (SIE; KRISHNA, 1999). The LTFTS is a multiphasic reaction (gas, liquid and solid) performed using mainly cobalt-based catalysts. It operates in temperatures such as 200-250 °C and generates diesel and wax (DRY, 2010).

Figure 1 – High-Temperature Fischer-Tropsch Synthesis (HTFT) and Low-Temperature Fischer-Tropsch Synthesis (LTFT) processes summarization



Source: Ahn *et al.* (2016).

The LTFTS Co-based catalysts present some advantages compared to Fe catalysts, since it presents high activity for FTS under ambient pressure, producing straight-chain hydrocarbons and negligible water-gas-shift reaction (WGS) activity. This means that the  $H_2/CO$  ratio has to be rigorously controlled and maintained close to stoichiometry due to the low water-gas-shift reaction activity (DRY, 2010). This requires the application of a WGS reactor prior to the FTS unit. Iron-based catalysts, on the other hand, requires higher pressures under reaction

conditions and has a stronger tendency to deactivation. The WGS activity is a relevant feature for iron as active phase since this reaction turns the catalyst more flexible for inlet H<sub>2</sub>/CO molar ratio (value ranges between 0.5-2.5) variations. Moreover, it is used more commonly for the production of olefins, aromatics, oxygenates and branched hydrocarbons (ABELLÓ; MONTANÉ, 2011).

The hydrocarbons formed in the LTFTS process are linear, such as *n*-alkenes and *n*-alkanes, branched such as largely monomethyl-substituted alkenes and alkanes, aromatics and oxygenates, mainly 1-alkanols, although ketones, aldehydes, and carboxylic acids are also found. The products can be used as synthetic natural gas, liquefied petroleum gas (LPG), motor gasoline, jet fuel, diesel fuel, lubricants, waxes and petrochemicals (PEREGO; BORTOLO; ZENNARO, 2009; PUSKAS; HURLBUT, 2003). The quality of the liquid fuels for final consumption is also determined by the refining design step (MAITLIS; KLERK, 2013). Equations (1)-(8) in Table 1 illustrate the stoichiometry of FTS reactions for the production of the most common products, with *n* being the carbon number of the products.

Table 1 – Main products from the FTS process and the respective chemical reactions

Product	H <sub>2</sub> /CO Ratio	Reaction	
Alkenes	2	$n\text{CO} + 2n\text{H}_2 \rightarrow (\text{CH}_2)_n + n\text{H}_2\text{O}$	(1)
Alkanes	$(2n+1)/n$	$n\text{CO} + (2n+1)\text{H}_2 \rightarrow \text{H}(\text{CH}_2)_n\text{H} + n\text{H}_2\text{O}$	(2)
Methanation	3	$\text{CO} + 3\text{H}_2 \rightarrow \text{CH}_4 + \text{H}_2\text{O}$ , $\Delta\text{H} = -206 \text{ kJ/mol}$	(3)
Alcohols	2	$n\text{CO} + 2n\text{H}_2 \rightarrow \text{H}(\text{CH}_2)_n\text{OH} + (n-1)\text{H}_2\text{O}$	(4)
Carbonyls	$(2n-1)/n$	$n\text{CO} + (2n-1)\text{H}_2 \rightarrow (\text{CH}_2)_n\text{O} + (n-1)\text{H}_2\text{O}$	(5)
Carboxylic Acids	$(2n-2)/n$	$n\text{CO} + (2n-2)\text{H}_2 \rightarrow (\text{CH}_2)_n\text{O}_2 + (n-2)\text{H}_2\text{O}$ , $n>1$	(6)
Aldehydes	-	$\text{H}(\text{CH}_2)_n\text{OH} \rightarrow \text{H}(\text{CH}_2)_{n-1}\text{COH} + \text{H}_2$	(7)
Water-gas-shift	-	$\text{CO} + \text{H}_2\text{O} \rightarrow \text{CO}_2 + \text{H}_2$	(8)

Source: Adapted from Maitlis and Klerk (2013).

Note: *n* represents the carbon number of the products.

The physical-chemical steps that describes the overall reaction rate and product distribution were detailed by Förtsch, Pabst and Gross-Hardt (2015):

- Diffusion of reactants into and inside the catalyst porous particle
- Adsorption of reactants onto active sites
- Chain initiation
- Chain growth
- Chain termination
- Product desorption

- Re-adsorption and further reaction
- Diffusion of products to the particle exterior

The product formation is ideally predicted by the Anderson-Schulz-Flory (ASF) arithmetic distribution. The ASF distribution describes a polymerization reaction that assumes that the chain growth probability  $\alpha$  is independent of the hydrocarbon chain length. The product distribution is given by Equation 1.

$$\frac{W_n}{n} = (1 - \alpha)^2 \cdot \alpha^{n-1} \quad 1$$

Where  $W_n$  is the mass fraction of the chain product with a carbon number (n) ratio and  $\alpha$  is the chain growth probability, which is defined as (Equation 2):

$$\alpha = \frac{R_p}{R_p + R_t} \quad 2$$

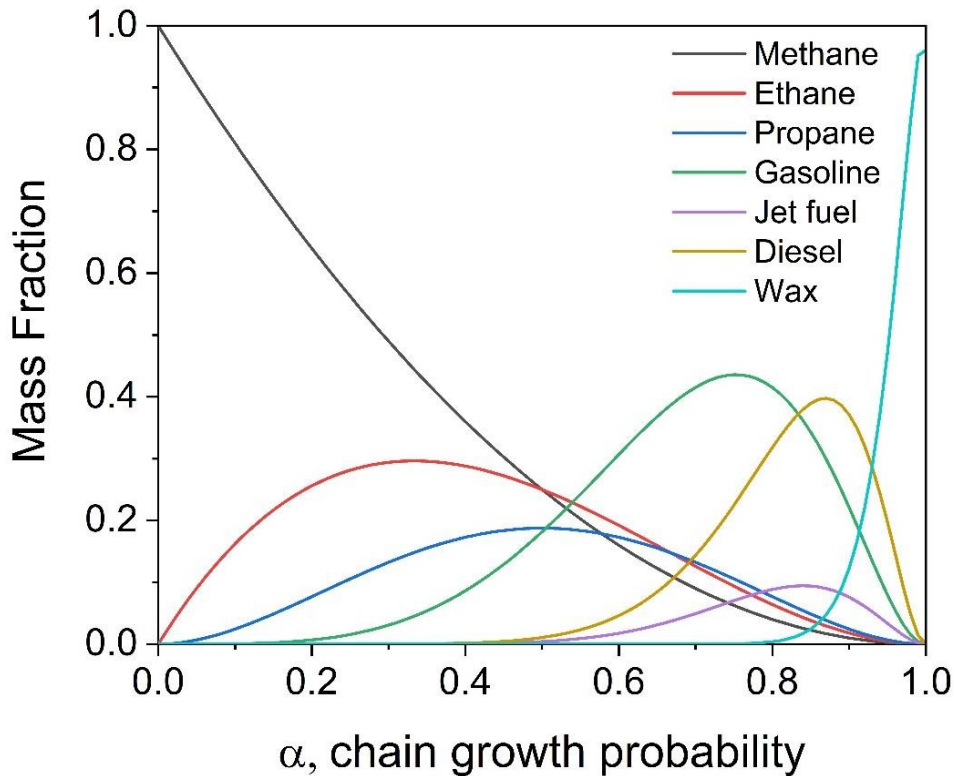
$R_p$  and  $R_t$  are the rate of propagation and termination, respectively (CLAEYS; VAN STEEN, 2005). Such definition is derived from the proposal of the polymerization mechanism for Fischer-Tropsch Synthesis for product distribution description. In the ideal surface polymerization, the value of  $\alpha$  is considered as constant.

To obtain  $\alpha$ , the Equation 1 is linearized, Equation 3.

$$\ln \frac{W_n}{n} = n \ln \alpha + \ln \left[ \frac{(1 - \alpha)^2}{\alpha} \right] \quad 3$$

Clearly, a semi-logarithmic plot of the product mole fraction as a function of carbon number produces a straight line and  $\alpha$  can be obtained from the slope. Such distribution is illustrated at Figure 2.

Figure 2 – Anderson-Schulz-Flory distribution of Fischer-Tropsch Synthesis products



Note: Gasoline ( $C_5$ - $C_{10}$ ), Jet fuel ( $C_{10}$ - $C_{12}$ ), Diesel ( $C_{10}$ - $C_{20}$ ) and Wax ( $C_{35+}$ ).

In practice, the ASF distribution presents some deviations. Overall, divergence occurs for  $C_1$  and  $C_2$  components, so applications of the distribution is recommended for  $n \geq 3$ . Other known deviation is for  $C_{10+}$ . Usually, catalysts that show the first deviation, also present divergences for higher hydrocarbons as well. In these cases, selectivity to  $C_1$  and  $C_{10+}$  is higher than to  $C_2$  and sometimes to  $C_3$ . Higher methane selectivity is explained by hotspots, while ethylene and, to some extent, propylene, present a higher reactivity, being quickly re-adsorbed and consumed to form higher hydrocarbons.

## 4 LITERATURE REVIEW

This section includes a review of the state-of-the-art of the FTS. Emphasis is on the general aspects that affect the reaction, such as the catalyst design and reactor technology, focusing on the development of advanced cobalt catalysts and its deactivation.

### 4.1 GENERAL ASPECTS OF FISCHER-TROPSCH PROCESSES

The FTS reaction is characterized as being a complex, exothermic transformation of syngas (a mixture of CO and H<sub>2</sub>) that results in a wide distribution of high-quality hydrocarbon products, such as middle-distillates, base-oils or waxes. The FTS is a heterogeneously catalyzed process, in which factors such as catalyst design, operating conditions and transport phenomena affect the catalyst performance.

#### 4.1.1 CATALYST DESIGN FOR FISCHER-TROPSCH SYNTHESIS

For this reaction takes place, the catalyst must present in its surface an active phase, such as a metallic nanoparticle. The active phase requirements are good H<sub>2</sub> adsorption and dissociative CO adsorption. Moreover, its oxide must be easily reducible under FT conditions (PEREGO; BORTOLO; ZENNARO, 2009).

Among all transition metals, currently, cobalt (Co)- and iron (Fe)-based catalysts are industrially applied due to economic and technical aspects, such as costs, availability, stability of the active phase and selectivity (AIL; DASAPPA, 2016). Iron-based catalysts are usual in High-Temperature FTS (HTFT) process for gasoline production and in Low-Temperature FTS (LTFT) process for the production of olefins. Co-based catalysts are more expensive than Fe, however, it is more resistant to deactivation. It is used for LTFT synthesis and suitable for the production of linear, heavy chain hydrocarbons, such as diesel. Along with its long lifetime and low water-gas-shift-reaction activity features, it is often used in industrial processes (DRY, 2004).

To modify the distribution of products from CO hydrogenation and to achieve a high yield, the selection of an adequate metallic load, dispersion and particle size, support and promoters is necessary due to its known impacts over product selectivity and catalyst stability. Promotion of cobalt-based catalysts is usually performed by adding small amounts of noble metals, such as

Ru, Re or Rh. The addition of noble metals improves metal reducibility, activity and dispersion. It can also reduce aggregation by reducing cluster's sizes (DIEHL; KHODAKOV, 2009). Cu addition also improves its activity and reduces the reduction temperature, but leads to enhanced CO<sub>2</sub> production rate (WANG et al., 2013).

There is a special effect of catalyst's crystalline phase or morphology into its activity and selectivity. Firstly, it is already known that Co nitrate precursors shows the highest basicity, degree of reduction and particle size, impacting positively in its FTS performance, although producing the highest amount of poor reducibility when supported over oxides (GHOLAMI; TIŠLER; RUBÁŠ, 2021). It is also known that nanoparticles < 20 nm are stable as pure face centered cubic (fcc)-Co. fcc-Co structure is formed at higher temperatures and is less active than its counterpart, hexagonal-close packed (hcp)-Co phase (ZHANG; KANG; WANG, 2010). Claeys (2016) has shown that Mn promotion altered the structure of cobalt carbide from presenting insignificant activity (it is in fact one of the reasons that cobalt catalyst deactivates – see section 4.4) and selectivity to form cobalt carbide nanoprisms, resulting in a catalyst presenting a selectivity to lower olefins as high as 61% at 523 K.

As aforementioned, another important factor in catalyst design is the support. Usually, alumina, silica, active carbon, zeolite or silica-alumina are employed as support material due to their high metallic dispersion and superficial area (SCHMAL, 2011). Other oxides, such as TiO<sub>2</sub>, ZrO<sub>2</sub>, MgO, and Nb<sub>2</sub>O<sub>5</sub> have also been studied for this reaction. Due to the existence of the strong-metal-support-interaction (SMSI) phenomena, niobia may be more advantageous than titania. The SMSI in niobia favors the production of high chain hydrocarbons and leads to a good resistance against destruction during the catalytic reaction, which is favorable for industrial applications (SILVA et al., 1993). Reuel and Bartholomew (1984) evaluated different oxides as supports and determined that the activity for CO hydrogenation is: Co/TiO<sub>2</sub> > Co/SiO<sub>2</sub> > Co/Al<sub>2</sub>O<sub>3</sub> > Co/C > Co/MgO.

Actual efforts are directed to the development of structuring at different scales (GÜTTEL; TUREK, 2016). Bezemer and coworkers (2006) showed that the reaction is structure insensitive and determined that the ideal cobalt particle size, in terms of stability, C selectivity and availability of active surface sites for the reaction ranges from 6-8 nm; smaller particles may easily deactivate due to oxidation, sintering, coking, among others. Hence, advanced oxide supports, such as SBA-15 and mesoporous alumina may play an important role by controlling the active phase particle size.

#### 4.1.2 REACTOR TECHNOLOGY FOR FISCHER-TROPSCH SYNTHESIS

Currently, it is widely accepted that reactor performance, including productivity, relies strongly on heat and mass transfer effectiveness. Diffusional limitations impact the catalyst performance at any given operating condition (IGLESIA et al., 1993). Reactors for this process are the multi-tubular fixed-bed operated in trickle flow regime (FBR) or slurry bubble column (SBCR).

The FBR is suitable for the production of heavier FTS products. It is easy, straightforward and safe to upscale. Issues presented by this reactor type are related to diffusional limitations for the overall reaction rate, radial temperature profiles due to the relatively poor heat conductivity and heat transfer to the tube walls and relevant pressure drop (SIE; KRISHNA, 1999). The slurry bubble column reactor (SBCR) is considered as suitable for the production of heavy hydrocarbons. However, upscaling of SBCR is not trivial. Backmixing, catalyst attrition and separation of the catalyst from the liquid products are major problems (VISCONTI et al., 2011). These issues, along with individual limitations of both reactors, have provided an incentive for researchers in presenting new solutions.

Reactors employing structured catalysts are aligned with such criteria, presenting itself as a suitable alternative. Some of the advantages of using such catalysts are high selectivity and flexible design at high productivities, while eliminating most of the issues of the conventional reactors (NIJHUIS et al., 2001). Some examples of structured catalysts are: honeycomb monoliths, foams, knitted wires, cross flow structures and microchannel reactors (ALMEIDA et al., 2011; HOLMEN et al., 2013; PANGARKAR et al., 2009; VISCONTI et al., 2009). Microchannel reactors are the most efficient in terms of heat removal (LEVINESS et al., 2014; ROBOTA et al., 2014). The monolithic loop reactor (MLR) is suggested as being the most suitable configuration for violently exothermal reactions (KREUTZER; KAPTEIJN; MOULIJN, 2006).

When used in the MLR configuration, ceramic monolithic pieces stacked inside of the reactor enables the creation of stages for reagent feed, cooling of liquid products or even water vapor removal. The usage of the external heat exchanger and oil circulation turns the cooling step independent of the reactor, which is important for the almost adiabatic ceramic monolith. This feature, along with its plug-flow regime behavior (Taylor flow) permits process modifications for the use of more active catalysts, without limiting both mass transfer or productivity (DE DEUGD; KAPTEIJN; MOULIJN, 2003). Finally, developing such technology could also bring

advantages in applications in distant places, such as for natural gas transformation in offshore platforms, which in turn could potentially reduce transportation and improve process feasibility for this application (SCHANKE; BERGENE; HOLMEN, 2001).

At last and as aforementioned, Güttel and Turek (2016) suggests that the trend for FTS performance optimization should be directed at structuring in different scales. For instance, in terms of catalyst development, Montes' research group recently published two studies using cobalt-based bimodal alumina catalysts (presenting both macro- and mesopores) over metallic monoliths (aluminum and FeCrAlloy) (MERINO; SANZ; MONTES, 2017a, 2017b). Both studies showed the effects of several parameters, such as catalyst layer thickness, thermal conductivity, cell density over the catalyst activity and selectivity. Moreover, the existence of macroporosity and efficient heat removal resulted in increased  $\text{C}_2$  selectivity and reduced methane selectivity. More recently, Fratalocchi *et al.* (2022) showed that an aluminum packed-Periodic Open Cellular Structure (POCS) reactor with Co/Pt/ $\text{Al}_2\text{O}_3$  presenting a 3D-printed metallic skin significantly improved temperature control inside the reactor, maintaining a good activity and selectivity performance. A maximum external temperature difference of 11 K was reached at  $T = 523$  K, in which a CO conversion of 85% and a  $\text{CH}_4$  selectivity of 23.4% was reached.

## 4.2 COBALT-BASED CATALYSTS DEVELOPMENT FOR FISCHER-TROPSCH SYNTHESIS

Cobalt-based catalysts for FTS have been applied industrially since the very beginning of the technology, with the first FTS plant of Ruhrchemie in 1935 using it as a “standard catalyst”. Its composition of 100 Co:100 Kieselguhr:18  $\text{ThO}_2$  (by weight) was used for 40 years (PICHLER, 1952). Currently, Co/ $\text{Al}_2\text{O}_3$  protected with  $\text{SiO}_2$  (VOGEL; VAN DYK; SAIB, 2015) or promoted with Pt (BOTES; VAN DYK; MCGREGOR, 2009) are examples of FTS catalysts applied in industry.

The cobalt-based catalysts historical development is divided into two important periods: Discovery and commercial development of the technology (1902 – 1949) and the Rediscovery of cobalt and GTL process (1975 - present) (BARTHOLOMEW, 2003).

Although the Discovery period has started with Sabatier and Senderens's study in 1902, which reported the formation of methane from a mixture of  $H_2$  and CO using Nickel (Ni) or Cobalt (Co) catalysts (SABATIER; SENDERENS, 1902), it was the patented process by the German scientists Franz Fischer and Hans Tropsch at 1926 that has marked the FT reaction. After the discovery, several implementations resulted in a standard catalyst, which was produced industrially using cobalt nitrate precursor. The pressure effect on the selectivity at Co-based catalysts was later found and optimized at the range of 5-20 atm (PICHLER, 1952).

The oxide supports can interact with cobalt nanoparticles, creating stable phases such as aluminates and silicates. Promotion with noble metals or other oxides can enhance cobalt nanoparticles reducibility (KHODAKOV; CHU; FONGARLAND, 2007) and reduce its aggregation by reducing cluster sizes (DIEHL; KHODAKOV, 2009). For silica supports, researchers used the silica surface functionalization with organosilanes to improve metal dispersion and active phase reducibility. For instance, Eyring and coworkers (2005) and, more recently, Jia *et al.* (2011) showed that SBA-15 (which is a ordered mesoporous silica, OMS) functionalization with hexamethyldisilazane (HMDS) prior to impregnation improved catalyst performance due to the hindrance of significant interactions between cobalt oxide species and SBA-15 surface.

Mandegari and coworkers (2014) performed a design of experiments (DOE, specifically a fractional factorial design) to establish a relationship among CO conversion,  $C_{5+}$  selectivity and methane selectivity to operational parameters, such as temperature, pressure, GHSV, and cobalt loading. They prepared a cobalt-based bulk monolithic catalyst composed of carbon nanotubes. The results not only corroborated the effects of the parameters over the catalyst performance, but the DOE also showed that pressure, pressure-cobalt loading and temperature-GHSV synergistic interactions presented the most significant effects over the  $C_{5+}$  and methane selectivities.

Tsolakis *et al.* (2017) performed a parametric study and a multiobjective optimization of a FBR with 37% Co/SiO<sub>2</sub> catalyst, using Matlab, in order to optimize the selectivity to carbon dioxide (CO<sub>2</sub>) and hydrocarbon products and the syngas conversion. Studies were carried out at  $1800 \leq GHSV \leq 7500 \text{ NmL.g}_{\text{cat}}^{-1}.\text{h}^{-1}$ ,  $470 \leq T \leq 530 \text{ K}$ ,  $1 \leq P \leq 30 \text{ bar}$  and  $1 \leq H_2/CO \leq 3.2$  molar ratio. Assumptions considered no mass or heat transfer hindrance. It was showed that CO conversion and  $C_{5+}$  selectivity are inversely related to all factors, except to pressure effect. Selectivity to methane (CH<sub>4</sub>) and CO<sub>2</sub> seems to follow the same trend as CO conversion (except for pressure

as well) and H<sub>2</sub> conversion, respectively. The olefins selectivity seems to be slightly affected by temperature and GHSV, while the olefin-to-paraffin ratio seems to be inversely affected by temperature. Results are summarized at Table 2. The best condition from the study was high pressure and H<sub>2</sub>/CO ratio and low temperature and GHSV.

Table 2 – Effect of operational factors over the reaction performance

		Factors			
		Temperature	Pressure	GHSV	H <sub>2</sub> /CO molar ratio
H <sub>2</sub> conversion	$X_{H_2}$	↑	↑	↓	↓
CO conversion <sup>a</sup>	$X_{CO}$	↑	↑	↓	↑
CH <sub>4</sub> selectivity <sup>b</sup>	$S_{CH_4}$	↑	↓	↓	↑
CO <sub>2</sub> selectivity	$S_{CO_2}$	↑	↑ <sup>c</sup>	↓	↓
Olefins selectivity	$S_{C_2-C_3}$	↑ <sup>c</sup>	↓	↓ <sup>c</sup>	↑
Olefin/paraffin ratio	$S_O/S_P$	↓	-	↓ <sup>c</sup>	↓ <sup>c</sup>
Light paraffins	$S_{C_2-C_7}$	↑	↓	-	↑
Liquid products	$S_{C_5+}$	↓	↑	↑	↓

Source: Moazami *et al.* (2017).

Notes: (a) – All the operating process conditions, except space velocity, have positive impact on CO conversion;

(b) – The effects of all process conditions on CH<sub>4</sub> and C<sub>5+</sub> products obtained completely on the opposite direction;

(c) – Slightly changed.

Gavrilović *et al.* (2021) studied the performance of a commercial type cobalt-based catalyst (20%Co-0.5%Re/γ-Al<sub>2</sub>O<sub>3</sub>) for the FTS reaction. H<sub>2</sub>/CO molar ratio, CO conversion, reaction temperature, and water addition effects were investigated, and data was used for mechanistic model fitting. Increasing CO conversion lead to increased C<sub>5+</sub> and CO<sub>2</sub> selectivities and decreased CH<sub>4</sub> selectivity and olefin-to-paraffin ratio. FTS reaction seemed to improve with water addition and CO conversion increase, resulting in increased selectivity to C<sub>5+</sub>, while the activity to WGS seemed to emerge as well at high CO conversion due to high water partial pressure and at low H<sub>2</sub>/CO molar ratios. Small cobalt nanoparticles re-oxidation seemed to be the main deactivation mechanism detected by the authors, while sintering may have occurred at higher temperature.

### 4.3 SBA-15 AS SUPPORT FOR FISCHER-TROPSCH SYNTHESIS

As previously mentioned, nonionic block copolymers, such as P123, could be used to the direct formation of OMS, giving birth to SBA-15 (ZHAO *et al.*, 1998). Although silica is an amorphous material, the resulting OMS presents a uniform pore size distribution with a large

specific surface area. Clearly, these features are advantageous for several applications, including heterogeneous catalysis. The advantages of employing SBA-15 as supports are greater active phase reducibility, enhanced Co nanoparticle dispersions, customizable porous structure and possibility of surface special modifications.

The hexagonal structure of SBA-15 was formed in three steps: spherical micelle formation of P123 block copolymer at the beginning of the reaction, which evolves to the formation of a cylindrical micelle due to the formation of hybrid organic-inorganic micelles and, finally, the aggregation of such micelles into a 2 dimensional (2D) hexagonal structure, whose connections are formed by the condensation of silicate species in the voids. The hydrothermal treatment and calcination leads to further condensation and densification of the silica structure (ZHOLOBENKO *et al.*, 2008).

When synthesizing this type of material, one can control its geometry (LEE *et al.*, 2010; ZHAO *et al.*, 2000), pore length and diameter (JOHANSSON; BALLEM, 2011; ZHANG *et al.*, 2004), and wall thickness (CHOI *et al.*, 2003). In other words, SBA-15 as a support material is important for fine tuning nanoparticle size, while maintaining high dispersion. Moreover, the same textural parameters also affected the diffusion of gaseous reactants and liquid products, which affected the catalyst activity and selectivity, as showed by Tang *et al.* (2006).

Díaz and coworkers (2003) showed that using the same load of Co (20 wt.%) over SBA-15 catalysts based on nitrate precursors led to a 1.5 times more active catalyst than employing conventional SiO<sub>2</sub> due to a higher dispersion (compared to the former), although maintaining a comparable intrinsic activity. Moreover, there was the formation of more hydrocarbons than alcohols or CO<sub>2</sub> under the same reaction conditions. The hydrocarbon product distribution was different: Co/SBA-15 catalyst produced more hydrocarbons in the gasoline range, while Co/SiO<sub>2</sub> presented a slightly higher selectivity to C<sub>10+</sub> products. Lower loadings (10 wt.%) resulted in less reducible catalysts affecting negatively the product distribution of hydrocarbons. Khodakov, Bechara, and Griboval-Constant (2003) also showed that the increased dispersion and narrow pores of mesoporous silica led to greater selectivity and reduced sintering of cobalt nanoparticles.

The pore size effect of SBA-15 support over the catalyst performance has also been assessed. Li and coworkers (2008) showed that, for a 30 wt.%Co/SBA-15 catalyst, an initial positive effect of increasing pore size over the catalyst activity (CO conversion ranges from ~19% to ~42%, then decreases) and C<sub>5+</sub> selectivity (ranging from ~75% to ~87%) occurs until reaching

a plateau. The range that presented the best results were of 6-15 nm pore size. In both studies cited earlier, cobalt nanoparticles were located both on SBA-15 internal and external surfaces. Khodakov *et al.* (2002) also demonstrated similar results using a 5 wt.% Co over silica mesoporous materials, including MCM-41 and SBA-15.

Arribas and coworkers (2009) showed the influence of the pore length over the catalyst features on a given pore diameter (11 nm) for a Co(Ru)/SBA-15 catalyst. Using larger SBA-15 pore lengths (>5  $\mu\text{m}$ ) resulted in catalysts with relevant intraparticle diffusional effects, affecting either active phase preparation (calcination and reduction steps) and performance under reaction conditions. Hence, the length can impact even more significantly than the pore size of the OMS. The medium length SBA-15 particles ( $\sim 1.15 \mu\text{m}$ ) prepared by these authors seem to present the best cost-benefit ratio. That is, although there is a slight difference between selectivity features of small- and medium-length SBA-15 particles of the same diameter (81.9 and 80.8%, respectively), the overall reduction temperature was smaller, and the catalytic activity, based on the steady Co-time-yield after a time-on-stream (TOS) of 8h, was the highest among the tested catalysts (285 and 269 mmol CO.g<sup>-1</sup>.h<sup>-1</sup> for the medium and small length, respectively). Overall, tuning the size of the pores (both length and diameter) of SBA-15 is crucial, since it dictates the total time that a molecule spends reacting within the particle (LEE *et al.*, 2010).

Albuquerque, Costa and Barbosa (2019) prepared SBA-15 supported catalyst, using cobalt as active phase and cerium as promoter, for the study of the formed products by the ASF distribution. Results showed that the ASF distribution must consider the higher hydrocarbons contribution, such as from waxes, for a more precise determination of the chain growth probability. The Co/Ce/SBA-15 catalyst deactivated considerably due to water formation and provided the highest production of HC in the range of light olefins, followed by gasoline, at T = 493 K, P = 20 bar and GHSV = 1.62 I<sub>syngas.g<sub>cat</sub></sub><sup>-1</sup>.h<sup>-1</sup> for 8h. GHSV in which data was acquired was not provided by authors.

Gupta *et al.* (2021) prepared two different 15% Co-0.1% Pd based catalysts, using mesoporous alumina (MA) and SBA-15 as supports. Results showed that the presence of Pd enhances Co reducibility and increases CO conversion. Moreover, the nature of the support affects the hydrocarbon selectivity, in which the SBA-15-based (silica) catalyst favored the production of lighter hydrocarbons in the C<sub>6</sub>-C<sub>12</sub> range while the MA-based favored the production of hydrocarbons in the C<sub>13</sub>-C<sub>20</sub> range. Noteworthy is the  $\alpha$  value of 0.80 for the MA-supported

catalyst, which was determined by linearization of the ASF distribution under a mole fraction base.

Toncón-Leal *et al.* (2021) evaluated Fe, Co and bimetallic Fe-Co catalysts supported over SBA-15. Activity and selectivity to hydrocarbons and CO<sub>2</sub> were measured under different temperatures (420-630 K), and a synergy between Fe and Co was observed, with bimetallic catalyst presenting a higher performance and low coke production. The SBA-15(7Fe3Co) showed the highest activity and selectivity to C<sub>2</sub>-C<sub>4</sub> and C<sub>5</sub>-C<sub>9</sub> at lower temperatures (480-510 K), followed by SBA-15(10Co)  $\approx$  SBA-15(3Fe7Co) (up to 573 K, from which the latter presented higher performance) and SBA-15(10Fe). Noteworthy is that SBA-15(3Fe7Co) presented higher selectivity to C<sub>10+</sub>, when compared to the SBA-15(10Co).

#### 4.4 COBALT CATALYST DEACTIVATION UNDER FISCHER-TROPSCH SYNTHESIS CONDITIONS

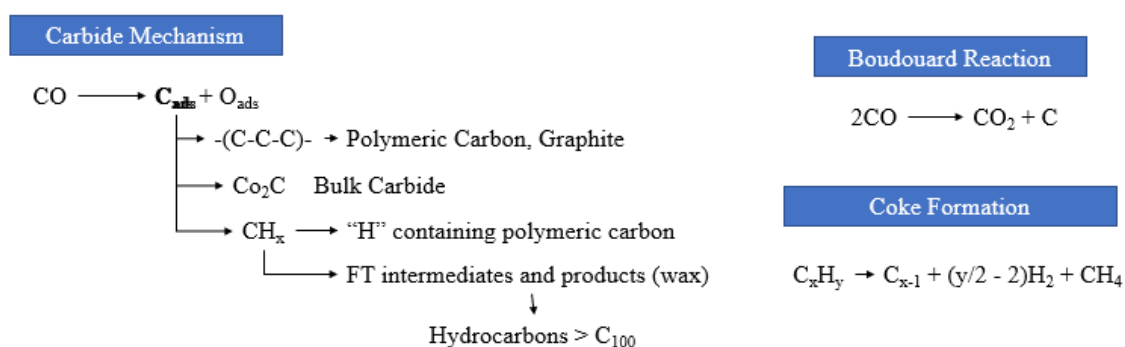
Catalyst deactivation may lead to loss of activity, hydrocarbons productivity, and altered selectivity. Involved costs affect process efficiency and therefore improving catalyst lifetime remains challenging. The most common deactivation mechanisms that can affect the catalyst performance over time are poisoning, the occurrence of Boudouard reaction, with the formation of coke over the catalyst active sites, sintering of cobalt crystallites due to high temperatures and hotspots due to reaction's exothermic nature, active phase carbidization and re-oxidation due to the presence of steam in high temperatures and pressures, which can also impact the support structure and sintering, along with metal-support interaction (TSAKOUMIS *et al.*, 2010).

Zhou *et al.* (2006) evaluated the effect of the H<sub>2</sub>/CO molar ratio over the deactivation of a Co/SiO<sub>2</sub>. The catalysts were tested under a high TOS prior to assessment. Results showed that higher H<sub>2</sub>/CO values (up to 3) led to higher deactivation rates due to the formation of silicates and/or hydrosilicates over the catalyst surface or small crystallites, while sintering was the less important deactivation mechanism. Deactivation seemed to be facilitated by high H<sub>2</sub> partial pressures, since H<sub>2</sub>O in tail gas was constant for all tested conditions.

Moodley (2008) also provided insights about cobalt-based catalyst deactivation. Fresh catalysts present a very sharp decline in activity, followed by a slow steady-state deactivation. Along with aforementioned deactivation mechanisms, fouling by wax, deposition of inert/deactivating

carbon phases and surface reconstruction were also given. The carbon formation over cobalt-based catalysts is complex and few possible modes are presented in the literature (Figure 3). The transition from less to more stable carbon over the catalyst (surface and bulk) is function of temperature, pressure and TOS, although support type (for instance, more acidic supports tends to increase carbon deposition) and partial pressure of CO and H<sub>2</sub>, along with the effects of combined parameters, can also impact carbon formation and stabilization

Figure 3 – Routes for carbon deposition in cobalt-based catalysts for Fischer-Tropsch Synthesis



Source: Adapted from Moodley (2008).

Yan *et al.* (2009) prepared a model Co/SiO<sub>2</sub> catalyst and studied the effect of temperature, and pressure on kinetics and chain growth probability. Results were very aligned to real catalysts, including turnover frequency (TOF) and activation energy (0.026 s<sup>-1</sup> and 93 kJ/mol, respectively). In this case, the catalyst was deactivated due to the formation of carbonaceous deposition, while oxidation or carbide formation was not observed.

Sadeqzadeh *et al.* (2014) investigated the deactivation mechanisms of a conventional 25% Co-0.1% Pt/ $\gamma$ -Al<sub>2</sub>O<sub>3</sub> catalyst at different syngas composition and temperatures by modelling considering three deactivation mechanisms: sintering, oxidation and coking. According to these authors, water-assisted sintering mechanism explains the initial deactivation rates, especially for low H<sub>2</sub>/CO molar ratios, while oxidation and coking, especially for increased temperature, explain long-term deactivation.

Lancelot *et al.* (2014) investigated the oxidation mechanism of a conventional 25% Co-0.1% Pt/ $\gamma$ -Al<sub>2</sub>O<sub>3</sub> catalyst at 220 °C and H<sub>2</sub>/CO of 2 by varying the temperature and GHSV, focusing on determining the temperature effect and long-term deactivation assessment. Under high CO conversion (~100 %) and higher temperatures ( $\geq 613$  K), a cobalt oxide shell is formed on the surface of metallic nanoparticles, which can be the major reason of catalyst deactivation. It can

be accompanied with the formation of hot spots at the beginning of the reaction and lead to cobalt nanoparticle sintering in such conditions. Noteworthy is that the test conducted at 513 K for a long period (~170 h) by authors also showed catalyst deactivation.

Wolf, Fischer and Claeys (2020) provided insightful remarks about the effect of water in inducing deactivation of cobalt-based catalysts by several mechanisms. Water partial pressure, along with a reasonable amount of CO, seemed to affect the catalyst deactivation over nanoparticle oxidation, hydrothermal sintering and the formation of metal-support compounds. Each deactivation type was affected either by nanoparticle size and/or support type. Overall, while the FTS reaction is occurring, CoO is formed due to CO dissociation. If the  $p_{H_2O}/p_{H_2}$  is high enough, formed CoO is unable to be regenerated by the presence of  $H_2$ . The authors discussed that the  $p_{H_2O}/p_{H_2}$  effect has a threshold that depends on the nanoparticle size, depending on the allotrope, although hcp is less stable, support type, especially SiO<sub>2</sub>, and CO conversion. If the nanoparticle is small enough, increased oxidation of thermodynamically unstable nanoparticles facilitates particle coalescence, leading to hydrothermal sintering, which can be hindered by metal-support interaction. The formation of metal-support compounds (MSC) via solid-state reactions is irreversible under FTS reaction conditions and is rather derived from CoO than from Co. Moreover, its formation is difficult to be identified and unlikely for Co/SiO<sub>2</sub>, but possible for Co/Al<sub>2</sub>O<sub>3</sub>.

#### 4.5 FINAL CONSIDERATIONS

Several studies on the literature have already evidenced some of the most relevant aspects of the catalysts for the Fischer-Tropsch Synthesis. Overall, catalyst performance (conversion and selectivity) using cobalt as active phase under a range of operational conditions, such as varying pressure, temperature, space velocity and inlet composition and varied support compositions, morphologies and textural features have been studied extensively. However, focus has been given on alumina and silica supports, whereas studies of deactivation with TOS have been most extensive for the former.

Considering the nature of the reaction, the literature suggests that a greater control of mass and heat transfer by structuring in different scales can improve the catalyst performance. In agreement to this suggestion, studies using SBA-15 have shown interesting results for the CO hydrogenation reaction. However, most studies are based on the effects of isolated features, e.g. catalyst morphology, textural features and metal load effect over its performance, with a recent

study focused on determining the ASF distribution for the SBA-15-based catalyst (ALBUQUERQUE; COSTA; BARBOSA, 2019). Studies focused on deactivation were more driven to understanding the water effect over the support structure, but few studies determined quantitatively (PRIETO et al., 2009) or qualitatively (TONCÓN-LEAL et al., 2021) the deactivation of this type of catalyst, especially focused on carbon formation with TOS using specific techniques such as Raman. In this study, a comprehensive understanding of Cobalt-based catalysts performance and deactivation for the CO hydrogenation reaction was investigated, including the effect of operating conditions and post-reaction carbon deposition.

## 5 MATERIALS AND METHODS

Materials and methods employed in the present study are succinctly described in this section. Appendix materials provides more details when necessary.

### 5.1 MATERIALS

The materials used for the preparation of the support SBA-15 and Alumina were: Pluronic<sup>®</sup> P123 triblock copolymer (molecular weight of ~ 5800 g/mol, BASF), Tetraethyl-*orto*-silicate (TEOS) 98% (GC) (Sigma-Aldrich), Hydrochloric Acid P.A. ACS reagent  $\geq 37\%$  (Fluka), Urea P.A. (Sigma-Aldrich), Aluminum Nitrate Nonahydrate  $\geq 98\%$  (Nuclear), Silver Nitrate P.A. (Casa Americana). For the impregnation of cobalt oxide, it was used Cobalt Nitrate Hexahydrate P.A. ACS reagent 98% (Vetec).

### 5.2 METHODS

In this section, a succinctly description of the methodology used in the present study is given. Equations for catalyst preparation, quantification, activity, selectivity, among others, are described in detail at APPENDIX A.

#### 5.2.1 SUPPORT PREPARATION

Details about support preparation (SBA-15 and alumina-based) are given in the following section.

##### 5.2.1.1 SBA-15 Synthesis

The SBA-15 support was prepared according to the literature (HEWER et al., 2018; ZHAO et al., 1998). In short, the SBA-15 preparation was performed using 8 g of Pluronic P123 in 250 mL with 2 M HCl solution at 313 K. After polymer dissolution, the solution was transferred to a magnetically stirred flask. The volume was set to 300 mL using deionized water and the temperature of the system was set to ~315 K. The temperature of the system was stabilized prior to the addition of 17.8 mL of TEOS; afterward, the reaction was allowed to occur in a controlled way for a period of 24 h. The prepared SBA-15 was submitted to hydrothermal solution during 48 h at 373 K in a 70 mL autoclave Teflon capsule. The SBA-15 was then filtered and washed

several times in a row using deionized water. The washing step proceeded until no chloride ion in the filtrate was qualitatively detected, using a 0.1 M silver nitrate solution. The resultant filtered SBA-15 was then dried at 333 K overnight prior to the thermal treatment. The calcination step was performed at 2 K/min under a N<sub>2</sub>-flow (~2 L/min) up to 813 K, followed by air-flow (~1.5 L/min, produced by an aquarium pump) step at a constant temperature for 4 h.

### 5.2.1.2 $\gamma$ -Al<sub>2</sub>O<sub>3</sub> Synthesis

The  $\gamma$ -Al<sub>2</sub>O<sub>3</sub> support was prepared using the urea synthesis method, reported in the literature (BRACKMANN; PEREZ; SCHMAL, 2014; VOGELS; KLOPROGGE; GEUS, 2005). The preparation was accomplished by mixing 100 mL aluminum nitrate solution (750 g/L) with a 200 mL urea solution (400 g/L), both kept at 323 K in order to allow the salts being completely dissolved. The mixed solution was mechanically stirred for 15 min and the temperature of the water bath was set at 363 K. The reaction was allowed to occur until the formation of a pseudo-boehmite (Al(OH)<sub>3</sub>) white gel, which occurred after ~ 20 h. The resultant gel was removed from the flask and cooled to the room temperature prior to the thermal treatment. The material was dried at 473 K for 2 h at a 2 K/min heating ramp and calcined at 773 K for 5 h in air-flow (1.5 L/min) at 5 K/min. The obtained  $\gamma$ -Al<sub>2</sub>O<sub>3</sub> support was manually grounded using a pistil and stored.

## 5.2.2 CATALYST PREPARATION

Details about catalyst preparation (SBA-15 and alumina-based) are given in the following section.

### 5.2.2.1 Co/ $\gamma$ -Al<sub>2</sub>O<sub>3</sub> Preparation

The  $\gamma$ -Al<sub>2</sub>O<sub>3</sub> support was impregnated with cobalt using cobalt nitrate precursor by the incipient wetness impregnation method, as described elsewhere (HILMEN et al., 2000). 2 g of  $\gamma$ -Al<sub>2</sub>O<sub>3</sub> support was dried for 24 h at 373 K prior to the impregnation step. The nominal w/w Co concentrations of the catalysts were 5, 10 and 15%. A multi-step procedure was performed in order to improve metal dispersion. The solution was added dropwise and repeated until reaching the desired metal content. The support plus the metal precursors were dried at 373 K for 1 h. The samples were dried at 393 K for 18 h and calcined in air at 573 K for 2 h. The support was

re-calcined in air following the same procedure, except that the calcination step was performed at 673 K for 2h.

#### **5.2.2.2 Co/SBA-15 Preparation**

The SBA-15 support was impregnated with Co using cobalt nitrate as precursor and employing the same method. 5 g of SBA-15 support was dried for 24 h at 373 K prior to the impregnation step. A multi-step procedure was performed similarly in order to improve metal dispersion. The support plus the metal precursor were dried at 373 K for 1 h. The nominal active phase load, expressed as Co weight percentage of the catalyst, was 15%.

### **5.3 CHARACTERIZATION METHODS**

In order to verify the efficiency of the preparation methods, several characterizations were performed. Table 3 summarize the catalysts/supports prepared and the characterizations performed for each material. The 10% Co/SBA-15 catalyst was not considered in this work due to reaction system equipment (PID Eng&Tech) limitations.

Table 3 – Characterizations performed for each sample developed in this study

Characterization	Samples						
	Support		Catalysts				
	ALU <sup>1</sup>	SBA <sup>2</sup>	5% Co/ ALU <sup>1</sup>	10% Co/ ALU <sup>1</sup>	15% Co/ ALU <sup>1</sup>	10% Co/ SBA <sup>2</sup>	15% Co/ SBA <sup>2</sup>
N <sub>2</sub> – Sorption	X	X	X	X	X	X	X
XRD	X	X	X	X	X	X	X
FTIR		X					
SEM	X	X	X	X	X		X
HR-TEM		X	X	X	X	X <sup>3</sup>	X
TGA/DTA	X	X	X	X	X	X	X
ICP-OES			X	X	X	X	X
H <sub>2</sub> -TPR			X	X	X	X	X
H <sub>2</sub> -TPD			X	X	X		X
CO-TPD							X
Raman (Pre-Reaction)			X	X	X	X	X
Raman (Post-Reaction)					X		X
TGA/DTA (Post-Reaction)					X		X

Notes: (1) – ALU stands for  $\gamma$ -Al<sub>2</sub>O<sub>3</sub>; (2) – SBA stands for SBA-15; (3) – the TEM analysis for the 10% Co/SBA-15 catalyst was only enough to allow qualitative evaluations of the catalyst (low resolution).

### 5.3.1 NITROGEN SORPTION ISOTHERMS

The textural characteristic, surface area and porous structure of the prepared sample were obtained by nitrogen sorption isotherms. Firstly, the samples were dried in vacuum at 523 K for 3 h. The nitrogen adsorption/desorption measurements were carried out measuring the volume of gas adsorbed to the surface of the particles at nitrogen boiling point, i.e. 77 K, using a Quantacrome (Model NOVAsin 1200) equipment. The volume and pore radius were determined by numerical integration method of Barrett, Joyner, and Halenda (BJH) on the isotherm desorption branch (BARRETT; JOYNER; HALENDA, 1951). The desorption isotherm was also used to calculate the same parameters using the Non Local Density Functional Theory (NLDFE) equilibrium phase transition model. More information about N<sub>2</sub>-sorption isotherm method, with a simplified understanding of the DFT method, is given in APPENDIX B.

### 5.3.2 X-RAY DIFFRACTION (XRD)

The XRD analyses of the support and catalysts were performed either using a Miniflex (Rigaku) and a D8 Discovery (Bruker) equipped with a Lynxeye detector. The powdered samples were dried at 373 K for 12 h prior to the analyses. The analyses were performed using Cu K $\alpha$  radiation. The spectra were collected at 40 kV and 20 mA, in a 10-90 ° Bragg angle ( $2\theta$ ) range, using a 0.05 degree step with a 2 s counting time *per* step. The crystallite phases present in the material were identified using International Centre for Diffraction Data (ICDD) databank crystallographic information files, specifically the *Powder Diffraction File* (PDF) of each material.

The size of the ordered crystalline domain ( $L_{hkl}$ ) and the interplanar space ( $d_{hkl}$ ) were determined by Scherrer's Equation and Bragg's Law, respectively (Equations 4 and 5).

$$L_{hkl} = \frac{k \cdot \lambda}{\beta \cdot \cos \theta} \quad 4$$

$$d_{hkl} = \frac{\lambda}{2 \cdot \sin \theta} \quad 5$$

Whereas  $k$  is the dimensionless shape factor, whose values varies depending on the actual shape of the crystallite;  $\lambda$  is the X-Ray wavelength;  $\beta$  is the line broadening at half maximum intensity;  $\theta$  is the Bragg angle. For obtaining the full width at half maximum (FMHW), the  $\gamma$ -Al<sub>2</sub>O<sub>3</sub> and SBA-15 support profiles were used as baseline for further subtraction due to overlapped peaks. The subtraction was performed normalizing the  $\gamma$ -Al<sub>2</sub>O<sub>3</sub> and SBA-15 contributions using the (440) peak and the amorphous, broad peak phases, respectively, hence providing Co<sub>3</sub>O<sub>4</sub> contribution solely (BULAVCHENKO et al., 2009). Peak fitting was performed using Pseudo Voight nonlinear fitting (Nonlinear Fitting Analysis using Category *Peak Functions*, Function *PsdVoigt1*, Iteration Algorithm *Levenberg Marquadt* at Origin 2020, see APPENDIX C), which is recommended for diffraction peaks due to Lorentzian crystallite size broadening contribution (HEREIN, 2008).

### 5.3.3 FOURIER TRANSFORM INFRARED SPECTROSCOPY (FT-IR)

The Fourier transform infrared (FTIR) provides information about the molecular structure of the samples. The spectra acquisition was conducted on an IR-Prestige-21 Shimadzu spectrometer. The spectra data were recorded in the 400-4000 cm<sup>-1</sup> wavenumber range, with 20

accumulations and  $1 \text{ cm}^{-1}$  of resolution. The solid samples (1 wt.%) were embedded in KBr prior to the formation of pellets suitable for the analysis.

#### **5.3.4 SCANNING ELECTRON MICROSCOPY (SEM)**

The morphology of the materials was assessed using two different techniques. In the first case, a JEOL SEM-FEG model FSM 7401F scanning electron microscope was used. The samples were dispersed in isopropanol or water and sonicated for 10 minutes. Afterward, 50  $\mu\text{L}$  of the prepared suspension were deposited over a carbon tape. The solvent was evaporated prior to the analysis. In the second case, a JEOL SEM model JSM-6610LV scanning electron microscope was used, in which powdered sample was carefully deposited over the carbon tape prior to analysis.

#### **5.3.5 TRANSMISSION ELECTRON MICROSCOPY (TEM)**

The TEM analyzes were performed on a microscope JEOL JEM 2100 to evaluate in details the morphology of the material. A small amount of the sample used in the analysis was dispersed in isopropanol and submitted to sonication for 10 minutes prior to its application over a carbon-coated copper grid. The grid was dried overnight prior to the analysis. The analysis was performed using the bright field imaging mode.

#### **5.3.6 THERMOGRAVIMETRIC ANALYSIS (TGA)**

The TGA curves were acquired using a Shimadzu model DTG-60H thermobalance. The assays were performed to evaluate singular events based on the mass loss profile of the samples in an oxidative atmosphere at a given temperature range. Analyses were performed under a 100 mL/min air-flow at 10 K/min, according to the literature (WIGZELL; JACKSON, 2017).

#### **5.3.7 INDUCTIVELY COUPLED PLASMA OPTICAL EMISSION SPECTROMETRY (ICP-OES)**

For the determination of the Co amount of the synthesized catalysts in this study, the ICP-OES technique was used. The calcinated catalyst samples (5, 10 and 15 wt.% Co/ $\gamma$ -Al<sub>2</sub>O<sub>3</sub> and 15 wt.% Co/SBA-15) were digested using nitric acid and fluoridric acid concentrated solutions in a heated digester block (*DigiPrep*, SCP Science) prior to analyses using Ar as inductive plasma in an ICP-OES (Arcos, Spectro) with Radial view (SOP).

### 5.3.8 HYDROGEN TEMPERATURE PROGRAMMED REDUCTION (H<sub>2</sub>-TPR)

The H<sub>2</sub>-TPR analysis was performed at a homemade equipment at NUCAT-COPPE /UFRJ equipped with a TCD detector in order to determine the reduction temperature profile of the active phase over the prepared catalysts. The equipment is equipped with a thermal conductivity detector (TCD) and was performed using Ar as reference gas. The analysis consisted of the addition of 15 mg of active phase inside a quartz reactor. First, the material was dried using a 30 mL/min Ar-flow, in which a heating ramp of 5 K/min was applied until the temperature reached 623 K, followed by an isothermal treatment at the same temperature for 1 h. Afterward, the reduction step was carried out using a 30 mL/min<sup>-1</sup> 10% H<sub>2</sub>/Ar mixture at 10 K/min up to 1273 K, followed by an isothermal treatment at the same temperature for 1 h.

### 5.3.9 TEMPERATURE PROGRAMMED DESORPTION (H<sub>2</sub>-TPD AND CO-TPD)

The H<sub>2</sub>-TPD analysis was performed with a Chemisorb 2750 equipped with a TCD. H<sub>2</sub>-TPD and CO-TPD analyses were performed at a homemade equipment at NUCAT-COPPE /UFRJ equipped with a Mass Spectrometer (Pfeiffer). Overall, the method consists of drying, reduction, adsorption, cleaning and desorption. Approximately 200 mg of each catalyst was used for the analysis. Drying of the material was performed using a 60 mL.min<sup>-1</sup> Ar-flow, in which a heating ramp of 5 K/min was applied until the temperature reached 623 K, followed by an isothermal treatment at the same temperature for 1 h. The reduction step was carried out using a 30 mL.min<sup>-1</sup> 10% H<sub>2</sub>/Ar mixture at 10 K/min for each catalyst up to the selected temperature, which was kept for 1h. A pure Ar or He-flow (30 mL/min) was then used to remove superficial probe molecule excess for at least 1h. Gas concentrations used for adsorption were 10%H<sub>2</sub>/Ar and 5% CO/He. H<sub>2</sub>-TPD analysis using TCD was then performed up to 1073 K at 2 K/min, hold for 1 h, while H<sub>2</sub>-TPD and CO-TPD analysis using MS were performed up to 873 K and 773 K, respectively. Data were treated using Origin (OriginLab) and Excel (Microsoft Office). See APPENDIX D for further details.

### 5.3.10 RAMAN MICROSCOPY

The analysis of pre- and post-reaction catalysts were performed using a small amount of material (spatula tip) in an aluminum plate. Raman measurements were performed using a Raman Microscope Instrument (Renishaw InVia Raman Microscope, Renishaw plc, UK),

equipped with a 50 mW,  $\lambda = 532$  nm argon laser using different magnification lens. Exposure time, laser power and accumulations varied for each sample, and was performed at room temperature. Data acquisition and treatment was conducted using WiRE 5.2 software.

### 5.3.11 CATALYTIC TESTS

The reaction was carried out using an automated PID Eng&Tech system in a 9.1 mm I.D. Hastelloy-C reactor. Approximately 50 mg of active phase was employed (Table 4). When necessary, quartz beads (2.0 mm diameter) were used to complete a 1 cm<sup>3</sup> of catalyst bed volume.

Table 4 – Catalyst and Total Active Phase Mass (mg) used for Catalytic Tests

Catalyst	Mass (g)	Total Active Phase (mg)
15% Co/SBA-15	0.38	48.96
15% Co/ $\gamma$ -Al <sub>2</sub> O <sub>3</sub> .	0.38	48.84

For the reactions, a pressurized system consisting of the reactor, hot trap, a high temperature separator at 403 K for wax-water mixture, and a cold trap at  $\sim 288$  K for small-chain hydrocarbons was used. Gases, water and small-chain hydrocarbons were separated in the cold trap; liquids were collected in different flasks for further mass balance, while gases were analyzed online in a Carboxen-1010 PLOT (Supelco, USA) in a GC-2010 Plus chromatograph (Shimadzu, Japan) using a thermal conductivity detector (TCD). Results were used for conversion calculation. The selectivity was calculated based on an online analysis of all products in series, using a Carboxen-1010 PLOT (Supelco, USA) for TCD and a Rtx-1 (Shimadzu, Japan) for FID analyses in the same equipment for  $\sim 24$  h reaction. Analysis using the Carboxen-1010 PLOT (Supelco, USA) were performed with using a thermal conductivity detector (TCD) at 260.0 °C and 70 mA. Helium was used as carrier gas at linear velocity of 26.6 cm/s, 3.0 mL/min purge flow and split ratio of 20 (total analysis time of 19.92 min). Programmed oven temperature was hold 7 min for 30 °C, followed by a temperature raise of 24 °C/min up to 220 °C and hold for 5 min. The online analysis was performed simultaneously with the same column at detector conditions aforementioned for gases, following the light hydrocarbons and liquids oven program. For light hydrocarbons and liquids, a Rtx-1 (Shimadzu, Japan) column was employed, using a FID detector at 260 °C. Helium was also used as carrier gas at linear velocity of 30.0 cm/s, 3.0 mL/min purge flow and split ratio of 15

(total analysis time of 150.00 min). Programmed oven temperature was hold 7 min for 30 °C, followed by a temperature raise of 10 °C/min up to 250 °C and hold for 5 min.

Operating conditions values were selected for industrial relevance (especially pressure and temperature) and for comparison with the literature (especially WHSV), following Prieto et al. (2009) method. Tables 5 and 6 displays the experimental design in details. At first, total WHSV was changed by altering the inlet inert flow, maintaining the syngas WHSV constant; the last evaluation at 543 K was performed by altering the syngas WHSV, maintaining total WHSV constant. Here it was also possible to evaluate if the reaction was under kinetic regime. Finally, the WHSV value was kept constant and temperature effect evaluation was performed. At the end, total WHSV was returned to initial values for yield loss assessment at stationary state.

Firstly, the catalyst was reduced *in situ* at normal pressure using 30 mL/min pure H<sub>2</sub> at 2 K/min heating ramp up to the reduction temperature, and hold for a long time. Afterwards, the reactor was cooled down to the reaction temperature (~ 453 K). Pressure and temperature were simultaneously increased with syngas flow (H<sub>2</sub>:CO of 2:1) diluted with N<sub>2</sub>, used as internal standard. The CO conversion ( $X_{CO}$ (%)) and selectivities ( $S_i$ (%)) of component  $i$ ) were calculated as described in APPENDIX A. Noteworthy is that the HC selectivities were calculated by subtracting the CO<sub>2</sub> formation, i.e., although the sum of HCs selectivities reaches 100%, it does in reference to a selectivity of 100% -  $S_{CO_2}$ . The system shutoff consisted of decreasing the pressure, switching the feed composition to inert gas (N<sub>2</sub>), then cleaning the whole system (line, reactor and separators) for at least 6 h prior to decreasing the temperature from 543 K to ambient. After shutoff, the catalyst was kept in closed vial for further post-reaction analyses. APPENDIX E summarizes the results for both catalysts (Table E.1 for the 15% Co/SBA-15 catalyst and Table E.2 for the 15% Co/ $\gamma$ -Al<sub>2</sub>O<sub>3</sub> catalyst), whereas APPENDIX F details the test performed with the empty reactor for system validation. Figure 4 summarizes the procedure used for both catalysts.

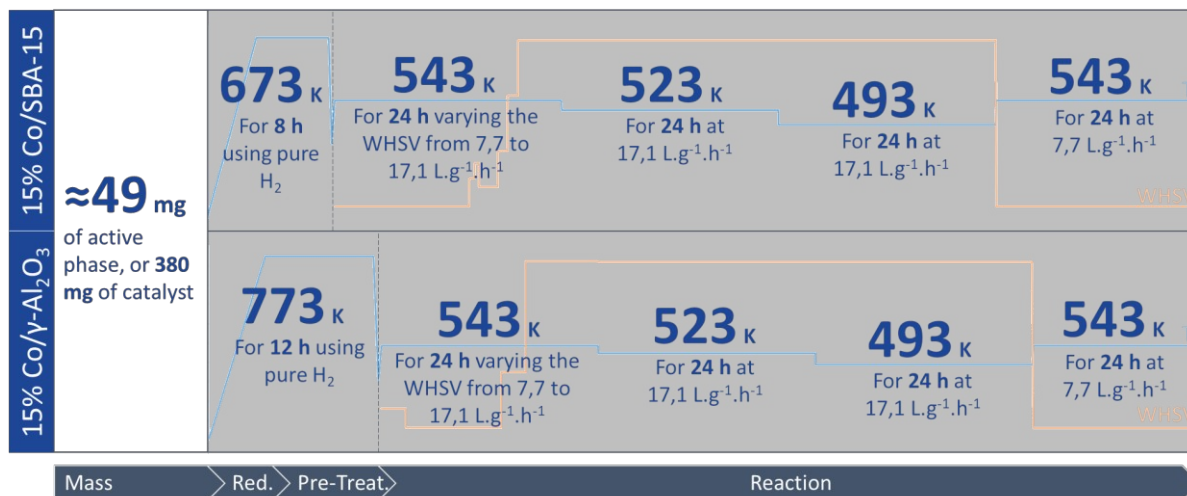
Figure 4 – Catalytic tests summary for 15% Co/SBA-15 and 15% Co/ $\gamma$ -Al<sub>2</sub>O<sub>3</sub> catalysts.

Table 5 – Conditions used for 15 % Co/SBA-15 catalytic test

Step	Classification	Conditions	Assessments										
			Time (h)	Pressure (bar)	Temperature (K)	WHSV (mL <sub>n</sub> ·g <sub>cat</sub> <sup>-1</sup> ·h <sup>-1</sup> ) <sup>a</sup>	Syngas (mL <sub>n</sub> ·g <sub>cat</sub> <sup>-1</sup> ·h <sup>-1</sup> ) <sup>b</sup>	WHSV	CO conversion	Selectivity CO <sub>2</sub> /CH <sub>4</sub>	Paraffins C <sub>2</sub> -C <sub>21</sub>	Olefins C <sub>2</sub> -C <sub>10</sub>	
Pre-Treatment	Reduction	- Temperature: 673 K, 2 K/min - Time: 8 h - Pure H <sub>2</sub> flow: 30 mL/min											
	Pre-Treatment	- Temperature: 453 K, 10 K/min, maintaining H <sub>2</sub> flow - Syngas inlet and simultaneous temperature and pressure increase to reaction conditions.											
Reaction			24		543	7,673	6,903	×	×	×	---	---	---
						8,774		×	×	×	---	---	---
						9,245		×	×	×	---	---	---
						10,110	6,903	×	×	×	---	---	---
						10,818		×	×	×	---	---	---
						13,962		×	×	×	---	---	---
						17,107		×	×	×	---	---	---
						17,107		×	×	×	×	×	×
			48		523	17,160	5,755	---	---	×	×	×	×
			72		493	17,160	5,755	---	---	×	×	×	×
			96		543	7,673	6,903	×	×	×	×	×	×

Notes: (a) – Stand for total WHSV at STP (normal conditions, 1.01 bar and 273 K), which is composed by H<sub>2</sub>:CO mol ratio of 2:1 and N<sub>2</sub>. At 543 K, 24 h of reaction, the N<sub>2</sub> volume flow varied in order to increase the WHSV up to WHSV = 17,160 NmL·g<sub>cat</sub><sup>-1</sup>·h<sup>-1</sup>, where simultaneous variation of N<sub>2</sub> and syngas was performed, maintaining total volume flow; (b) – Stands for WHSV calculated considering only the H<sub>2</sub>:CO mol ratio of 2:1 syngas mixture.

Table 6 – Conditions used for 15 % Co/ $\gamma$ -Al<sub>2</sub>O<sub>3</sub> catalytic test

Step	Classification	Conditions
Pre-Treatment	Reduction	- Temperature: 773 K, 2 K/min - Time: 12 h - Pure H <sub>2</sub> flow: 30 mL/min
	Pre-Treatment	- Temperature: 453 K, 10 K/min, maintaining H <sub>2</sub> flow - Syngas inlet and simultaneous temperature and pressure increase to reaction conditions.

Reaction	Time (h)	Pressure (bar)	Temperature (K)	WHSV		Assessments					
				Total (mL <sub>in</sub> .g <sub>cat</sub> <sup>-1</sup> .h <sup>-1</sup> ) <sup>a</sup>	Syngas (mL <sub>in</sub> .g <sub>cat</sub> <sup>-1</sup> .h <sup>-1</sup> ) <sup>b</sup>	WHSV	CO conversion	Selectivity CO <sub>2</sub> /CH <sub>4</sub>	Paraffins C <sub>2</sub> -C <sub>21</sub>	Olefins C <sub>2</sub> -C <sub>10</sub>	
Reaction	24	20	543	8,785		×	×	×	---	---	
				7,681	6,909	×	×	×	---	---	
				10,836		×	×	×	---	---	
				17,145		×	×	×	---	---	
				17,160	5,773	×	×	×	×	×	
				17,160	5,773	---	×	×	×	×	
	48	72	96	543	17,160		---	×	×	×	×
					17,160	5,773	---	×	×	×	×
					17,160		---	×	×	×	×
					17,160		---	×	×	×	×
					17,160	5,773	---	×	×	×	×
					17,160	5,773	---	×	×	×	×

Notes: (a) – Total WHSV at STP (normal conditions, 1,01 bar and 273 K), which is composed by H<sub>2</sub>:CO mol ratio of 2:1 and N<sub>2</sub>. At 543 K, 24 h of reaction, the N<sub>2</sub> volume flow varied in order to increase the WHSV up to WHSV = 17,160 NmL.g<sub>cat</sub><sup>-1</sup>.h<sup>-1</sup>, where simultaneous variation of N<sub>2</sub> and syngas was performed, maintaining total volume flow. (b) – H<sub>2</sub>SV calculated considering only the H<sub>2</sub>:CO mol ratio of 2:1 syngas mixture. ° the catalyst started at 7,681 NmL.g<sub>cat</sub><sup>-1</sup>.h<sup>-1</sup> and have changed to 8,785 NmL.g<sub>cat</sub><sup>-1</sup>.h<sup>-1</sup> due to a problem with automation. After 5 points recorded, the reaction returned to the initial condition.

## 6 RESULTS AND DISCUSSION

Here, obtained results and discussions are given in details in the following order –pre-reaction characterizations, catalytic tests and post-reaction characterizations.

### 6.1 CHARACTERIZATION

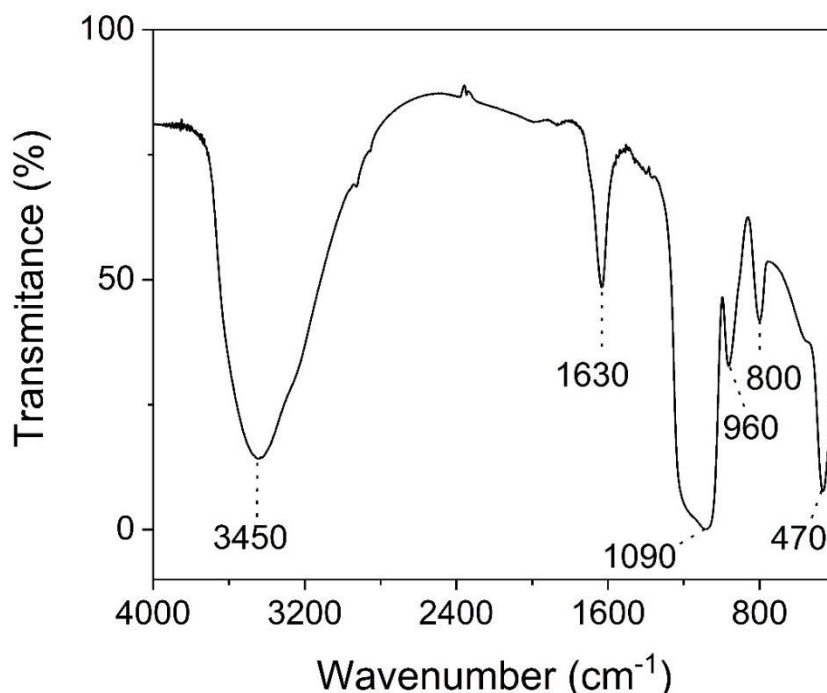
The following characterizations were performed for all prepared supports and catalysts prior to the catalytic tests. Here, focus was given on evaluating the catalysts texture, morphology, metallic load and determining the adequate pre-treatment conditions for reaction. Moreover, characterizations used for control at each preparation step, such as FT-IR and TGA/DTA, and also characterizations performed in order to obtain insights when comparing with the post-reaction analysis, such as TGA/DTA and Raman, are presented and discussed.

Noteworthy is that the supports were impregnated with different amounts of metal load. It was planned on this study to evaluate the effect of the metal load over the catalysts morphology, texture and catalytic performance. However, due to reaction system equipment (PID Eng&Tech) limitations such as broken system or impossibility of performing vital characterizations, some of the catalysts were prioritized. Namely, the 10% Co/SBA-15 was characterized, but the results are not shown; 5% Co/ $\gamma$ -Al<sub>2</sub>O<sub>3</sub> catalyst was characterized, but due to poor results at H<sub>2</sub>-TPD analysis, the catalyst was disregarded for further tests and analysis. 10% Co/ $\gamma$ -Al<sub>2</sub>O<sub>3</sub> catalyst was eligible for catalytic test performance, but due to limitations from the equipment aforementioned, only 15% Co/SBA-15 and 15% Co/ $\gamma$ -Al<sub>2</sub>O<sub>3</sub> catalysts were evaluated.

#### 6.1.1 FOURIER TRANSFORM INFRARED SPECTROSCOPY (FT-IR) ANALYSIS

The SBA-15 support was analyzed by FT-IR after calcination. The analysis was performed focusing on identifying whether the calcination method was able to remove the precursor. The results in the 4000-400 cm<sup>-1</sup> wavenumber range are displayed in Figure 5.

Figure 5 – SBA-15 support Infrared Spectroscopy analysis (FTIR) in the 4000-400  $\text{cm}^{-1}$  wavenumber range



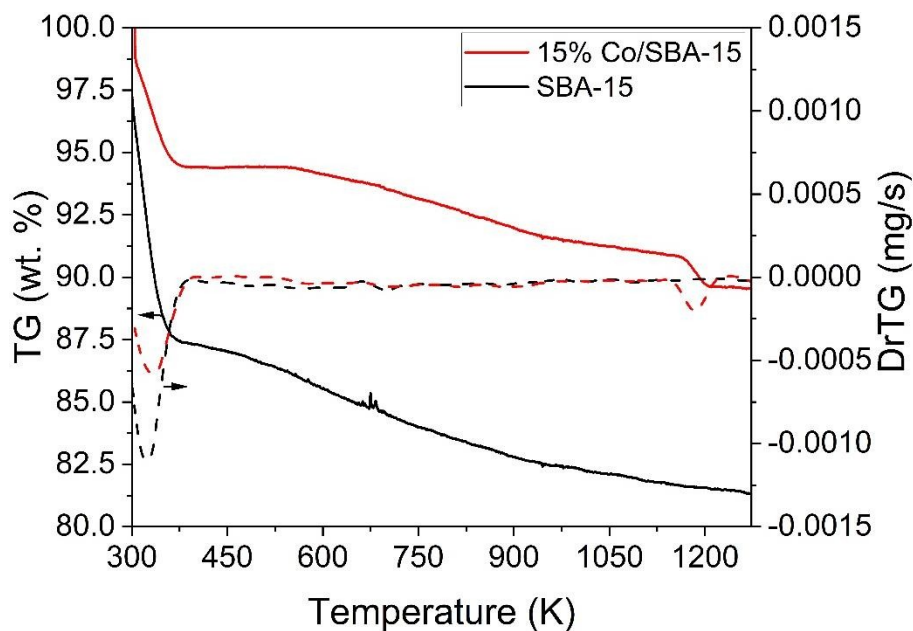
These bands show the absorption related to Si-OH, Si-O, Si-O-Si and O-H bonds. The broad band around 3450  $\text{cm}^{-1}$  is attributed to the hydroxyls (O-H and Si-OH) stretching bands. The bands around 1220  $\text{cm}^{-1}$  and at 960  $\text{cm}^{-1}$  are related to stretching vibrations of free Si-OH group of amorphous samples at the surface, while the band at 800  $\text{cm}^{-1}$  is attributed to the symmetrical stretching vibration of Si-O-Si bonds of ring structures. The band at 1090  $\text{cm}^{-1}$  is a characteristic band of the antisymmetric stretching vibrations of Si-O-Si of silica. In fact, these bands are according to the literature ascribed as characteristic bands of an amorphous silica. On the other hand, the band around 1630  $\text{cm}^{-1}$  is related to bending vibrations of O-H bond, and the band at 470  $\text{cm}^{-1}$  to the Si-O-Si bond bending vibrations (AZIMOV et al., 2012; LAUNER, 2015). Since no carbon peaks were detected, the calcination was successfully performed.

### 6.1.2 THERMOGRAVIMETRIC ANALYSIS (TGA)

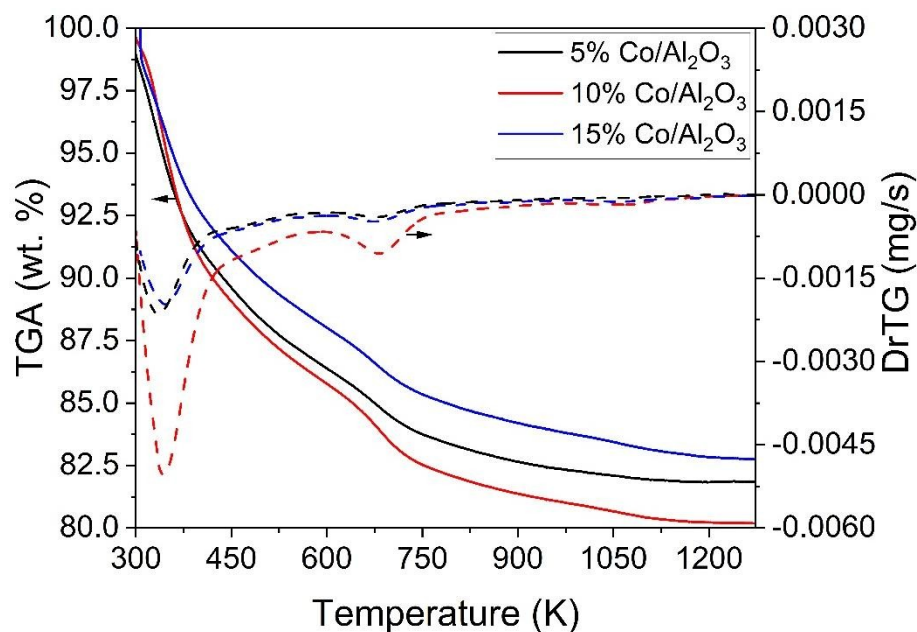
After impregnation and first calcination, the catalysts and the respective support (SBA-15 only) were analyzed by TGA/DTA in order to evaluate if the calcination step was successfully performed. This was necessary since the selection of the calcination step, at first, was performed based on the literature. In case of persistent existence of the precursor, a new calcination step is mandatory. Figure 6 (A) and (B) show the thermogravimetric profiles of the SBA-15 and  $\gamma$ -

$\text{Al}_2\text{O}_3$  supports and catalysts, respectively. Table 7 presents the mass losses and DTA curves, and the corresponding temperatures.

Figure 6 – Thermogravimetric Analyses (TGA/DrTGA) for (A) SBA-15 (in black) and catalyst (15% Co/SBA-15, in red) and (B) alumina-supported catalysts (5, 10 and 15 wt. % Co/ $\gamma$ - $\text{Al}_2\text{O}_3$  catalysts in black, red and blue, respectively)



(a)



(b)

Table 7 –Thermogravimetric Analysis (TGA) for SBA-15 and cobalt catalysts (SBA-15 and alumina-based catalysts)

Sample	Mass Loss (%)	Observations	Temperature (K) <sup>a</sup>
SBA-15	12.64	Water Loss	323.5
	5.58	Water Loss	334.0
15% Co/SBA-15	1.40	Co <sub>3</sub> O <sub>4</sub> Structural Transformation	1186.1
	9.32	Water Loss	334.9
5% Co/ $\gamma$ -Al <sub>2</sub> O <sub>3</sub>	3.32	Precursor Residual	676.6
	10.71	Water Loss	343.8
10% Co/ $\gamma$ -Al <sub>2</sub> O <sub>3</sub>	3.94	Precursor Degradation	682.7
	8.71	Water Loss	347.3
15% Co/ $\gamma$ -Al <sub>2</sub> O <sub>3</sub>	3.36	Precursor Degradation	673.8

Notes: (a) – Temperature in which DTG peak is at its maximum, while the mass loss is obtained at the end of the event.

Figure 6 (a) shows the mass loss (wt.%) profiles of the SBA-15 support and of the catalyst 15 wt.% Co/SBA-15. The mass loss of the support SBA-15 was lower than of the catalyst in the temperature range of 300-390 K, and both exhibited endothermic curves, which indicated loss of water or OH hydroxyls, in accordance with the observed FT-IR spectrum (broad O-H band at 3450 cm<sup>-1</sup>). The higher mass loss of the catalyst is probably due to the persistent existence of precursor residues and hydroxyls at the surface. Setiabudi *et al.* (2017) observed similar results for the Ni/SBA-15 catalysts.

Figure 6 (b) displays the mass loss (wt.%) of the catalysts supported on  $\gamma$ -Al<sub>2</sub>O<sub>3</sub> (5, 10 and 15 wt.% Co) after calcination at 573 K. From the TGA profile, two major peaks around 300-425 K and 620-750 K range are observed (Table 7). The first peak, as observed for the SBA-15 support, is due to water on the alumina surface. The second peak at higher temperature suggests elimination of residual OH hydroxyls or residual precursors from the alumina support, since the DTA curve is endothermic. Wigzell and Jackson (2017) observed that the cobalt nitrate on the silica support was fully decomposed at ~460 K to Co<sub>3</sub>O<sub>4</sub>, while on the alumina support two different decomposition occurred at higher temperatures (~610 K).

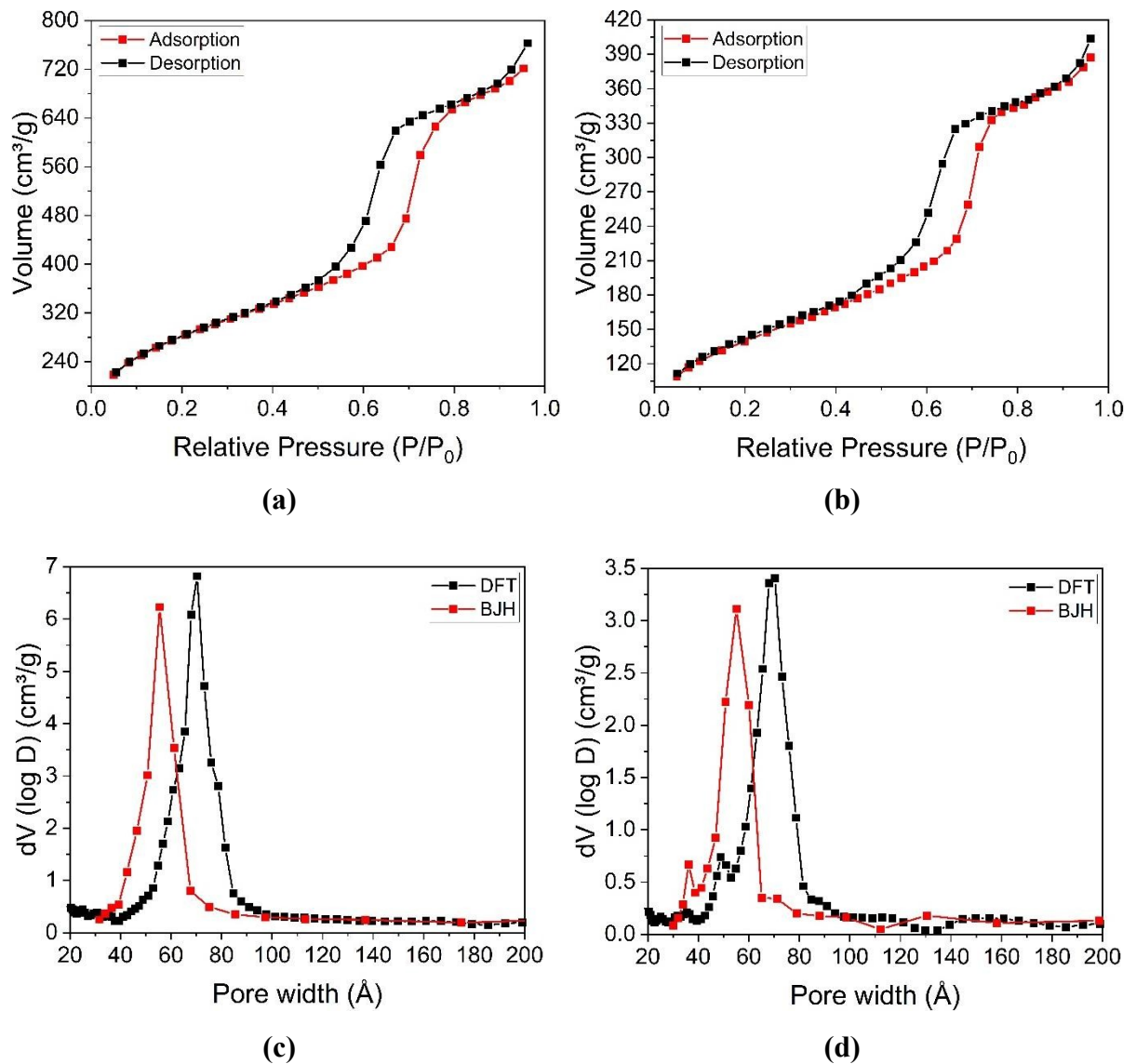
There is also a visible and very distinct peak for the 15%Co/SBA-15 catalyst at the 980-1220 K range, which may be due to the same phenomenon. The alumina-based catalyst shows an increase of peak from 5 to 10% and the appearance of another peak at ~1173 K.

### 6.1.3 N<sub>2</sub>-SORPTION ISOTHERM ANALYSIS

The N<sub>2</sub>-adsorption/desorption isotherm at 77 K were obtained for both supports and catalysts using Density Functional Theory (DFT), Brunauer, Emmet and Teller (BET) and Barrett-Joyner-Halenda (BJH) methods (THOMMES et al., 2015).

Figure 7 shows the SBA-15 sorption isotherm and the pore size distribution (PSD).

Figure 7 – Nitrogen adsorption/desorption isotherms of the fresh, calcined SBA-15 (a) and 15%Co/SBA-15 (b) catalyst and the pore size distribution (c) and (d)



These isotherms are characteristic of type IV presenting a H1 hysteresis loop (SING et al., 1985), which is typical of mesoporous materials. Zhao *et al.* (1998) observed three different regions for the SBA-15 material: monolayer-multilayer adsorption (up to P/P<sub>0</sub> ~ 0.5), capillary

condensation (at  $P/P_0 \sim 0,75$ ) and multilayer condensation at the surfaces. The plateau after  $P/P_0 \sim 0,75$  indicates complete mesopore filling (LOWELL et al., 2004), while the increasing volume above  $P/P_0 \sim 0,85$  suggests inter-particle voids condensation (SOTOMAYOR; CYCHOSZ; THOMMES, 2018). Results obtained for the support and the impregnated catalyst are very similar, with a discrete increase of the hysteresis related to micropores at the monolayer-multilayer adsorption region. Finally, the narrow range of the pore size distribution displayed in Figure 7 (c) and (d), calculated using BJH and NLDFT methods, suggests the classification of this material as ordered mesoporous. Two hypotheses may explain the results: after impregnation the metal blocked the pores, reducing pore volume; and reduction of pore volume and surface area.

The areas, pore volumes and mean pore diameters using BET, BJH and NLDFT were compared with the literature, as shown in Table 8.

Table 8 – Surface area, pore volume and mean pore diameter of the SBA-15 support and 15% Co/SBA-15 catalyst from different methods

Sample Type	Sample code	Superficial (m <sup>2</sup> /g)		Area	Pore Volume (cm <sup>3</sup> /g)		Mean Pore Diameter (nm)		Reference
		S <sub>BET</sub> <sup>a</sup>	S <sub>BJH</sub> <sup>b</sup>	S <sub>DFT</sub> <sup>c</sup>	V <sub>BJH</sub> <sup>b</sup>	V <sub>DFT</sub> <sup>c</sup>	PD <sub>BJH</sub> <sup>b</sup>	PD <sub>DFT</sub> <sup>c</sup>	
Support	SBA-15	952	623	962	1.05	1.14	5.55	7.03	This study
	11SBA_M	630	467	---	1.26	---	10.9	---	(1)
	7SBA_L	957	573	---	0.80	---	7.0	---	
	SBA-1	920	---	---	1.23	---	8.5	---	(2)
	SBA-2	780	---	---	0.80	---	6.0	---	
	S2-C	870	---	---	0.96	0.86	5.7	7.3	(3)
	S1	887	---	---	1.91	---	9.1	---	(4)
Catalyst	15%Co/SBA-15	480	351	484	0.59	0.60	5.50	7.03	This study
	20%Co/11SBA_M	423	---	---	---	---	---	---	(1)
	20%Co/7SBA_L	412	---	---	---	---	---	---	
	20%Co/S1	493	---	---	0.83	---	7.5	---	(4)

Notes: (a) – S<sub>BET</sub> is the total surface area, calculated using the Brunauer, Emmet and Teller model (BET); (b) – the mesopore surface area (S<sub>BJH</sub>), pore volume (V<sub>BJH</sub>) and mean pore diameter (D<sub>BJH</sub>) were calculated using the Barrer, Joynner and Halenda method (BJH); (c) – the pore surface area (S<sub>DFT</sub>), pore volume (V<sub>DFT</sub>) and mean pore diameter (D<sub>DFT</sub>) were calculated using the Non Local Density Functional Theory method (NLDFT, indexed as DFT). References: (1) Prieto *et al.* (2009); (2) Zhao et al. (1998); (3) Ravikovitch and Neimark (2001); (4) Khodakov, Bechara and Griboval-Constant (2003).

In fact, these results show that the model used for calculating parameters is relevant, since each model presents intrinsic limitations. The BET method does not consider part of the micropores, such as in the intrawall, while the BJH algorithm is suitable for the determination of the texture

parameters relative to mesopores (SCHMAL, 2011). The third method, the Non-Local Density Functional Theory (NLDFT), is recommended in the literature for mesoporous materials: the equilibrium phase transition model is applied over the desorption branch and provides accurate results for the pore size. NLDFT fitting of these data led to an error of 0.378%. The DFT method is advantageous since it can be used for combine micro and mesopores, accurately describing fluids in confined geometries (THOMMES, 2002), while BJH method underestimates pore size in 20-25% (RAVIKOVITCH; NEIMARK, 2001).

The BET results are in good agreement with the literature, which is in the range between 630-1040 m<sup>2</sup>/g, according to Zhao *et al.* (1998). Comparison with the literature (Prieto *et al.*, 2009 and Zhao *et al.*, 1998) for the SBA-15 shows good agreement. The pore sizes determined by BJH are similar to the SBA-2, SBA-15, S2-C and S1, but the pore volumes are different. Comparing the results of the 15%Co/SBA-15 catalyst and similar catalysts reported in the literature, similar trends are noticed, as described for the S1 catalyst. These results show that the impregnated support led to a higher reduction of the pore volume, pore surface area (BJH) and total surface area (BET), without significant variation of mean pore size.

Figure 8 shows the isotherms of  $\gamma$ -Al<sub>2</sub>O<sub>3</sub> support and the respective catalysts, while the pore size distribution (PSD), calculated using the BJH method, are displayed at Figure 9.

The isotherms of the  $\gamma$ -Al<sub>2</sub>O<sub>3</sub> support and catalysts in Figure 8 show isotherms of type IV (IUPAC). This isotherm, like the SBA-15 sample, is related to typical mesoporous materials ( $d_p > 2$  nm), with the formation of hysteresis loop associated with the occurrence of pore condensation. However, different from SBA-15, it presented the H2-type. This type of hysteresis loop is related to disordered material with the distribution of pore size and shapes not well defined (LOWELL et al., 2004). Thommes *et al.*, (2015) defined that hysteresis as H2(a), which can be attributed to the effect of pore blocking or cavitation in pores with narrow necks.

Figure 8 – Nitrogen adsorption/desorption isotherm of fresh, calcined (a)  $\gamma$ - $\text{Al}_2\text{O}_3$ , (b) 5%Co/ $\gamma$ - $\text{Al}_2\text{O}_3$ , (c) 10%Co/ $\gamma$ - $\text{Al}_2\text{O}_3$  and (d) 15%Co/ $\gamma$ - $\text{Al}_2\text{O}_3$

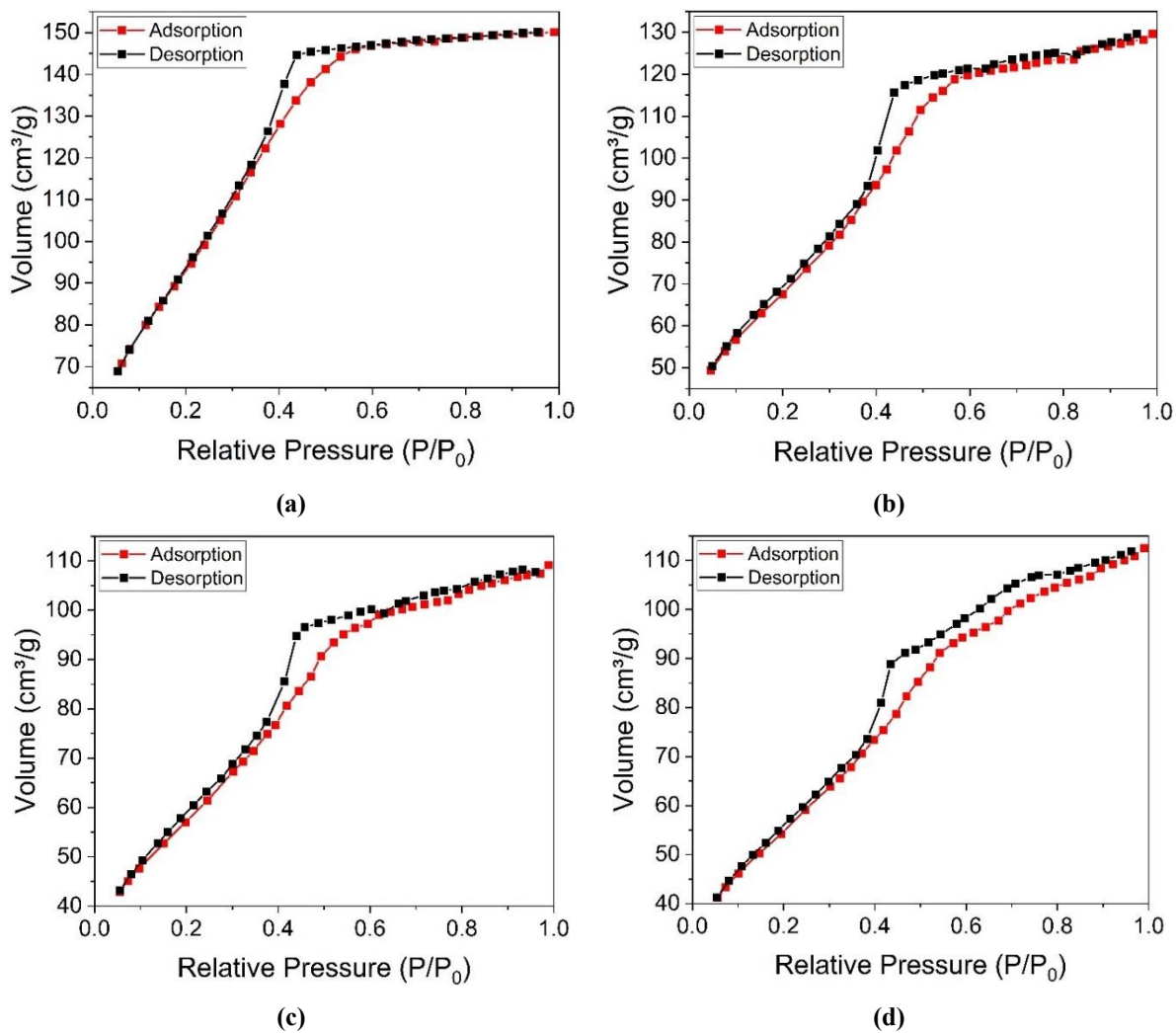
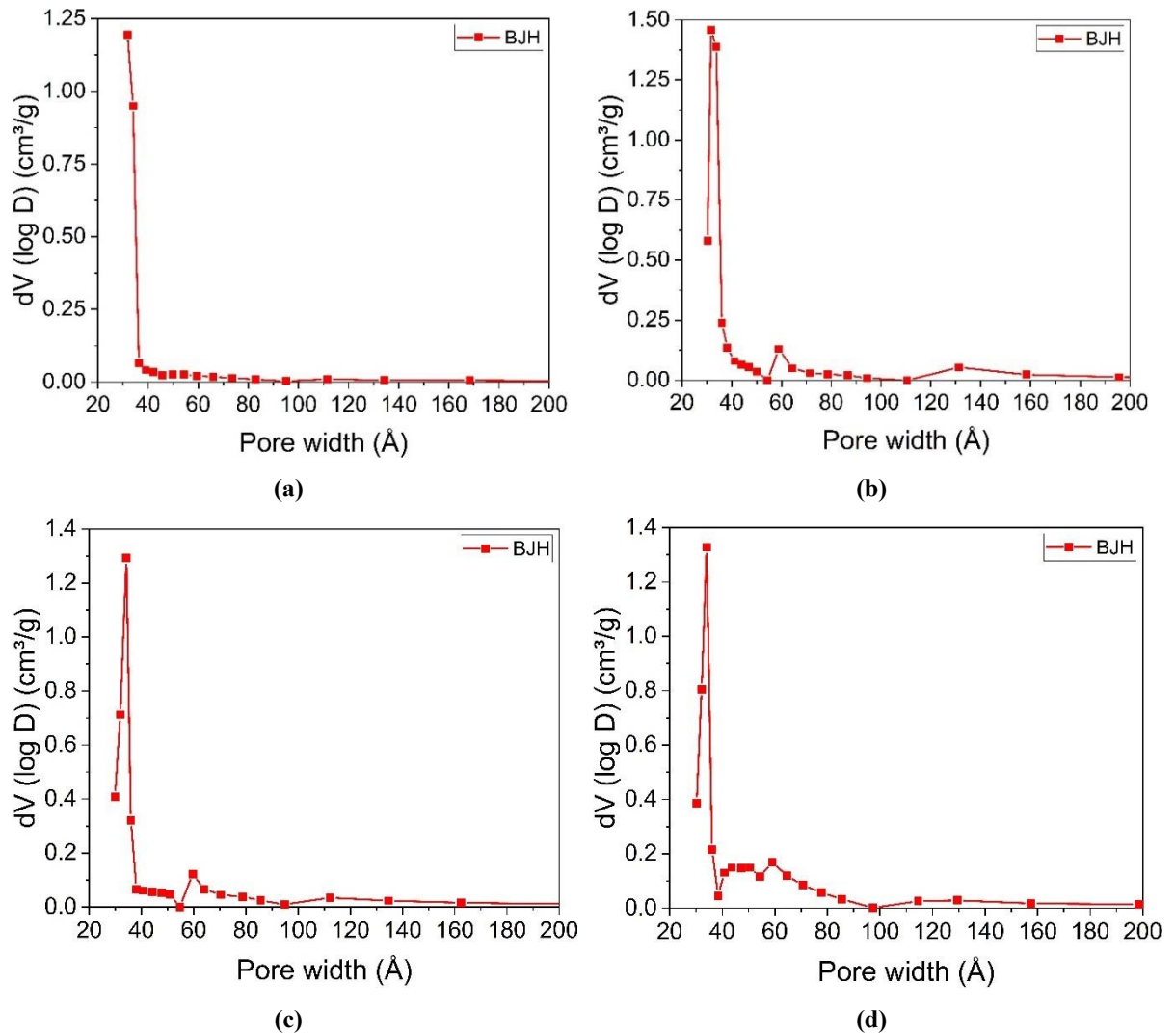


Figure 9 – Nitrogen adsorption/desorption isotherm of the fresh, calcined (a)  $\gamma$ -Al<sub>2</sub>O<sub>3</sub>, (b) 5%Co/ $\gamma$ -Al<sub>2</sub>O<sub>3</sub>, (c) 10%Co/ $\gamma$ -Al<sub>2</sub>O<sub>3</sub> and (d) 15%Co/ $\gamma$ -Al<sub>2</sub>O<sub>3</sub>



After cobalt impregnation with 10 to 15 wt. %, the hysteresis changed, evidencing the mesopore morphology. Figure 9 shows that after impregnation the pore diameter shifted to larger values and broadened the pore distribution with increasing metal loading.

Calculations of surface area, pore volume and mean pore diameter using BET and BJH were compared with the literature and are presented in Table 9.

Table 9 – Surface area, pore volume and mean pore diameter of the  $\gamma$ -Al<sub>2</sub>O<sub>3</sub> support and catalysts from BET and BJH methods

Sample Type	Sample code	Superficial Area (m <sup>2</sup> /g)		Pore Volume	Mean Pore Diameter (nm)	Reference
		S <sub>BET</sub> <sup>a</sup>	S <sub>BJH</sub> <sup>b</sup>	V <sub>BJH</sub> <sup>b</sup>	PD <sub>BJH</sub> <sup>b</sup>	
Support	$\gamma$ -Al <sub>2</sub> O <sub>3</sub>	343	88	0.08	3.2	This study
	$\gamma$ -Al <sub>2</sub> O <sub>3</sub> -n	203.73	---	0.14	2.78	(1)
	$\gamma$ -Al <sub>2</sub> O <sub>3</sub> -u	246	---	0.25	3.90	(2)
Catalyst	5%Co/ $\gamma$ -Al <sub>2</sub> O <sub>3</sub>	247	134	0.12	3.2	
	10%Co/ $\gamma$ -Al <sub>2</sub> O <sub>3</sub>	209	105	0.10	3.4	This study
	15%Co/ $\gamma$ -Al <sub>2</sub> O <sub>3</sub>	199	113	0.12	3.4	
	15%Co/ $\gamma$ -Al <sub>2</sub> O <sub>3</sub> -n	135.29	---	0.09	2.77	(1)

Notes: (a) – S<sub>BET</sub> is the total surface area, calculated using the Brunauer, Emmet and Teller model (BET); (b) – the mesopore surface area (S<sub>BJH</sub>), pore volume (V<sub>BJH</sub>) and mean pore diameter (PD<sub>BJH</sub>) were calculated using the Barrer, Joijner and Halenda method (BJH). References: (1) Marsih et al. (2012); (2) Morajkar and Fernandes (2010).

The surface area of the support (BET) was higher compared to the reported values in the literature, and pore volume and diameter were smaller. Park *et al.* (2017) obtained 196 m<sup>2</sup>/g for the 15% Co/ $\gamma$ -Al<sub>2</sub>O<sub>3</sub> catalyst, using a commercial  $\gamma$ -Al<sub>2</sub>O<sub>3</sub> support of 205 m<sup>2</sup>/g.

The BET surface area of the catalyst did not change with increasing metal load, from 10% to 15% nominal metal loading. However, the pore diameter, BJH surface area and pore volume increased. These data corroborate with the hypothesis aforementioned.

One possible explanation is that the changes occurred due to the balance of alumina dissolution during the impregnation step, which is affected by the number of surface hydroxyl groups. The literature shows that alumina dissolution occurs in the presence of hydroxyl ions since the dissolution rate depends on the characteristics of the alumina surface and in the presence of ions, such as Co, in solution (TRUEBA; TRASATTI, 2005). Moreover, the larger BET surface area of the support may also explain the isotherm profile-impregnation relationship, since a larger oxide/H<sub>2</sub>O interface exists, affecting the alumina dissolution rate, and leading to increased pore volume and pore surface area (BJH). At last, the successive increase of metal load and number of impregnation steps clearly show an increase in macropores at P/P<sub>0</sub> closer to 1.0, which may be explained by the particle agglomeration.

#### 6.1.4 X-RAY DIFFRACTION (XRD) ANALYSIS

The XRD technique is very important for identifying the crystalline phases and crystal defects. Both qualitative and quantitative analysis can be performed, providing the amount of metal, crystallite sizes, particle sizes and distribution (HEREIN, 2008).

The synthesized supports and catalysts were analyzed by XRD. The diffractograms for the SBA-15 support and 15% Co/SBA-15, after calcination, are displayed in Figure 10.

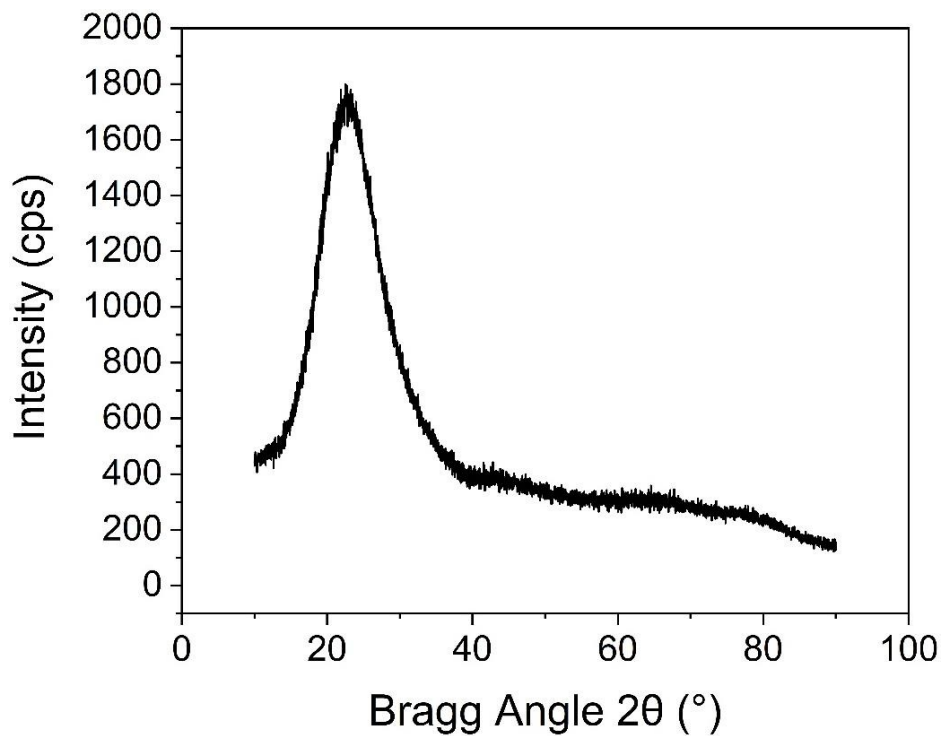
The diffractogram of the SBA-15 in Figure 10 (a) shows a broad peak between 20-30°, which characterizes a derived-silica material and corroborates with the FT-IR analysis (ROQUE, 2015). Crystallite sizes below 3.0 to 5.0 nm cannot be detected by x-ray pattern (FARRAUTO; HOBSON, 2003). Figure 10 (b) displays the XRD pattern of the catalysts. The silica phase is amorphous and the peaks are attributed to the cobalt-derived nanoparticle crystallites after calcination, evidencing the formation of cobalt oxide phases. Comparing with the crystallographic patterns of  $\text{Co}_3\text{O}_4$  (PDF#00-043-1003) and  $\text{CoO}$  (PDF#00-043-1004), it was possible to identify prevailing formation of the  $\text{Co}_3\text{O}_4$  nanoparticles.

Figure 11 displays the diffractograms of the  $\gamma\text{-Al}_2\text{O}_3$  support and of the  $\text{Co}/\gamma\text{-Al}_2\text{O}_3$  catalysts after calcination.

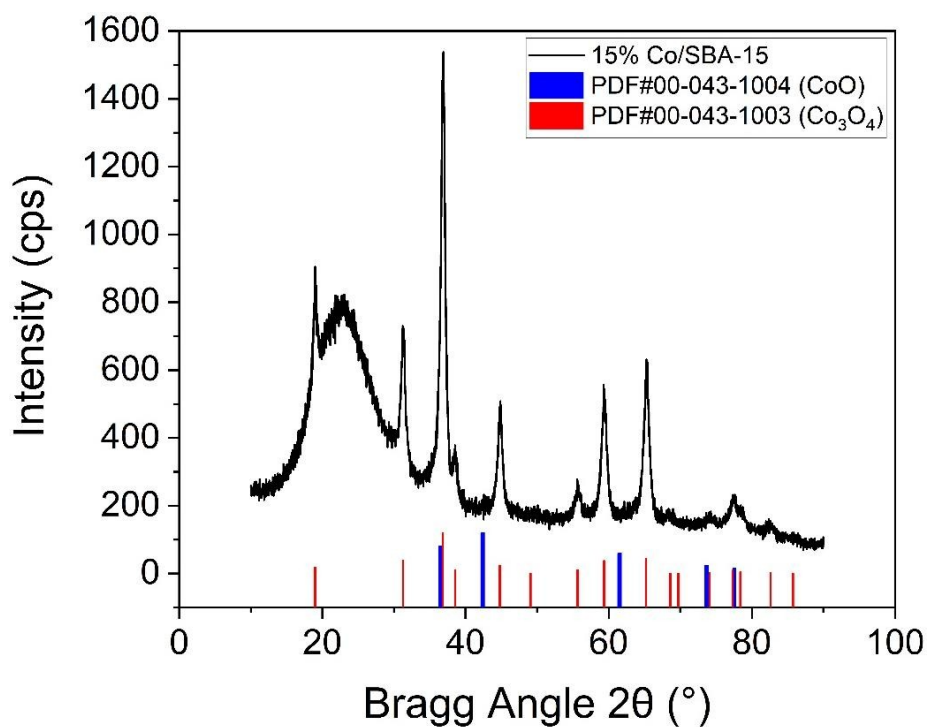
The crystallite size of the  $\gamma\text{-Al}_2\text{O}_3$  was estimated using the Scherrer equation for  $L_{111}$  plane, and was equal to 2.5 nm. The  $\gamma$ -alumina support was prepared following the calcination of a pseudo-boehmite gel, formed by aluminum forced-hydrolysis by thermal decomposition of urea. Boehmite is already known to present a low degree of crystallization under selected calcination conditions (AGRAFIOTIS; TSETSEKOU, 2000).

Figure 11 displays also the diffractogram of the catalysts. The peaks associated to the cobalt oxide phase, both on SBA-15 and alumina, were identified at  $2\theta = 19^\circ, 31^\circ, 36^\circ, 37^\circ, 44^\circ, 59^\circ$  and  $77^\circ$ . The identified cobalt oxide is the cobaltous oxide, with crystallites in the cubic normal spinel structure, face-centered cubic lattice cell, fcc, with the space group  $F\bar{d}3m$  (CHEN; WU; SELLONI, 2011). Its spinel structure is  $(\text{A}^{2+})(\text{B}^{3+})_2\text{O}_4$  (HILL; CRAIG; GIBBS, 1979), formed by both  $\text{Co}^{2+}$  and  $\text{Co}^{3+}$  ions.

Figure 10 – (a) SBA-15 support and (b) 15% Co/SBA-15 catalyst X-ray diffractograms in the  $10^\circ \leq 2\theta \leq 90^\circ$  Bragg angle range



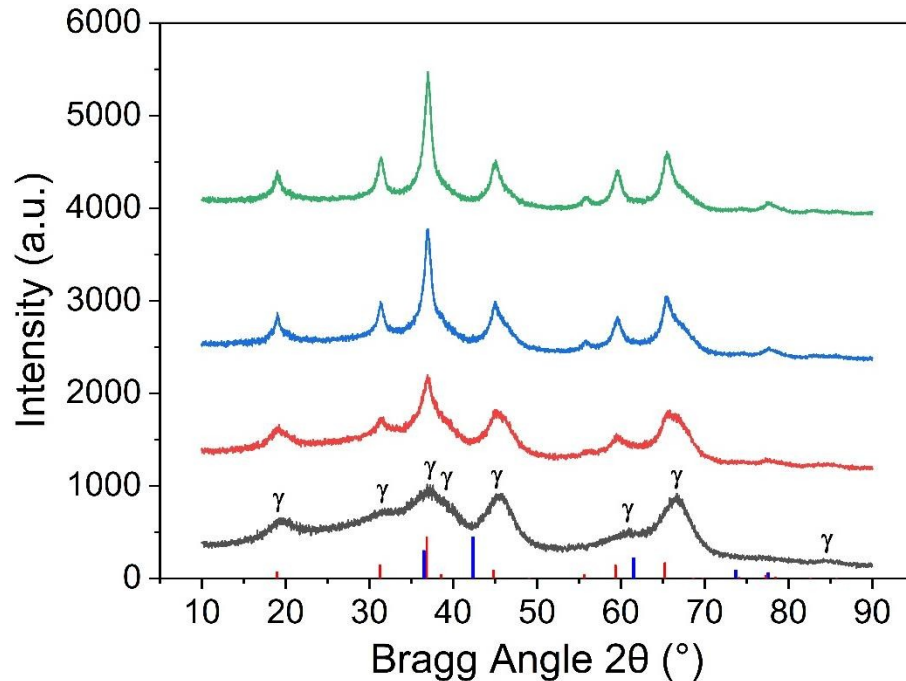
(a)



(b)

Note: The codes in (b) refers to the data obtained in crystallographic reference of  $\text{Co}_3\text{O}_4$  (PDF#00-043-1003) and  $\text{CoO}$  (PDF#00-043-1004).

Figure 11 – X-Ray diffractograms of  $\gamma$ -Al<sub>2</sub>O<sub>3</sub> support and of the Co/ $\gamma$ -Al<sub>2</sub>O<sub>3</sub> catalysts in the  $10^\circ \leq 2\theta \leq 90^\circ$  Bragg angle range



Note: The reference codes of the data of crystallographic patterns of Co<sub>3</sub>O<sub>4</sub> (PDF#00-043-1003) and CoO (PDF#00-043-1004) and  $\gamma$ -Al<sub>2</sub>O<sub>3</sub> phase (PDF#00-010-0425). Green line for the 15% Co/ $\gamma$ -Al<sub>2</sub>O<sub>3</sub>; Blue line for the 10% Co/ $\gamma$ -Al<sub>2</sub>O<sub>3</sub>; Red line for the 5% Co/ $\gamma$ -Al<sub>2</sub>O<sub>3</sub>; Gray line for the  $\gamma$ -Al<sub>2</sub>O<sub>3</sub> support. The red column is the reference pattern of Co<sub>3</sub>O<sub>4</sub> (PDF#00-043-1003); blue column, of CoO (PDF#00-043-1004).

The crystallite sizes were calculated from the (311) and (111) (*hkl*) plane faces and the parameters are presented in Table 10.

Table 10 – Crystallite sizes and parameters for the catalysts

Sample	Peak (°) <sup>a</sup>		FMHW (°) <sup>a</sup>		Ordered Crystalline Domain Size (nm)		Interplanar Space (Å)	
	(311)	(111)	(311)	(111)	<i>L</i> <sub>311</sub>	<i>L</i> <sub>111</sub>	<i>d</i> <sub>311</sub>	<i>d</i> <sub>111</sub>
15% Co/SBA-15	36.86	18.97	0.68	0.63	12.2	12.6	2.44	4.68
5% Co/ $\gamma$ -Al <sub>2</sub> O <sub>3</sub>	36.93	18.99	1.67	1.05	5.0	7.6	2.43	4.67
10% Co/ $\gamma$ -Al <sub>2</sub> O <sub>3</sub>	36.92	19.01	0.86	0.59	9.6	13.6	2.43	4.67
15% Co/ $\gamma$ -Al <sub>2</sub> O <sub>3</sub>	36.96	19.00	0.96	0.82	8.7	9.8	2.43	4.67

Note: (a) – Data obtained using the Pseudo Voigt function (PsdVoigt1) for peak fitting in Origin<sup>®</sup> software.

The mean crystallite sizes were obtained from the dataset (APPENDIX C) using Pseudo-Voigt fitting method with R<sup>2</sup> larger than 0.7 and compared with a modified Scherrer equation (MONSHI; FOROUGH; MONSHI, 2012), as presented in Table 11. This method assumes in

the range  $2\theta$  0-180° that the nanocrystallite have identical L values for all peaks, reducing the effect of systemic errors.

Table 11 – Mean Crystallite size determination and the different parameters used for each catalyst

Sample	Mean $L_{hkl}$ (nm)	Modified Scherrer Equation	
		Mean $L_{hkl}$ (nm)	$R^2$
15% Co/SBA-15	10.45±1.89	12.78	0.8486
5% Co/ $\gamma$ -Al <sub>2</sub> O <sub>3</sub>	6.60±1.63	7.30	0.4569
10% Co/ $\gamma$ -Al <sub>2</sub> O <sub>3</sub>	9.30±2.25	12.20	0.8801
15% Co/ $\gamma$ -Al <sub>2</sub> O <sub>3</sub>	7.83±1.73	10.48	0.8816

The results show the different Co<sub>3</sub>O<sub>4</sub> crystallite sizes. Notice that the direct correlation between crystallite size and metallic loading. However, the 10% Co/ $\gamma$ -Al<sub>2</sub>O<sub>3</sub> presented the highest L value. The 15% Co/ $\gamma$ -Al<sub>2</sub>O<sub>3</sub> presented smaller crystallite sizes than the 10% Co/ $\gamma$ -Al<sub>2</sub>O<sub>3</sub>, which is probably due to the number of steps of metal loading. On the other hand, the 15% Co/SBA-15 and the 10% Co/ $\gamma$ -Al<sub>2</sub>O<sub>3</sub> catalysts have similar crystallite sizes. Note that this value is higher than the pore diameter of the SBA-15 support (~7.0 nm). In fact, the SBA-15 feature lead to high dispersion of nanoparticles, along with reduced metal oxide-support interaction, resulting in agglomeration when compared to its counterpart. Moreover, the crystallite size of Co<sub>3</sub>O<sub>4</sub> over the SBA-15 support is in good agreement with the reported values in the literature employing the same impregnation method (11.4-13.8 nm range) (PRIETO et al., 2009). It is also relevant that there is a tendency for crystallite size reduction after the reduction step (BEZEMER et al., 2006).

### 6.1.5 INDUCTIVELY COUPLED PLASMA OPTICAL EMISSION SPECTROMETRY (ICP-OES) ANALYSIS

The synthesized materials were analyzed by ICP-OES and compared with the nominal values. According to the XRD, cobaltic oxide was formed, which was considered as base for calculations to allow the comparison. Table 12 presents the results for the studied catalysts, based on the quantified amount of Co element on each sample. Errors < 5.00 % were obtained for all catalysts. The samples analyzed through this technique were calcined and submitted to analysis, which means that the amount of Co quantified relates to the oxidized form of the active phase over the respective support. It is important to cite that the obtained ICP content was

corrected by the water content (%) present in each catalyst, since the samples used for the analysis were not dried prior to analysis. Thus, the considered water content was the same obtained from TGA analysis at Table 7.

Table 12 – Inductively coupled plasma optical emission spectrometry (ICP-OES) analysis results for Co quantification

Sample	Mean Co (wt.%) <sup>a</sup>	Water (%) <sup>b</sup>	Water-Corrected Mean Co (wt.%) <sup>c</sup>	Nominal Co/Co <sub>3</sub> O <sub>4</sub> (wt.%) <sup>d</sup>	Error (%) <sup>e</sup>	Achieved Co Load (wt.%) <sup>f</sup>
15% Co/SBA-15	12.83	5.58	13.59%	14.23	4.50%	14.29%
5% Co/ $\gamma$ -Al <sub>2</sub> O <sub>3</sub>	4.48	9.32	4.94%	4.91	0.50%	5.03%
10% Co/ $\gamma$ -Al <sub>2</sub> O <sub>3</sub>	8.20	10.71	9.18%	9.65	4.85%	9.50%
15% Co/ $\gamma$ -Al <sub>2</sub> O <sub>3</sub>	12.84	8.71	14.07%	14.23	1.14%	14.82%

Notes: (a) – The mean value was based on analysis performed by two replicates; (b) – The water amount was obtained from the TGA performed at section 6.1.2; (c) – The Water-Corrected Mean Co was calculated by removing the water weight % effect over the Mean Co%, i.e., dividing Mean Co% by (1 - Water%), which was not considered while calculating the weight percentage obtained directly by ICP-OES analysis; (d) – The Nominal Co/Co<sub>3</sub>O<sub>4</sub> (wt.%) was calculated based on the nominal Co load expected on the catalyst with the active phase at oxidized state (Co<sub>3</sub>O<sub>4</sub>, selected based on XRD analysis) (see Equation (A.4), where the nominal Co load (5, 10 or 15%) corresponds to z); (e) – The error was calculated based on the nominal Co/Co<sub>3</sub>O<sub>4</sub> load in comparison with the calculated Co (wt.%), and the absolute value was used; (f) – The achieved Co load (wt.%) is the real Co load, i.e. on the catalyst in a condition of 100% reduction and is comparable to nominal values (see Equation (A.4), where the calculated Co corresponds to x).

### 6.1.6 SCANNING ELECTRON MICROSCOPY (SEM) ANALYSIS

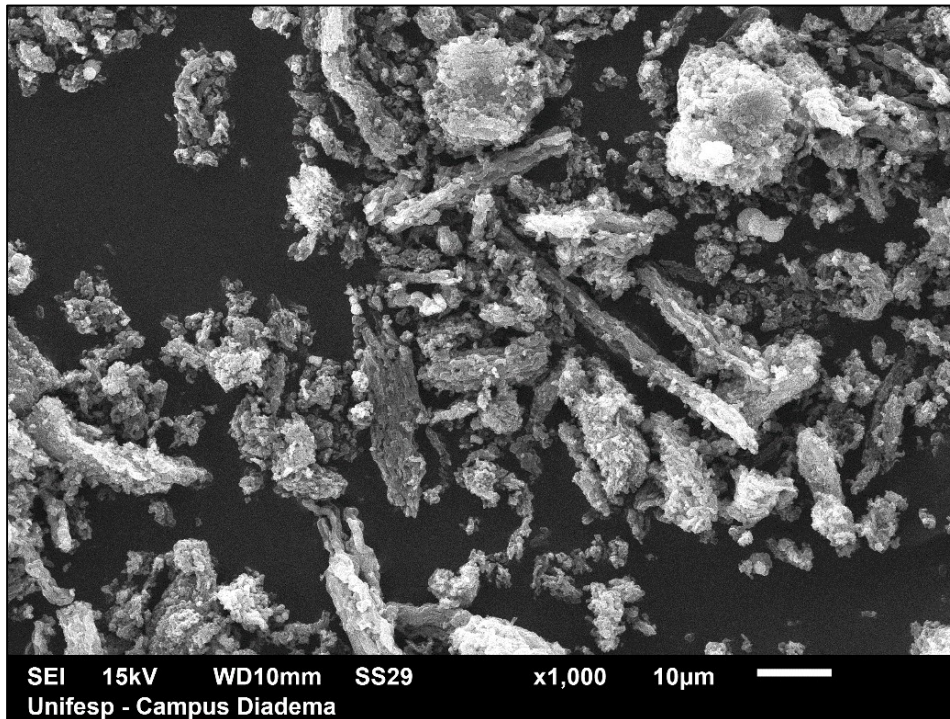
The catalysts were analyzed by SEM, which shows important morphological modifications of catalyst particles, providing information about the catalyst size, shape and spatial arrangement.

The prepared SBA-15 support and catalyst SEM analyses are displayed in Figure 12.

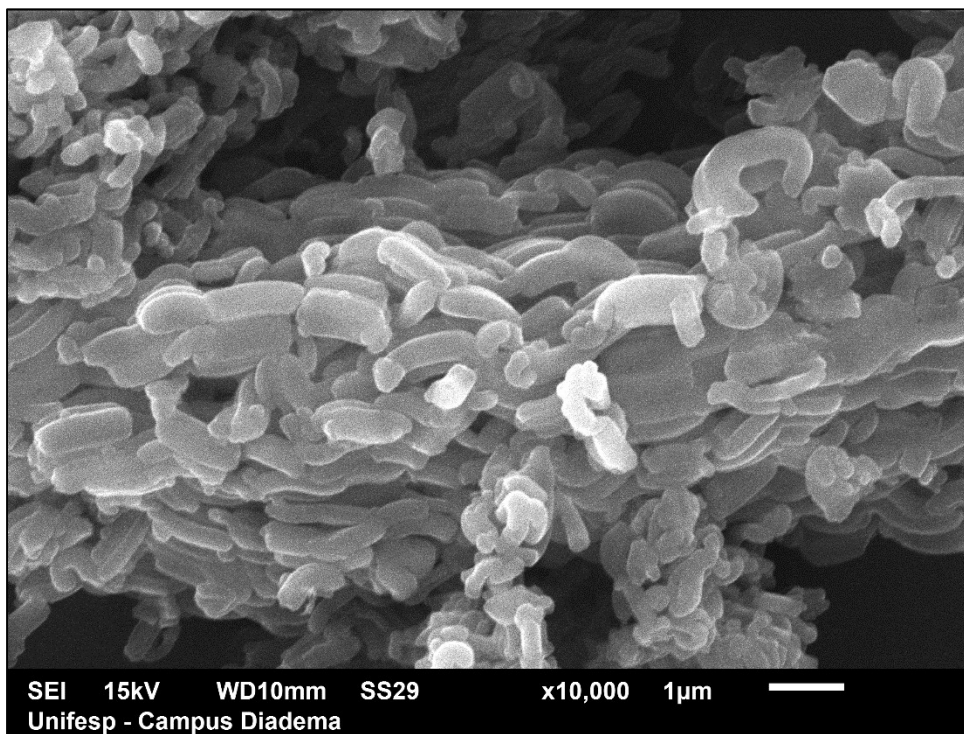
The magnification in Figure 12 (a) suggests the formation of aggregates of several sizes and shapes. Figure 12 (b), at a higher magnification, displays the typical aggregated rod-like SBA-15 morphology. Analyzing particles with the same contrast, it was possible to determine a mean particle width of  $0.39 \pm 0.09 \mu\text{m}$  and a mean length of  $1.07 \pm 0.14 \mu\text{m}$  (16 random points) in good agreement with the literature (PRIETO et al., 2009).

The morphology change of the catalyst was also assessed (Figure 13). Figure 13 (b) shows that the individual dispersed SBA-15 particles were preserved. The particles with the same contrast indicate a mean particle width of  $0.13 \pm 0.05 \mu\text{m}$  and a mean length of  $0.33 \pm 0.07 \mu\text{m}$  (20 random points).

Figure 12 – SEM images of SBA-15 support in different magnifications

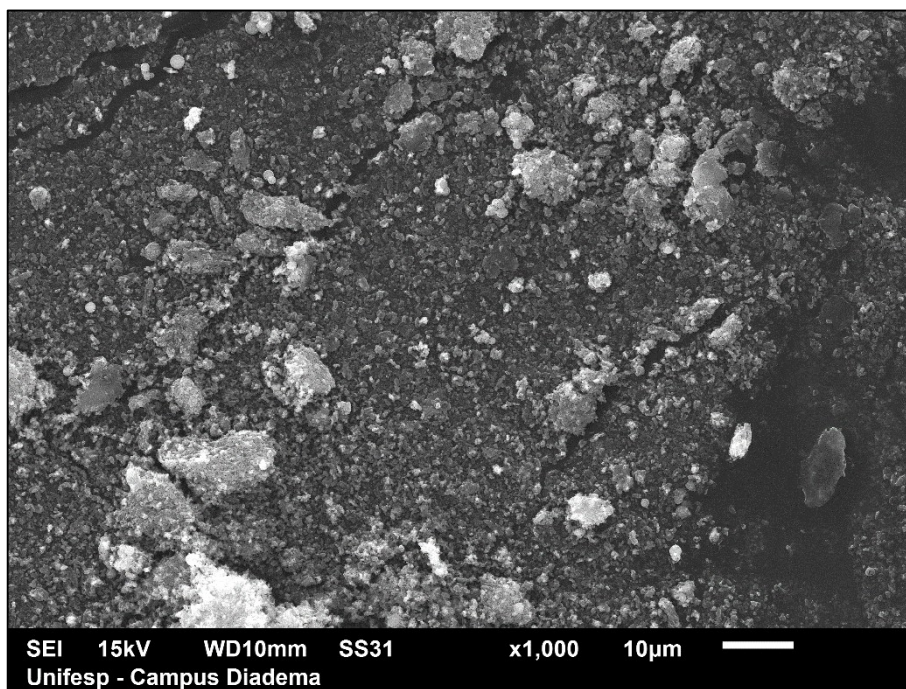


(a)

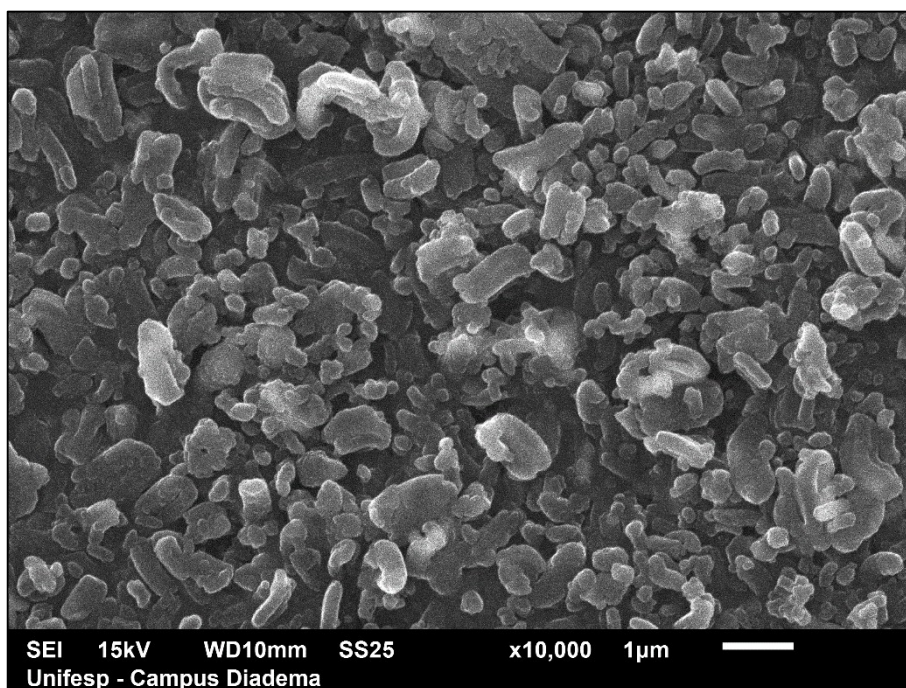


(b)

Figure 13 – SEM images of 15 wt.% Co/SBA-15 catalyst in different magnifications



(a)



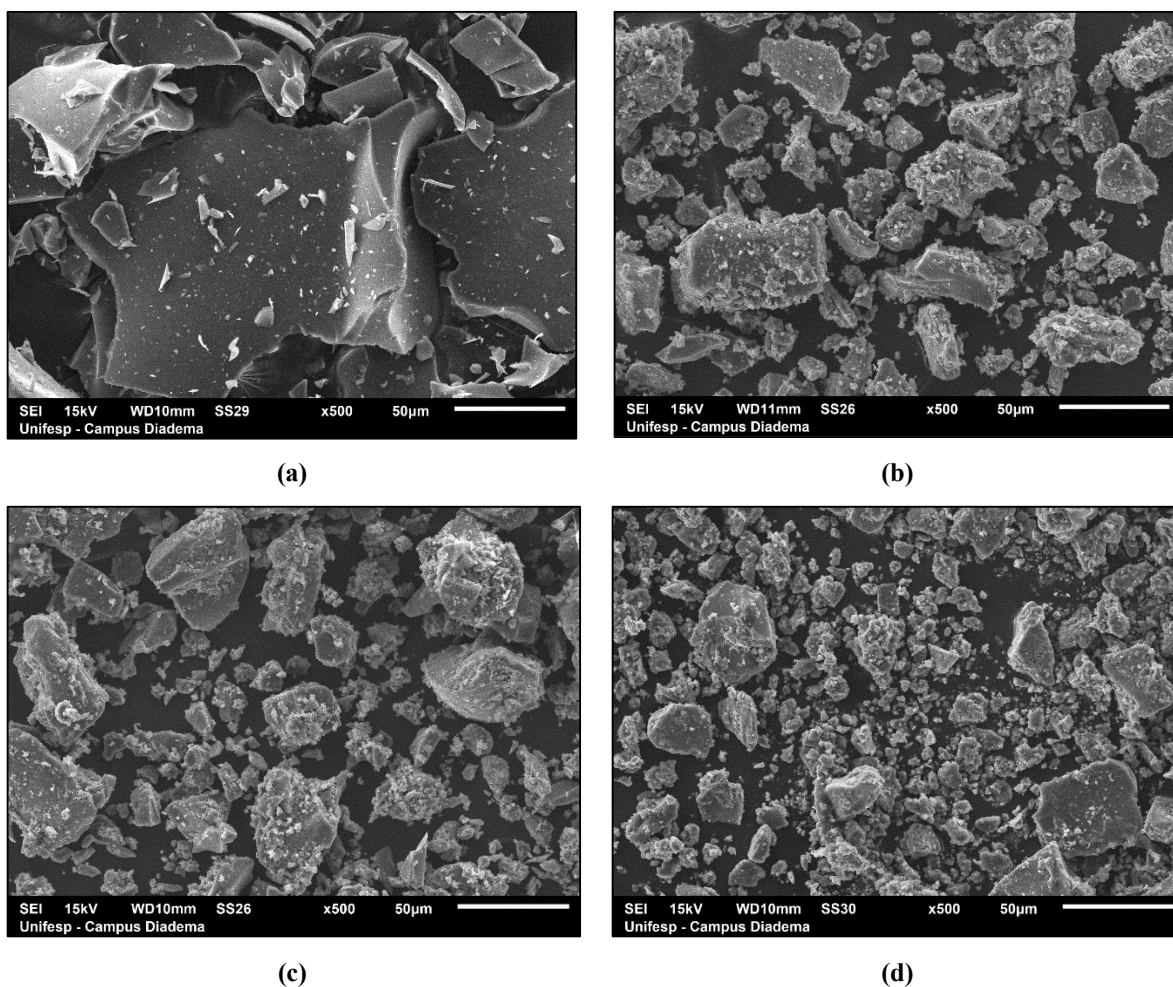
(b)

The differences in particle sizes are probably due to the fact that SBA-15 may dissolve in water at  $\text{pH} \geq 7$  (PHAM; SEDLAK; DOYLE, 2012), causing particle dissolution, most likely reducing its overall size and increasing its pore wall diameter, not observed (Table 8) or even breaking down due to the micropores, which are formed as a consequence of triblock-copolymer ethylene

oxides (EO) temperature-hydrophobicity relationship (KRUK et al., 2000) that before dissolution would occur rapidly. Fragmentation is an important factor over dissolution since it is known to improve surface area and to have an important effect over dissolution kinetics (SEAGER et al., 2018). Although the micropores increased (Figure 9 (C) and (D)), Khodakov *et al.* (2005) observed that cobalt impregnation inexpressively impacts the SBA-15 structure up to a 20 wt.% load. On the other hand, if the size variation after impregnation may be explained by a difference in depth of the SEM images, particle proportions (length/width ratio, or L/W) are kept constant. In fact, we have estimated a L/W ratio of  $2.52 \pm 1.00 \mu\text{m}$  and of  $2.74 \pm 0.71 \mu\text{m}$  for SBA-15 and 15% Co/SBA-15, respectively. A bilateral t-test disclosed a non-significant variation between each value, validating such hypothesis at a 1% significance.

The SEM analyses for the synthesized  $\gamma\text{-Al}_2\text{O}_3$  support and catalysts are displayed in Figure 14.

Figure 14 – SEM images of (a)  $\gamma\text{-Al}_2\text{O}_3$  support, (b) 5 % Co/ $\gamma\text{-Al}_2\text{O}_3$ , (c) 10 % Co/ $\gamma\text{-Al}_2\text{O}_3$ , and (d) 15 % Co/ $\gamma\text{-Al}_2\text{O}_3$  catalysts in the same magnification (500x)



In Figure 14 (a), the SEM images of  $\gamma\text{-Al}_2\text{O}_3$  support and the catalysts are displayed. The formation of very large particles ( $> 50 \mu\text{m}$ ) of the support after the thermal treatment can be observed. Before impregnation, the support was also macerated, reducing the particle size (in the sampled material, it is possible to determine a size  $\leq 50 \mu\text{m}$ ). All samples showed heterogeneous distribution, although the sizes were quite similar as shown in Figure 14 (b)-(d). Emphasis must be given to the caution at generalization, since the SEM analysis is constituted of a only a very small fraction of the prepared material.

### 6.1.7 TRANSMISSION ELECTRON MICROSCOPY (TEM) ANALYSIS

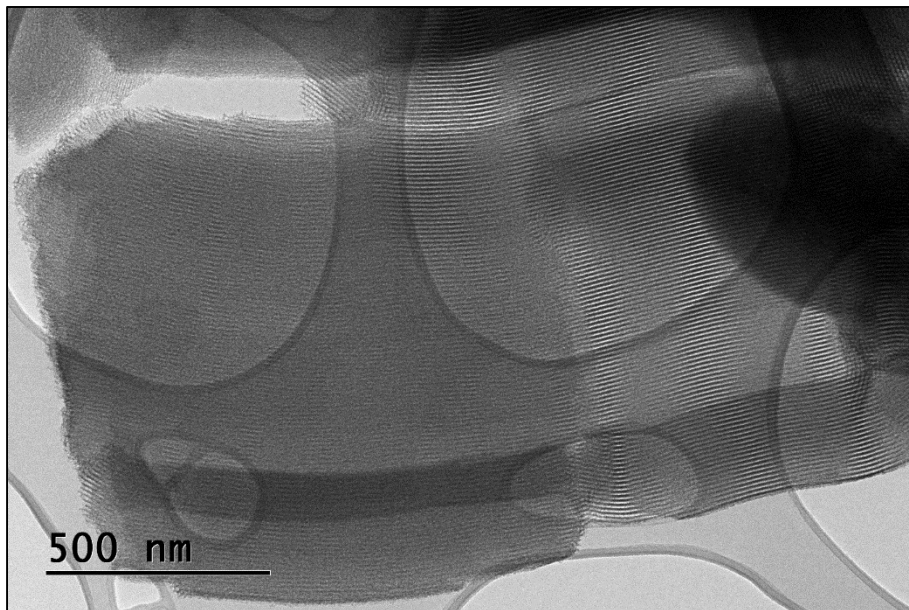
The transmission electron microscopy provides structural information through direct observation of the surface particle sizes and crystalline orientation. The SBA-15 support and the catalysts, along with the  $\gamma\text{-Al}_2\text{O}_3$ -supported catalysts, were analyzed.

The mesopore structure of SBA-15 as synthesized is showed in Figure 15. Figure 15 (A) shows the formation of ordered mesoporous parallel channels. Figure 15 (B) denotes the hexagonally ordered structure of the well-defined mesopores.

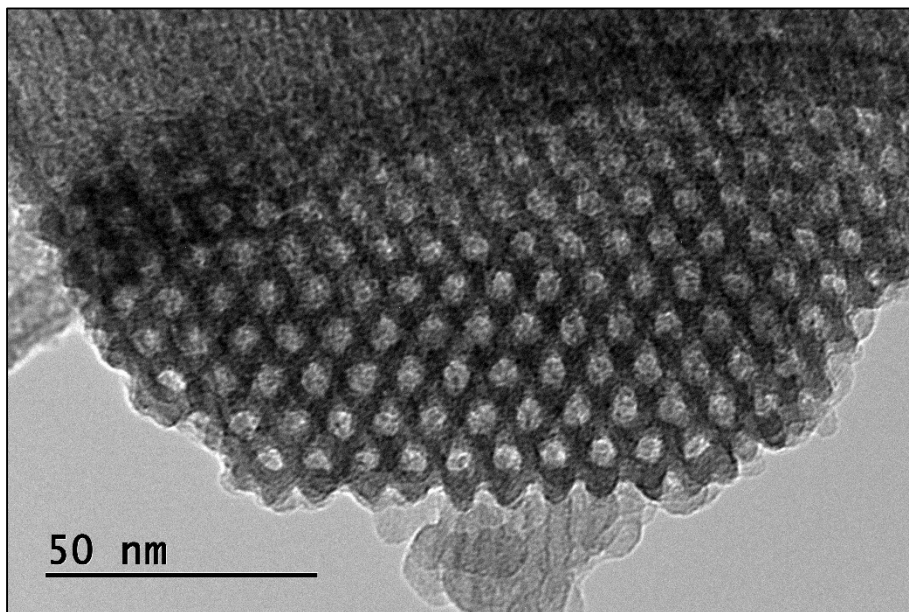
Noteworthy is that Figure 15 (B) allows the determination of the support pore diameters and wall sizes, exhibiting  $6.80 \pm 0.40 \text{ nm}$  (through 20 randomly selected regions), which is within the range obtained by BJH and NLDFIT calculations, but closer to the latter method, with errors of 3.32% and 22.46% for NLDFIT and BJH, respectively. The wall thickness of  $3.71 \pm 0.27 \text{ nm}$  was also measured and it is within the range reported in the literature, 3.0 to 6.5 nm (KLEITZ, 2008). Therefore, TEM images shows that the SBA-15 structure was successfully synthesized and results corroborates with  $\text{N}_2$ -sorption isotherm.

Different magnifications of the transmission electron microscopy analysis of SBA-15-supported catalyst are displayed at Figure 16.

Figure 15 – Transmission Electron Microscopy (TEM) of the prepared SBA-15 with a resolution of (a) 500 nm (lateral view); (b) 50 nm (cross-section view) displaying parallel channels of the ordered silica and the hexagonal structure of the channels

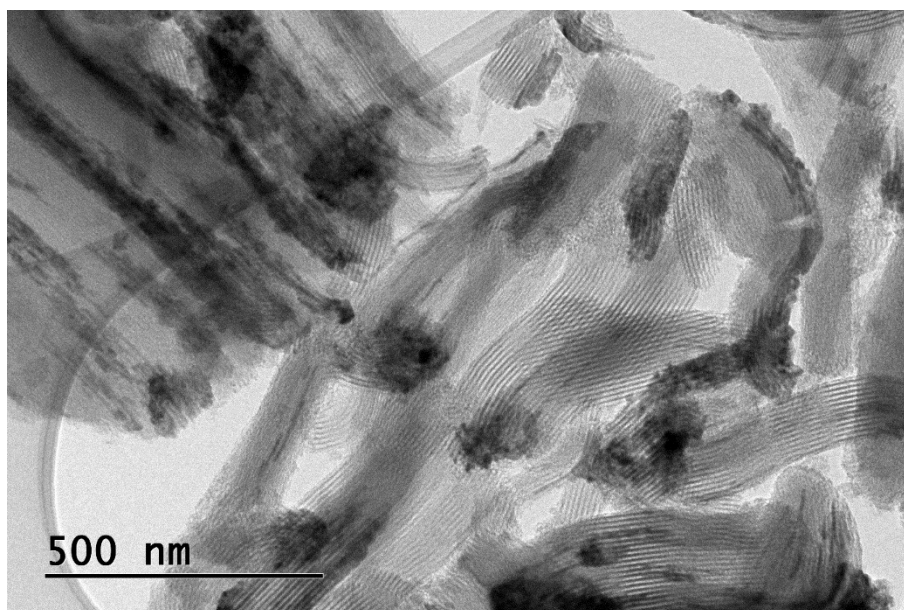


(a)

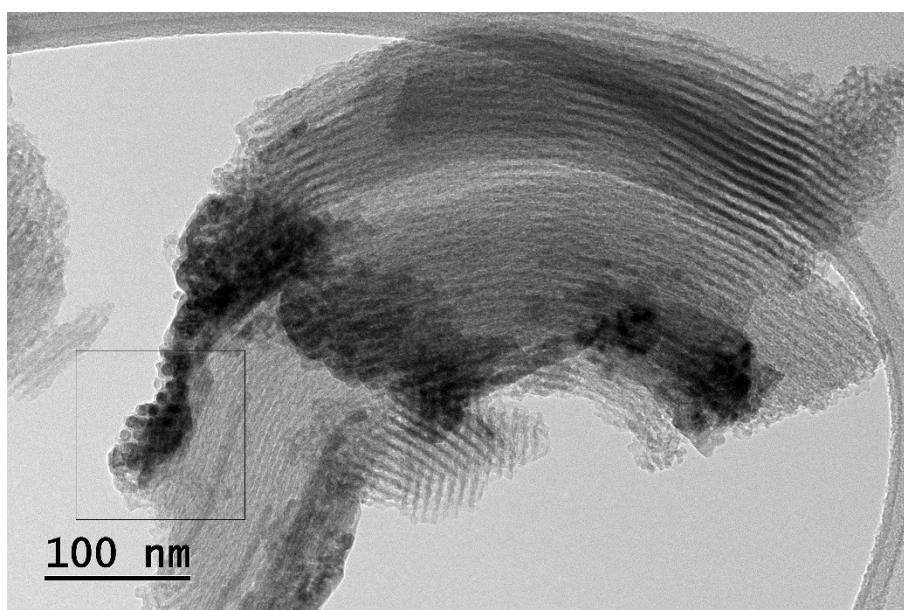


(b)

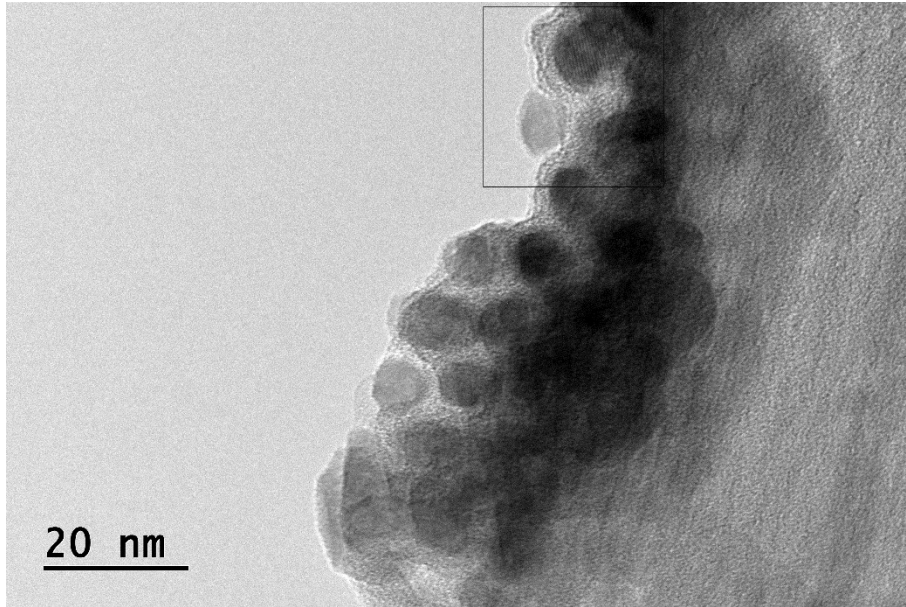
Figure 16 – Transmission Electron Microscopy (TEM) of the prepared 15%Co/SBA-15 with a resolution of (a) 500 nm; (b) 100 nm; (c) 20 nm; and (d) 5 nm displaying parallel channels of the ordered silica and successful cobalt impregnation (contrast)



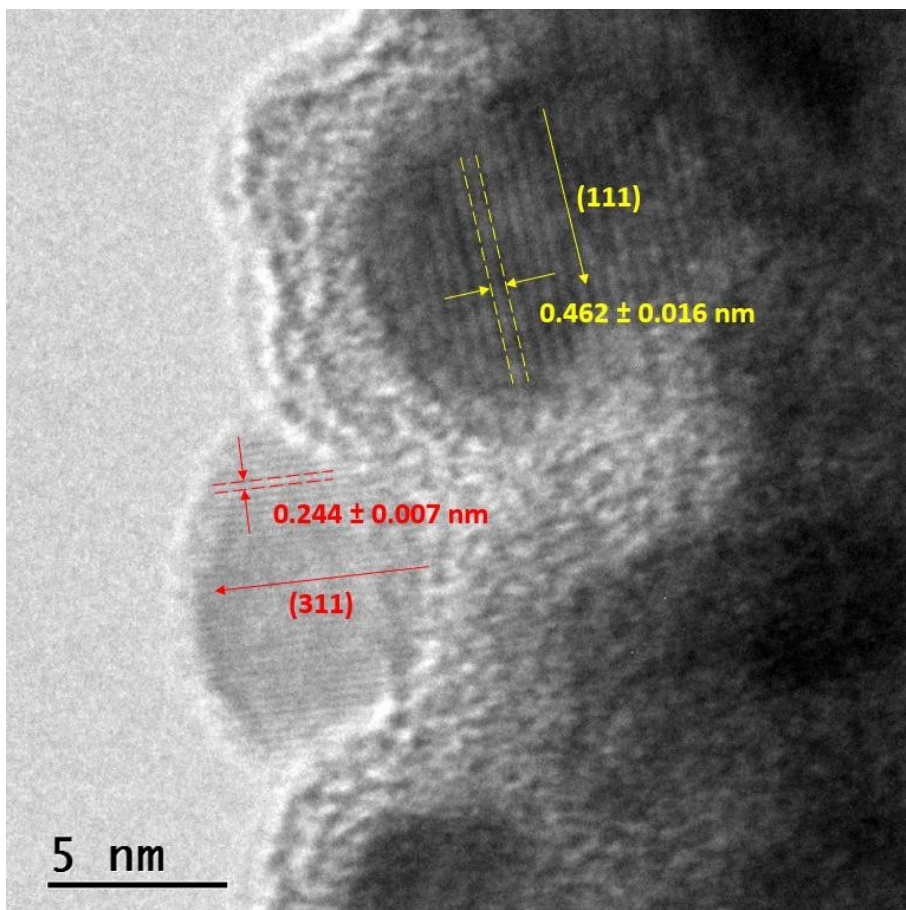
(a)



(b)



(c)



(d)

The cobalt oxide is well distinguished due to the contrast with the ordered, amorphous, silica structure. Figure 16 (a) shows that all cobalt oxide particles are homogeneously dispersed in all particles, but heterogeneously distributed over the support. Noteworthy is that the cobalt nanoparticles entered the SBA-15 mesopores, visible at Figure 16 (b), but also concentrated at pore extremities. Emphasis must be given to the caution regarding generalization, since the TEM analysis is constituted of a very small fraction of the prepared material. As aforementioned and visible at Figure 16 (c), SBA-15 presented ordered mesopores size, although it is not clear if the particle was actually inside or outside the pores. However, two factors can affect the metal dispersion over the support surface: interaction between precursor solution and support at its interface and the metal-support interaction; in this way, conventional impregnation generally result in the agglomeration of metal nanoparticles (SINGH et al., 2018), especially due to the low cobalt-silica interaction (JACOBS et al., 2002). The 15%Co/SBA-15 pore ( $6.72 \pm 0.53$  nm) and wall ( $3.74 \pm 0.31$  nm) sizes were also measured and were close to the value obtained for the support obtained from 20 random measurements. The measured values present errors of 3.32% and 22.46% for NLDFT and BJH, respectively. Figure 16 (c) and (d) show cobalt nanoparticles with increasing magnifications. The crystallographic orientation of two cobalt nanoparticles were identified at Figure 16 (d) and marked with red and yellow for each individual nanoparticle, along with the respective interplanar spaces (20 random data points for each crystallite). These data allowed to identify the (311) and (111) interplanar spaces of the cobalt oxide cubic crystal system ( $\text{Co}_3\text{O}_4$ ), using the PDF Card #00-043-1003 reference pattern. The crystallite sizes were of  $7.76 \pm 0.01$  nm and  $11.29 \pm 0.04$  nm, respectively.

TEM images of the alumina-based catalysts are shown in Figures 17 to 19 for 5 to 15% Co/ $\gamma$ - $\text{Al}_2\text{O}_3$  catalysts, respectively.

All alumina-supported catalysts images showed different contrasts within the same specimen. At first, a straightforward approach can be considered, in which supported cobalt nanoparticles are evidenced by contrast, similarly to SBA-15-supported catalyst. Based solely on the contrast, several EDX evaluations were carried out for 5% and 10% Co/ $\gamma$ - $\text{Al}_2\text{O}_3$ , but no pattern was identified. For instance, Figure 17 (D) shows that site b, with lower contrast compared to its vicinity including site a, presents a higher concentration of Co. On the other hand, Figure 18 (B) shows the cobalt oxide (311) crystallographic orientation identified for 10% Co/ $\gamma$ - $\text{Al}_2\text{O}_3$ , whose identified crystallites present mean sizes of  $9.6 \pm 0.3$  nm, which is very close to the value obtained by XRD measurement, calculated by the Scherrer Equation. The difficulty in

identifying cobalt nanoparticles over alumina support can be due to some effects that occur concomitantly, such as Bragg contrast, mass-thickening contrast and nanoparticle location.

Mass-thickness contrast is dependent on thickness and atomic number of the elements, along with density differences (WILLIAMS; CARTER, 2009). Table 13 shows the density and atomic number of the materials that composes the synthesized catalysts. Based on the atomic number of elements, cobalt should be easily distinguished in both catalysts; however, the relative density between oxides shows that this effect is significant only between  $\text{SiO}_2$  and  $\text{Co}_3\text{O}_4$ . At the same time, the most significant scattering effect of TEM occurs, which is the Bragg contrast. In this case, it is expected that crystals present higher contrast due to the electron diffraction. This is evident for the Co/SBA-15 catalyst, whose OMS is amorphous, as corroborated by XRD analysis, enhancing contrast between silica and cobalt nanoparticles. Since both alumina and cobalt oxide presents polycrystalline natures, the contrast due to the crystallinity can be neglected. Finally, it is possible that the metal loading methods employed in this study led to the formation of small cobalt nanoparticles inside of the pores, which were formed by impregnation itself, as suggested by XRD and  $\text{N}_2$ -sorption analysis (detailed above).

Table 13 – Densities of catalysts' compounds

Compound	Formula	Element (Atomic Number)	Density (g.cm <sup>-3</sup> )	Relative Density <sup>a</sup>
Cobaltic Oxide	$\text{Co}_3\text{O}_4$	Co (27)	6.11	1.00
Silicon Dioxide (vitreous)	$\text{SiO}_2$	Si (14)	2.196	2.78
Aluminum Oxide	$\text{Al}_2\text{O}_3$	Al (13)	3.986	1.53

Source: Williams (1996).

Note: (a) – the Relative Density is the ratio between cobaltic oxide density and the support (silicon dioxide or aluminum oxide).

Figure 17 – Transmission Electron Microscopy (TEM) of the prepared 5%Co/ $\gamma$ -Al<sub>2</sub>O<sub>3</sub> with a resolution of (a) 500 nm; (b) 100 nm; (c) 50 nm; and (d) 20 nm along with EDS analyses of two selected spots (a and b). Detected copper (Cu) is due to the grid composition

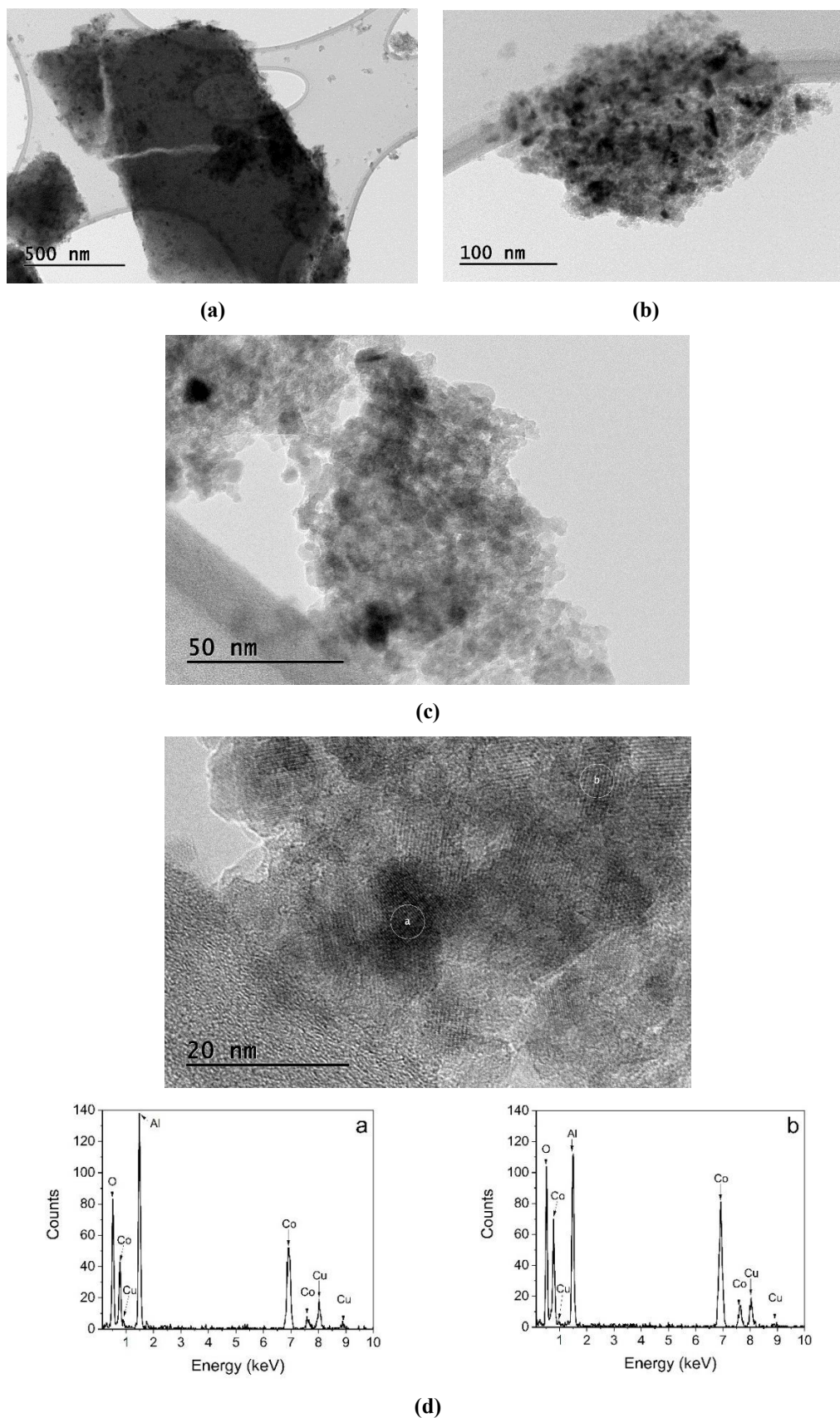
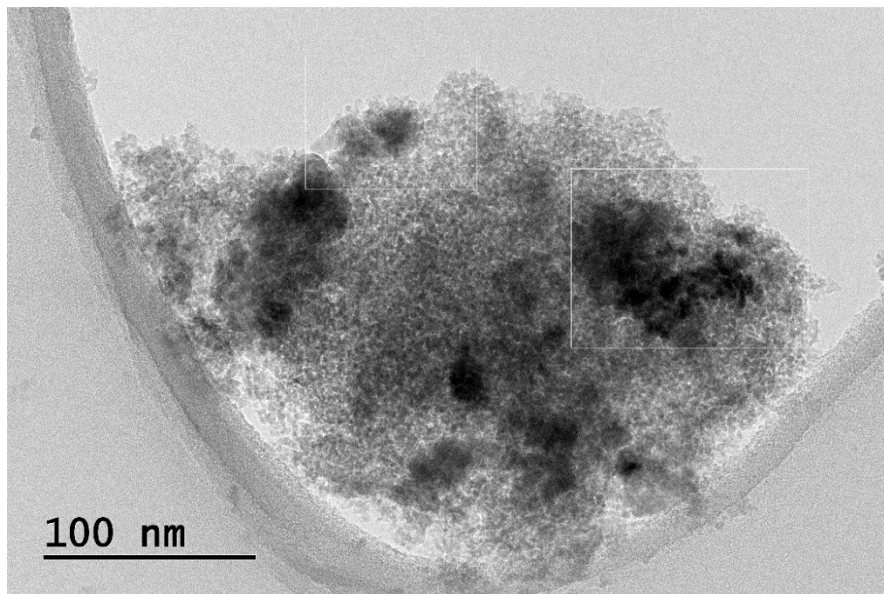
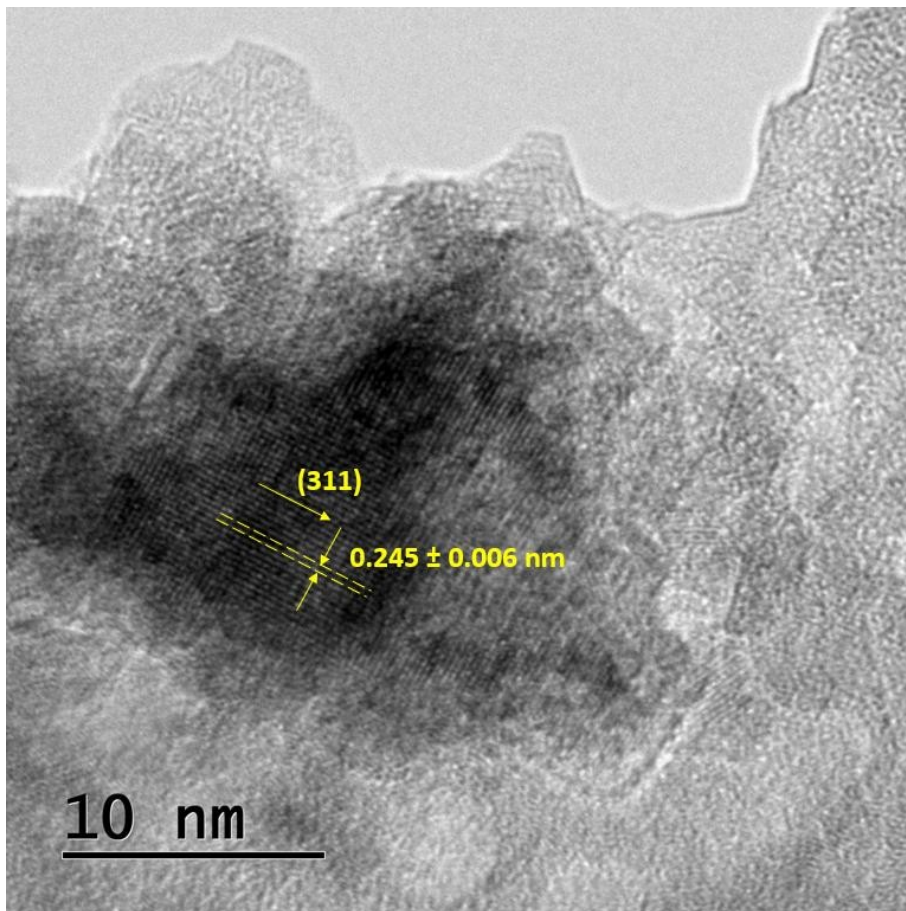


Figure 18 – Transmission Electron Microscopy (TEM) of the prepared 10 % Co/ $\gamma$ -Al<sub>2</sub>O<sub>3</sub> with a resolution of (a) 100 nm; and (b) 10 nm, presenting one identified crystallographic orientation

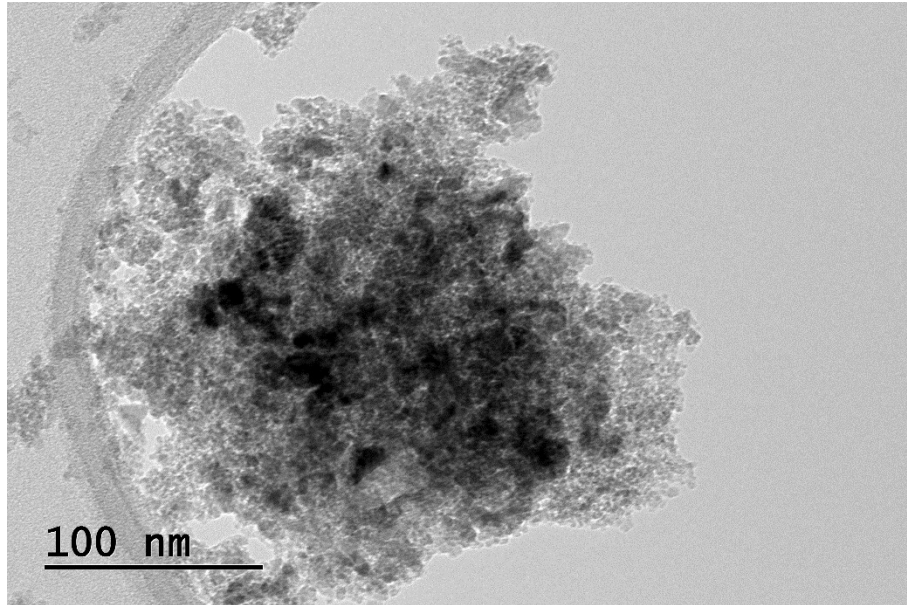


(a)

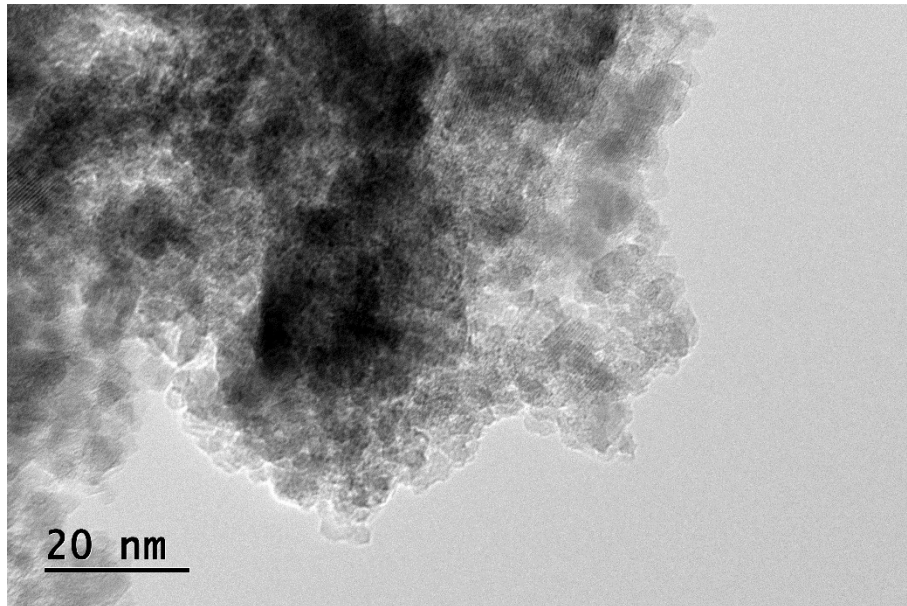


(b)

Figure 19 – Transmission Electron Microscopy (TEM) of the prepared 15 % Co/ $\gamma$ -Al<sub>2</sub>O<sub>3</sub> with a resolution of (a) 100 nm; and (b) 20 nm



(a)



(b)

### 6.1.8 RAMAN SPECTROSCOPY ANALYSIS

The Raman spectroscopy uses the interaction between a characteristic photon, usually using a laser as a monochromatic source, and the sample molecule. The photon inelastic scattering (Stokes and anti-Stokes Raman scattering) rare event that results from this interaction provides information about the sample (a “fingerprint”), such as chemical and structural information, which can be used for its identification, with little sample preparation. Such scattering results

from an interaction between matter and light, which leads to specific molecule vibrations. For Raman effect to occur, a change in molecular polarizability is required during the vibration. Succinctly, the measured Raman spectra results from the intensity of the measured Raman shift ( $\text{cm}^{-1}$ ), which is obtained by the inverse variation between the wavelength of the excitation laser and the wavelength of the Raman scatter.

The Raman spectra of each synthesized catalyst are shown at Figure 20.

Figure 20 – Raman spectra of prepared catalysts: 5% Co/ $\gamma$ -Al<sub>2</sub>O<sub>3</sub> (a), 10% Co/ $\gamma$ -Al<sub>2</sub>O<sub>3</sub> (b), 15% Co/ $\gamma$ -Al<sub>2</sub>O<sub>3</sub> (c) and 15% Co/SBA-15 (d)

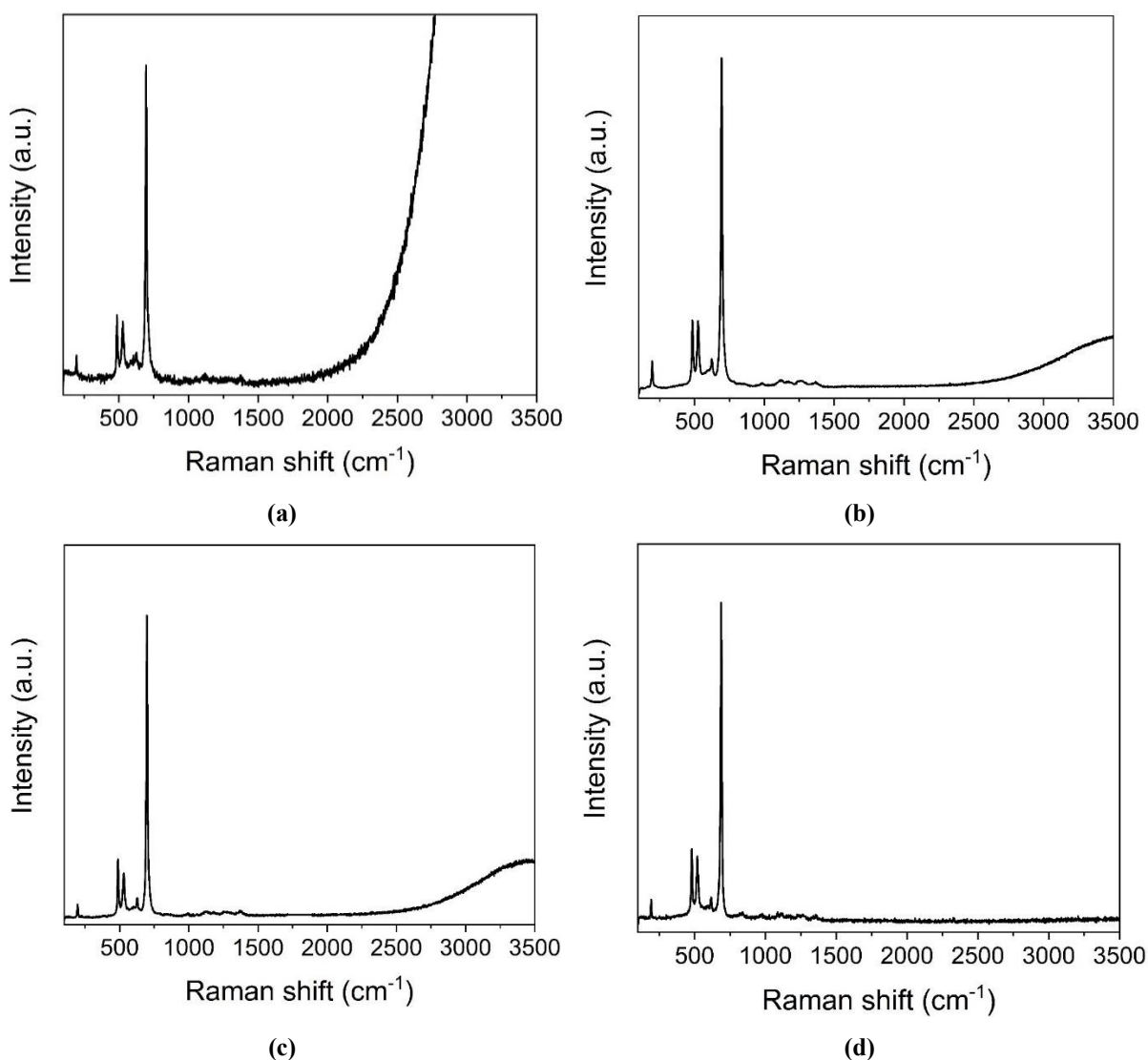


Figure 20 displays the formation of five bands for all prepared catalysts in a range of 100-1000  $\text{cm}^{-1}$ . The frequencies of vibration observed depend on the masses of the atoms involved and the bond strength. Therefore, heavy atoms with weak bonds have low Raman shifts, whereas light atoms with strong bonds have high Raman shifts. Indeed, in this case, bands that represent

the cobalt oxide fingerprint are expected, because they are quite similar. This shows that a considerable amount of active phase is distributed over the catalyst surface for all tested samples.

Alumina materials are known to present fluorescence, which is easy to identify in Figure 20 (a), (b) and (c), and seems to be affected by the metal load, which reduced the fluorescence of the material (TAHERI NAJAFABADI et al., 2016). The similar profiles among different supports can be explained by the fact that alumina materials are not Raman active (ZHANG et al., 2005b), while SBA-15 bands were very weak (see Figure G.1 in APPENDIX G), therefore the active phase bands are predominant. Table 14 shows the identified bands for each catalyst.

Table 14 – Bands identified in Raman spectrum of each prepared catalyst

Catalyst	Band				
	1	2	3	4	5
5% Co/ $\gamma$ -Al <sub>2</sub> O <sub>3</sub>	196.4	486.1	529.2	627	696.5
10% Co/ $\gamma$ -Al <sub>2</sub> O <sub>3</sub>	196.3	484.1	525.1	622.2	693.0
15% Co/ $\gamma$ -Al <sub>2</sub> O <sub>3</sub>	196.5	488.0	530.7	627.7	697.6
15% Co/SBA-15	194.6	480.6	519.9	617.0	687.6

Noteworthy is that bands 1-5 correspond to the Raman active vibrational modes of Co<sub>3</sub>O<sub>4</sub> spinel, namely F<sub>2g</sub> (194.4 cm<sup>-1</sup>), E<sub>g</sub> (482.4 cm<sup>-1</sup>), F<sub>2g</sub> (521.6 cm<sup>-1</sup>), F<sub>2g</sub> (618.4 cm<sup>-1</sup>) and A<sub>1g</sub> (691.0 cm<sup>-1</sup>), as reported elsewhere (HADJIEV; ILIEV; VERGILOV, 1988). Although the bands and their assignments are clear in the literature, the vibrational modes of Co<sub>3</sub>O<sub>4</sub> are not so clear and details are very hard to find. Nonetheless, knowing the Co<sub>3</sub>O<sub>4</sub> spinel structure (Co<sup>2+</sup>(Co<sup>3+</sup>)<sub>2</sub>O<sub>4</sub><sup>2-</sup>) with Co<sup>2+</sup> and Co<sup>3+</sup> positioned at the tetrahedral and octahedral sites (HADJIEV; ILIEV; VERGILOV, 1988) and considering it as a general structure ABO<sub>4</sub>, Rivas-Murias and Salgueiriño (2017) claim that the A<sub>1g</sub> vibration mode involves the A-O stretching and deformation of three octahedral sites nearest to each oxygen, which relies upon A<sup>2+</sup> and B<sup>3+</sup> occupations. The other modes are related to different motions of the AO<sub>4</sub> unit, with the F<sub>2g</sub> being assigned as a complete translation of the AO<sub>4</sub> unit within the spinel lattice.

Overall, it is possible to visualize in Table 14 that the Raman shift of alumina-based catalysts are similar, whereas the SBA-15 catalyst presents a more dissonant shift for all evaluated bands. The clear difference might be explained by the effect of the metal-support interaction, perhaps indirectly, due to its effects over dispersion and hence over crystallite size and particle agglomeration, which reportedly shifts the Raman band to lower values and also leads to band

broadening (LORITE et al., 2012; ZUO et al., 1998), especially for 15%Co/SBA-15 (e.g. see particle agglomeration in Figure 16). It must be stated that the temperature also affects the results. Moreover, no characteristic  $\text{CoAl}_2\text{O}_4$  peaks were identified and two weak bands at  $\sim 409$  and  $\sim 786 \text{ cm}^{-1}$  were expected, as identified by Zhang *et al.* (2005b). This means that, at least superficially and under measurement limitation, no aluminate was formed during calcination.

### 6.1.9 HYDROGEN-TEMPERATURE PROGRAMMED REDUCTION ANALYSIS ( $\text{H}_2$ -TPR)

The  $\text{H}_2$ -TPR analysis was performed determining the total amount of hydrogen gas consumption and the degree of reduction (DR), which in turn provides information about the oxidation state, support-metal oxide interaction, among others.

The results for the SBA-15- and alumina-supported catalysts are displayed in Figure 21 (A) and (B), respectively, in the temperature range of 300-1273 K. For the alumina-based catalysts the analysis was also performed isothermally at 1273 K for  $\sim 1$  h. There are singular reduction profiles for the analyzed catalysts.

The reduction steps occur at different temperatures for the pure active phase. Such steps may also occur individually in distinct temperatures depending on the support or promoters used for the catalyst preparation (JACOBS et al., 2002).

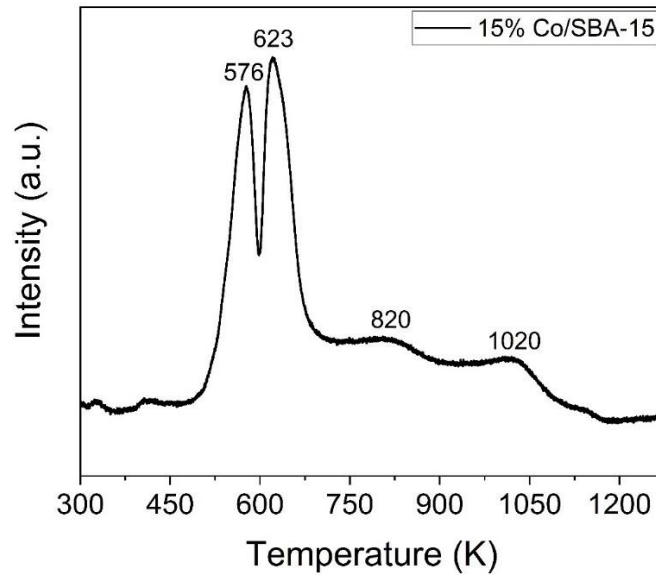
Figure 21 (A) displays the profile for the 15 wt.% Co/SBA-15 catalyst and shows four different peaks. The first peak occurs at 576 K and can be attributed to the first reduction step, following the equation (9). The second peak, which occurs at 623 K, is attributed to the equation (10) (KHODAKOV et al., 1997).



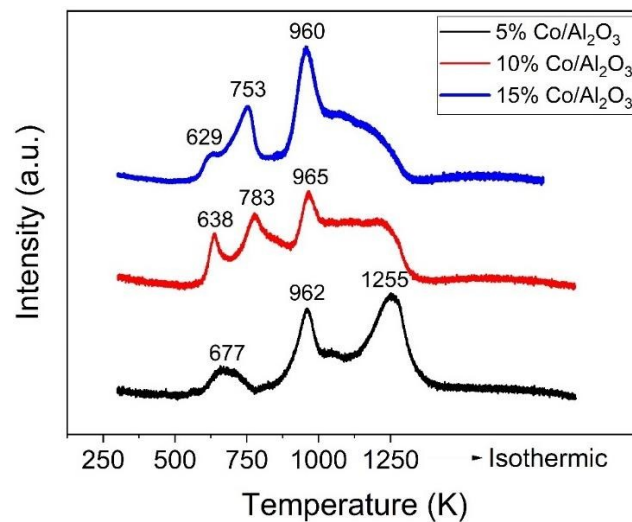
The following peaks occurs at very high temperatures (820 and 1020 K) and might be related to the reduction of silicates ( $\text{CoSiO}_3$ ), which were formed, as suggested by Wigzell and Jackson (2017) and Lualdi *et al.* (2011).

The  $\text{H}_2$ -TPR profiles for the alumina supported catalysts exhibited three different peaks and a broad peak at higher temperature.

Figure 21 – Hydrogen-Temperature Programmed Reduction ( $H_2$ -TPR) analyses for (a) 15% Co/SBA-15 and (b) 5, 10 and 15 wt.% Co/ $\gamma$ - $Al_2O_3$  catalysts (y-offset plots)



(a)



(b)

The 5 wt.% Co/ $\gamma$ - $Al_2O_3$  catalyst profile shows the first peak at 677 K, the second at 962 K and one at 1255 K. The first two peaks indicate the transformations of oxides to metallic cobalt ( $Co_3O_4 \rightarrow CoO \rightarrow Co^0$ ). In fact, the reduction of CoO species starts immediately after the complete reduction of  $Co_3O_4$  (BORG et al., 2007). This leads to the conclusion that a synergy of such features may affect the amount of reducible oxide metal present at the catalyst surface. Finally, the peak at higher temperature suggests the metal oxide-support interaction occurs around 1255 K. This suggests the formation of well-dispersed, small clusters of reducible cobalt nanoparticles over the alumina support surface (TIERNAN et al., 2001).

The catalysts with 10 and 15 wt.% show the first peak about 638 and 629 K, which can be respectively attributed to the transformation given by the equation (9); the second peak at 783 and 753 K, according to the equation equation (10). The peaks at 960 K increased with increased cobalt loading. Finally, the peaks at 1273 K indicate the reduction of cobalt aluminates ( $\text{CoAl}_2\text{O}_4$ ).

The degree of reduction was calculated based on the total consumption of hydrogen. The calculated values are presented in Table 15. It indicates that the degree of reduction increases with increasing Co content.

Table 15 – H<sub>2</sub>-uptake and degree of reduction (DR, %) for the prepared catalysts

Sample	H <sub>2</sub> -uptake ( $\mu\text{mol.g}_{\text{cat}}^{-1}$ )	DR <sub>ICP</sub> (%) <sup>a</sup>	DR <sub>nom</sub> (%) <sup>b</sup>
15% Co/SBA-15	682.17	90.94	82.38
5% Co/ $\gamma$ -Al <sub>2</sub> O <sub>3</sub>	516.25	62.97	57.29
10% Co/ $\gamma$ -Al <sub>2</sub> O <sub>3</sub>	601.62	78.54	66.37
15% Co/ $\gamma$ -Al <sub>2</sub> O <sub>3</sub>	687.15	88.14	79.13

Notes: (a) – DR<sub>ICP</sub> (%) is the degree of reduction value, in percentage, calculated based on the full run analysis for all catalysts, assuming that the Co content of each catalyst was that obtained from the ICP-OES analysis; (b) – DR<sub>nom</sub> (%) is the degree of reduction value, in percentage, calculated based on the full run analysis for all catalysts, assuming the nominal Co content of each catalyst.

As expected, the degree of reduction (DR) decrease with increasing loading, which suggests that there is an interaction between the alumina support and the cobalt nanoparticles. In fact, Raman data aforementioned showed that, superficially, no aluminate is formed, and it is possible that any unreducible cobalt might be inside impregnation-induced modified alumina structure. Interestingly, the degree of reduction for the 15% Co/SBA-15 and 15% Co/ $\gamma$ -Al<sub>2</sub>O<sub>3</sub> catalysts were very similar.

#### 6.1.10 TEMPERATURE PROGRAMMED DESORPTION ANALYSIS (H<sub>2</sub>-TPD AND CO-TPD)

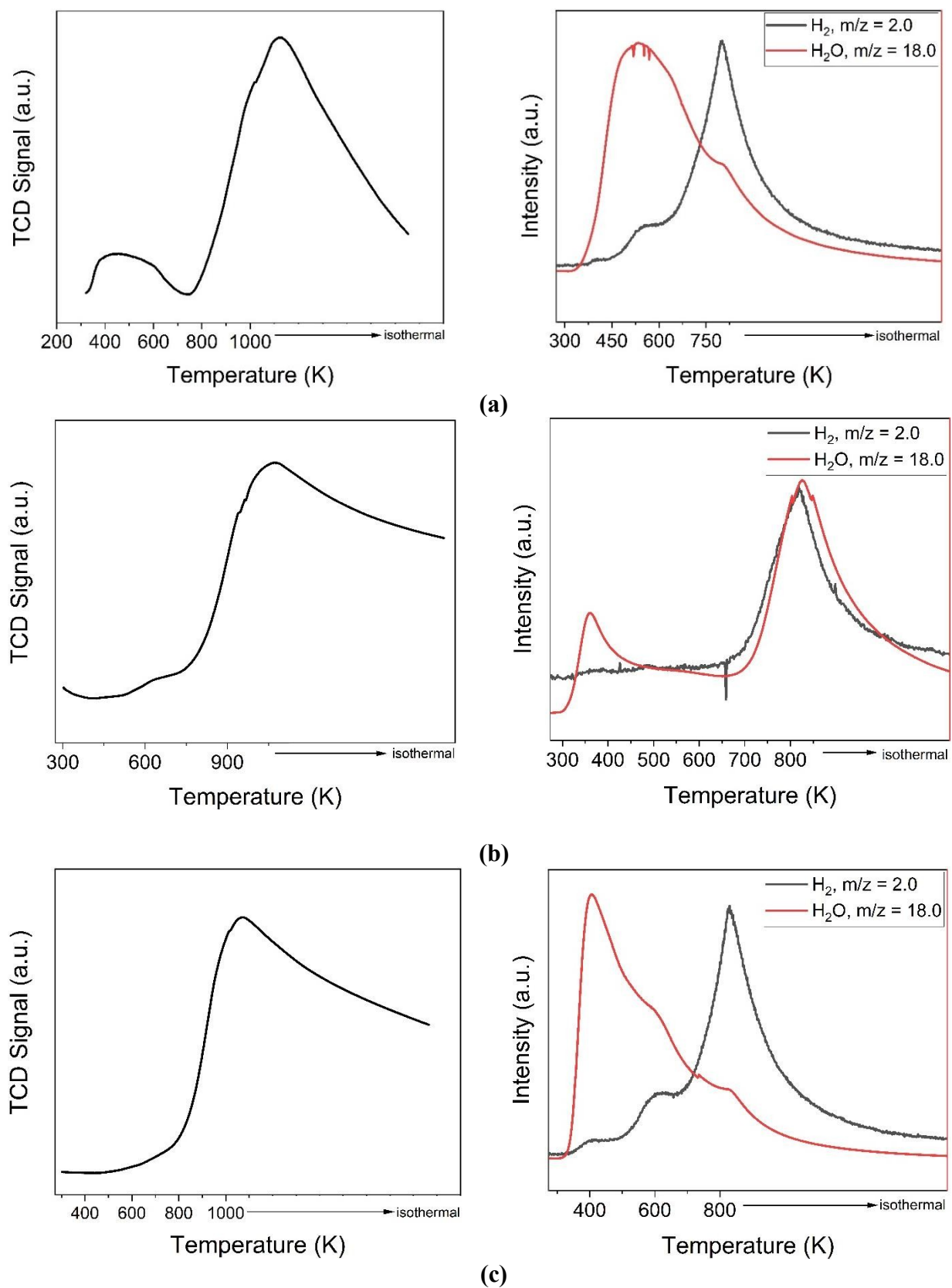
The TPD analysis provides qualitative and quantitative data about the desorption of a probe molecule – in this case, H<sub>2</sub> and CO – adsorbed on active center. Table 16 shows selected key fragment ions that can be determined by Mass Spectrometry.

Table 16 – Key Fragment Ion data for Mass Spectrometry

Mass Number (m/z)	Key Fragments	Probable Parent Molecule(s)	Additional Mass Number (m/z)
2	H <sub>2</sub> <sup>+</sup>	H <sub>2</sub>	1
	He <sup>++</sup>	He	4
12	C <sup>+</sup>	CO	28, 29
	C <sup>+</sup>	CO <sub>2</sub>	28, 29, 44
	C <sup>+</sup>	C <sub>x</sub> H <sub>y</sub>	13, 14, 26, 27 etc
16	O <sup>+</sup>	O <sub>2</sub>	32, 34
	O <sup>+</sup>	H <sub>2</sub> O	17, 18
	CH <sub>4</sub> <sup>+</sup>	CH <sub>4</sub>	12, 13, 14, 15
	NH <sub>2</sub> <sup>+</sup>	NH <sub>3</sub>	14, 15, 17
18	H <sub>2</sub> O <sup>+</sup>	H <sub>2</sub> O	16, 17
28	N <sub>2</sub> <sup>+</sup>	N <sub>2</sub>	7, 14, 29
	C <sub>2</sub> H <sub>4</sub> <sup>+</sup>	C <sub>x</sub> H <sub>y</sub>	12, 13, 14, 24, 26
	CO <sup>+</sup>	CO	6, 12, 29
	CO <sup>+</sup>	CO <sub>2</sub>	6, 12, 29, 44
42	C <sub>3</sub> H <sub>6</sub> <sup>+</sup>	C <sub>x</sub> H <sub>y</sub>	12, 13, 14, 24, 26, 27, 28, 38, 39
44	C <sub>3</sub> H <sub>8</sub> <sup>+</sup>	C <sub>3</sub> H <sub>8</sub>	41, 42, 43
	CO <sub>2</sub> <sup>+</sup>	CO <sub>2</sub>	6, 12, 28, 29
	C <sub>2</sub> H <sub>4</sub> OH <sup>+</sup>	C <sub>2</sub> H <sub>5</sub> OH (alcohol)	31, 43, 45, 46
	N <sub>2</sub> O <sup>+</sup>	N <sub>2</sub> O	14, 16, 28
56	C <sub>4</sub> H <sub>8</sub> <sup>+</sup>	C <sub>x</sub> H <sub>y</sub>	12, 13, 14, 26, 27, 28, 39, 41, 56

Source: Adapted from Hufsky (1986), NIST (2014) and Pfeiffer (2005).

The desorption profiles, intensity versus temperature, for 15%Co/SBA-15, 15%Co/ $\gamma$ -Al<sub>2</sub>O<sub>3</sub> and 10%Co/ $\gamma$ -Al<sub>2</sub>O<sub>3</sub> using TCD, mass spectrometer and hydrogen as probe molecule are displayed in Figure 22. The respective H<sub>2</sub>-TPR performed at adequate reduction temperatures are presented in Figure D.1. Since the 5% Co/ $\gamma$ -Al<sub>2</sub>O<sub>3</sub> catalyst presented a poor H<sub>2</sub>-TPD analysis performance using TCD (data not shown), this catalyst was removed from further analyses and catalytic tests. Mass spectrometer results for different m/z does not present the same scale (plot was performed in different axes).

Figure 22 – Temperature Programmed Desorption ( $H_2$ -TPD) profiles

Note: (TCD signal versus temperature on the left and mass spectrometry intensity on the right) using  $H_2$  as probe molecule for (a) – 15%Co/SBA-15, (b) – 15%Co/ $\gamma$ -Al<sub>2</sub>O<sub>3</sub>; (c) – 10%Co/ $\gamma$ -Al<sub>2</sub>O<sub>3</sub> catalysts. The profiles were obtained after reducing the catalyst, adsorbing the probe molecule and cleaning with Ar.

Figure 22 (A) shows the TPD profile of the 15%Co/SBA-15. TCD analysis exhibited one broad peak from 400 to 600 K and a shoulder and pronounced peak above 900 K, whereas the mass spectrometry (MS) analysis shows a broad peak at  $m/z = 18$  (water) at temperatures  $< 600$  K, which is lower than the temperature used for TPR analysis, and three “stepped” peaks with  $m/z = 2$  ( $H_2$ ) at temperatures  $> 400$  K. The TCD desorption profiles of 15%Co/ $\gamma$ - $Al_2O_3$  and 10%Co/ $\gamma$ - $Al_2O_3$  in Figure 22 (B) and (C) indicate that for 15% Co there are sites in the region of 400 and 600 K, and relatively less metallic sites for 10% Co on alumina. The peak above 800 K was also detected in these catalysts. On the other hand, MS profiles shows a very similar profile between 15% Co/SBA-15 and 10% Co/ $\gamma$ - $Al_2O_3$ , in which water desorbs mostly at lower temperatures and hydrogen desorption clearly seems to be of the same nature. For the 15% Co/ $\gamma$ - $Al_2O_3$ , however, two distinct water peaks are visible, at 350 K and at 873K, whereas the peak at 873 coincides with the individual H peak. Clearly, the desorption of water for all catalysts at temperatures higher than the reduction indicates the evolution of remaining cobalt oxide reduction to metallic cobalt. Concomitantly, the H peaks above 400 K indicates the preferred adsorption on metallic cobalt sites as metallic or as ionic  $Co^{2+}$  sites, as observed in the TPR results. The MS profiles for all catalysts also suggests that water originates from surface hydroxyls (OH) present over the support at lower temperatures and, when visible on TCD analysis, it occurs at a small intensity due to the hydrogen highest conductivity compared to steam, which is closer to the Argon thermal conductivity values. The broad peak above 600 K, similar for all catalysts, could indicate the desorption of  $H_2$  stored in the micropores or in the surface of the support. However, Barbier *et al.* (2001) showed that the intensity of peaks at higher temperatures correlates inversely with the metallic cobalt diameter size, in which the formation of broad peaks at temperatures higher than 900 K occurs for catalysts presenting particle sizes  $< 10$  nm. Lin *et al.* (2019) showed that the 20% Co/ $SiO_2$  formed a unique peak at  $\sim 1000$  K and, by TEM, presented a  $Co^0$  particle size of  $\sim 16$  nm. Catalyst promotion with Mn reduced the  $H_2$ -TPD peak width and intensity from  $\sim 1000$  K to  $\sim 800$  K, indicating that such peak could as well be related with the hydrogen adsorption strength over cobalt sites.

The  $Co^0$  particle size of each catalyst was also obtained from  $H_2$ -TPD analysis (Table 17). The 5% Co/ $\gamma$ - $Al_2O_3$  catalyst was removed from further analysis due to its difficult reduction. Noteworthy is that catalysts reduction using hydrogen was performed at  $\geq 723$  K, which is reported to produce the more thermodynamically stable fcc-Co phase (DE LA PEÑA O'SHEA *et al.*, 2009), so the formation of such crystalline structure to perform calculations was considered. Table 17 shows the particle size, dispersion and metallic superficial area measured

by H<sub>2</sub>-TPD using TCD and MS detectors and calculated following the methodology detailed at APPENDIX D. XRD-estimated particle sizes are also given for Scherrer and Modified Scherrer Equation measurement methods to calculate cobalt oxide crystallite sizes.

Table 17 – Particle size, Dispersion and Metallic Superficial Area measured by H<sub>2</sub>TPD using TCD and MS detectors

Sample	$d_p(\text{Co}^0)_{\text{XRD}}$ (nm) <sup>a</sup>	$d_p(\text{Co}^0)_{\text{XRD-MSE}}$ (nm) <sup>a, b</sup>	$d_p(\text{Co}^0)_{\text{TPD, fcc}}$ (nm) <sup>c</sup>		$D_{\text{cor}}$ (%)		$S_{\text{sp}}$ (m <sup>2</sup> /g <sub>cat</sub> )	
			TCD	MS	TCD	MS	TCD	MS
15% Co/SBA-15	7.84±1.42	9.59	7.56	7.06	13.25	14.18	68.20	72.99
15% Co/ $\gamma$ -Al <sub>2</sub> O <sub>3</sub>	5.87±1.30	7.86	10.17	15.06	9.84	6.65	27.97	18.90
10% Co/ $\gamma$ -Al <sub>2</sub> O <sub>3</sub>	6.98±1.69	9.15	5.28	3.47	18.97	28.85	51.58	78.46

Notes: (a) – Metallic cobalt diameter, calculated by the conversion of Co<sub>3</sub>O<sub>4</sub> to Co relationship corresponding to the relative molar volumes of each component,  $d_p(\text{Co}^0) = 0.75 \cdot d(\text{Co}_3\text{O}_4)$  (LUALDI et al., 2012); (b) – MSE stands for Modified Scherrer Equation; (c) – fcc stands for face-centered cubic lattice cell.

The 15% Co/SBA-15 and 10% Co/ $\gamma$ -Al<sub>2</sub>O<sub>3</sub> catalysts showed a coherent value between XRD and TPD measurements. Noteworthy is that values from the former also are very similar to the support pore size measured by N<sub>2</sub>-isotherm sorption (NLDFT) and TEM, especially for MS analysis. Divergences can be explained by water positive contribution in TCD area and MS analysis limited to a lower temperature negative contribution. XRD and MS values are unlikely due to fitting and premises involved in such methods. Alumina-based catalysts resulted in higher deviation due to some factors: at analysis conditions, part of the hydrogen was clearly consumed for the cobalt oxide reduction; the 15% Co, with higher load, had the lowest dispersion, which might increase the chance of active phase sintering at reduction conditions (JONGSOMJIT; PANPRANOT; GOODWIN, 2001).

The CO-TPD analysis of the 15% Co/SBA-15 catalyst is displayed in Figure 23. Hydrocarbons are displayed in Figure 24. The profiles were obtained after reducing the catalyst, adsorbing the probe molecule and cleaning with Ar. Legend displays the m/z integer values as showed in Table 16.

Figure 23 – Temperature Programmed Desorption (CO-TPD) profile using mass spectrometry as detector for 15%Co/SBA-15

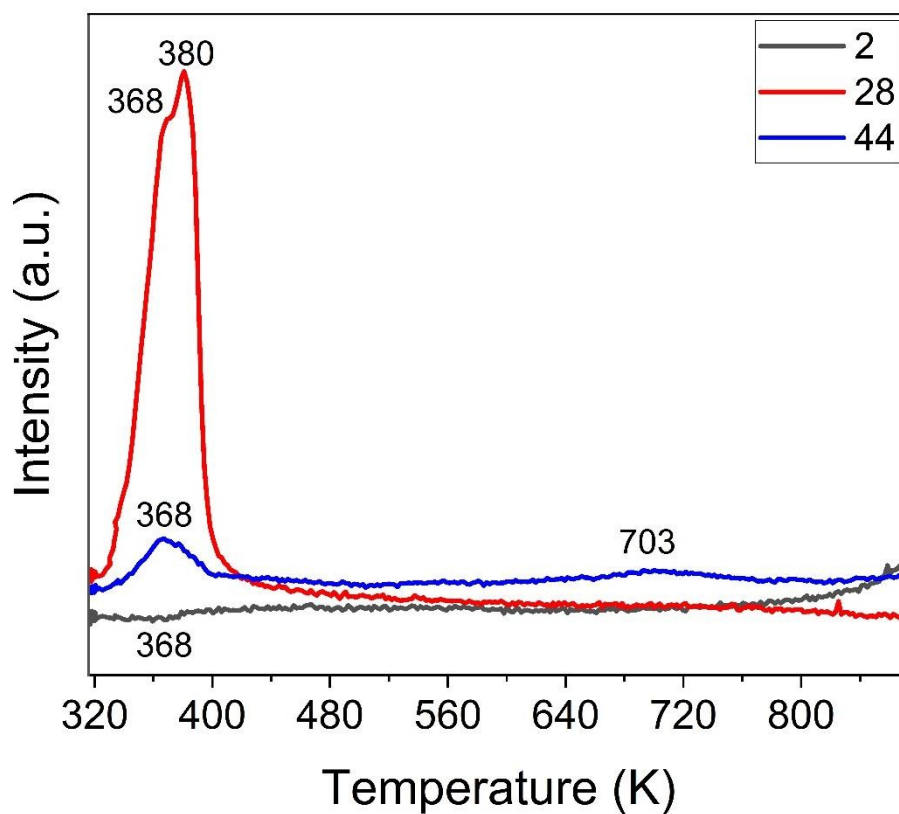
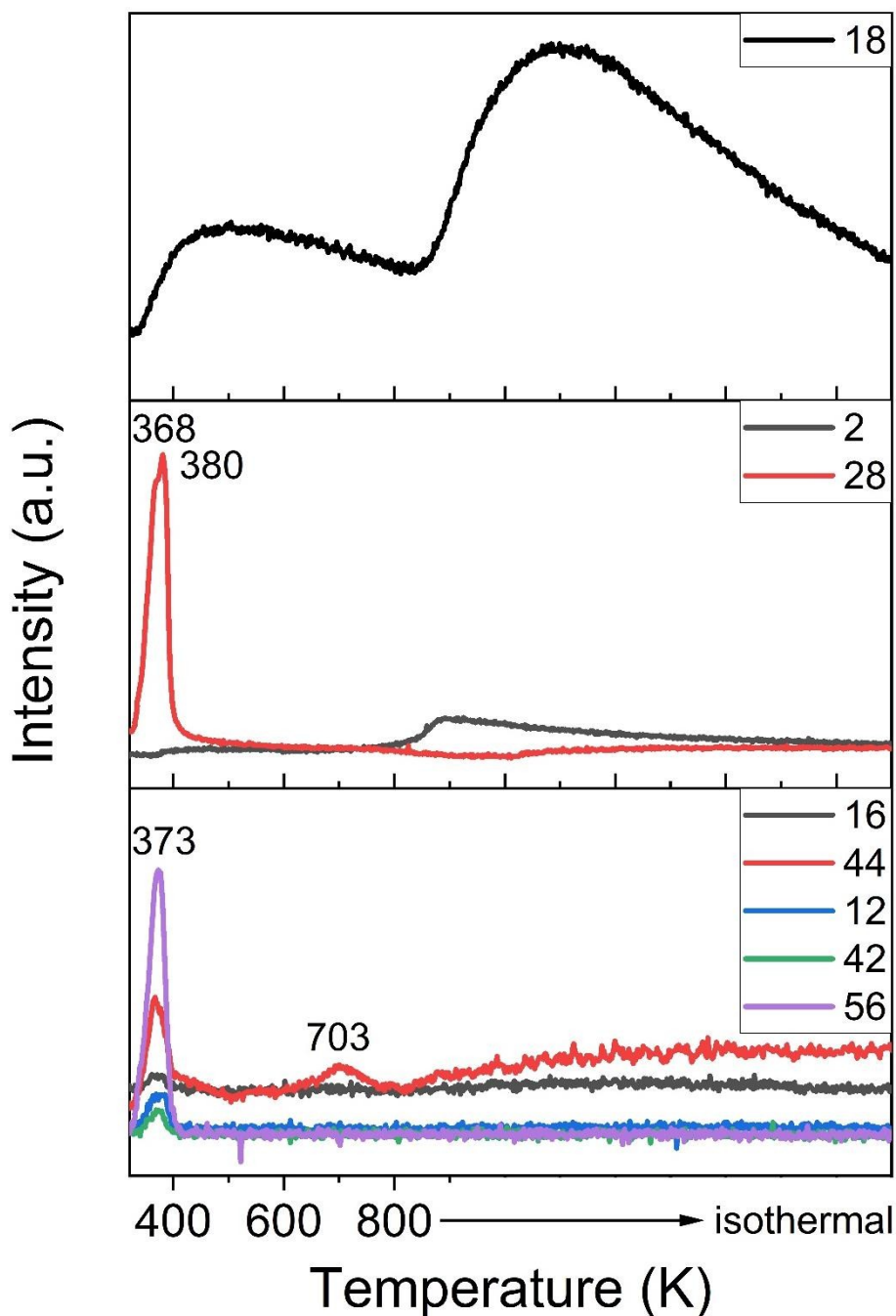


Figure 24 – Temperature Programmed Desorption (CO-TPD) profile using mass spectrometry as detector for 15%Co/SBA-15



First, the catalyst was reduced with  $H_2$ . The  $H_2$ -TPD results showed that  $H_2$  adsorbs onto cobalt's active centers starting at low temperature (400 K). The CO molecules react with the adsorbed  $H_2$  forming hydrocarbons, which are desorbed at higher temperatures. Besides, the mass spectra of  $m/z$  28 and 44 integer values are composed of CO and  $CO_2$ , as shown in Figure 24.

Overall, CO-TPD results suggest two different active sites on the 15% Co/SBA-15 catalyst, promoting the hydrogenation reaction. The CO<sub>2</sub> desorption occurs concomitantly with the desorption of the CO peak. Water, H<sub>2</sub> and C<sub>x</sub>H<sub>y</sub> peaks evolution seem to be more aligned with the peak at 380 K. Water also originates from surface hydroxyls (OH) present on the support. The evolution of H<sub>2</sub>, water and CO<sub>2</sub>, along with decreasing CO, suggest the occurrence of water-gas-shift, Boudouard and methanation reactions simultaneously, according to equations (11) to (13), respectively (FISCHER; VAN STEEN; CLAEYS, 2013):



## 6.2 CO HYDROGENATION TESTS

The catalytic tests were evaluated varying the space velocity and temperature as previously described in section 5.3.11, in Tables 5 and 6, for 15% Co/SBA-15 and 15% Co/ $\gamma$ -Al<sub>2</sub>O<sub>3</sub> catalysts, respectively. As aforementioned, summarized results for both catalysts are shown in APPENDIX E (Table E.1 for the 15% Co/SBA-15 catalyst and Table E.2 for the 15% Co/ $\gamma$ -Al<sub>2</sub>O<sub>3</sub> catalyst). An empty reactor test validation was performed under reaction conditions (see APPENDIX F). The following results were obtained:

- Catalyst activity, expressed as conversion and cobalt-time-yield;
- Selectivity to methane, carbon dioxide, light paraffins and olefins (C<sub>2</sub>-C<sub>4</sub>), gasoline (C<sub>5</sub>-C<sub>10</sub>) and diesel (C<sub>10</sub>-C<sub>20</sub>). Selectivity to C<sub>5+</sub> was obtained as well;
- Catalyst stability to evaluate the yield loss by comparison of CO effective reaction rate at the same conditions on the beginning and at the end of the test run, at a TOS of ~96h.

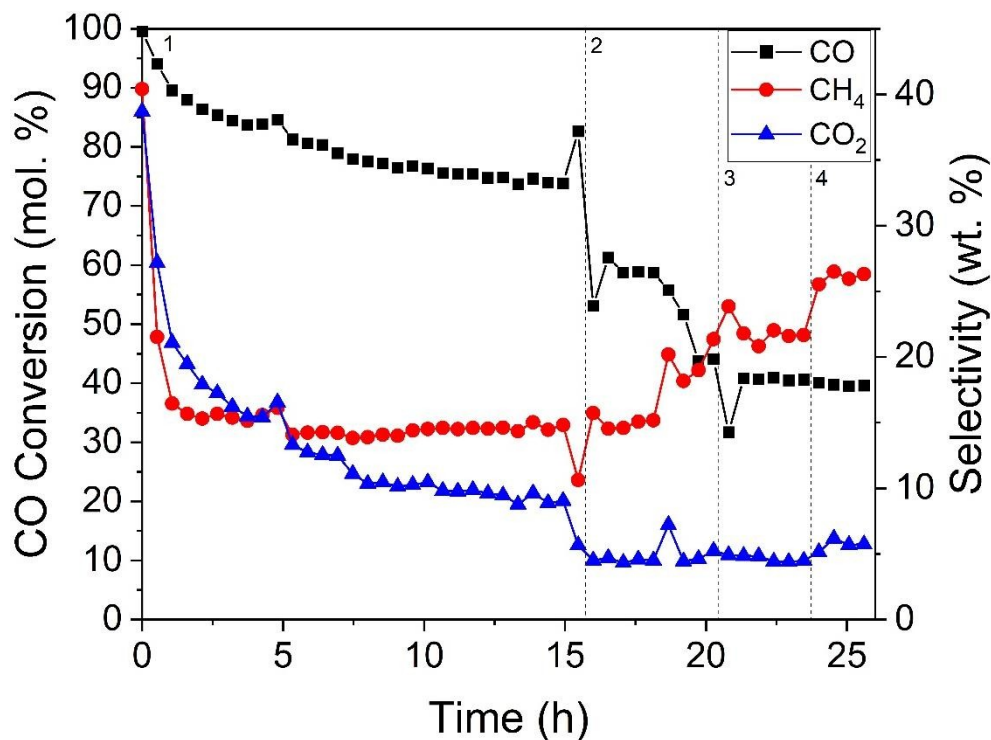
Moreover, the effects of the space velocity and temperature over conversion and hydrocarbons selectivity were evaluated. The reaction rates,  $-r_{\text{CO},eff}$ ,  $r_{\text{CO}_2,eff}$  and  $r_{\text{CH}_4,eff}$  were also determined. The 10% Co/ $\gamma$ -Al<sub>2</sub>O<sub>3</sub> was disregarded from analysis due to limitations with the reaction system.

Noteworthy is that, for all Figures, continuous lines do not represent a model fit. Instead, it was plotted only to facilitate trend visualization.

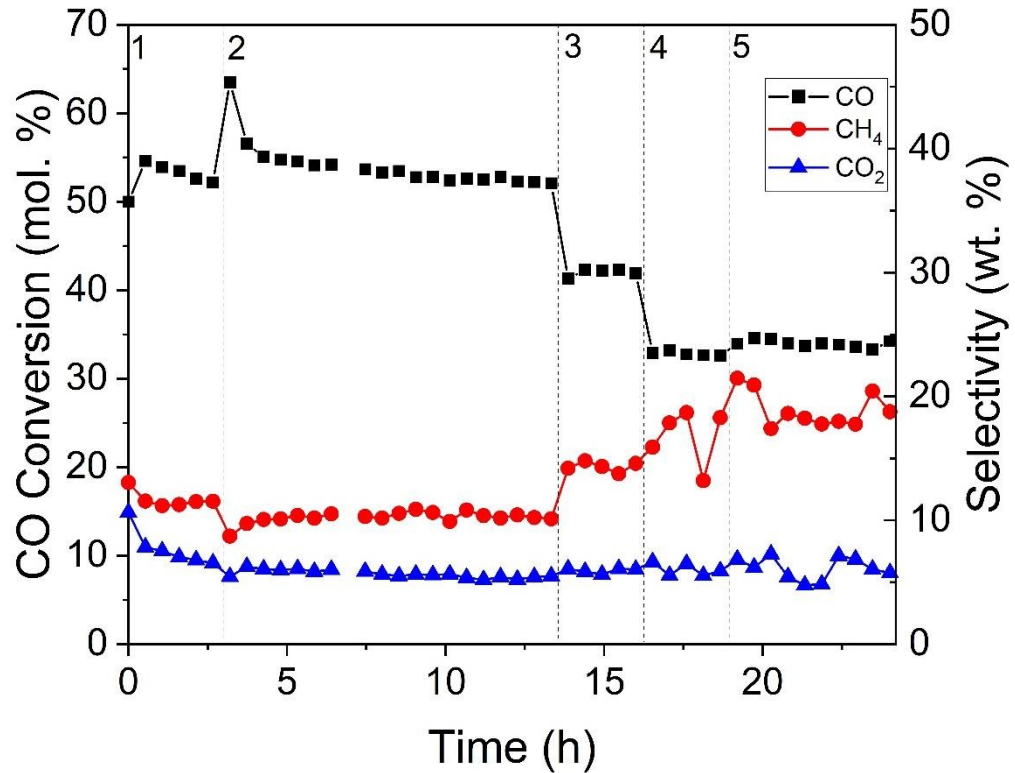
### 6.2.1 CO CONVERSION AND TOS

Figure 25 shows the conversion of CO (molar) and selectivity to CH<sub>4</sub> and CO<sub>2</sub> profiles at 543 K, for H<sub>2</sub>/CO molar ratio of 2:1 and 20 bar, during ~25h TOS, according to Equations (A.8) (A.9), (A.11) and (A.12) in APPENDIX A for both catalyts. The tests were carried out varying the space velocity between 7.67 and 17.11 L<sub>n</sub>.g<sub>cat</sub><sup>-1</sup>.h<sup>-1</sup> (Total WHSV|Syngas WHSV). For 15% Co/SBA-15, conditions were: 1) 7.67|6.90; 2) 10.11|6.90; 3) 17.11|6.90; and 4) 17.11|5.75 L<sub>n</sub>.g<sub>cat</sub><sup>-1</sup>.h<sup>-1</sup>|L<sub>n</sub>.g<sub>cat</sub><sup>-1</sup>.h<sup>-1</sup>, as indicated by regions 1 to 4 in Figure 25 (a). For , conditions were: 1) 8.79|6.90; 2) 7.68|6.90; 3) 10.84|6.90; 4) 17.15|6.90; 5) 17.16|5.75 L<sub>n</sub>.g<sub>cat</sub><sup>-1</sup>.h<sup>-1</sup>|L<sub>n</sub>.g<sub>cat</sub><sup>-1</sup>.h<sup>-1</sup>, as indicated by regions 1 to 5 in Figure 25 (b).

Figure 25 – Catalytic test of (a) 15% Co/SBA-15 at 543 K, H<sub>2</sub>/CO molar ratio of 2:1, 20 bar and (b) 15% Co/ $\gamma$ -Al<sub>2</sub>O<sub>3</sub> at 543 K, H<sub>2</sub>/CO molar ratio of 2:1, 20 bar.



(a)



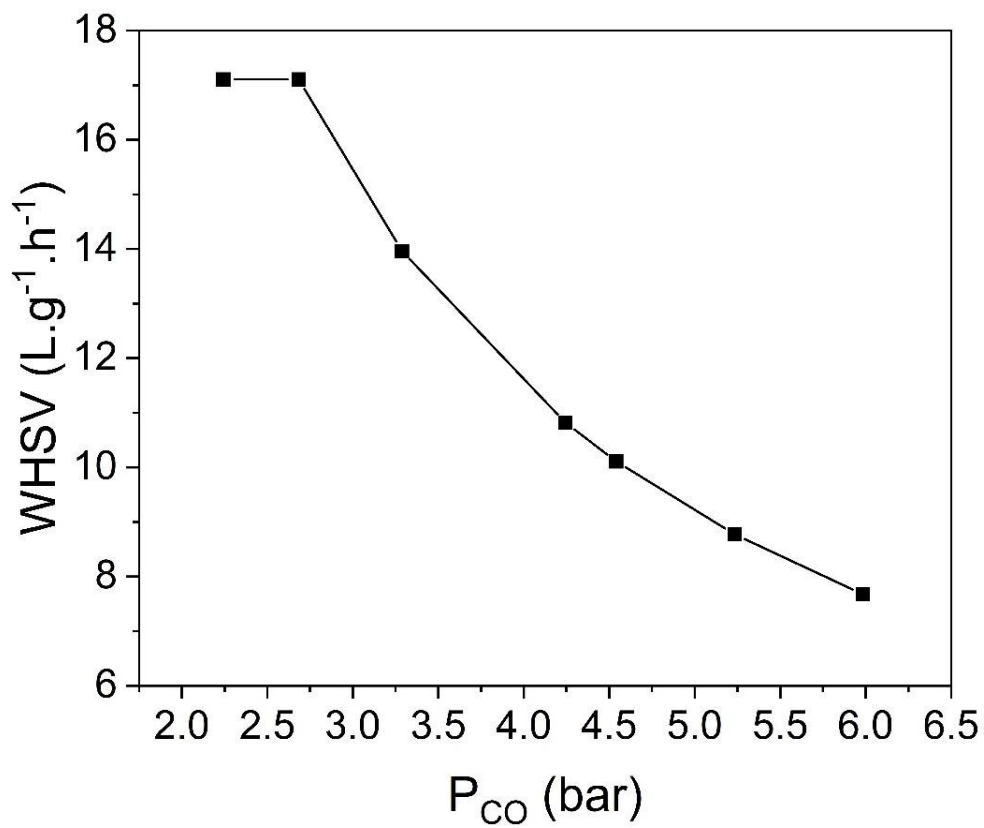
(b)

Figure 25 shows in region 1 the conversion of CO decreasing with TOS, a constant selectivity of methane around 15% and decreasing CO<sub>2</sub> selectivity after 15h. These results indicate that the CO hydrogenation to methane ( $\text{CO} + \text{H}_2 \rightarrow \text{CH}_4 + \text{H}_2\text{O}$ ), besides the CO decomposition reaction ( $2\text{CO} \rightarrow \text{C} + \text{CO}_2$ ) are taking place. In fact, carbon is deposited over the surface cobalt metallic sites. In addition, the CO<sub>2</sub> production is directly related to the WGS reaction ( $\text{H}_2\text{O} + \text{CO} \rightleftharpoons \text{CO}_2 + \text{H}_2$ ).

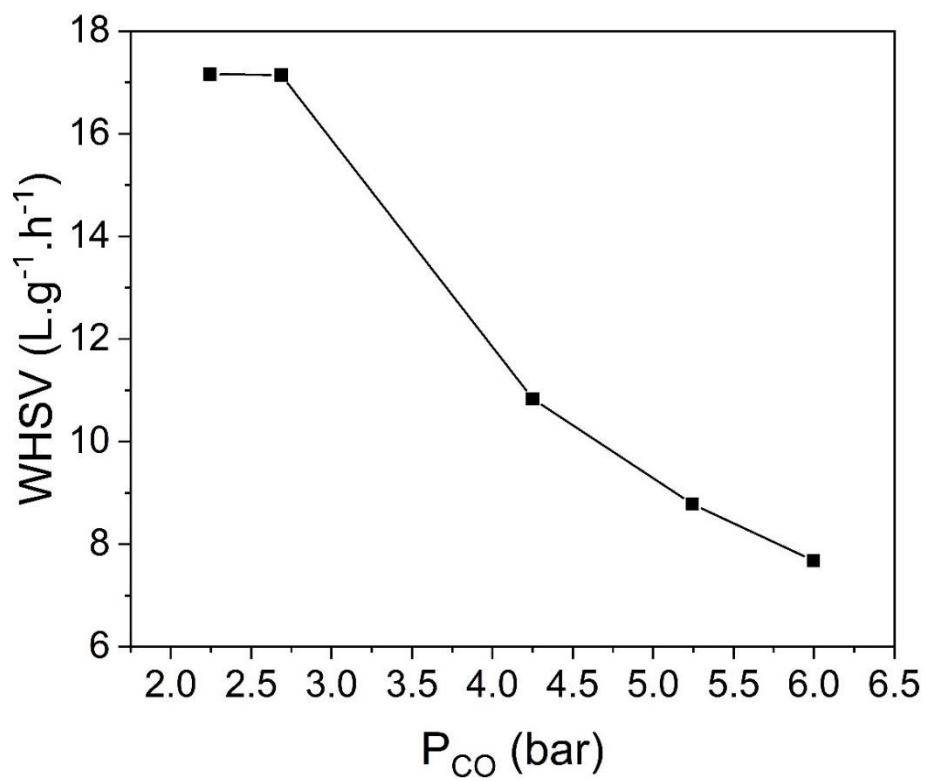
With increasing space velocity from 7.67 to 17.11  $\text{L}_g \cdot \text{g}_{\text{cat}}^{-1} \cdot \text{h}^{-1}$  the CO conversion decreased and then stabilized, increasing methane and decreasing CO<sub>2</sub> selectivities. Therefore, the conversion is inversely proportional to the residence time. In fact, increasing the space velocity about 2 times resulted in the conversion diminished 2 times as well, so the reaction was performed under kinetic regime. The same behavior was found using the 15% Co/ $\gamma$ -Al<sub>2</sub>O<sub>3</sub> catalyst.

As shown at Table 5 and Table 6, there is a relationship between WHSV and the partial pressure of CO,  $P_{\text{CO}}$ . Indeed, the experiments in this work were designed with the variation of the space velocity by changing the gas inlet composition by altering the N<sub>2</sub> flow. Figure 26 shows the relationship between WHSV and  $P_{\text{CO}}$  used in the experiments for both catalysts.

Figure 26 – Relationship between WHSV and  $P_{CO}$  for the (a) 15% Co/SBA-15 and (b) 15% Co/ $\gamma$ -Al<sub>2</sub>O<sub>3</sub> experiments.



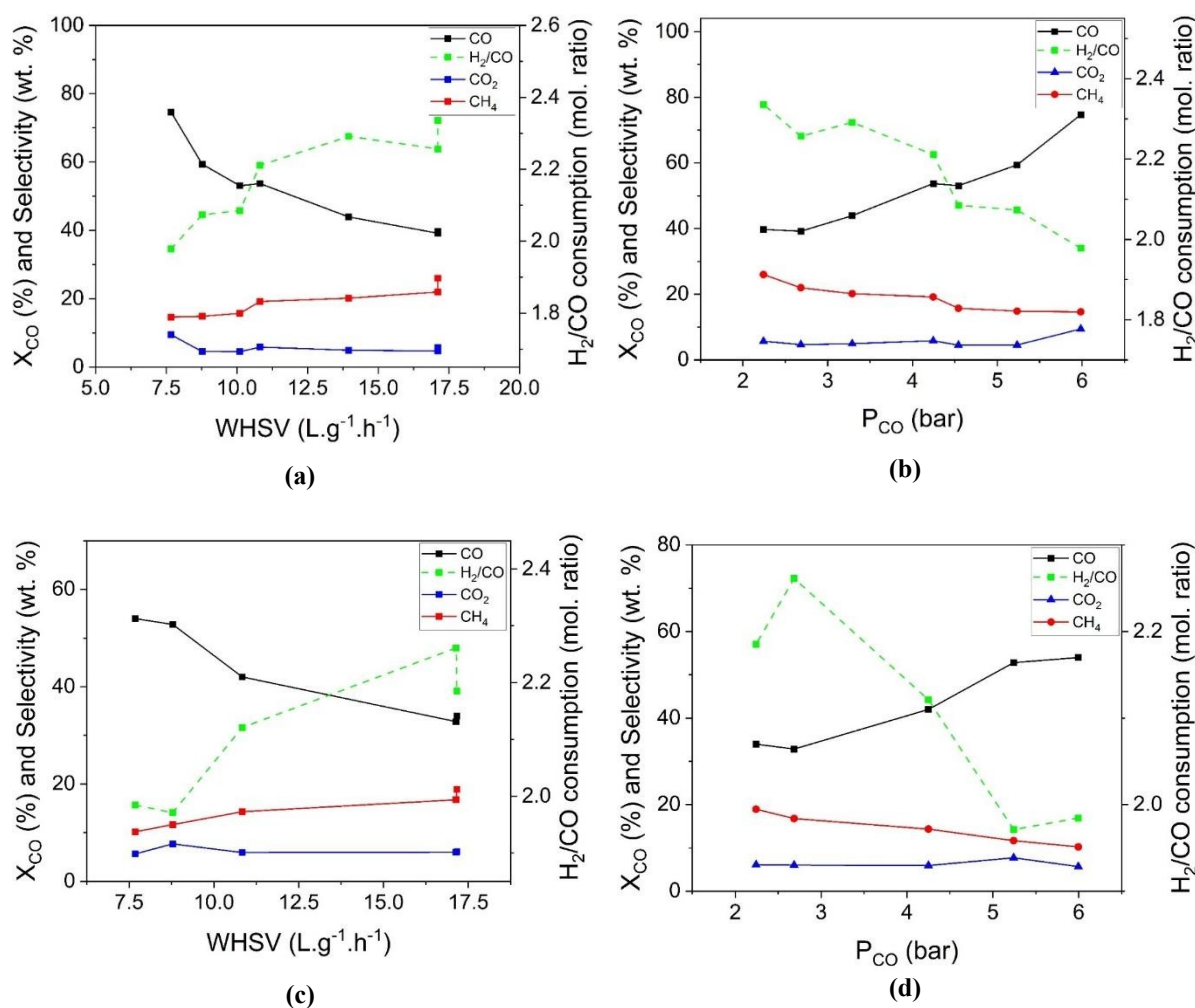
(a)



(b)

For better understanding the relationship of the catalyst performance with the WHSV, the effects of the  $P_{CO}$ , and WHSV on the CO conversion ( $X_{CO}$ ),  $CO_2$  and  $CH_4$  selectivities and the  $H_2/CO$  molar ratio consumption are depicted at Figure 27.

Figure 27 – Effects of (a) WHSV and (b)  $P_{CO}$  over 15% Co/SBA-15 and (c) WHSV and (d)  $P_{CO}$  over 15% Co/ $\gamma$ - $Al_2O_3$  conversion and  $CO_2$  and  $CH_4$  selectivities at 543 K,  $H_2/CO$  molar ratio of 2:1 and 20 bar.



As showed at Figure 27 (a) and (c), increasing space velocity decreases both CO conversion and  $CO_2$  selectivity, whereas methane selectivity and the  $H_2/CO$  molar ratio consumption increases. 15% Co/SBA-15 presented a higher CO conversion and methane selectivity, whereas the  $CO_2$  selectivity was higher for the 15% Co/ $\gamma$ - $Al_2O_3$ . Overall, the FTS and WGS reaction rates are affected negatively with increasing WHSV. According to the literature, increasing space velocity from 2000 to 6000  $NmL.g_{cat}^{-1}.h^{-1}$  favors the production of long chain hydrocarbons and reduces  $CH_4$  selectivity (MOAZAMI et al., 2017).

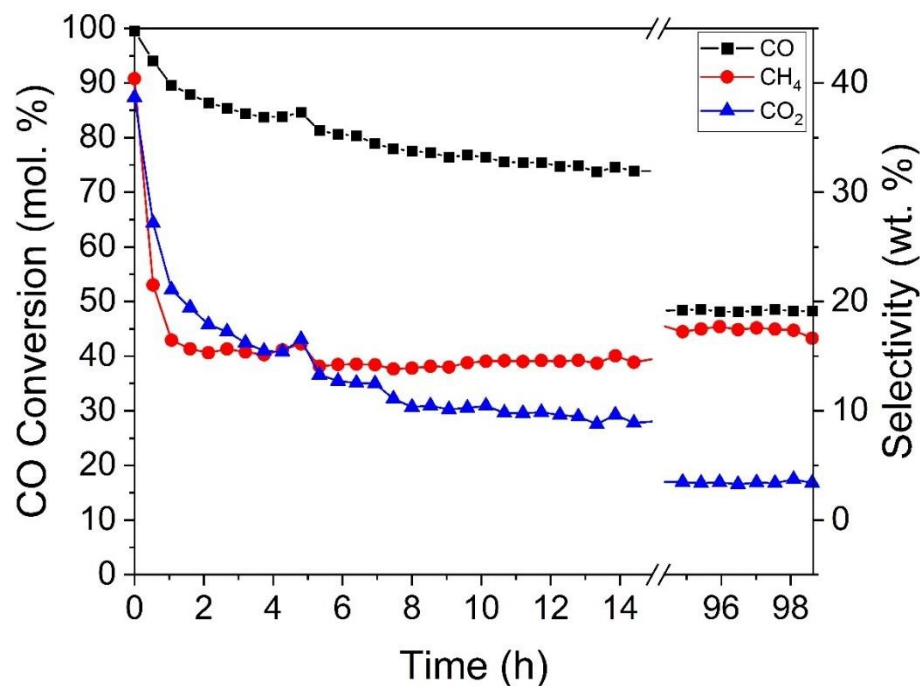
As aforementioned, inert flow change was the selected method to alter the WHSV in this study. It is already known that the FTS reaction kinetics is affected by CO and H<sub>2</sub> partial pressures (ZENARO; TAGLIABUE; BARTHOLOMEW, 2000). Therefore, overall, the results from this study were based on a mixed effect between WHSV, which is expected to increase the conversion when partial pressures of reactants are kept constant, and feed composition, which is expected to decrease conversion at constant WHSV.

Figure 28 shows the catalyst performance as a function of TOS at the same operating conditions ( $P = 20$  bar,  $T = 543.15$  K,  $H_2/CO = 2:1$  and  $WHSV = 7.67$  L.g<sup>-1</sup>.h<sup>-1</sup>), on the beginning and at the end of the run, for both catalysts. For the 15% Co/SBA-15, only the last 4 h of analysis were recorded, totalizing a TOS of  $\approx 98.6$  h, whereas for its counterpart the whole run was recorded, totalizing a TOS of  $\approx 96.3$  h. It is important to notice that region 1 (Figure 28 (b)) was omitted based on the operating conditions for direct comparison.

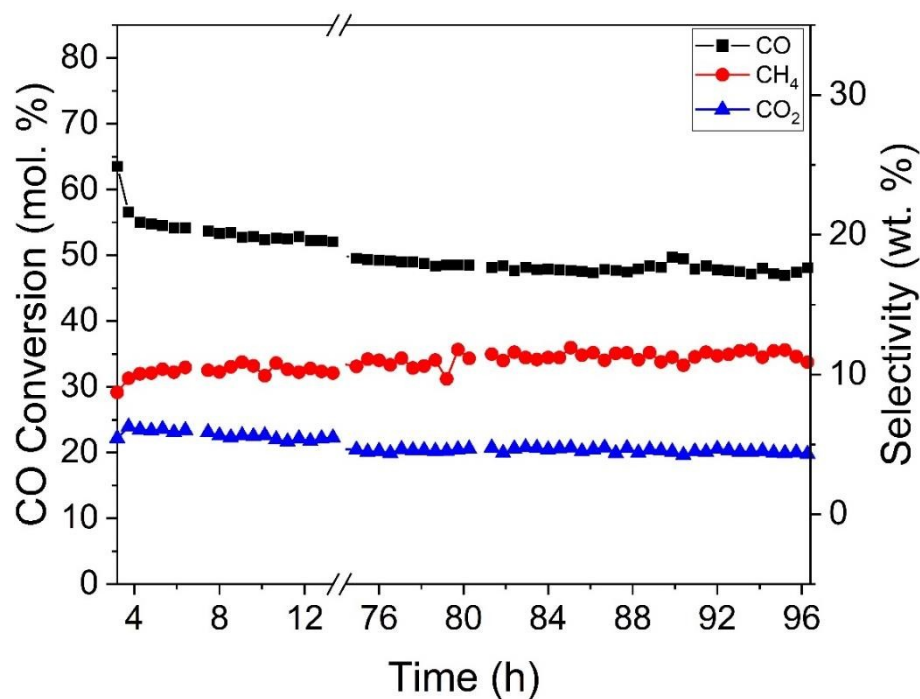
Noteworthy is that returning to the initial space velocity the CO conversion was not recovered, but the CH<sub>4</sub> formation increased from 15% to about 18% and the CO<sub>2</sub> decayed from 10 to 4%. This observation indicates the occurrence of the reverse water gas shift and suggests methane activation due to surface carbon hydrogenation with methane formation.

An overall assessment of the CO conversion with TOS profile suggests the occurrence of two types of deactivation - a rapid, initial deactivation, followed by a slow, long-term deactivation. The literature suggests that at high initial CO conversions, the oxidation of small Co nanoparticles can occur due to hotspots and/or relatively high partial H<sub>2</sub>O pressure ( $p_{H_2O}/p_{H_2}$ ), evidenced by a high WGS reaction rate, resulting in a  $\sim 40\%$  selectivity to CO<sub>2</sub>. In fact, under such conditions, oxidation and formation of irreversible metal-support compounds can occur (WOLF; FISCHER; CLAEYS, 2020; ZHOU et al., 2006). At last, under high temperature, deactivation by carbon formation explains the results obtained at the end of the run. Further assessments of the formed carbon are showed in section 6.3.

Figure 28 – (a) 15% Co/SBA-15 and (b) 15% Co/ $\gamma$ -Al<sub>2</sub>O<sub>3</sub> catalyst performance as function of Time-on-Stream (TOS) at 20 bar, 543.15 K, H<sub>2</sub>/CO = 2:1 and WHSV = 7.7 L<sub>g</sub><sup>-1</sup>.h<sup>-1</sup>.



(a)



(b)

In comparison to the 15% Co/ $\gamma$ -Al<sub>2</sub>O<sub>3</sub> catalyst, the initial deactivation was less pronounced. One explanation can be the reactor startup, since the alumina-based catalyst started at a milder

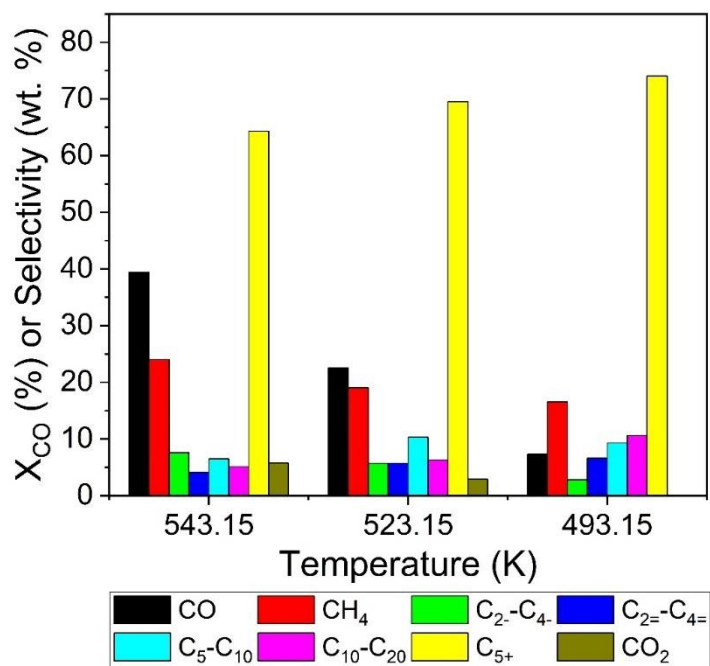
reaction condition based on the feed composition. However, even under such conditions, a high conversion (~55% and up to 65% at WHSV of  $7.68 \text{ L}_{\text{n.g.cat}}^{-1} \cdot \text{h}^{-1}$ ) was achieved, which is the major reason for catalyst deactivation (LANCELOT et al., 2014). On the other hand, although the prepared SBA-15 support was submitted to hydrothermal treatment to prevent support sintering (ZHANG et al., 2005a) and post-calcination characterization did not show significant modifications on the catalyst texture in comparison to the support, this cannot be excluded as a possible explanation of the rapid activity loss at the beginning of the reaction, due to the presence of steam, leading to the formation of silicates and reducing the catalyst surface area (HUBER et al., 2001).

### 6.2.2 PRODUCT SELECTIVITY

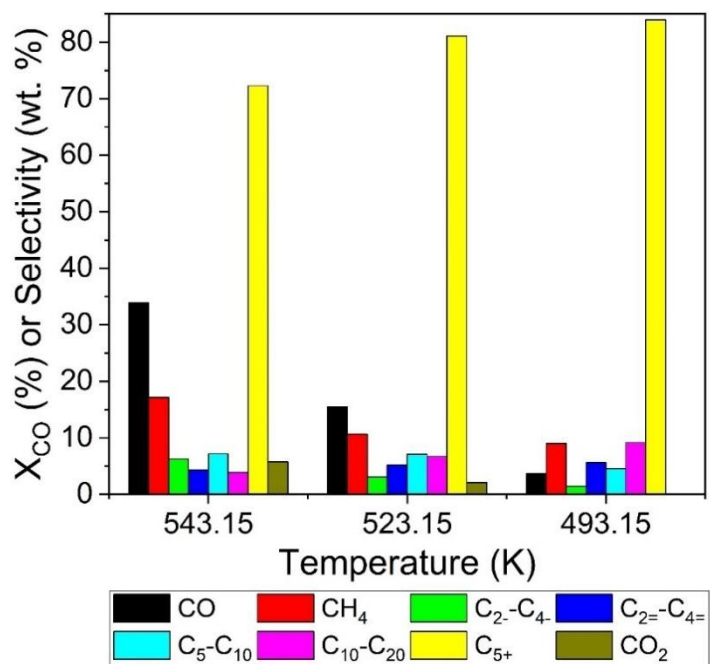
The temperature effect over the catalyst performance at constant operating conditions ( $P = 20$  bar,  $\text{WHSV} = 17.11 \text{ NL}_{\text{g}}^{-1} \cdot \text{h}^{-1}$ ;  $\text{H}_2/\text{CO}$  ratio = 2:1) for both catalysts are shown in Figure 29. The data were retrieved after ~24 h of reaction at each condition.  $\text{C}_{2-}\text{-C}_{4=}$ ,  $\text{C}_{5-}\text{-C}_{10}$  and  $\text{C}_{10-}\text{-C}_{20}$  stands for paraffins and  $\text{C}_{2-}\text{-C}_{4=}$  stands for olefins selectivities, while the  $\text{C}_{5+}$  stands for the selectivity for all hydrocarbons with 5 or more carbons.

Overall, the product distribution tends to the formation of linear hydrocarbons and olefins as seen in Table E.1 and Table E.2. The initial composition is predominantly methane. Reducing the temperature at constant WHSV decreased conversion, but increased the selectivity to higher-chain hydrocarbons, improving the chain growth probability. It is well known that, due to vapor-liquid equilibrium (VLE), the desorption rate of hydrocarbon products decreases at lower temperatures, relatively higher  $\text{C}_{5+}$  hydrocarbons and lower  $\text{CH}_4$  and  $\text{C}_{2-}\text{-C}_4$  paraffins. Noteworthy is that the  $\text{C}_{5-}\text{-C}_{10}$  selectivity reached a maximum value of 10.3% at 523 K. A similar behavior was found for the 15%  $\text{Co}/\gamma\text{-Al}_2\text{O}_3$  catalyst. Quantitatively, however, it seems that the temperature reduction affected more the alumina-based catalyst, in which, e.g. at 493 K, the 15%  $\text{Co}/\text{SBA-15}$  conversion was 2 times the conversion of its counterpart, although a higher selectivity to  $\text{C}_{5+}$  was obtained for this catalyst (74% versus 84%). Therefore, it is quite clear that the temperature affects significantly the catalyst performance.

Figure 29 – Temperature effect over (a) 15% Co/SBA-15 and (b) 15% Co/ $\gamma$ -Al<sub>2</sub>O<sub>3</sub> performance.



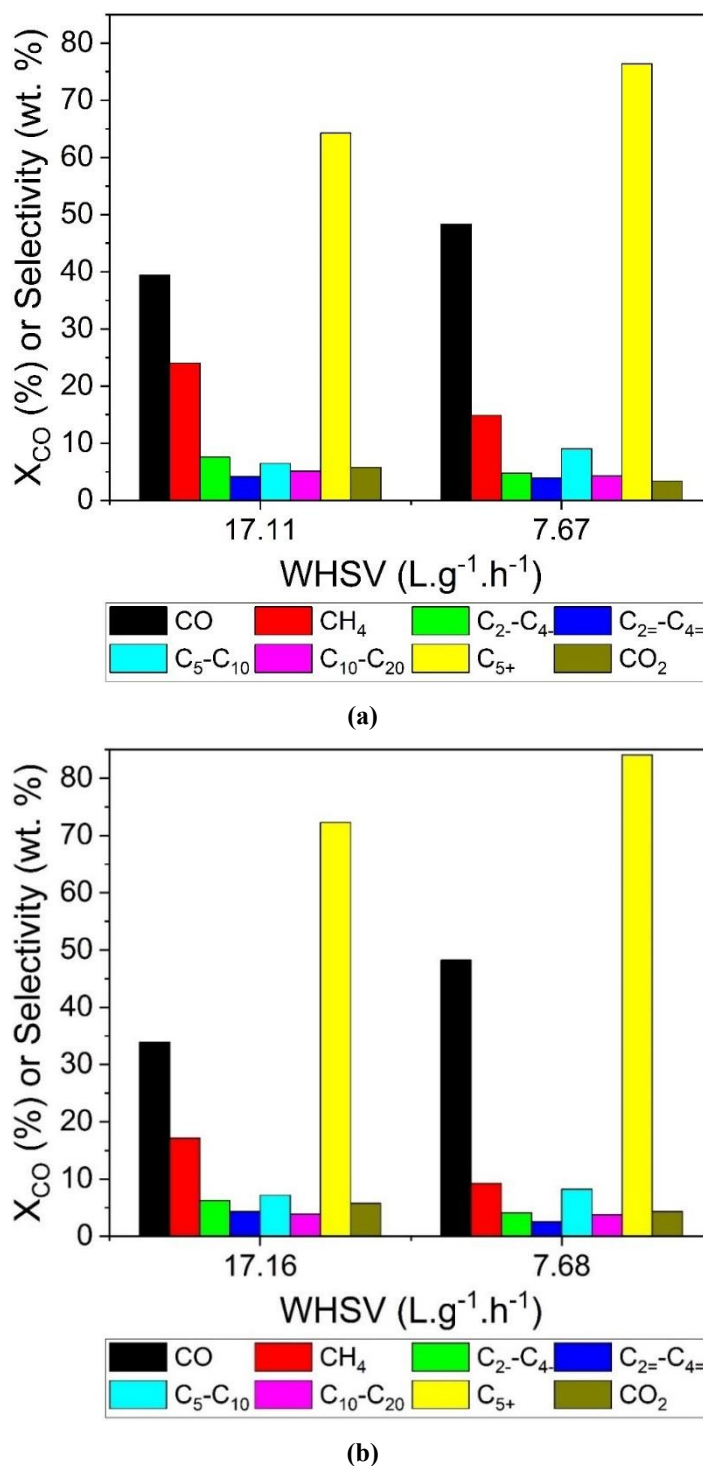
(a)



(b)

Note: Data was retrieved after ~24 h of reaction at each condition. C<sub>2</sub>-C<sub>4</sub> stands for paraffins in the C<sub>2</sub>-C<sub>4</sub> range; C<sub>2</sub>=C<sub>4</sub> stands for olefins in the same range.

Figure 30 shows the effect of WHSV over the catalyst activity and selectivity at 20 bar, 543.15 K and H<sub>2</sub>/CO ratio = 2:1. The data were retrieved after ~24 h of reaction at each condition. Again, C<sub>2</sub>-C<sub>4</sub>, C<sub>5</sub>-C<sub>10</sub> and C<sub>10</sub>-C<sub>20</sub> stands for paraffins and C<sub>2</sub>=C<sub>4</sub> stands for olefins selectivities, while the C<sub>5+</sub> stands for the selectivity for all hydrocarbons with 5 or more carbons.

Figure 30 – WHSV effect over (a) 15% Co/SBA-15 and (b) 15% Co/ $\gamma$ -Al<sub>2</sub>O<sub>3</sub> performances.

Notes: Data was retrieved after ~24 h of reaction at each condition. C<sub>2</sub>-C<sub>4</sub> stands for paraffins in the C<sub>2</sub>-C<sub>4</sub> range; C<sub>2</sub>=-C<sub>4</sub>= stands for olefins in the same range.

Reducing the WHSV to less than half the original value and consequent CO partial pressure increase, according to the WHSV versus P<sub>CO</sub> curve, at constant temperature, shows an increasing overall FTS performance. Interestingly, the selectivity to C<sub>5</sub>-C<sub>10</sub> also reached 9.3%,

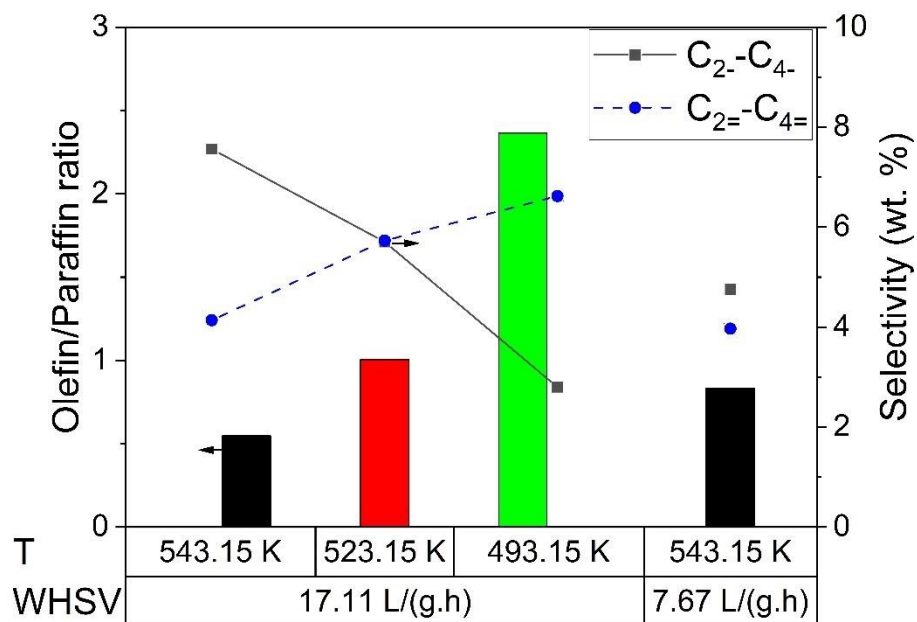
with a concomitant relative reduction in the CH<sub>4</sub> selectivity of almost 34%, whereas the WGS reaction rate decreased, evidenced by the relative CO<sub>2</sub> selectivity reduction of almost 41%. No significant effect over the selectivity to light olefins occurred (relative variation of 4%).

The alumina-based catalyst produced less CH<sub>4</sub> than its counterpart at both conditions and, interestingly, the selectivity to C<sub>5+</sub> was higher and similar at lower WHSV than for the reaction at 493 K for the 15% Co/SBA-15 and 15% Co/ $\gamma$ -Al<sub>2</sub>O<sub>3</sub>, respectively. Here, it is shown that the effect of the WHSV is quite important for the overall performance of the catalysts.

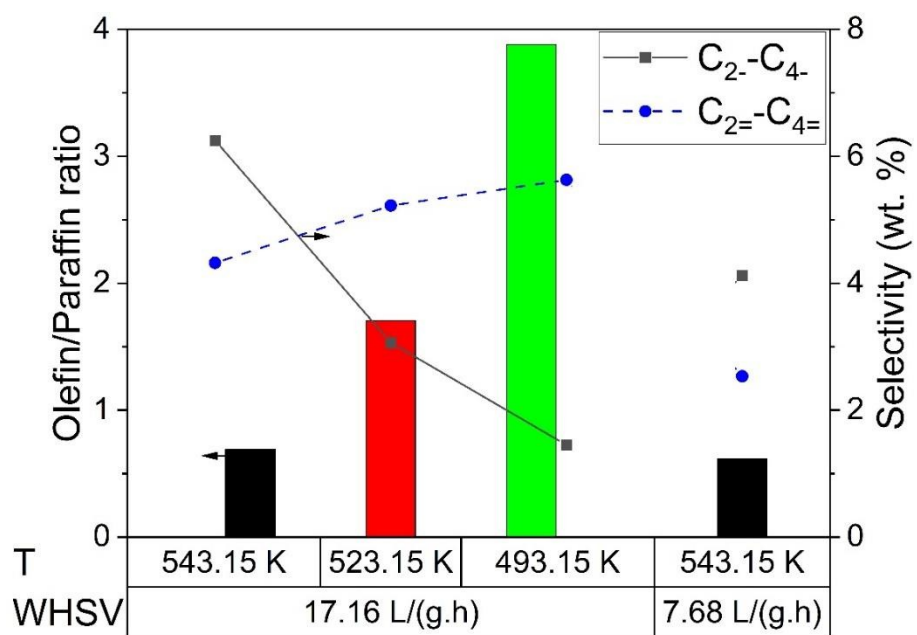
The effect of temperature and WHSV on the olefin-to-paraffin ratio in the C<sub>2</sub>-C<sub>4</sub> range is shown in Figure 31.

Reducing the temperature and, likewise, the WHSV influenced directly and inversely the selectivity to light paraffins and light olefins, respectively. In fact, the literature shows that the selectivity to olefins increases with reaction temperature, at least for promoted catalysts (GARONA et al., 2021; MOAZAMI et al., 2017). Pedersen, Svenum and Blekkan (2018) showed that the unpromoted Co/alumina catalyst produced more light olefins at lower CO conversions and lower temperatures, corroborating these results. The study also showed that the selectivity to olefins is more affected by CO conversion than by the temperature and that Mn-promoted Co/alumina catalysts behaves differently. Figures 29 and Figure 30 show that, for each condition (T and WHSV), the CO conversion varied as such, which was most likely responsible for increasing olefin-to-paraffin ratio, as shown in Figure 31. Qualitative comparison with the 15% Co/ $\gamma$ -Al<sub>2</sub>O<sub>3</sub> shows that the behavior is very similar for both catalysts. The alumina-based catalysts present a higher olefin-to-paraffin ratio performance than its counterpart. Notwithstanding, the selectivity to olefins for both catalysts are quite similar, with the 15% Co/SBA-15 catalyst presenting a slightly higher selectivity to lower olefins. This suggests that the higher olefin-to-paraffin observed for the alumina-based catalyst is merely a reflex of the higher selectivity to higher hydrocarbons at similar C<sub>2</sub>=-C<sub>4</sub>= selectivity levels than the favored olefin production effect due to the nature of the support.

Figure 31 – Olefin-to-Paraffin ratio and selectivity to paraffins and olefins with varying operating conditions (Temperature and WHSV) for (a) 15% Co/SBA-15 and (b) 15% Co/ $\gamma$ -Al<sub>2</sub>O<sub>3</sub>



(a)



(b)

### 6.2.2.1 The Anderson-Schulz-Flory distribution

The Anderson-Schulz-Flory distribution was obtained and is shown in Figure 30. The ASF distribution, as aforementioned, is a polymerization model that describes the ideal production of hydrocarbons. Figure 32 presents the distribution and the olefins ( $\alpha_o$ ), paraffins ( $\alpha_p$ ) and their sum ( $\alpha_{sum}$ ) chain growth probability at each condition.

Since the production of paraffins and olefins are interrelated – paraffins and olefins are not only produced by termination differences, but paraffins might also be produced from olefins re-adsorption, a fast secondary reaction. Modelling based on the carbon number, independent of its origin (namely, sum distribution and  $\alpha_{sum}$ ), was also considered (GU; KHODAKOV; ORDOMSKY, 2018).

Firstly, one can readily notice in Figure 32 (a) and (e) a higher deviation considering paraffins and the sum distribution for higher carbon numbers, which is expected, as stated earlier. However, Figure 32 (d) and (h) shows that, at 543 K and lower WHSV values, a negative distribution was obtained. Interestingly, some studies have described this behavior as derived from a small crystallite size. Yang, Pen and Zhong (1992) adapted the ASF formula to consider the particle size distribution effect, which fitted fairly with experimental data from the literature. However, Davis (2003) discussed that this cutoff effect is given, in fact, by other factors, such as condensation of products in the catalyst and/or reactor or in downstream pipping, and errors associated with the use of multiple product collection traps. In this study, products transportation was carried out by a heated line at constant temperature, at first at the same pressure as the system and, afterwards, at ambient pressure. Albuquerque, Costa and Barbosa (2019) presented the ASF as a straight line from the C<sub>4</sub>-C<sub>12</sub> range correcting the distribution, including the wax fraction. The experiments in this study were performed in series and the wax was continuously collected at the hot trap. Visconti and Mascellaro (2013) presented experimental and theoretical (VLE model) results of fractions collected in a hot trap (25 bar and 383 K) and a cold trap (25 bar and 273 K). The authors obtained the vapor phase leaving from the cold trap, contained C<sub>1</sub>-C<sub>9</sub> hydrocarbons (all methane, ethane and most of the C<sub>3</sub>-C<sub>5</sub> hydrocarbons), and liquid phase composed by water and C<sub>4</sub>-C<sub>18</sub>. The liquid trap containing wax was composed by all produced C<sub>20+</sub> and part of hydrocarbons C<sub>5</sub>-C<sub>20</sub>. Thus, the real  $\alpha$  value was calculated by conservatively selecting the C<sub>4</sub>-C<sub>8</sub> range for all temperatures (for olefins and paraffins), which is an apparent  $\alpha$  value.

Figure 32 – Anderson-Schulz-Flory distribution for (a) to (d) 15% Co/SBA-15 and (e) to (h) 15% Co/ $\gamma$ -Al<sub>2</sub>O<sub>3</sub> at each operational conditions: (a) and (e) 543 K at the beginning of the run (WHSV of 17.11 L<sub>n</sub>.g<sup>-1</sup>.h<sup>-1</sup>); (b) and (f) 523 K; (c) and (g) 493 K; (d) and (h) 543 K at the end of run (WHSV of 7.67 L<sub>n</sub>.g<sup>-1</sup>.h<sup>-1</sup>).

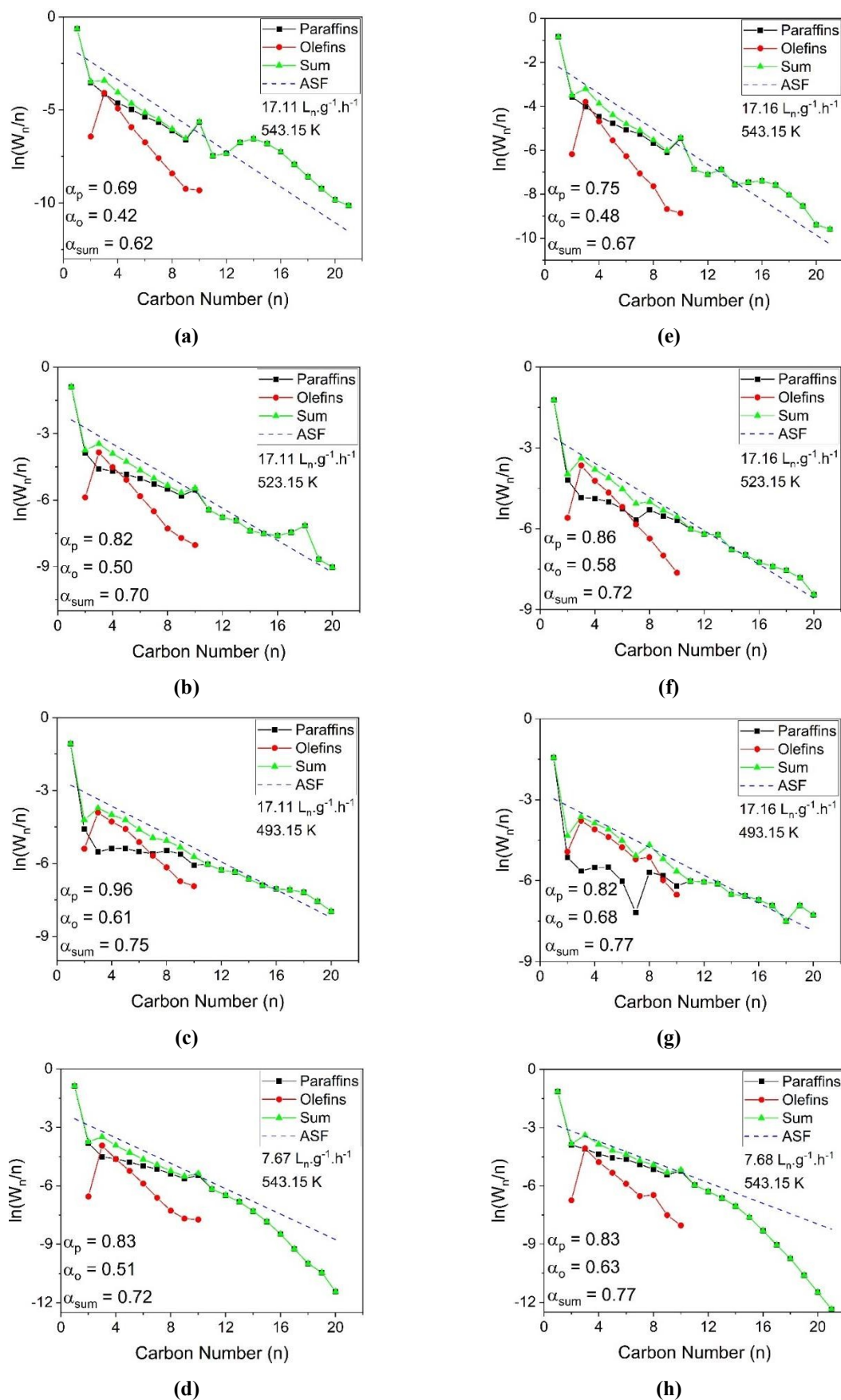


Figure 32 shows that the ASF distribution presents high deviation for C<sub>4</sub> and ethene, as expected. It was possible to notice that the C<sub>3</sub> is the most produced olefin product. In Figure 32 (a), the ASF distribution shows deviation for higher carbon numbers, which characterizes a non-ideal distribution of the ASF equation. The 15% Co/ $\gamma$ -Al<sub>2</sub>O<sub>3</sub> catalyst showed similar profiles as can be seen in Figure 32 (e).

Decreasing the temperature, an increasing value of the chain growth probability for olefins and paraffins, from  $\alpha = 0.69$  to 0.96 was noticed. Table 18 shows the  $\alpha$  values for 15% Co/SBA-15 and for the 15% Co/ $\gamma$ -Al<sub>2</sub>O<sub>3</sub>.

Table 18 – Calculated Chain Growth Probability ( $\alpha$ ) for each reaction conditions.

Catalyst	Conditions		$\alpha_p$	$R_p^2$	$\alpha_o$	$R_o^2$	$\alpha_{sum}$	$R_{sum}^2$
	T (K)	WHSV (L.g <sub>cat</sub> <sup>-1</sup> .h <sup>-1</sup> )						
15% Co/SBA-15	543	17.11	0.69	99.62	0.42	99.85	0.62	99.53
	523	17.11	0.82	99.09	0.50	99.76	0.70	99.90
	493	17.11	0.96	41.41	0.61	99.15	0.75	97.41
	543	7.67	0.83	99.39	0.51	99.90	0.72	99.81
15% Co/ $\gamma$ -Al <sub>2</sub> O <sub>3</sub>	543	17.16	0.75	98.92	0.48	99.62	0.67	99.24
	523	17.16	0.86	60.61	0.58	99.58	0.72	93.03
	493	17.16	0.82	21.01	0.68	91.81	0.77	73.77
	543	7.68	0.83	97.03	0.63	93.35	0.77	99.41

The absolute  $\alpha$  values in Table 18 shows that, overall, the alumina-based catalyst presents a higher chain growth probability than its counterpart, including olefins. Since the WHSV was kept constant, the low CO conversion may have positively affected the production of high-chain hydrocarbons, increasing  $\alpha$ , both for olefins and paraffins, although not in the same magnitude. It is important to acknowledge that for low temperatures, the chain growth probability presents poor fit. This explains the exception for  $\alpha_p$ , in which a deviation that occurs from C<sub>5</sub> to C<sub>7</sub> is evident as seen in Figure 32 (e) to (h). Moreover, the  $\alpha_o$  increased inversely with temperature and for different catalysts. Analyzing Figure 31, although similar amounts of light olefins are produced by both catalysts for each tested operating conditions, the individual composition of the selected range is different.

Prieto *et al.* (2009) used a RuCo/SBA-15 catalyst and evaluated its performance under similar conditions (H<sub>2</sub>/CO = 2, T = 493 K, P = 20 bar and initial syngas WHSV of 6.9 L<sub>n.g<sub>cat</sub></sub><sup>-1</sup>.h<sup>-1</sup>).

Their catalyst presented a selectivity of 13.5%, 14.0% and 72.5% for  $C_2-C_4$  and  $C_{5+}$ , respectively. It is not possible to compare directly the results, but for ~48% conversion at 543 K and WHSV of  $7.67 \text{ L}_{n\cdot\text{g}_{\text{cat}}^{-1}\cdot\text{h}^{-1}}$ , this study provided better results in terms of  $C_{5+}$  selectivity (~76 wt.%, comparable to %C).

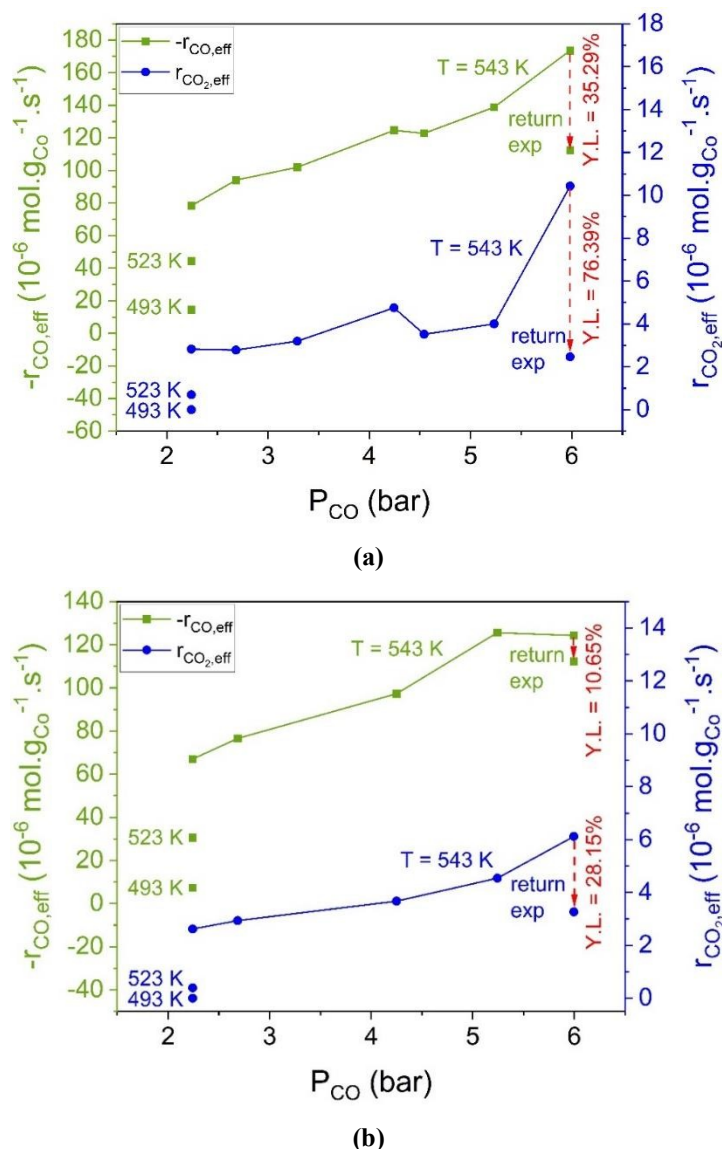
Lu *et al.* (2015) evaluated the cobalt loading and pore size effect of Co/SBA-15 catalysts over its catalytic performance for FTS at 518 K, 20 bar,  $H_2/CO = 2$  and GHSV =  $2000 \text{ h}^{-1}$ . The maximum CO conversion was achieved for Co load equal to 20% and pore size of 7.2 nm, leading to CO conversion of 35.6 %,  $CO_2$ , methane,  $C_2-C_4$  and  $C_{5+}$  selectivities of 1.6 %, 20.3 %, 16.9 % and 62.8 %, respectively, and  $\alpha = 0.83$ .

### 6.2.3 REACTION RATES

The CO and  $CO_2$  reaction rates with the partial pressure of CO, varying temperature and WHSV, were calculated and are shown in Figure 33.

The CO and  $CO_2$  reaction rates increased with temperature increasing. At the end of the run, the temperature was set to the initial conditions. In fact, a high yield loss for  $CO_2$  than for CO was observed, 76.39% and 35.29%, respectively. The test was performed at steady-state at the beginning and end of the run. Thus, the deactivation is intrinsically correlated with the long-term deactivation mechanism, i.e. the formation of carbon. Prieto *et al.* (2009) obtained 42% loss for the RuCo/SBA-15 catalyst. Noteworthy is that the yield loss in the experiments in the present study was attributed solely to the steady-state (long-term deactivation), in which the effect of full yield loss from the beginning of the reaction, i.e. a TOS of 6 h was attributed. When evaluated at the same basis, the SBA-15 based catalyst evaluated in this study suffered a much less pronounced deactivation of 19%, even at a higher temperature. Similar behavior was observed for the alumina-based catalyst, but the reaction rate was lower and more affected by the temperature. The 15% Co/ $\gamma$ - $Al_2O_3$  deactivated less than the SBA-15-based catalyst.

Figure 33 – CO and CO<sub>2</sub> effective reaction rates with P<sub>CO</sub> (bar) for each condition for (a) 15% Co/SBA-15 and (b) 15% Co/ $\gamma$ -Al<sub>2</sub>O<sub>3</sub>



Note: Y.L. stands for Yield Loss, measured as described in APPENDIX A, equation A.31.

In terms of reaction performance, at the end of the run (TOS > 90h), both catalysts presented the same reaction rates,  $112.2 \cdot 10^{-6}$  and  $112.4 \cdot 10^{-6} \text{ mol}_{\text{CO}} \cdot \text{g}_{\text{Co}}^{-1} \cdot \text{s}^{-1}$  for 15% Co/ $\gamma$ -Al<sub>2</sub>O<sub>3</sub> and 15% Co/SBA-15 catalysts, respectively. Given the fact that the SBA-15-based catalysts present higher degree of reduction and higher dispersion when compared to its counterpart and that the same amount of active phase was employed for the reaction for both catalysts, the main differences in activity may not be explained by intrinsic differences between the active phases at each support and the existence of a support-metal interaction, but instead to the amount of active sites available for the reaction (see Table 17). Park *et al.* (2017) prepared a 15% Co/ $\gamma$ -Al<sub>2</sub>O<sub>3</sub> catalyst using a facile method (melt infiltration and thermal treatment). The catalyst was

tested under pressure of 10 and 20 bar, temperature in the range 503 K – 533 K, H<sub>2</sub>/CO molar ratio of 2:1 and GHSV of 6.8 NL.g<sub>cat</sub><sup>-1</sup>.h<sup>-1</sup>. Table 19 summarizes the results. It is possible to notice that the catalyst from the literature presents a higher conversion than the catalysts in this study, regarding similar, but not equal, reaction conditions. However, it seems that the selectivity to higher hydrocarbons from the catalysts from this study was higher, despite the higher temperature of operation. Finally, the converted cobalt-time-yield (CTY) at 523 K obtained by this work catalysts was lower. Since data about feed composition was not provided, comparison based on the partial pressure of reactants cannot be performed.

Table 19 – Comparison between catalyst performance the 15% Co/γ-Al<sub>2</sub>O<sub>3</sub>, 15% Co/SBA-15 and the 15% Co/γ-Al<sub>2</sub>O<sub>3</sub> from Park *et al.* (2017).

Catalyst	CTY (10 <sup>-5</sup> mol <sub>CO</sub> .g <sub>Co</sub> <sup>-1</sup> .s <sup>-1</sup> )	X <sub>CO</sub> (%) <sup>c</sup>	A <sup>c</sup>	Selectivity (wt. %) <sup>f</sup>			
				CH <sub>4</sub>	C <sub>2</sub> -C <sub>4</sub>	C <sub>2</sub> =-C <sub>4</sub> =	C <sub>5</sub> +
15% Co/SBA-15	11.0 <sup>b</sup>	48.3	0.72	14.91	4.19	3.62	77.28
15% Co/γ-Al <sub>2</sub> O <sub>3</sub>	7.3 <sup>b</sup>	48.2	0.77	9.25	4.12	2.53	84.09
15% Co/γ-Al <sub>2</sub> O <sub>3</sub> <sup>a</sup>	15	76	0.79	29.7	10.4	2.3	57.6

Note: (a) - Catalyst prepared by Park *et al.* (2017). (b) - values calculated for comparison at the same WHSV basis and considering the total amount of Co load, by converting directly the calculated CTY at 523K and the respective WHSV to 6.80 L<sub>n</sub>.g<sub>cat</sub><sup>-1</sup>.h<sup>-1</sup>. (c) - values from our study at the end of run (543 K and WHSV of 7.7 L<sub>n</sub>.g<sub>cat</sub><sup>-1</sup>.h<sup>-1</sup>) versus the performance of the catalyst from the literature at T = 533 K and 6.80 L<sub>n</sub>.g<sub>cat</sub><sup>-1</sup>.h<sup>-1</sup>; the presented α values are in fact the α<sub>sum</sub>.

The catalyst referred in the literature presented an CTY of 149.10<sup>-3</sup> mol<sub>CO</sub>.g<sub>Co</sub><sup>-1</sup>.h<sup>-1</sup> at steady-state conditions (TOS > 8h), which is higher than the one obtained for the 15% Co/SBA-15 (49.4.10<sup>-3</sup> mol<sub>CO</sub>.g<sub>Co</sub><sup>-1</sup>.h<sup>-1</sup>) and for the 15% Co/γ-Al<sub>2</sub>O<sub>3</sub> (25.3.10<sup>-3</sup> mol<sub>CO</sub>.g<sub>Co</sub><sup>-1</sup>.h<sup>-1</sup>) in this study. However, the CTY from this study was obtained after 70h of reaction, in which the catalyst already deactivated and was submitted to two different reaction temperatures. Moreover, it must be stated that the presence of Ru as a promoter may hinder re-oxidation of the active phase by decreasing the reduction temperature of the catalyst, therefore reducing yield loss, and increasing the catalyst performance in terms of CO conversion and selectivity for high-chain hydrocarbons, and improving the number of active sites (ZHANG; KANG; WANG, 2010).

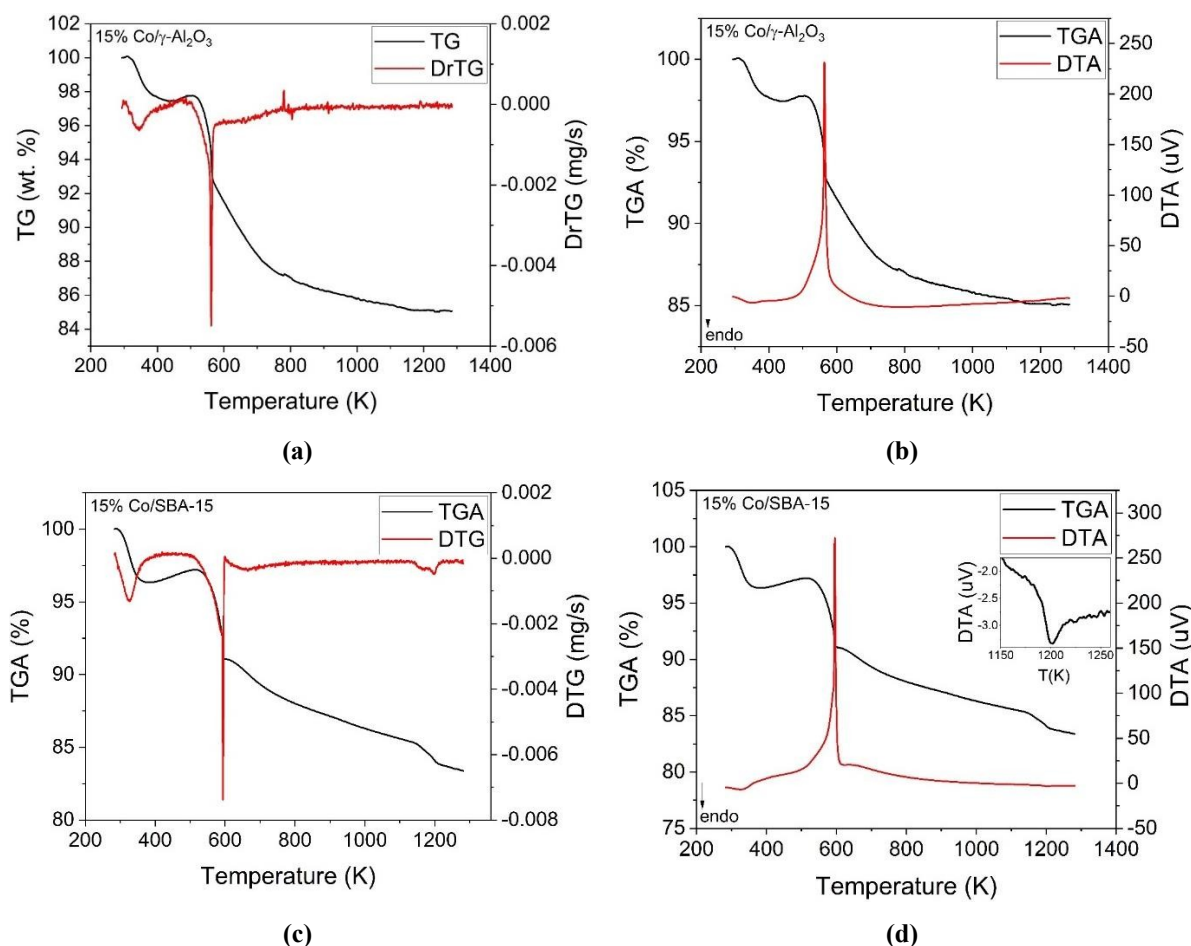
### 6.3 POST-REACTION ANALYSIS

Results showed that the activity of the cobalt-based catalysts deactivated with TOS. The post-reaction analysis was performed focusing on the carbon formation over the catalyst surface.

### 6.3.1 THERMOGRAVIMETRIC ANALYSIS (TGA)

Thermogravimetric analyses, TGA/DTA and TGA/DTG, of the catalysts post-reaction are shown in Figure 34.

Figure 34 – Thermogravimetric analysis, performed in air, organized as TGA/DTG and TGA/DTA (a) and (b) for 15% Co/SBA-15 and as (c) and (d) for 15% Co/ $\gamma$ -Al<sub>2</sub>O<sub>3</sub>, respectively



The profiles for both catalysts showed residues on its surface and are very similar evidencing similar nature of the events. Figure 34 (A) and (C) show the same profiles for temperatures below 700 K, being the second region the most relevant. The 15% Co/SBA-15 catalyst presented a small peak at higher temperatures (1150-1250 K). The TG-DTA profiles show endothermic peaks, while the second is exothermic with a small shoulder. The third region for the SBA-15-based catalyst showed a small endothermic peak. Table 20 presents the temperature of the peaks, and mass loss.

Table 20 – Thermogravimetric Analysis (TGA) for spent cobalt catalysts and mass loss

Sample	Mass Loss (%)	Event	Temperature (K) <sup>a</sup>
15% Co/SBA-15	3.58	Water Loss	326.7
	11.90	Carbon Degradation	595.3
	1.59	Co <sub>3</sub> O <sub>4</sub> Structural Transformation	1201.0
15% Co/ $\gamma$ -Al <sub>2</sub> O <sub>3</sub>	2.64	Water Loss	351.8
	12.69	Carbon Degradation	563.4

Note: (a) – is the temperature in which DTG peak is at its maximum, while the mass loss is obtained at the end of the event.

The first region of both catalysts indicates loss of water. In sequence, there is a small mass increasing with an exothermic shoulder in the DTA profile. This can be attributed to the oxidation or combustion of light hydrocarbon species adsorbed on the surface. In fact, a similar profile was shown by Khan (2018) for a spent Co<sub>2</sub>C/ $\gamma$ -Al<sub>2</sub>O<sub>3</sub>. The gain of mass is less than 3%. The CO and CO<sub>2</sub> formation was attributed to oxidation of carbon deposition at the surface. The mass increase was 0.79 and 0.33% for 15% Co/SBA-15 and 15% Co/ $\gamma$ -Al<sub>2</sub>O<sub>3</sub> catalysts, respectively. Mass gain can be attributed to cobalt oxidation: stoichiometric calculations for the re-oxidation of the reduced fraction of Co-load for each catalyst, from CoO to Co<sub>3</sub>O<sub>4</sub> (CoO + O<sub>2</sub> → Co<sub>3</sub>O<sub>4</sub>), based on ICP and TPR results, estimates a mass gain of 0.82% and 0.46% for 15% Co/SBA-15 and 15% Co/ $\gamma$ -Al<sub>2</sub>O<sub>3</sub> catalysts, respectively.

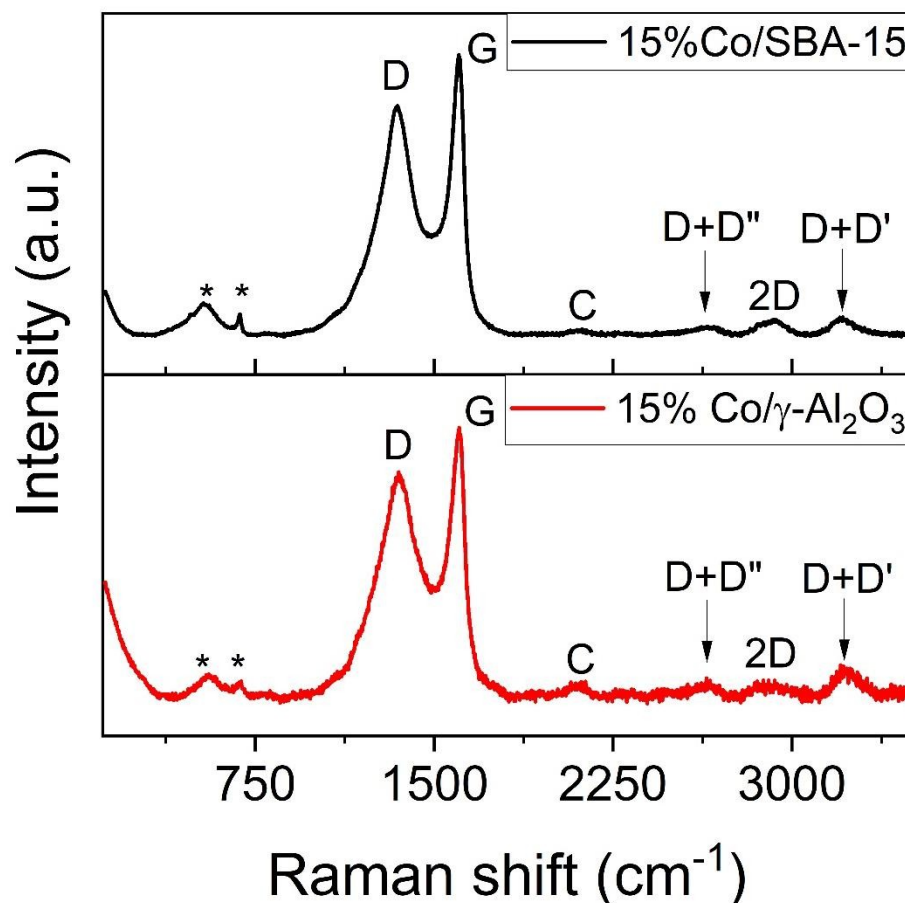
Both catalysts presented a significant mass loss around 600 K in TGA with energy dissipation in DTA profiles, which is consistent with combustion of any surface material, probably due to the higher chain hydrocarbons or polymeric carbons, releasing CO or CO<sub>2</sub>. Interesting is the SBA-based catalyst presented a peak at higher temperature, which suggests simultaneously the oxidation of a higher amounts of wax or higher chain hydrocarbons, compared to the Al<sub>2</sub>O<sub>3</sub>-based catalyst. Hence, it is possible that the nature of carbon material deposited on each catalyst is different. It is also noteworthy that more carbon deposition was observed on the Co/ $\gamma$ -Al<sub>2</sub>O<sub>3</sub>, which did not reflect the yield loss compared to Co/SBA-15 catalyst. Probably there is carbon migration in the support due to the CH<sub>4</sub> dissociation over the Co/Al<sub>2</sub>O<sub>3</sub>, which occurs less on the Co/SiO<sub>2</sub> catalyst. In fact, according to the literature (BOSKOVIC; SMITH, 1997) the Co/SiO<sub>2</sub> catalyst showed high hydrogenation activity and low C<sub>6</sub> formation, with a “C<sub>6</sub>” formation. The Co/SBA-15 catalyst has a different mechanism responsible for the catalyst deactivation.

The last TGA event for the SBA-15-based catalyst is similar for the fresh catalyst, as seen in Figure 6 and Table 7, which shows the phase transition of  $\text{Co}_3\text{O}_4$  for temperatures around 970 to 1200 K, in which a  $\text{Co}^{3+}$  ion spin configuration change occurred and the cubic spinel structure is retained (KALE; PANDIT; JACOB, 1988).

### 6.3.2 RAMAN SPECTROSCOPY

Spent catalysts were analyzed by Raman spectroscopy using 1% laser power with a 532 nm excitation. The Raman spectra for 15% Co/SBA-15 and 15% Co/ $\gamma\text{-Al}_2\text{O}_3$  are shown in Figure 35.

Figure 35 – Raman analysis performed for 15 wt.% Co/SBA-15 and 15 wt.% Co/ $\gamma\text{-Al}_2\text{O}_3$  catalysts after reaction



The Raman spectra at low wavenumbers identified different cobalt bands compared to the fresh catalyst. Figure 35 shows two bands marked with \*, and a small shoulder is also seen on the SBA-15-based spectrum, as presented in Table 21.

Table 21 – Bands identified in Raman spectrum for spent catalyst at lower Raman wavenumber values

Catalyst	Band		
	1	2	3
15% Co/ $\gamma$ -Al <sub>2</sub> O <sub>3</sub>	---	553.0	688.5
15% Co/SBA-15	479.4	530.1	685.3

Comparing the fresh and spent catalysts, it was observed a superficial cobalt transformation after reaction. Indeed, the active phase of cobalt can be easily oxidized to some extent (PATANOUE et al., 2018). Moreover, Ravindra, Behera and Padhan (2014) observed that the laser induced structural transformation of CoO nanoparticles. In this work, it was possible to visualize that the band at 488 nm suggest the oxidation of CoO to Co<sub>3</sub>O<sub>4</sub> spinel phase. Note that the fcc-CoO nanoparticles, observed at 5.0 mW (equivalent to 10.0% laser power of the used equipment) indicate the formation of bands at 489, 540 and 690 cm<sup>-1</sup>, which are assigned as the A<sub>1g</sub>, E<sub>g</sub> and T<sub>2g</sub> vibration modes. Such vibration modes are observed due to the Co<sup>2+</sup> ions octahedrally coordinated to six O<sup>2-</sup> ions. This means that, at least superficially, part of the active phase of the catalysts was oxidized to CoO.

The carbon signal of the spectra shows the D and G bands in the first region between 800-1800 cm<sup>-1</sup> and the 2D, D+D'' and D+D' bands in the second region between 2100-3400 cm<sup>-1</sup>. The first and second order peaks are interrelated, and the 2D band indicates the formation of a graphitic carbon (HODKIEWICZ, 2010). C bands between 1800-2200 cm<sup>-1</sup> were also observed for both catalysts.

The D (disordered) and G (graphite) bands are assigned to the C=C sp<sup>2</sup> stretching vibration of polyaromatic rings and conjugated olefins (DE SMIT et al., 2010). The G band, specifically, is associated with the graphite structure and is sensitive to any aromatic rings or olefinic molecules, while the D band is associated with graphite defects and C-C bonds between aromatic rings with not less than 6 rings. These groups are also responsible for fluorescence (XU et al., 2021). At last, the identified C band is discrete and can be attributed to all linear carbon chains, resulted from sp-hybridized carbon atoms interconnection, such as polyynes or  $\alpha$ -carbynes, alternating triple and single bonds, or polycumulenes or  $\beta$ -carbynes, only double bonds. The former is expected to be semiconducting, while the latter is expected to present a metallic behavior. Such “carbynes” might be crystalline carbons containing heteroatoms (H, N, O, Si, Fe) that can lead to graphite-like carbon by a subsequent crosslinking (KAVAN, 1994). Ravagnan *et al.* (2007) prepared sp-sp<sup>2</sup> carbon films with cumulenes as dominant species. The

authors showed that the C band is composed of a mixture of each carbyne.  $\alpha$ -carbynes (sub-band at  $2100\text{ cm}^{-1}$  Raman shift) remained stable up to 325 K, whereas  $\beta$ -carbynes (sub-band  $1980\text{ cm}^{-1}$  Raman shift) is much more unstable and rearranges to form graphitic structures, such as nano-islands, at ambient temperature. The hypothesis is that the formation of such structure is somewhat related to the mechanism of formation of the lamellar carbon structure reported by Fei Tan *et al.* (2010).

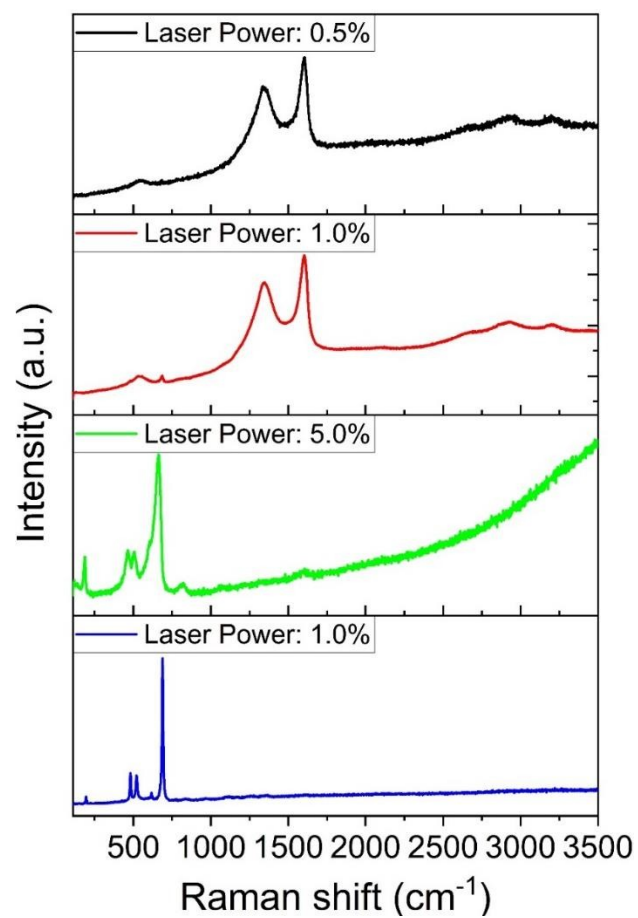
The literature is scarce and do not allow cobalt carbide identification by Raman scattering. However, Zhang *et al.* (2018) identified D and G bands after a few minutes of cobalt carbidization using XPS and Raman in situ and assigned it to the formation of small amount of superficial graphite. The identified carbon peaks may, thus, be solely assigned to the formation of carbon deposits. In this work, D bands at  $1367$  and  $1345\text{ cm}^{-1}$  and G bands at  $1582$  and  $1603\text{ cm}^{-1}$  were determined for the 15% Co/ $\gamma$ -Al<sub>2</sub>O<sub>3</sub> and for the 15% Co/SBA-15. The I<sub>D</sub>/I<sub>G</sub> ratio of 0.82 shows a high degree of defects on the formed carbon. Mignoli (2020) presented the same value for the 15% Co/rGO catalyst post-reaction.

The analysis was performed by increasing the laser power until visualizing the carbon peaks with good resolution, which in turn also permitted to visualize cobalt oxide peaks. It is possible that the identified Co-O bonds has been formed due to laser-induced oxidation. The Raman spectra obtained with lower laser energy (1%) are shown in Figure G.2 in APPENDIX G, evidencing that the main carbon peaks were identified as previously discussed.

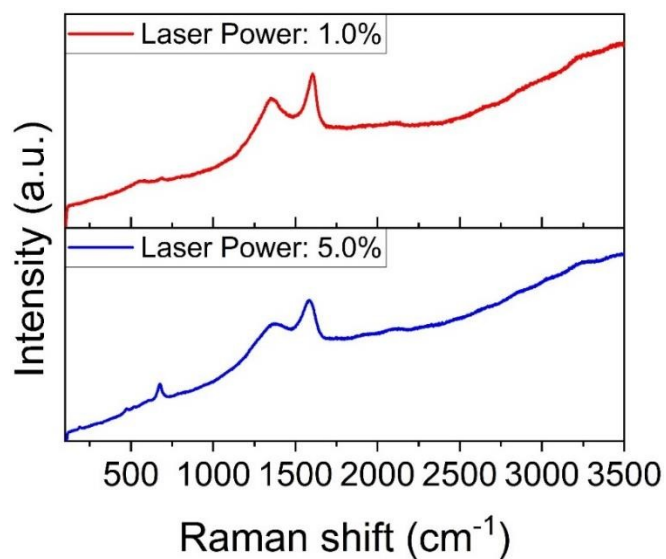
### **6.3.2.1 The effect of Raman Scattering Laser Power**

As previously discussed the laser effects may affect the surface species of the catalyst, so an experiment was performed to identify the effect of laser power over the phase transition and the formation of any superficial metal-support material. Figure 36 shows the effect of the laser power over the catalyst transformation for both catalysts.

Figure 36 – Raman scattering analysis depicting the laser power effect over the post-reaction 15% Co/SBA-15 (a) and 15% Co/ $\gamma$ -Al<sub>2</sub>O<sub>3</sub> (b) catalyst samples



(a)



(b)

The gradual increase of laser power clearly affects the surface of the catalyst. For the 15% Co/SBA-15 catalyst at low laser intensity, it is possible to notice the CoO E<sub>g</sub> vibration mode

along with the D and G carbon peaks. Details are shown in Table 21. Increasing laser power increased the intensity of CoO bands up to a full modification of the spectra. At 5.0%, the formation of broad bands can be assigned to spinel  $\text{Co}_3\text{O}_4$ . The visible bands at 816.4 and 1594.4  $\text{cm}^{-1}$  may be due to the support or to traces of carbon deposit. When reducing the laser power to lower values, it is possible once again to visualize the spinel  $\text{Co}_3\text{O}_4$  profile, which is similar to the fresh catalyst. The resultant spinel  $\text{Co}_3\text{O}_4$  vibration modes occurs at 194.9, 481.3, 520.3, 617.7 and 689.5  $\text{cm}^{-1}$  and no carbon peaks were detected. Zuo *et al.* (1998) showed that there are a direct correlation with Raman shift to higher values and grain size for  $\text{MnO}_4$  powders, which suggests that the 15% Co/SBA-15 catalyst active phase may have sintered. Such phenomenon possibly occurred at the beginning of the reaction, in which a high CO conversion at high temperature (543 K) was achieved, leading to hotspots and increasing particle size. The literature shows that cobalt nanoparticles in the 5-22 nm range can present surface atoms mobility at LTFTS typical conditions (473-513 K) (WOLF *et al.*, 2017). However, sintering due to the laser power effect cannot be discarded.

For the 15% Co/ $\gamma$ - $\text{Al}_2\text{O}_3$  catalyst, a similar profile with its counterpart was obtained at 1.0% laser power. At 5.0% laser power, peaks related to the oxidation of CoO to spinel  $\text{Co}_3\text{O}_4$  peaks are identified along with carbon bands. The resultant spinel  $\text{Co}_3\text{O}_4$  vibration modes occur at 189.0, 472.1, 519.3, 606.7 and 675.5  $\text{cm}^{-1}$ . In the case of the carbon peaks, there was a shift in the profile, in which broader D and G bands are visible. Moreover, it is possible to notice an increase in the G band relative intensity in comparison to the D band, which may indicate a reduction of defects in the carbon structure. By analogy, the results are shifted due to the high laser energy. Perhaps, the laser power increase has led to superficial amorphous carbon oxidation, increasing the relative amount of crystalline carbon. Increasing the laser power to 10.0% resulted in a very high amount of fluorescence at higher Raman shifts in such a way that retrieving a complete spectrum was not possible. Nonetheless, D and G carbon peaks were still visible as seen in Figure G.3 in APPENDIX G. Since superficial cobalt oxidized to its more stable state, it is possible that carbon deposits were not solely deposited over cobalt particles, if any, but also over the alumina support. This result gives a new perspective over the carbon migration phenomenon hypothesis that occurs for alumina-based catalyst.

In summary, analysis of both catalysts showed the formation of superficial carbon of similar quality, as evidenced by the  $I_D/I_G$  ratio. Along with the 2D band on the spectra, results suggest the formation of defective graphitic carbon. The presence of C bands suggests the formation of superficial  $\alpha$ -carbynes, which may be somewhat linked to the formation of lamellar carbon and

graphene nano-islands. Although it was not possible to visualize the formation of any metal-support material for the alumina-based catalyst, it was possible to identify that the formed carbon is strongly linked to the surface of the catalyst, suggesting the occurrence of carbon migration to the support over the alumina-based catalyst. It was not possible to detect the cobalt carbidization by the applied methods of investigation. Finally, active phase sintering for the 15% Co/SBA-15 catalyst under initial conditions of reaction is suggested, although the effect of the laser power cannot be discarded.

## 7 CONCLUSIONS AND SUGGESTIONS

In this section, conclusions from this work and suggestions for further studies are presented.

### 7.1 CONCLUSIONS

This work proposed the preparation, characterization and a comprehensive evaluation of catalysts for the CO hydrogenation reaction, followed by the investigation of the catalyst deactivation.

The catalysts preparation was successfully performed, as evidenced by a small metal load error < 5.00%, adequate particle size range to hinder the diffusional limitations under reaction, high superficial area and mesoporous morphology, which resulted in well-dispersed cobalt nanoparticles on the catalyst's surface.

The CO-TPD analysis for the 15% Co/SBA-15 catalyst suggest two different sites at lower temperatures, evidenced by the evolution of CO<sub>2</sub>, followed by hydrocarbons formed due to residual H<sub>2</sub> used in the pre-treatment, adsorbed on the active sites.

The catalytic tests showed the co-occurrence of WGS and FTS reactions. By increasing the space velocity, by increasing the inert (N<sub>2</sub>) flow, results in lower CO conversion and higher CO<sub>2</sub> selectivity, along with lower chain growth probability and decreased selectivity to lower olefins. Decreasing the temperature, however, reduced the CO conversion and CO<sub>2</sub> selectivity, but increased  $\alpha$  and selectivity to lower olefins. The alumina-based catalyst presented the highest olefin-to-paraffin ratio, although the selectivity to olefins were similar to the SBA-15 based catalyst. To produce more desirable products, it is important to operate under lower temperatures and WHSVs, in which an optimum  $\alpha$  value for the desired hydrocarbon range, such as gasoline-diesel, can be achieved.

The 15% Co/SBA-15 catalyst presented the most significant deactivation, most likely due to Co sintering and due to the carbon migration phenomenon over the alumina-based catalyst. Both catalysts are promising for the CO hydrogenation reaction, with the 15% Co/SBA-15 catalyst presenting the best results among them for the production of fuels of lower carbon chains and lower olefins due to its highest activity and selectivity in the gasoline range (C<sub>5</sub>-C<sub>10</sub> paraffins) and slightly higher selectivity to C<sub>2</sub>=-C<sub>4</sub>= than its counterpart, while the 15% Co/ $\gamma$ -

Al<sub>2</sub>O<sub>3</sub> presented a greater selectivity to higher chain HC and higher olefin-to-paraffin ratio based on its high C<sub>5+</sub> selectivity.

## 7.2 SUGGESTIONS FOR FURTHER STUDIES

Overall, further studies that can be more directly assessed using the same catalysts and system should aim at performing an even broader analysis of operational conditions, such as employing different working pressure and gas inlet composition by varying the H<sub>2</sub>/CO ratio. Moreover, the assessment of a tail gas recovery by employing a simulated recycle may be valuable in an industrial process and perhaps can be achieved by evaluating the effect of small quantities of HC at the inlet, such as methane, ethane or/and water over product distribution, catalyst performance and deactivation over TOS.

More complex studies should aim at improving catalyst and reactor performance. At first, one can focus on improving the mass transferring on a mesoscale (such as employing an alumina-based catalysts with more similar features as its counterpart, such as an ordered mesopore diameter with similar length). With similar features, reactant consumption hindrances and product distribution are even more directly comparable and can bring light on the effect of the support over the catalyst performance.

At last, research should also be focused more on a desirable range of specific product (such as light olefins or C<sub>5+</sub>), in which operational conditions and catalyst design can be more refined, with the employment of specific promoters to improve the performance by reducing hindrances. In this case it is also suggested improving the reactor performance by employing a secondary support (catalytic monoliths) and/or other structured reactors.

## REFERENCES<sup>1</sup>

- ABELLÓ, S.; MONTANÉ, D. Exploring iron-based multifunctional catalysts for fischer-tropsch synthesis: A review. **ChemSusChem**, v. 4, n. 11, p. 1538–1556, 2011.
- AGRAFIOTIS, C.; TSETSEKOU, A. The effect of powder characteristics on washcoat quality. Part I: Alumina washcoats. **Journal of the European Ceramic Society**, v. 20, p. 815–824, 2000.
- AHN, C. IL; PARK, Y. M.; CHO, J. M.; LEE, D. H.; CHUNG, C. H.; CHO, B. G.; BAE, J. W. Fischer-Tropsch Synthesis on Ordered Mesoporous Cobalt-Based Catalysts with Compact Multichannel Fixed-Bed Reactor Application: A Review. **Catalysis Surveys from Asia**, v. 20, n. 4, p. 210–230, 2016.
- AIL, S. S.; DASAPPA, S. Biomass to liquid transportation fuel via Fischer Tropsch synthesis - Technology review and current scenario. **Renewable and Sustainable Energy Reviews**, v. 58, p. 267–286, 2016.
- ALBUQUERQUE, J. S.; COSTA, F. O.; BARBOSA, B. V. S. Fischer–Tropsch Synthesis: Analysis of Products by Anderson–Schulz–Flory Distribution Using Promoted Cobalt Catalyst. **Catalysis Letters**, v. 149, n. 3, p. 831–839, 2019.
- ALMEIDA, L. C.; ECHAVE, F. J.; SANZ, O.; CENTENO, M. A.; ARZAMENDI, G.; GANDÍA, L. M.; SOUSA-AGUIAR, E. F.; ODRIOZOLA, J. A.; MONTES, M. Fischer-Tropsch synthesis in microchannels. **Chemical Engineering Journal**, v. 167, n. 2–3, p. 536–544, 2011.
- AURELIUS, M. **Marcus Aurelius: Meditations, Books 1-6**. Oxford University Press, 2013.
- AZIMOV, F.; MARKOVA, I.; STEFANOVA, V.; SHARIPOV, K. SYNTHESIS AND CHARACTERIZATION OF SBA-15 AND Ti-SBA-15 NANOPOROUS MATERIALS FOR DME CATALYSTS. **Sharipov Journal of the University of Chemical Technology and Metallurgy**, v. 47, n. 3, p. 333–340, 2012.
- BARBIER, A.; TUEL, A.; MARTIN, G. A.; ARCON, I.; ARCON, I.; KODRE, A.; KODRE, A. Characterization and catalytic behavior of CO/SiO<sub>2</sub> catalysts: Influence of dispersion in the

---

<sup>1</sup> De acordo com a Associação Brasileira de Normas Técnicas (ABNT NBR 6023:2018).

Fischer-Tropsch reaction. **Journal of Catalysis**, v. 200, n. 1, p. 106–116, 2001.

BARRETT, E. P.; JOYNER, L. G.; HALEND, P. P. The Determination of Pore Volume and Area Distributions in Porous Substances. I. Computations from Nitrogen Isotherms. **Journal of the American Chemical Society**, v. 73, n. 1, p. 373–380, jan. 1951.

BARTHOLOMEW, C. H. History of cobalt catalysts design for FTS. **AIChE National Spring Meeting**, p. 83b, 2003.

BEZEMER, G. L.; BITTER, J. H.; KUIPERS, H. P. C. E.; OOSTERBEEK, H.; HOLEWIJN, J. E.; XU, X.; KAPTEIJN, F.; VAN DIJLEN, A. J.; DE JONG, K. P. Cobalt particle size effects in the Fischer-Tropsch reaction studied with carbon nanofiber supported catalysts. **Journal of the American Chemical Society**, v. 128, n. 12, p. 3956–3964, 2006.

BORG, Ø.; RØNNING, M.; STORSTER, S.; VAN BEEK, W.; HOLMEN, A. Identification of cobalt species during temperature programmed reduction of Fischer-Tropsch catalysts. **Studies in Surface Science and Catalysis**, v. 163, p. 255–272, 2007.

BOSKOVIC, G.; SMITH, K. J. Methane homologation and reactivity of carbon species on supported Co catalysts. **Catalysis Today**, v. 37, n. 1, p. 25–32, 1997.

BOTES, F. G.; VAN DYK, B.; MCGREGOR, C. The Development of a Macro Kinetic Model for a Commercial Co/Pt/Al<sub>2</sub>O<sub>3</sub> Fischer-Tropsch Catalyst. **Industrial and Engineering Chemistry Research**, v. 48, n. 23, p. 10439–10447, 2009.

BRACKMANN, R.; PEREZ, C. A.; SCHMAL, M. LaCoO<sub>3</sub> perovskite on ceramic monoliths - Pre and post reaction analyzes of the partial oxidation of methane. **International Journal of Hydrogen Energy**, v. 39, n. 26, p. 13991–14007, 2014.

BRONKHORST. **General instructions digital Mass Flow / Pressure instruments laboratory style / IN-FLOWInstruction manual**, 2011. Disponível em: <<http://www.bronkhorst.fr/>>

BULAVCHENKO, O. A.; CHEREPANOVA, S. V.; MALAKHOV, V. V.; DOVLITOVA, L. S.; ISHCHEKOV, A. V.; TSYBULYA, S. V. In situ XRD study of nanocrystalline cobalt oxide reduction. **Kinetics and Catalysis**, v. 50, n. 2, p. 192–198, 2009.

CHEN, J.; WU, X.; SELLONI, A. Electronic structure and bonding properties of cobalt oxide in the spinel structure. **Physical Review B - Condensed Matter and Materials Physics**, v. 83,

n. 24, p. 1–24, 2011.

CHOI, M.; HEO, W.; KLEITZ, F.; RYOO, R. Facile synthesis of high quality mesoporous SBA-15 with enhanced control of the porous network connectivity and wall thickness. **Chemical communications (Cambridge, England)**, v. 75, n. 12, p. 1340–1341, 2003.

CLAEYS, M. Cobalt gets in shape. **Nature**, v. 538, n. 7623, p. 44–45, 2016.

CLAEYS, M.; VAN STEEN, E. **Winnacker-Küchler Chemische Technik: Prozesse und Produkte. Energieträger, organische Grundstoffe**. 5. ed. Wiley-VCH, 2005. v. 4

DAVIS, B. H. **Anderson-Schulz-Flory Product Distribution – Can it be Avoided for Fischer-Tropsch Synthesis?** Technology. **Anais...2003**

DE DEUGD, R. M.; KAPTEIJN, F.; MOULIJN, J. A. Trends in Fischer-Tropsch reactor technology - Opportunities for structured reactors. **Topics in Catalysis**, v. 26, n. 1–4, p. 29–39, 2003.

DE LA PEÑA O'SHEA, V. A.; DE LA PISCINA, P. R.; HOMS, N.; AROMÍ, G.; FIERRO, J. L. G. Development of hexagonal closed-packed cobalt nanoparticles stable at high temperature. **Chemistry of Materials**, v. 21, n. 23, p. 5637–5643, 2009.

DE SMIT, E.; CINQUINI, F.; BEALE, A. M.; SAFONOVA, O. V.; VAN BEEK, W.; SAUTET, P.; WECKHUYSEN, B. M. Stability and reactivity of  $\epsilon$ -X- $\theta$  iron carbide catalyst phases in fischer-tropsch synthesis: Controlling  $\mu$ c. **Journal of the American Chemical Society**, v. 132, n. 42, p. 14928–14941, 2010.

DIEHL, F.; KHODAKOV, A. Y. Promotion of Cobalt Fischer-Tropsch Catalysts with Noble Metals: a Review. **Oil & Gas Science and Technology - Revue de l'IFP**, v. 64, n. 1, p. 11–24, 8 jan. 2009.

DRY, M. E. Present and future applications of the Fischer-Tropsch process. **Applied Catalysis A: General**, v. 276, n. 1–2, p. 1–3, 2004.

DRY, M. E. **Fischer-Tropsch Synthesis - Industrial**, 2010. (Nota técnica).

FARRAUTO, R. J.; HOBSON, M. C. Catalyst Characterization. In: MEYERS, R. A. (Ed.). . **Encyclopedia of Physical Science and Technology**. Third ed. Tarzana, California, USA: Elsevier, 2003. p. 501–526.

FARZAD, S.; RASHIDI, A.; HAGHTALAB, A.; MANDEGARI, M. A. Study of effective parameters in the Fischer Tropsch synthesis using monolithic CNT supported cobalt catalysts. **Fuel**, v. 132, p. 27–35, 2014.

FEI TAN, K.; XU, J.; CHANG, J.; BORGNA, A.; SAEYS, M. Carbon deposition on Co catalysts during Fischer-Tropsch synthesis: A computational and experimental study. **Journal of Catalysis**, v. 274, n. 2, p. 121–129, 2010.

FIGUERES, C.; SCHELLNHUBER, H. J.; WHITEMAN, G.; ROCKSTRÖM, J.; HOBLEY, A.; RAHMSTORF, S. Three years to safeguard our climate. **Nature**, v. 546, n. 7660, p. 593–595, 2017.

FISCHER, N.; VAN STEEN, E.; CLAEYS, M. Structure sensitivity of the Fischer-Tropsch activity and selectivity on alumina supported cobalt catalysts. **Journal of Catalysis**, v. 299, p. 67–80, 2013.

FÖRTSCH, D.; PABST, K.; GROSS-HARDT, E. The product distribution in Fischer-Tropsch synthesis: An extension of the ASF model to describe common deviations. **Chemical Engineering Science**, v. 138, p. 333–346, 2015.

FRATALOCCHI, L.; GROPPI, G.; VISCONTI, C. G.; LIETTI, L.; TRONCONI, E. Packed-POCS with skin : A novel concept for the intensification of non-adiabatic catalytic processes demonstrated in the case of the Fischer-Tropsch synthesis. **Catalysis Today**, v. 383, p. 15–20, 2022.

GARONA, H. A.; CAVALCANTI, F. M.; DE ABREU, T. F.; SCHMAL, M.; ALVES, R. M. B. Evaluation of Fischer-Tropsch synthesis to light olefins over Co- and Fe-based catalysts using artificial neural network. **Journal of Cleaner Production**, v. 321, n. December 2020, p. 129003, 2021.

GAVRILOVIĆ, L.; JØRGENSEN, E. A.; PANDEY, U.; PUTTA, K. R.; ROUT, K. R.; RYTTER, E.; HILLESTAD, M.; BLEKKAN, E. A. Fischer-Tropsch synthesis over an alumina-supported cobalt catalyst in a fixed bed reactor – Effect of process parameters. **Catalysis Today**, v. 369, n. August 2020, p. 150–157, 2021.

GHOLAMI, Z.; TIŠLER, Z.; RUBÁŠ, V. Recent advances in Fischer-Tropsch synthesis using cobalt-based catalysts: a review on supports, promoters, and reactors. **Catalysis Reviews - Science and Engineering**, v. 63, n. 3, p. 512–595, 2021.

GU, B.; KHODAKOV, A. Y.; ORDOMSKY, V. V. Selectivity shift from paraffins to  $\alpha$ -olefins in low temperature Fischer-Tropsch synthesis in the presence of carboxylic acids. **Chemical Communications**, v. 54, n. 19, p. 2345–2348, 2018.

GUPTA, P. K.; MAHATO, A.; GUPTA, G. K.; SAHU, G.; MAITY, S. Fischer-Tropsch synthesis over Pd promoted cobalt based mesoporous supported catalyst. **Oil and Gas Science and Technology**, v. 76, 2021.

GÜTTEL, R.; TUREK, T. Improvement of Fischer-Tropsch Synthesis through Structuring on Different Scales. **Energy Technology**, v. 4, n. 1, p. 44–54, 2016.

HADJIEV, V. G.; ILIEV, M. N.; VERGILOV, I. V. The Raman spectra of Co<sub>3</sub>O<sub>4</sub>. **Journal of Physics C: Solid State Physics**, v. 21, n. 7, p. L199–L201, 1988.

HEREIN, D. Structure and Morphology: X-Ray Powder Diffraction. **Handbook of Heterogeneous Catalysis**, 2008.

HEWER, T. L. R.; SOUZA, A. G. F.; ROSENO, K. T. C.; MOREIRA, P. F.; BONFIM, R.; ALVES, R. M. B.; SCHMAL, M. Influence of acid sites on the hydrodeoxygenation of anisole with metal supported on SBA-15 and SAPO-11. **Renewable Energy**, v. 119, p. 615–624, 2018.

HILL, R. J.; CRAIG, J. R.; GIBBS, G. V. Systematics of the spinel structure type. **Physics and Chemistry of Minerals**, v. 4, n. 4, p. 317–339, 1979.

HILMEN; BERGENE; LINDVAG; SCHANKE; ERI; HOLMEN. Fischer-tropsch synthesis using monolithic catalysts. **Studies in Surface Science and Catalysis**, v. 130 B, p. 1163–1168, 2000.

HODKIEWICZ, J. **Characterizing Carbon Materials with Raman Spectroscopy** *Journal of Physical Chemistry B* Madison, WI, USA Thermo Fischer Scientific, , 2010. Disponível em: <[www.thermo.com](http://www.thermo.com)>

HOLMEN, A.; VENVIK, H. J.; MYRSTAD, R.; ZHU, J.; CHEN, D. Monolithic, microchannel and carbon nanofibers/carbon felt reactors for syngas conversion by Fischer-Tropsch synthesis. **Catalysis Today**, v. 216, p. 150–157, 2013.

HUBER, G. W.; GUYMON, C. G.; CONRAD, T. L.; STEPHENSON, B. C.; BARTHOLOMEW, C. H. **Hydrothermal Stability of Co/SiO<sub>2</sub> Fischer-Tropsch Synthesis Catalysts**. Elsevier Masson SAS, 2001. v. 139

HUFSEY, F. Novel Methods for the Analysis of Small Molecule Fragmentation Mass Spectra. **Mathematik und Informatik**, v. Dr. rer. n, n. DIN-ISO 9706, 1986.

IGLESIA, E.; REYES, S. C. C.; MADON, R. J. J.; SOLED, S. L. L. Selectivity Control and Catalyst Design in the Fischer-Tropsch Synthesis: Sites, Pellets, and Reactors. **Advances in Catalysis**, v. 39, n. C, p. 221–302, 1993.

INTERNATIONAL ENERGY AGENCY. **Key World Energy Statistics**. Paris, France: IEA Publications, 2017.

JACOBS, G.; DAS, T. K. K.; ZHANG, Y.; LI, J.; RACOILLET, G.; DAVIS, B. H. H. Fischer-Tropsch synthesis: Support, loading, and promoter effects on the reducibility of cobalt catalysts. **Applied Catalysis A: General**, v. 233, n. 1–2, p. 263–281, 2002.

JIA, L.; JIA, L.; LI, D.; HOU, B.; WANG, J.; SUN, Y. Silylated Co/SBA-15 catalysts for Fischer-Tropsch synthesis. **Journal of Solid State Chemistry**, v. 184, n. 3, p. 488–493, 2011.

JOHANSSON, E. M.; BALLEM, M. A. Rapid Synthesis of SBA-15 Rods with Variable Lengths , Widths , and Tunable Large Pores. p. 4994–4999, 2011.

JONGSOMJIT, B.; PANPRANOT, J.; GOODWIN, J. G. Co-support compound formation in alumina-supported cobalt catalysts. **Journal of Catalysis**, v. 204, n. 1, p. 98–109, 2001.

KALE, G. M.; PANDIT, S. S.; JACOB, K. T. THERMODYNAMICS OF COBALT(II, III) OXIDE ( $\text{Co}_3\text{O}_4$ ): EVIDENCE OF PHASE TRANSITION. **Transactions of the Japan Institute of Metals**, v. 29, n. 2, p. 125–132, 1988.

KAVAN, L. Carbyne forms of carbon: continuation of the history. **Carbon**, v. 32, n. 8, p. 1533–1536, 1994.

KHAN, F. M. Transition Metal Carbides for Thermocatalytic Conversion of Carbon Dioxide via Reverse Water Gas Shift and Sabatier Reactions. 2018.

KHODAKOV, A. Y.; LYNCH, J.; BAZIN, D.; REBOURS, B.; ZANIER, N.; MOISSON, B.; CHAUMETTE, P. Reducibility of cobalt species in silica-supported Fischer-Tropsch catalysts. **Journal of Catalysis**, v. 168, n. 1, p. 16–25, 1997.

KHODAKOV, A. Y.; GRIBOVAL-CONSTANT, A.; BECHARA, R.; ZHOLOBENKO, V. L. Pore Size Effects in Fischer Tropsch Synthesis over Cobalt-Supported Mesoporous Silicas.

**Journal of Catalysis**, v. 206, p. 230–241, 2002.

KHODAKOV, A. Y.; ZHOLOBENKO, V. L.; BECHARA, R.; DURAND, D. Impact of aqueous impregnation on the long-range ordering and mesoporous structure of cobalt containing MCM-41 and SBA-15 materials. **Microporous and Mesoporous Materials**, v. 79, n. 1–3, p. 29–39, 2005.

KHODAKOV, A. Y.; BECHARA, R.; GRIBOVAL-CONSTANT, A. Fischer-Tropsch synthesis over silica supported cobalt catalysts: Mesoporous structure versus cobalt surface density. **Applied Catalysis A: General**, v. 254, n. 2, p. 273–288, 2003.

KHODAKOV, A. Y.; CHU, W.; FONGARLAND, P. Advances in the Development of Novel Cobalt Fischer – Tropsch Catalysts for Synthesis of Long-Chain Hydrocarbons and Clean Fuels Advances in the Development of Novel Cobalt Fischer – Tropsch Catalysts for Synthesis of Long-Chain Hydrocarbons and Clean Fuel. **American Chemical Society**, v. 107, n. 5, p. 1692–1744, 2007.

KIM, D. J.; DUNN, B. C.; COLE, P.; TURPIN, G.; ERNST, R. D.; PUGMIRE, R. J.; KANG, M.; KIM, J. M.; EYRING, E. M. Enhancement in the reducibility of cobalt oxides on a mesoporous silica supported cobalt catalyst. **Chemical communications (Cambridge, England)**, n. 11, p. 1462–4, 2005.

KLEITZ, F. Ordered Mesoporous Materials. In: **Handbook of Heterogeneous Catalysis**. p. 178–219.

KREUTZER, M. T.; KAPTEIJN, F.; MOULIJN, J. A. Shouldn't catalysts shape up? Structured reactors in general and gas-liquid monolith reactors in particular. **Catalysis Today**, v. 111, n. 1–2, p. 111–118, 2006.

KRUK, M.; JARONIEC, M.; KO, C. H.; RYOO, R. Characterization of the Porous Structure of SBA-15. n. 9, p. 1961–1968, 2000.

LANCELOT, C.; ORDOMSKY, V. V.; STÉPHAN, O.; SADEQZADEH, M.; KARACA, H.; LACROIX, M.; CURULLA-FERRÉ, D.; LUCK, F.; FONGARLAND, P.; GRIBOVAL-CONSTANT, A.; KHODAKOV, A. Y. Direct evidence of surface oxidation of cobalt nanoparticles in alumina-supported catalysts for fischer-tropsch synthesis. **ACS Catalysis**, v. 4, n. 12, p. 4510–4515, 2014.

- LAUNER, P. J. Infrared analysis of organosilicon compounds: Spectra-structure correlation. **Microelectronic Engineering**, v. 137, n. January 2013, p. 75–78, 2015.
- LE VAN MAO, R.; YAN, H. T.; MUNTASAR, A.; AL-YASSIR, N. Blending of Non-Petroleum Compounds with Current Hydrocarbon Feeds to Use in the Thermo-Catalytic Steam-Cracking Process for the Selective Production of Light Olefins. In: **New and Future Developments in Catalysis: Hybrid Materials, Composites, and Organocatalysts**. Elsevier B.V., 2013. p. 143–173.
- LEE, H. I.; KIM, J. H.; STUCKY, G. D.; SHI, Y.; PAK, C.; KIM, J. M. Morphology-selective synthesis of mesoporous SBA-15 particles over micrometer, submicrometer and nanometer scales. **Journal of Materials Chemistry**, v. 20, n. 39, p. 8483, 2010.
- LEVINESS, S.; DESHMUKH, S. R.; RICHARD, L. A.; ROBOTTA, H. J. Velocys fischer-tropsch synthesis technology - New advances on state-of-the-art. **Topics in Catalysis**, v. 57, n. 6–9, p. 518–525, 2014.
- LIN, Q.; LIU, B.; JIANG, F.; FANG, X.; XU, Y.; LIU, X. Assessing the formation of cobalt carbide and its catalytic performance under realistic reaction conditions and tuning product selectivity in a cobalt-based FTS reaction. **Catalysis Science and Technology**, v. 9, n. 12, p. 3238–3258, 2019.
- LORITE, I.; DEL CAMPO, A.; ROMERO, J. J.; FERNÁNDEZ, J. F. Isolated nanoparticle raman spectroscopy. **Journal of Raman Spectroscopy**, v. 43, n. 7, p. 889–894, 2012.
- LOWELL, S.; SHIELDS, J. E.; THOMAS, M. A.; THOMMES, M. **Characterization of Porous Solids and Powders: Surface Area, Pore Size and Density**. Dordrecht/Boston/London: Kluwer Academic Publishers, 2004.
- LU, Y.; ZHOU, P.; HAN, J.; YU, F. Fischer–Tropsch synthesis of liquid hydrocarbons over mesoporous SBA-15 supported cobalt catalysts. **RSC Advances**, v. 5, n. 73, p. 59792–59803, 2015.
- LUALDI, M.; LÖGDBERG, S.; DI CARLO, G.; JÄRÅS, S.; BOUTONNET, M.; VENEZIA, A. M.; BLEKKAN, E. A.; HOLMEN, A. Evidence for diffusion-controlled hydrocarbon selectivities in the fischer-tropsch synthesis over cobalt supported on ordered mesoporous silica. **Topics in Catalysis**, v. 54, n. 16–18, p. 1175–1184, 2011.

- LUALDI, M.; DI CARLO, G.; LÖGDBERG, S.; JÄRÅS, S.; BOUTONNET, M.; LA PAROLA, V.; LIOTTA, L. F.; INGO, G. M.; VENEZIA, A. M. Effect of Ti and Al addition via direct synthesis to SBA-15 as support for cobalt based Fischer-Tropsch catalysts. **Applied Catalysis A: General**, v. 443–444, p. 76–86, 2012.
- MAITLIS, P. M.; KLERK, A. DE. **Greener Fischer-Tropsch Processes for Fuels and Feedstocks**. Weinheim, Germany: WILEY-VCH Verlag, 2013.
- MARSIH, I. N.; MAKERTIHARTHA, I.; PRASERTHDAM, P.; PANPRANOT, J.  $\gamma$ -Alumina Nanotubes Prepared by Hydrothermal Method as Support of Iron, Cobalt and Nickel for Fischer-Tropsch Catalysts. v. 2, n. 3, p. 31–39, 2012.
- MARTÍNEZ, A.; LÓPEZ, C.; MÁRQUEZ, F.; DÍAZ, I. Fischer-Tropsch synthesis of hydrocarbons over mesoporous Co/SBA-15 catalysts: The influence of metal loading, cobalt precursor, and promoters. **Journal of Catalysis**, v. 220, n. 2, p. 486–499, 2003.
- MERINO, D.; SANZ, O.; MONTES, M. Effect of catalyst layer macroporosity in high-thermal-conductivity monolithic Fischer-Tropsch catalysts. **Fuel**, v. 210, n. August, p. 49–57, 2017a.
- MERINO, D.; SANZ, O.; MONTES, M. Effect of the thermal conductivity and catalyst layer thickness on the Fischer-Tropsch synthesis selectivity using structured catalysts. **Chemical Engineering Journal**, v. 327, p. 1033–1042, 2017b.
- MIGNOLI, T. R. **Nanopartículas de cobalto suportadas em grafeno e promovidas com lantânio para produção de combustíveis**. University of São Paulo, 2020.
- MOAZAMI, N.; WYSZYNSKI, M. L.; RAHBAR, K.; TSOLAKIS, A. Parametric Study and Multiobjective Optimization of Fixed-Bed Fischer-Tropsch (FT) Reactor: The Improvement of FT Synthesis Product Formation and Synthetic Conversion. **Industrial and Engineering Chemistry Research**, v. 56, n. 34, p. 9446–9466, 2017.
- MONSHI, A.; FOROUGHI, M. R.; MONSHI, M. R. Modified Scherrer Equation to Estimate More Accurately Nano-Crystallite Size Using XRD. **World Journal of Nano Science and Engineering**, v. 02, n. 03, p. 154–160, 2012.
- MOODLEY, D. J. **On the Deactivation of Cobalt-based Fischer-Tropsch Synthesis Catalysts**.
- MORAJKAR, P. P.; FERNANDES, J. B. A new facile method to synthesize mesoporous  $\gamma$ -

Al<sub>2</sub>O<sub>3</sub> of high surface area and catalytic activity. **Catalysis Communications**, v. 11, n. 5, p. 414–418, 2010.

NIJHUIS, T. A.; BEERS, A. E. W.; VERGUNST, T.; HOEK, I.; KAPTEIJN, F.; MOULIJN, J. Preparation of monolithic catalysts. **Catalysis Reviews**, v. 43, n. 4, p. 345–380, 2001.

NIST. **NIST Standard Reference Database 69: NIST Chemistry WebBook - 1-Butene**. Disponível em: <<https://webbook.nist.gov/cgi/cbook.cgi?ID=C106989&Mask=200#>>. Acesso em: 26 set. 2021.

PANGARKAR, K.; SCHILDHAUER, T. J.; VAN OMMEN, J. R.; NIJENHUIS, J.; MOULIJN, J. A.; KAPTEIJN, F. Experimental and numerical comparison of structured packings with a randomly packed bed reactor for Fischer-Tropsch synthesis. **Catalysis Today**, v. 147, n. SUPPL., p. 2–9, 2009.

PARK, J. C.; KWON, J. I.; KANG, S. W.; CHUN, D. H.; LEE, H. T.; JUNG, H.; YANG, J. IL. Large-scale synthesis of uniformly loaded cobalt nanoparticles on alumina for efficient clean fuel production. **RSC Advances**, v. 7, n. 15, p. 8852–8857, 2017.

PATANOU, E.; TSAKOUMIS, N. E.; MYRSTAD, R.; BLEKKAN, E. A. The impact of sequential H<sub>2</sub>-CO-H<sub>2</sub> activation treatment on the structure and performance of cobalt based catalysts for the Fischer-Tropsch synthesis. **Applied Catalysis A: General**, v. 549, n. April 2017, p. 280–288, 2018.

PEDERSEN, E. Ø.; SVENUM, I. H.; BLEKKAN, E. A. Mn promoted Co catalysts for Fischer-Tropsch production of light olefins – An experimental and theoretical study. **Journal of Catalysis**, v. 361, p. 23–32, 2018.

PEREGO, C.; BORTOLO, R.; ZENNARO, R. Gas to liquids technologies for natural gas reserves valorization: The Eni experience. **Catalysis Today**, v. 142, n. 1–2, p. 9–16, 2009.

PFEIFFER. **Mass Spectrometer Catalog**. Asslar, Germany: Pfeiffer Vacuum GmbH Headquarters/Germany, 2005.

PHAM, A. L. T.; SEDLAK, D. L.; DOYLE, F. M. Dissolution of mesoporous silica supports in aqueous solutions: Implications for mesoporous silica-based water treatment processes. **Applied Catalysis B: Environmental**, v. 126, p. 258–264, 2012.

PICHLER, H. Twenty-five Years of Synthesis of Gasoline by Catalytic Conversion of Carbon

Monoxide and Hydrogen. **Advances in Catalysis**, v. 4, n. C, p. 271–341, 1952.

PRIETO, G.; MARTÍNEZ, A.; MURCIANO, R.; ARRIBAS, M. A. Cobalt supported on morphologically tailored SBA-15 mesostructures: The impact of pore length on metal dispersion and catalytic activity in the Fischer-Tropsch synthesis. **Applied Catalysis A: General**, v. 367, n. 1–2, p. 146–156, 2009.

PUSKAS, I.; HURLBUT, R. S. Comments about the causes of deviations from the Anderson-Schulz-Flory distribution of the Fischer-Tropsch reaction products. **Catalysis Today**, v. 84, n. 1–2, p. 99–109, 2003.

RAND, A. **For the new intellectual: The philosophy of Ayn Rand**. Penguin, 1963.

RAND, A. **Atlas shrugged**. Penguin, 2005.

RAVAGNAN, L.; PISERI, P.; BRUZZI, M.; MIGLIO, S.; BONGIORNO, G.; BASERGA, A.; CASARI, C. S.; LI BASSI, A.; LENARDI, C.; YAMAGUCHI, Y.; WAKABAYASHI, T.; BOTTANI, C. E.; MILANI, P. Influence of cumulenic chains on the vibrational and electronic properties of sp-sp<sup>2</sup> amorphous carbon. **Physical Review Letters**, v. 98, n. 21, p. 25–28, 2007.

RAVIKOVITCH, P. I.; NEIMARK, A. V. Characterization of micro- and mesoporosity in SBA-15 materials from adsorption data by the NLDFT method. **Journal of Physical Chemistry B**, v. 105, n. 29, p. 6817–6823, 2001.

RAVINDRA, A. V.; BEHERA, B. C.; PADHAN, P. Laser induced structural phase transformation of cobalt oxides nanostructures. **Journal of Nanoscience and Nanotechnology**, v. 14, n. 7, p. 5591–5595, 2014.

REUEL, R. C.; BARTHOLOMEW, C. H. Effects of support and dispersion on the CO hydrogenation activity/selectivity properties of cobalt. **Journal of Catalysis**, v. 85, n. 1, p. 78–88, 1984.

RIVAS-MURIAS, B.; SALGUEIRIÑO, V. Thermodynamic CoO–Co<sub>3</sub>O<sub>4</sub> crossover using Raman spectroscopy in magnetic octahedron-shaped nanocrystals. **Journal of Raman Spectroscopy**, v. 48, n. 6, p. 837–841, 2017.

ROBOTA, H. J.; RICHARD, L. A.; DESHMUKH, S.; LEVINESS, S.; LEONARDUZZI, D.; ROBERTS, D. High Activity and Selective Fischer–Tropsch Catalysts for Use in a Microchannel Reactor. **Catalysis Surveys from Asia**, v. 18, n. 4, p. 177–182, 2014.

ROQUE, J. M. F. **Desenvolvimento de diferentes tipos de nanocontainers com inibidor dodecilamina encapsulado para aditivação de primers com propriedades de autorreparação**. Universidade de São Paulo, 2015.

SABATIER, P.; SENDERENS, J. B. Direct hydrogenation of oxides of carbon in presence of various finely divided metals. **CR Acad Sci**, v. 134, p. 689–691, 1902.

SADEQZADEH, M.; CHAMBREY, S.; HONG, J.; FONGARLAND, P.; LUCK, F.; CURULLA-FERRÉ, D.; SCHWEICH, D.; BOUSQUET, J.; KHODAKOV, A. Y. Effect of different reaction conditions on the deactivation of alumina-supported cobalt Fischer-Tropsch catalysts in a milli-fixed-bed reactor: Experiments and modeling. **Industrial and Engineering Chemistry Research**, v. 53, n. 17, p. 6913–6922, 2014.

SAHA, D.; GRAPPE, H. A.; CHAKRABORTY, A.; ORKOULAS, G. Postextraction Separation, On-Board Storage, and Catalytic Conversion of Methane in Natural Gas: A Review. **Chemical Reviews**, v. 116, n. 19, p. 11436–11499, 12 out. 2016.

SAWIN, J. L.; SEYBOTH, K.; SVERRISSON, F. Advancing the global renewable energy transition. **Renewable energy policy network for the 21st century**, p. 45, 2017.

SCHANKE, D.; BERGENE, E.; HOLMEN, A. **FISCHER-TROPSCH SYNTHESIS**, 2001.

SCHMAL, M. Catálise heterogênea. **Rio de Janeiro: Synergia**, 2011.

SEAGER, R. J.; ACEVEDO, A. J.; SPILL, F.; ZAMAN, M. H. Solid dissolution in a fluid solvent is characterized by the interplay of surface area-dependent diffusion and physical fragmentation. **Scientific Reports**, v. 8, n. 1, p. 1–17, 2018.

SETIABUDI, H. D.; LIM, K. H.; AINIRAZALI, N.; CHIN, S. Y. CO<sub>2</sub> reforming of CH<sub>4</sub> over Ni/SBA-15: Influence of Ni loading on the metal- support interaction and catalytic activity. **Journal of Materials and Environmental Sciences**, v. 8, n. 2, p. 573–581, 2017.

SIE, S. T.; KRISHNA, R. Fundamentals and selection of advanced Fischer–Tropsch reactors. **Applied Catalysis A: General**, v. 186, n. 1–2, p. 55–70, 1999.

SILVA, R. R. C. M.; SCHMAL, M.; FRETAY, R.; DALMON, J. A. Effect of the support on the fischer-tropsch synthesis with Co/Nb<sub>2</sub>O<sub>5</sub> catalysts. **Journal of the Chemical Society, Faraday Transactions**, v. 89, n. 21, p. 3975, 1993.

SING, K. S. W.; EVERETT, D. H.; HAUL, R. A. W.; MOSCOU, L.; PIEROTTI, R. A.; ROUQUEROL, J.; SIEMIENIEWSKA, T. International union of pure and applied chemistry, IUPAC. **Pure Appl. Chem**, v. 57, p. 603, 1985.

SINGH, S.; KUMAR, R.; SETIABUDI, H. D.; NANDA, S.; VO, D. V. N. Advanced synthesis strategies of mesoporous SBA-15 supported catalysts for catalytic reforming applications: A state-of-the-art review. **Applied Catalysis A: General**, v. 559, n. January, p. 57–74, 2018.

SOTOMAYOR, F. J.; CYCHOSZ, K. A.; THOMMES, M. Characterization of Micro/Mesoporous Materials by Physisorption: Concepts and Case Studies. **Acc. Mater. Surf. Res**, v. 3, n. 2, p. 34–50, 2018.

STENGER, H. G.; ASKONAS, C. F. Thermodynamic product distributions for the Fischer-Tropsch synthesis. **Industrial & Engineering Chemistry Fundamentals**, v. 25, n. 3, p. 410–413, ago. 1986.

TAHERI NAJAFABADI, A.; KHODADADI, A. A.; PARNIAN, M. J.; MORTAZAVI, Y. Atomic layer deposited Co/ $\gamma$ -Al<sub>2</sub>O<sub>3</sub> catalyst with enhanced cobalt dispersion and Fischer-Tropsch synthesis activity and selectivity. **Applied Catalysis A: General**, v. 511, p. 31–46, 2016.

TANG, Q.; WANG, P.; ZHANG, Q.; WANG, Y. Utilization of Microporous and Mesoporous Materials as Supports of Cobalt Catalysts for Regulating Product Distributions in Fischer-Tropsch Synthesis. **Chemistry Letters**, v. 35, n. 4, p. 366–367, 2006.

THOMMES, M. **Pore Size Analysis by Gas Adsorption Part I: Aspects of the Application of Density Functional Theory (DFT) and Monte Carlo simulation (MC) for micro/mesopore size analysis** Quantachrome Instruments, 2002.

THOMMES, M.; KANEKO, K.; NEIMARK, A. V.; OLIVIER, J. P.; RODRIGUEZ-REINOSO, F.; ROUQUEROL, J.; SING, K. S. W. Physisorption of gases, with special reference to the evaluation of surface area and pore size distribution (IUPAC Technical Report). **Pure and Applied Chemistry**, v. 87, n. 9–10, p. 1051–1069, 2015.

TIERNAN, M. J.; FESENKO, E. A.; BARNES, P. A.; PARKES, G. M. B.; RONANE, M. The application of CRTA and linear heating thermoanalytical techniques to the study of supported cobalt oxide methane combustion catalysts. **Thermochimica Acta**, v. 379, n. 1–2, p. 163–175, 2001.

TONCÓN-LEAL, C. F.; MÚNERA, J. F.; ARROYO-GÓMEZ, J. J.; SAPAG, K. Fe, Co and Fe/Co catalysts supported on SBA-15 for Fischer-Tropsch Synthesis. **Catalysis Today**, n. February, 2021.

TORRES GALVIS, H. M.; DE JONG, K. P. Catalysts for production of lower olefins from synthesis gas: A review. **ACS Catalysis**, v. 3, n. 9, p. 2130–2149, 2013.

TRUEBA, M.; TRASATTI, S. P.  $\gamma$ -alumina as a support for catalysts: A review of fundamental aspects. **European Journal of Inorganic Chemistry**, n. 17, p. 3393–3403, 2005.

TSAKOUMIS, N. E.; RØNNING, M.; BORG, Ø.; RYTTER, E.; HOLMEN, A. Deactivation of cobalt based Fischer-Tropsch catalysts: A review. **Catalysis Today**, v. 154, n. 3–4, p. 162–182, 2010.

VISCONTI, C. G.; TRONCONI, E.; LIETTI, L.; GROPPI, G.; FORZATTI, P.; CRISTIANI, C.; ZENNARO, R.; ROSSINI, S. An experimental investigation of Fischer-Tropsch synthesis over washcoated metallic structured supports. **Applied Catalysis A: General**, v. 370, n. 1–2, p. 93–101, 2009.

VISCONTI, C. G.; TRONCONI, E.; GROPPI, G.; LIETTI, L.; IOVANE, M.; ROSSINI, S.; ZENNARO, R. Monolithic catalysts with high thermal conductivity for the Fischer-Tropsch synthesis in tubular reactors. **Chemical Engineering Journal**, v. 171, n. 3, p. 1294–1307, 2011.

VISCONTI, C. G.; MASCELLARO, M. Calculating the product yields and the vapor–liquid equilibrium in the low-temperature Fischer–Tropsch synthesis. **Catalysis Today**, v. 214, p. 61–73, 2013.

VOGEL, A. P.; VAN DYK, B.; SAIB, A. M. GTL using efficient cobalt Fischer-Tropsch catalysts. **Catalysis Today**, v. 259, p. 323–330, 2015.

VOGELS, R. J. M. J.; KLOPROGGE, J. T.; GEUS, J. W. Homogeneous forced hydrolysis of aluminum through the thermal decomposition of urea. **Journal of Colloid and Interface Science**, v. 285, n. 1, p. 86–93, 2005.

WANG, J.; CHERNAVSKII, P. A.; WANG, Y.; KHODAKOV, A. Y. Influence of the support and promotion on the structure and catalytic performance of copper-cobalt catalysts for carbon monoxide hydrogenation. **Fuel**, v. 103, p. 1111–1122, 2013.

WIGZELL, F. A.; JACKSON, S. D. The genesis of supported cobalt catalysts. **Applied**

**Petrochemical Research**, v. 7, n. 1, p. 9–21, 2017.

WILLIAMS, D. B.; CARTER, C. B. **Transmission electron microscopy: A textbook for materials science**.

WILLIAMS, M. L. **CRC Handbook of Chemistry and Physics, 76th edition**. v. 53

WOLF, M.; KOTZÉ, H.; FISCHER, N.; CLAEYS, M. Size dependent stability of cobalt nanoparticles on silica under high conversion Fischer–Tropsch environment. **Faraday Discuss.**, 2017.

WOLF, M.; FISCHER, N.; CLAEYS, M. Water-induced deactivation of cobalt-based Fischer–Tropsch catalysts. **Nature Catalysis**, v. 3, n. 12, p. 962–965, 2020.

XIONG, H.; ZHANG, Y.; LIEW, K.; LI, J. Fischer-Tropsch synthesis: The role of pore size for Co/SBA-15 catalysts. **Journal of Molecular Catalysis A: Chemical**, v. 295, n. 1–2, p. 68–76, 2008.

XU, J.; HE, Q.; XIONG, Z.; YU, Y.; ZHANG, S.; HU, X.; JIANG, L.; SU, S.; HU, S.; WANG, Y.; XIANG, J. Raman spectroscopy as a versatile tool for investigating thermochemical processing of coal, biomass, and wastes: Recent advances and future perspectives. **Energy and Fuels**, v. 35, n. 4, p. 2870–2913, 2021.

YAN, Z.; WANG, Z.; BUKUR, D. B.; GOODMAN, D. W. Fischer-Tropsch synthesis on a model Co/SiO<sub>2</sub> catalyst. **Journal of Catalysis**, v. 268, n. 2, p. 196–200, 2009.

YANG, Y.; PEN, S.; ZHONG, B. A new product distribution formulation for Fischer-Tropsch synthesis. Effect of metal crystallite size distribution. **Catalysis Letters**, v. 16, n. 3, p. 351–357, 1992.

ZENNARO, R.; TAGLIABUE, M.; BARTHOLOMEW, C. H. Kinetics of Fischer-Tropsch synthesis on titania-supported cobalt. **Catalysis Today**, v. 58, n. 4, p. 309–319, 2000.

ZHANG, F.; YAN, Y.; YANG, H.; MENG, Y.; YU, C.; TU, B.; ZHAO, D. Understanding effect of wall structure on the hydrothermal stability of mesostructured silica SBA-15. **The journal of physical chemistry. B**, v. 109, p. 8723–8732, 2005a.

ZHANG, H.; SUN, J.; MA, D.; BAO, X.; KLEIN-HOFFMANN, A.; WEINBERG, G.; SU, D.; SCHLÖGL, R. Unusual mesoporous SBA-15 with parallel channels running along the short

axis. **Journal of the American Chemical Society**, v. 126, n. 24, p. 7440–7441, 2004.

ZHANG, Q.; KANG, J.; WANG, Y. Development of Novel Catalysts for Fischer-Tropsch Synthesis: Tuning the Product Selectivity. **ChemCatChem**, v. 2, n. 9, p. 1030–1058, 2010.

ZHANG, Y.; XIONG, H.; LIEW, K.; LI, J. Effect of magnesia on alumina-supported cobalt Fischer-Tropsch synthesis catalysts. **Journal of Molecular Catalysis A: Chemical**, v. 237, n. 1–2, p. 172–181, 2005b.

ZHANG, Y.; ZHU, Y.; WANG, K.; LI, D.; WANG, D.; DING, F.; MENG, D.; WANG, X.; CHOI, C.; ZHANG, Z. Controlled synthesis of Co<sub>2</sub>C nanochains using cobalt laurate as precursor: Structure, growth mechanism and magnetic properties. **Journal of Magnetism and Magnetic Materials**, v. 456, p. 71–77, 2018.

ZHAO, D.; FENG, J.; HUO, Q.; MELOSH, N.; FREDRICKSON, G. H.; CHMELKA, B. F.; STUCKY, G. D. Triblock Copolymer Syntheses of Mesoporous Silica with Periodic 50 to 300 Angstrom Pores. **Science**, v. 279, n. 5350, p. 548–552, 1998.

ZHAO, D.; SUN, J.; LI, Q.; STUCKY, G. D.; BARBARA, S. Morphological Control of Highly Ordered Mesoporous Silica SBA-15. **Communications**, v. 12, n. 22, p. 275–279, 2000.

ZHOLOBENKO, V. L.; KHODAKOV, A. Y.; IMPÉROTOR-CLERC, M.; DURAND, D.; GRILLO, I. Initial stages of SBA-15 synthesis: An overview. **Advances in Colloid and Interface Science**, v. 142, n. 1–2, p. 67–74, 2008.

ZHOU, W.; CHEN, J. G.; FANG, K. G.; SUN, Y. H. The deactivation of Co/SiO<sub>2</sub> catalyst for Fischer-Tropsch synthesis at different ratios of H<sub>2</sub> to CO. **Fuel Processing Technology**, v. 87, n. 7, p. 609–616, 2006.

ZUO, J.; XU, C.; LIU, Y.; QIAN, Y. Crystallite size effects on the Raman spectra of Mn<sub>3</sub>O<sub>4</sub>. **Nanostructured Materials**, v. 10, n. 8, p. 1331–1335, 1998.

## APPENDIX A – FORMULAS AND DEFINITIONS

The following sections details most of the calculations performed in the study for catalyst impregnation, ICP-OES conversion, Space Velocity (WHSV), Conversion, Selectivity, Reaction Rate, Yield Loss and Mass Balance Assessment, along with a parallel solution.

### A.1. CATALYST IMPREGNATION

The catalyst preparation requires the calculation of the amount of metal to be impregnated. For the incipient wetness impregnation, firstly it is required the determination of the support's total pore volume. Such determination is performed after drying the support in an oven overnight, usually considering the water removal temperature given by thermogravimetric analysis. Water is then added to the support dropwise, using a burette, up to the turning point, where the support turns into a paste.

After the pore volume determination, the metal mass added to the support must be calculated. Equation (A.1) shows the formula used for a general  $x$  Co wt/wt impregnation.

$$\begin{aligned}
 m_{\text{support}} + m_{\text{Co}} &= m_{\text{total}} \\
 m_{\text{Co}} &= x \cdot m_{\text{total}} \\
 m_{\text{Co}} &= x \cdot (m_{\text{Co}} + m_{\text{support}}) \\
 (1 - x) \cdot m_{\text{Co}} &= x \cdot m_{\text{support}} \\
 m_{\text{Co}} &= \frac{x \cdot m_{\text{support}}}{(1 - x)}, \quad 0 \leq x \leq 1
 \end{aligned} \tag{A.1}$$

Where  $m_{\text{Co}}$  is the metal (i.e. cobalt, g) load required to achieve  $x$  wt/wt % metal load and  $m_{\text{support}}$  is the support mass (g). The denominator is a correction value, which considers the mass variation of metal over metal + support final mass.

After obtaining  $m_{\text{Co}}$  the mass of precursor needs to be calculated. The mass of precursor required for the impregnation is given by Equation (A.2).

$$m_{\text{precursor}} = \frac{1}{p} \cdot \frac{m_{\text{Co}}}{\text{MM}_{\text{Co}}} \cdot \text{MM}_{\text{precursor}} \cdot n \tag{A.2}$$

The cobalt precursor used in this study, hexahydrated cobalt nitrate ( $\text{Co}(\text{NO}_3)_2 \cdot 6\text{H}_2\text{O}$ ), presents a metal-precursor equimolar proportion ( $n = 1$ ) with a purity of 98% ( $p = 0.98$ ) and a molar mass ( $MM_{\text{precursor}}$ ) of 291.035  $\text{g}\cdot\text{mol}^{-1}$ . The cobalt molar mass is  $MM_{\text{Co}} = 58.93 \text{ g}\cdot\text{mol}^{-1}$

## A. 2. ICP-OES CALCULATION

The ICP-OES analysis is one of the available methods of obtaining the composition of a catalyst. In this study, it was possible to obtain the amount of Co in the sample. However, it must be considered that the sample provided for analysis was a supported cobalt oxide, not the reduced catalyst, containing adsorbed water. First, water removal was performed by correcting the total mass used for quantification with the estimated water adsorbed water, provided by thermogravimetric analysis:

$$m_{\text{total}} = m_{\text{catalyst}} + m_{\text{water}}$$

$$m_{\text{water}} = w \cdot m_{\text{total}}$$

$$m_{\text{catalyst}} = m_{\text{total}} - w \cdot m_{\text{total}}$$

$$m_{\text{catalyst}} = m_{\text{total}} \cdot (1 - w)$$

Where  $m_{\text{catalyst}}$  is the total mass of the catalyst,  $m_{\text{total}}$  is the mass of the catalyst containing adsorbed water,  $m_{\text{water}}$  is the mass of the adsorbed water over the catalyst,  $w$  is the fraction of water adsorbed on the catalyst, in weight percentage, as determined by TGA.

Since the sample used for ICP-OES analysis was a cobalt metal over a given support, the amount of available active phase must be determined in order to directly compare the results with the nominal metallic percentage. Considering a cobalt monometallic catalyst, the following equations may be considered:

$$m_{\text{total}} = m_{\text{Co}_3\text{O}_4} + m_{\text{support}} + m_{\text{water}}$$

$$\text{ICP} = \frac{m_{\text{Co}}}{m_{\text{total}}} = \frac{m_{\text{Co}}}{m_{\text{catalyst}}} \cdot (1 - w)$$

$$m_{\text{Co}} = y \cdot m_{\text{Co}_3\text{O}_4}$$

Where  $m_{catalyst}$  is the total mass of the catalyst,  $m_{Co_3O_4}$  is the mass of the cobalt oxide ( $Co_3O_4$ ),  $m_{support}$  is the mass of the support,  $m_{Co}$  is the mass of cobalt on the catalyst,  $ICP$  is the fraction of cobalt on the catalyst determined by ICP and  $y$  is the percentage of cobalt in its respective oxide as given by Equation (A.3). The oxide can be identified by XRD. In this case, it was  $Co_3O_4$ .

$$y = \frac{3 \times MM_{Co}}{MM_{Co_3O_4}} = \frac{3 \times 58.933}{(3 \times 58.933 + 4 \times 15.999)} = 0.734 \quad (A.3)$$

The amount of cobalt over the catalyst for a total conversion of  $Co_3O_4$  to cobalt, is calculated as  $z$ .

$$z = \frac{m_{Co}}{(m_{Co} + m_{support})} = \frac{m_{Co}}{m_{Co} + (m_{catalyst} - m_{Co_3O_4})}$$

From which the Equation (A.4) can be achieved.

$$z = \frac{ICP}{ICP + ((1 - w) - \frac{ICP}{y})} \quad (A.4)$$

For a given  $DR$  (degree of reduction), the Equation (A.5) is derived.

$$z = \frac{ICP \cdot DR}{ICP \cdot DR + ((1 - w) - \frac{ICP \cdot DR}{y})} \quad (A.5)$$

Considering the 15%Co/ $Al_2O_3$  catalyst, ICP-OES analysis lead to a quantification of 12.84%. This is the amount of Co in a  $Co_3O_4/Al_2O_3$  sample, as identified by the XRD analysis (Table A.1):

Table A.1 – Converted ICP-OES results for the 15% Co/ $\gamma$ - $Al_2O_3$  catalyst

Sample	w (% wt.)	Mean $\pm$ SD (% wt.)	Nominal Active Phase (% wt.)	Active Phase based on ICP value (z) (% wt.)	Error (%)
15% Co/ $\gamma$ - $Al_2O_3$	8.71	12.84 $\pm$ 0.16	15.00	14.82	1.20

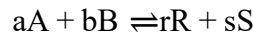
### A. 3. SPACE VELOCITY (WHSV)

The space velocity, given by Equation (A.6), for heterogeneous catalysis is calculated as the total volume flow rate ( $\dot{q}_{in}$ ) relative to the catalyst mass ( $m_{cat}$ ) (HAGEN, 2015a).

$$WHSV = \text{Space Velocity} = \frac{\dot{q}_{in}}{m_{cat}} \quad (\text{A.6})$$

#### A. 4. CONVERSION

The conversion is defined as the globally or instantaneously transformed number of moles of the limiting reactant (e.g., A) in relation to its initial number of moles. Its value can go from 0 to 1 for irreversible reactions and from 0 to  $X_{A,e}$  to reversible reactions (SCHMAL, 2018). For continuous systems, considering the following reaction,



conceptually, the conversion is given by Equation A.7.

$$X_A = \frac{F_{A,0} - F_A}{F_{A,0}}, \quad 0 \leq X_A \leq 1 \quad (\text{A.7})$$

For a reversible reaction:

$$X_{A,e} = \frac{F_{A,0} - F_{A,e}}{F_{A,0}}, \quad X_{A,e} < 1$$

Where  $F_i$  is the molar flow of the reactant  $i$  at the beginning (0) or at equilibrium ( $e$ ).

Thus the CO conversion can be calculated using two approaches:

- Molar flow of reactant (Equation A.8):

$$X_{CO} (\%) = \frac{F_{CO,in} - F_{CO,out}}{F_{CO,in}} \times 100 = \left(1 - \frac{F_{CO,out}}{F_{CO,in}}\right) \times 100 \quad (\text{A.8})$$

With  $F_{CO,in} = N_{CO,in} \cdot \dot{q}_{in} = \left(\frac{P_{CO}}{RT}\right)_{in} \cdot \dot{q}_{in}$  and  $F_{CO,out} = N_{CO,out} \cdot \dot{q}_{out} = \left(\frac{P_{CO}}{RT}\right)_{out} \cdot \dot{q}_{out}$  Ideal gas conditions are considered since the inlet or outlet flow measurement is given by the mass flow controller at STP conditions (BRONKHORST, 2011).

- $N_2$  internal standard correction as given by Equation A.9 was selected for this study:

$$X_{CO} (\%) = \frac{\frac{A_{CO,in}}{A_{N_2,in}} - \frac{A_{CO,out}}{A_{N_2,out}}}{\frac{A_{CO,in}}{A_{N_2,in}}} \times 100 = \left[ 1 - \frac{\left(\frac{A_{CO,out}}{A_{N_2,out}}\right)}{\left(\frac{A_{CO,in}}{A_{N_2,in}}\right)} \right] \times 100 \quad (A.9)$$

Where  $F_i$  stands for component  $i$  molar flow at the inlet ( $F_{i,in}$ ) or outlet ( $F_{i,out}$ ),  $N_i$  is the molar concentration (mol/mL) of component  $i$  obtained by chromatographic analysis,  $\dot{q}$  is the measured volume flow (mL<sub>n</sub>/min) at STP.  $A_i$  stands for the chromatographic area of the component  $i$  at inlet (in) or outlet (out).

The measurements of  $\dot{q}_{out}$  were performed using a mass flow meter (Bronkhorst High-Tech B.V., Nederland) with a conversion factor ( $C$ ) of 1 at STP, configured with N<sub>2</sub>. In order to obtain the true flow at any given moment (e.g. to calculate conversion),  $C_{mix}$  must be calculated as given by Equation A.10. It is a function of the gas composition  $x_i$  (%), the volumetric fraction, and its individual conversion factors,  $C_i$ . In fact, the conversion factor is function of the specific heat and density of a compound (gas to be measured) relative to the reference (gas calibrating) (BRONKHORST, 2011).

$$C_{mix} = \frac{1}{\sum_i \frac{x_i (\%)}{C_i}} \quad (A.10)$$

Table A.2 shows some of the individual conversion factors from compounds found in this study.

Table A.2 – Conversion Factor  $C_i$  of some compounds relative to the FTS reaction

Compound $i$	Conversion Factor, $C_i$
CO	1.00
H <sub>2</sub>	1.01
N <sub>2</sub>	1.00
Methane	0.76
Ethylene	0.60
Ethane	0.49
Propene	0.40
Propane	0.34
Butene	0.29
Butane	0.25
Pentene	0.23
Pentane	0.21
CO <sub>2</sub>	0.74

Source: Bronkhorst (2011).

## A. 5. SELECTIVITY

Selectivity was obtained using two approaches: the C atom basis and the weight percentage. A little difference exists between each approach. Theoretically, the calculations performed in a carbon atom basis is preferred. Commercially, products are sold on a mass or volume basis (DRY, 2004). It is relevant to cite that CO<sub>2</sub> was treated as undesired product and excluded from selectivity calculations.

For gases (weight basis) (HAGEN, 2015a):

- Methane Selectivity

$$S_{\text{CH}_4}(\%) = \frac{\dot{m}_{\text{CH}_4,\text{out}} - \dot{m}_{\text{CH}_4,\text{in}}}{\dot{m}_{\text{CO},\text{in}} - \dot{m}_{\text{CO},\text{out}} - \dot{m}_{\text{CO}_2,\text{out}}} \times 100 \quad (\text{A.11})$$

- CO<sub>2</sub> Selectivity

$$S_{\text{CO}_2}(\%) = \frac{\dot{m}_{\text{CO}_2,\text{out}} - \dot{m}_{\text{CO}_2,\text{in}}}{\dot{m}_{\text{CO},\text{in}} - \dot{m}_{\text{CO},\text{out}}} \times 100 \quad (\text{A.12})$$

Using the liquid data:

In C atom basis, Equation (A.13)-(A.16):

- Methane Selectivity

$$S_{\text{CH}_4}(\%) = \frac{F_{\text{CH}_4,\text{out}} - F_{\text{CH}_4,\text{in}}}{F_{\text{CO},\text{in}} - F_{\text{CO},\text{out}} - F_{\text{CO}_2,\text{out}}} \times 100 \quad (\text{A.13})$$

- CO<sub>2</sub> Selectivity

$$S_{\text{CO}_2}(\%) = \frac{F_{\text{CO}_2,\text{out}} - F_{\text{CO}_2,\text{in}}}{F_{\text{CO},\text{in}} - F_{\text{CO},\text{out}}} \times 100 \quad (\text{A.14})$$

- Paraffins (C<sub>n</sub>H<sub>2n+2</sub>, 1 ≤ n ≤ 21) Selectivity

$$S_{\text{C}_n\text{H}_{2n+2}}(\%) = \frac{n \cdot F_{\text{C}_n\text{H}_{2n+2},\text{out}} - n \cdot F_{\text{C}_n\text{H}_{2n+2},\text{in}}}{F_{\text{CO},\text{in}} - F_{\text{CO},\text{out}} - F_{\text{CO}_2,\text{out}}} \times 100 \quad (\text{A.15})$$

- Olefins (C<sub>n</sub>H<sub>2n</sub>, 2 ≤ n ≤ 10) Selectivity

$$S_{\text{C}_n\text{H}_{2n}}(\%) = \frac{n \cdot F_{\text{C}_n\text{H}_{2n},\text{out}} - n \cdot F_{\text{C}_n\text{H}_{2n},\text{in}}}{F_{\text{CO},\text{in}} - F_{\text{CO},\text{out}} - F_{\text{CO}_2,\text{out}}} \times 100 \quad (\text{A.16})$$

In weight percentage, Equations (A.17)-(A.23):

- Methane Selectivity

$$S_{\text{CH}_4}(\%) = \frac{(\dot{m}_{\text{CH}_4,\text{out}} - \dot{m}_{\text{CH}_4,\text{in}})}{\dot{m}_{\text{CO},\text{in}} - \dot{m}_{\text{CO},\text{out}} - \dot{m}_{\text{CO}_2,\text{out}}} \times 100 \quad (\text{A.17})$$

- CO<sub>2</sub> Selectivity

$$S_{\text{CO}_2}(\%) = \frac{(\dot{m}_{\text{CO}_2,\text{out}} - \dot{m}_{\text{CO}_2,\text{in}})}{\dot{m}_{\text{CO},\text{in}} - \dot{m}_{\text{CO},\text{out}} - \dot{m}_{\text{CO}_2,\text{out}}} \times 100 \quad (\text{A.18})$$

- Paraffins (C<sub>n</sub>H<sub>2n+2</sub>, 1 ≤ n ≤ 21) Selectivity

$$S_{\text{C}_n\text{H}_{2n+2}}(\%) = \frac{(\dot{m}_{\text{C}_n\text{H}_{2n+2},\text{out}} - \dot{m}_{\text{C}_n\text{H}_{2n+2},\text{in}})}{\dot{m}_{\text{CO},\text{in}} - \dot{m}_{\text{CO},\text{out}} - \dot{m}_{\text{CO}_2,\text{out}}} \times 100 \quad (\text{A.19})$$

- Ranging from C<sub>2</sub>-C<sub>4</sub> (C<sub>2</sub>-C<sub>4</sub>-)

$$S_{\text{C}_2\text{-C}_4}(\%) = \frac{\sum_{n=2}^4 (\dot{m}_{\text{C}_n\text{H}_{2n+2},\text{out}} - \dot{m}_{\text{C}_n\text{H}_{2n+2},\text{in}})}{\dot{m}_{\text{CO},\text{in}} - \dot{m}_{\text{CO},\text{out}} - \dot{m}_{\text{CO}_2,\text{out}}} \times 100 \quad (\text{A.20})$$

- Ranging from C<sub>5</sub>-C<sub>10</sub> (gasoline)

$$S_{C_5-C_{10}} (\%) = \frac{\sum_{n=5}^{10} (\dot{m}_{C_nH_{2n+2},out} - \dot{m}_{C_nH_{2n+2},in})}{\dot{m}_{CO,in} - \dot{m}_{CO,out} - \dot{m}_{CO_2,out}} \times 100 \quad (A.21)$$

○ Ranging from C<sub>10</sub>-C<sub>20</sub> (diesel) (SONG, 2000)

$$S_{C_{10}-C_{20}} (\%) = \frac{\sum_{n=10}^{20} (\dot{m}_{C_nH_{2n+2},out} - \dot{m}_{C_nH_{2n+2},in})}{\dot{m}_{CO,in} - \dot{m}_{CO,out} - \dot{m}_{CO_2,out}} \times 100 \quad (A.22)$$

- Olefins (C<sub>n</sub>H<sub>2n</sub>, 2 ≤ n ≤ 10) Selectivity

$$S_{C_nH_{2n}} (\%) = \frac{(\dot{m}_{C_nH_{2n},out} - \dot{m}_{C_nH_{2n},in})}{\dot{m}_{CO,in} - \dot{m}_{CO,out} - \dot{m}_{CO_2,out}} \times 100 \quad (A.23)$$

- C<sub>5+</sub> Selectivity

$$S_{C_{5+}} (\%) = 100 - S_{CH_4} - S_{C_2-C_4} - S_{C_{2-}-C_{4-}} \quad (A.24)$$

The selectivity to olefins related to the paraffins is given by the olefin-to-paraffin ratio, Equation (A.25).

- Olefin-to-paraffin ratio ( $m_{O/P}$ )

$$m_{O/P} = \frac{\sum_{n=2}^4 (\dot{m}_{C_nH_{2n},out} - \dot{m}_{C_nH_{2n},in})}{\sum_{n=2}^4 (\dot{m}_{C_nH_{2n+2},out} - \dot{m}_{C_nH_{2n+2},in})} \quad (A.25)$$

Where  $F_i$  stands for component  $i$  molar flow at the inlet ( $F_{i,in}$ ) or outlet ( $F_{i,out}$ ),  $N_i$  is the molar concentration (mol/mL) of component  $i$  obtained by chromatographic analysis,  $\dot{q}$  is the measured volume flow (mL<sub>n</sub>/min) at STP,  $P_i$  stands for the partial pressure of component  $i$ ,  $R$  is the Universal Gas Constant [0.082057459 atm.L/(mol.K)],  $T$  is the temperature at STP (273 K).

## A. 6. REACTION RATE

### *Carbon Monoxide*

The reaction rate of carbon monoxide consumption are usually calculated relatively to total catalyst mass (HAGEN, 2015b) as given by Equation (A.26). However, this study calculated the reaction rates based on the total  $m_{CO}$  of the catalyst, which is also known as the cobalt-time-yield (CTY) (PARK et al., 2017), as given by Equation (A.27).

$$r_{CO,eff} = - \frac{1}{m_{cat}} \cdot \frac{dn_{CO}}{dt} \quad (A.26)$$

$$CTY = - \frac{1}{m_{Co}} \cdot \frac{dn_{CO}}{dt} = \frac{(F_{CO,in} - F_{CO,out})}{m_{Co}} \quad (A.27)$$

An alternative way of calculating the reaction rate is based on the catalyst's specific surface area (S), as given by Equation (A.28):

$$r_{CO,S} = - \frac{1}{S} \cdot \frac{dn_{CO}}{dt} = \frac{(F_{CO,in} - F_{CO,out})}{S} \quad (A.28)$$

### *Methane*

Following the same trend as for carbon monoxide, the reaction rates were calculated according to Equations (A.29) and (A.30).

$$r_{CH_4,eff} = - \frac{1}{m_{cat}} \cdot \frac{dn_{CH_4}}{dt} = \frac{(F_{CH_4,in} - F_{CH_4,out})}{m_{Co}} \quad (A.29)$$

$$r_{CO_2,eff} = - \frac{1}{m_{cat}} \cdot \frac{dn_{CO_2}}{dt} = \frac{(F_{CO_2,in} - F_{CO_2,out})}{m_{Co}} \quad (A.30)$$

## **A. 7. YIELD LOSS**

The yield loss (%) was considered as a way to evaluate the catalyst deactivation. It was calculated as the mean CTY variation at the beginning and at the end of the reaction at the same reaction conditions (temperature, pressure, WHSV,  $H_2/CO$  molar ratio). It is described by Equation (A.31), whereas  $(-\bar{r}_{CO,eff}|_{t=0})$  was evaluated as the mean CO effective rate at stable conditions (same T and WHSV) at the beginning of the run and  $(-\bar{r}_{CO,eff}|_{t=TOS})$  was evaluated as the mean CO effective rate at stable conditions at the end of run.

$$Y(\%) = \frac{(-\bar{r}_{CO,eff}|_{t=0}) - (-\bar{r}_{CO,eff}|_{t=TOS})}{(-\bar{r}_{CO,eff}|_{t=0})} \quad (A.31)$$

## **A. 8. SYSTEM MASS BALANCE ASSESSMENT**

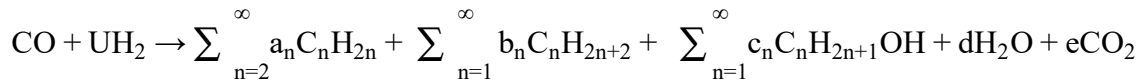
The mass balance was performed in order to evaluate the system consistency and accuracy of both reactor system and analysis (VAN DER LAAN, 1999). For instance, carbon atomic balances derived from each liquid evaluation using the GC were calculated, for a continuous system, as:

$$\Delta C = \frac{C_{\text{out}}}{C_{\text{in}}} \times 100 \quad (\text{A.32})$$

$$\Delta C = \frac{(N_{\text{CO}_{\text{out}}} + 1 \cdot N_{\text{CO}_{2\text{out}}} + \sum_{n=1}^{\infty} n \cdot N_{\text{C}_n\text{H}_{2n+2}} + \sum_{n=2}^{\infty} n \cdot N_{\text{C}_n\text{H}_{2n}} + \dots) \cdot \dot{q}_{\text{out}}}{N_{\text{CO}_{\text{in}}} \cdot \dot{q}_{\text{in}}} \times 100$$

#### A.9. PARALLEL SOLUTION TO THE PROBLEM OF SYSTEM MASS BALANCE ASSESSMENT

The problem in such correlation is that data for all products is not available. In order to verify the system mass balance, a correlation between the amount of CO converted and H<sub>2</sub>O produced has been considered. Firstly, the overall chemical reaction given by Stenger and Askonas (1986).



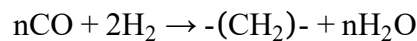
Where  $U$  is the hydrogen per carbon monoxide usage ratio and  $a_n$ ,  $b_n$ ,  $c_n$ ,  $d$  and  $e$  are the stoichiometric coefficients. Such parameters are undetermined and depends on product distribution, which may vary with catalyst features and operating conditions. The several reactions that occur over the catalyst surface are described at Frame A. 1.

Frame A. 1 – Fischer-Tropsch reactions over the catalyst surface

<i>Main Reactions</i>	
Methane	$\text{CO} + 3\text{H}_2 \rightarrow \text{CH}_4 + \text{H}_2\text{O}$
Paraffins	$n\text{CO} + (2n + 1)\text{H}_2 \rightarrow \text{C}_n\text{H}_{2n+2} + n\text{H}_2\text{O}$
Olefins	$n\text{CO} + 2n\text{H}_2 \rightarrow \text{C}_n\text{H}_{2n} + n\text{H}_2\text{O}$
Water-gas shift (WGS) reaction	$\text{CO} + \text{H}_2\text{O} \rightarrow \text{CO}_2 + \text{H}_2$
<i>Side reactions</i>	
Alcohols	$n\text{CO} + 2n\text{H}_2 \rightarrow \text{C}_n\text{H}_{2n+1}\text{OH} + n\text{H}_2\text{O}$
Boudouard reaction	$2\text{CO} \rightarrow \text{C} + \text{CO}_2$
<i>Catalyst modifications</i>	
Catalyst oxidation/reduction	$\text{M}_x\text{O}_y + y\text{H}_2 \rightarrow y\text{H}_2\text{O} + x\text{M}$ $\text{M}_x\text{O}_y + y\text{CO} \rightarrow y\text{CO}_2 + x\text{M}$
Bulk carbide formation	$y\text{C} + x\text{M} \rightarrow \text{M}_x\text{C}_y$

Source: James et al. (2012).

It is known that, for cobalt catalysts, the WGS activity is negligible and the deactivation due to oxidation is only relevant for particles < 5 nm. The Boudouard reaction effect may not be relevant as well, since the amount of CO<sub>2</sub> produced is very low at stationary state. Moreover, active phase reduction is performed at higher temperatures than that used for the reaction per se, which guarantees that the active phase is at its most reduced state at reaction conditions. This means that paraffins and olefins are the main products, as expected. A complementary view over this problem is the simple monomeric correlation for FTS, where the correlation between carbon monoxide, hydrogen, methylene (intermediate) and water is given by



Such information can provide basis to the assumption that, since hydrocarbons are the main products, a gross estimative between an easy to measure reactant (CO) and a product (H<sub>2</sub>O) can be derived, which is given by a H<sub>2</sub>O-to-CO mol ratio. Each hydrocarbon of a given chain length consumes an amount of n CO molecules, which is therefore considered by multiplying the number of mols of the produced hydrocarbon by n, which is the basis for the C-atom selectivity calculation. Such reaction is also directly responsible to the formation of the same number of mols of water. Therefore:

$$\left( \sum_{n=1}^{21} n \cdot N_{\text{C}_n\text{H}_{2n+2}} + \sum_{n=2}^{10} n \cdot N_{\text{C}_n\text{H}_{2n}} + \dots \right) \cdot \dot{q}_{\text{out}} \approx n_{\text{H}_2\text{O produced}} = \frac{m_{\text{H}_2\text{O, out}}}{MM_{\text{H}_2\text{O}}}$$

This correlation may as well be considered as a system mass balance assessment at the end of analysis for each catalyst. Therefore:

$$\Delta C = \frac{C_{out}}{C_{in}} \times 100 = (N_{CO_{out}} \cdot \dot{q}_{out} + \frac{m_{H_2O,out}}{MM_{H_2O}}) \cdot \left( \frac{1}{N_{CO_{in}} \cdot \dot{q}_{in}} \right) \times 100$$

Since the water is measured at the end of each analysis ( $t \cong 24h$ ) the mass balance is calculated as given by Equation (A.33).

$$\Delta C = \left( \bar{F}_{CO_{out}} \cdot t + \frac{m_{H_2O,out}|_t}{MM_{H_2O}} \right) \cdot \left( \frac{1}{\bar{F}_{CO_{in}} \cdot t} \right) \times 100 \quad (A.33)$$

Where  $m_{H_2O,out}$  is the water mass (g) measured at the end of each run for each catalyst and temperature and  $MM_{H_2O}$  is the water molar mass (g/mol).  $\bar{F}_{CO}$  is the average molar flow of carbon monoxide (mol.min<sup>-1</sup>). It is an easier to measure product for carbon mass balance calculation, which must be close to 100%. Water is a condensable product, which is easily removed from the system, providing a more accurate, although gross, measurement of CO transformation to products for cobalt catalysts. Another advantage is the fact that the amount of water is measured online for each reaction temperature, while the hydrocarbon products assessment is performed only up to C<sub>21</sub> for paraffins and to C<sub>10</sub> for olefins. Due to the specificity of the system used in this study, the hot trap mass measurement is performed only at the end of the analysis, giving a mixture of all wax produced at all reaction conditions, which cannot be used to calculate the carbon mass balance at each step of analysis.

## REFERENCES

BRONKHORST. **General instructions digital Mass Flow / Pressure instruments laboratory style / IN-FLOW Instruction manual**, 2011. Disponível em: <<http://www.bronkhorst.fr/>>

DRY, M. E. **Chemical concepts used for engineering purposes**. In: Studies in Surface Science and Catalysis. Elsevier B.V., 2004. v. 152p. 196–257.

HAGEN, J. **Introduction**. In: Industrial catalysis: a practical approach. 3rd. ed. John Wiley & Sons, 2015a.

HAGEN, J. **Heterogeneous catalysis: Fundamentals**. In: Industrial catalysis: a practical approach.

JAMES, O. O.; CHOWDHURY, B.; MESUBI, M. A.; MAITY, S. **Reflections on the chemistry of the Fischer-Tropsch synthesis**. RSC Advances, v. 2, n. 19, p. 7347–7366, 2012.

PARK, J. C.; KWON, J. I.; KANG, S. W.; CHUN, D. H.; LEE, H. T.; JUNG, H.; YANG, J. **IL. Large-scale synthesis of uniformly loaded cobalt nanoparticles on alumina for efficient clean fuel production**. RSC Advances, v. 7, n. 15, p. 8852–8857, 2017.

SCHMAL, M. **Cinética e reatores: Aplicação à engenharia química (3a Edição)**. Synergia, 2018.

SONG, C. **Chemistry of diesel fuels**. CRC Press, 2000.

STENGER, H. G.; ASKONAS, C. F. **Thermodynamic product distributions for the Fischer-Tropsch synthesis**. Industrial & Engineering Chemistry Fundamentals, v. 25, n. 3, p. 410–413, ago. 1986.

VAN DER LAAN, G. P. **Kinetics, Selectivity and Scale Up of the Fischer-Tropsch Synthesis**.



## APPENDIX B – N<sub>2</sub>-SORPTION ISOTHERMS

The following section summarizes the N<sub>2</sub>-sorption isotherm in terms of experimental methodology and presents a basic understanding of the DFT method.

### B.1. INTRODUCTION

Although the adsorption/desorption analysis using N<sub>2</sub> and other gases initiated with Dewar, it was due to Langmuir that the interpretations of adsorption data was renewed. Brunauer and Emmett proposed the adoption of gas adsorption for the determination of surface area, which, afterwards, was the base for the Brunauer-Emmett-Teller (BET) theory, established as the standard procedure for surface area determination. Its use for pore size analysis is based on the application of a corrected Kelvin equation, and the Barrett, Joyner and Halenda (BJH) method remains the most popular way of deriving pore size distribution from an appropriate nitrogen isotherm (SING, 2001). BJH is most widely used for calculations of pore size distribution (PSD) over the mesopore and part of the macropore range (GROEN; PEFFER; PÉREZ-RAMÍREZ, 2003).

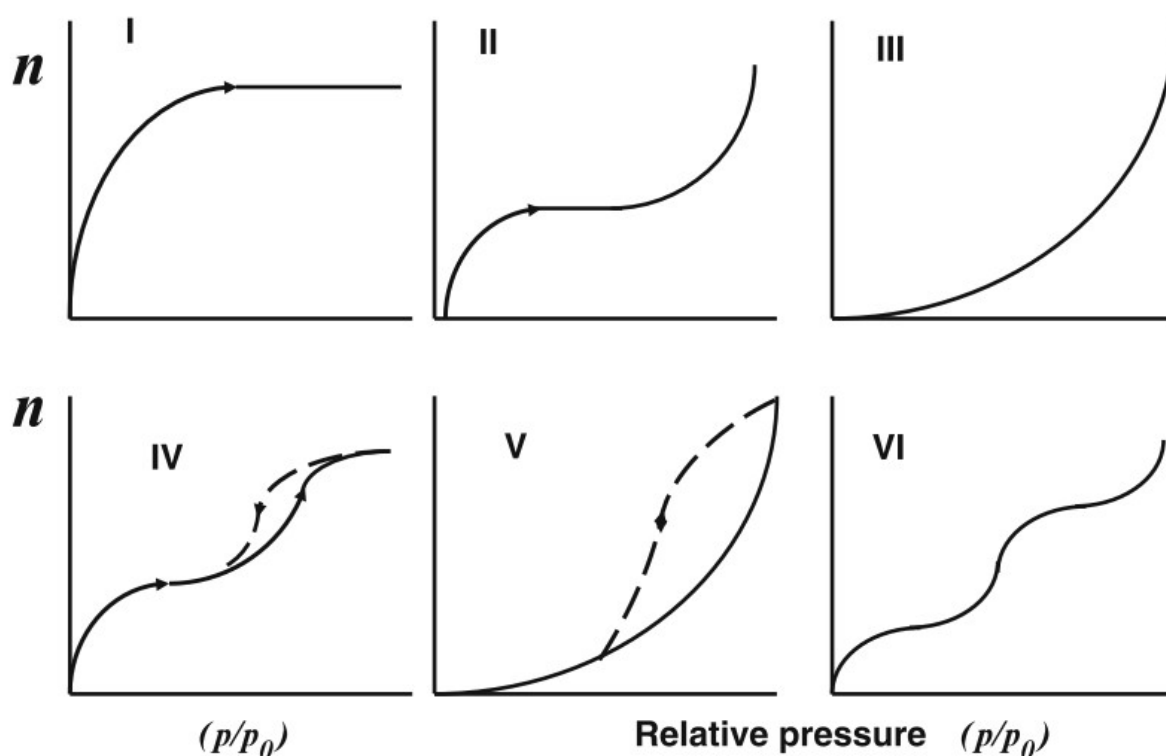
### B.2. METHODOLOGY

Overall, the sorption isotherms are an evaluation of the amount of a previously selected probe molecule gas that physically adsorbs and desorbs onto the surface of a porous material, namely sorbate, at a constant temperature. Different probe gases can be used, such as Ar, CO<sub>2</sub> and N<sub>2</sub>, and appropriate selection relies on the nature of the adsorbent and the information required. For instance, N<sub>2</sub> at 77 K is used for routine quality control and investigation of new materials; Ar at 87.5 is used for precise determination of micropore size distribution (STORCK; BRETINGER; MAIER, 1998) and is especially useful for slit-shaped pores carbons (applying the Horvath-Kawazoe model) and zeolites (applying the Saito-Foley model). In the case of (activated) carbons, CO<sub>2</sub> at nearly ambient temperature is often the preferred adsorptive, and the usage of high-pressure CO<sub>2</sub> adsorption can provide measurement for a larger range of micropores (GROEN; PEFFER; PÉREZ-RAMÍREZ, 2003).

The general method used for the ‘volumetric determination’ of adsorption isotherms is gas adsorption manometry, i.e. the pressure variation measurement, and the conventional technique is discontinuous, in which successive amounts of nitrogen is injected into the system and

allowed to reach equilibrium. The technique is relatively fast and easy and provides valuable information about the pore characteristics of solid materials and post-synthesis treatment modifications. Isotherms are generally obtained by plotting the relative pressure (or partial equilibrium pressure,  $p/p_0$ ) versus volume adsorbed, and, as aforementioned, frequently  $N_2$  probe molecule at 77 K and at sub-atmospheric pressures is used. Such probe gas, when applied over a wide range of relative pressures, can provide information on size distributions in the micro-, meso- and macro-porosity range (approximately 0.5-200 nm) (GROEN; PEFFER; PÉREZ-RAMÍREZ, 2003). Most isotherms can be grouped into six types, Figure B.1, following IUPAC classification.

Figure B.1 – Typical adsorption isotherms.



Source: Schmal (2016).

From the six types of isotherms depicted above, type IV is the most frequently found isotherm type in heterogeneous catalysts, in which one can notice the multilayer adsorption and the formation of capillary condensation in mesoporous materials. More information about isotherms and hysteresis can be found in the literature (LOWELL et al., 2004; SCHMAL, 2016).

With time, new methods have been developed. Traditional computational procedures for the measurement of mesopore size analysis relies on Kelvin equation, whose validity decreases for

pore sizes lower than narrow mesopores (SING; WILLIAMS, 2004). Modern methods, which involves the non-local density functional theory (NLDFT), provides a more elegant treatment for the analysis of meso- and micropores, since it provides a more realistic description of the thermodynamic properties of the fluid inside the pores.

#### *Density Functional Theory Method*

The density functional theory is a microscopic treatment that can describe the configuration and behavior of the adsorbed phase confined in well-defined pore structures at the molecular level. Based on the fundamentals of statistical mechanics, it describes the distribution of adsorbent in pores, which is hence dependent on the chosen pore model. Indeed, the density profiles obtained by applying the DFT-theory and Monte Carlo simulations are based on the fluid-fluid and fluid-solid interactions and allows calculating the equilibration density profile for all locations in the pore. From the DFT-approaches, the NLDFT and the Monte Carlo computer simulation techniques provide an accurate structure of a fluid confined to narrow pores (THOMMES, 2002).

As expected, two relevant variables of the pore model are shape (e.g. slit, cylinder, spherical and hybrid geometries) and adsorbent composition (such as carbon, silica and zeolite). Finally, the method calculates a series of theoretical isotherms (namely kernel) in pores of different widths for the particular pore shape and adsorptive/adsorbent pair (THOMMES et al., 2015). The calculation (deconvolution) of the pore size distribution,  $f(D)$ , is based on the solution of the general adsorption isotherm (GAI) equation (Equation B.1), which correlates both the kernel ( $N(p/p_0, D)$ ) and the experimental adsorption isotherm ( $N(p/p_0)$ ).

$$N(p/p_0) = \int_{D_{\min}}^{D_{\max}} N(p/p_0, D) \cdot f(D) \cdot dD \quad (\text{B.1})$$

In other words, the method assumes that the experimental isotherm consists of a weighted sum of the theoretical isotherms in pores of different diameters (kernel) as selected previously for the system analyzed (such as composition and pore type) (OJEDA et al., 2003). The solution is given as the pore size distribution related to the kernel can best describe the experimental data. A clear limitation of this method is the necessity of previous determination of the adsorbent structure or surface compositions. Disregarding the compatibility of the experimental adsorptive/adsorbent system and the chosen kernel can lead to a significant error, which is therefore a serious drawback to apply such method in industry and routine analysis

(THOMMES et al., 2015). Finally, considering the structure of SBA-15 (and related micro-mesoporous materials), whose intrawall pores can present up to 30% of total porosity, the NLDFT allows an accurate pore size distribution of the main mesoporous channels and the total volume of the intrawall pores (RAVIKOVITCH; NEIMARK, 2001).

## REFERENCES

- GROEN, J. C.; PEFFER, L. A. A.; PÉREZ-RAMÍREZ, J. **Pore size determination in modified micro- and mesoporous materials.** Pitfalls and limitations in gas adsorption data analysis. *Microporous and Mesoporous Materials*, v. 60, n. 1–3, p. 1–17, 2003.
- LOWELL, S.; SHIELDS, J. E.; THOMAS, M. A.; THOMMES, M. **Characterization of Porous Solids and Powders: Surface Area, Pore Size and Density.** Dordrecht/Boston/London: Kluwer Academic Publishers, 2004.
- LUISA OJEDA, M.; MARCOS ESPARZA, J.; CAMPERO, A.; CORDERO, S.; KORNHAUSER, I.; ROJAS, F. **On comparing BJH and NLDFT pore-size distributions determined from N<sub>2</sub> sorption on SBA-15 substrata.** *Physical Chemistry Chemical Physics*, v. 5, n. 9, p. 1859, 2003.
- RAVIKOVITCH, P. I.; NEIMARK, A. V. **Characterization of micro- and mesoporosity in SBA-15 materials from adsorption data by the NLDFT method.** *Journal of Physical Chemistry B*, v. 105, n. 29, p. 6817–6823, 2001.
- SCHMAL, M. **Heterogeneous Catalysis and its Industrial Applications.** São Paulo: Springer International Publishing Switzerland, 2016.
- SING, K. **The use of nitrogen adsorption for the characterisation of porous materials.** *Colloids and Surfaces A: Physicochemical and Engineering Aspects*, v. 187–188, p. 3–9, 2001.
- SING, K. S. W.; WILLIAMS, R. T. **The use of molecular probes for the characterization of nanoporous adsorbents.** *Particle and Particle Systems Characterization*, v. 21, n. 2, p. 71–79, 2004.
- STORCK, S.; BRETINGER, H.; MAIER, W. F. **Characterization of micro- and mesoporous solids by physisorption methods and pore-size analysis.** *Applied Catalysis A: General*, v. 174, n. 1–2, p. 137–146, 1998.

THOMMES, M. **Pore Size Analysis by Gas Adsorption Part I: Aspects of the Application of Density Functional Theory (DFT) and Monte Carlo simulation (MC) for micro/mesopore size analysis.** Quantachrome Instruments, 2002.

THOMMES, M.; KANEKO, K.; NEIMARK, A. V.; OLIVIER, J. P.; RODRIGUEZ-REINOSO, F.; ROUQUEROL, J.; SING, K. S. W. **Physisorption of gases, with special reference to the evaluation of surface area and pore size distribution (IUPAC Technical Report).** Pure and Applied Chemistry, v. 87, n. 9–10, p. 1051–1069, 2015.





## APPENDIX C – CATALYST XRD ANALYSIS

After obtaining the diffractograms of the support and the catalysts, it was necessary to remove the effect of the support in order to accurately measure the metal crystallite sizes using Scherrer Equation. It must be stated that, for nanoparticles and for supported nano-metal catalysts, the crystallite size measured by Scherrer's provides particle dimensions (HEREIN, 2008).

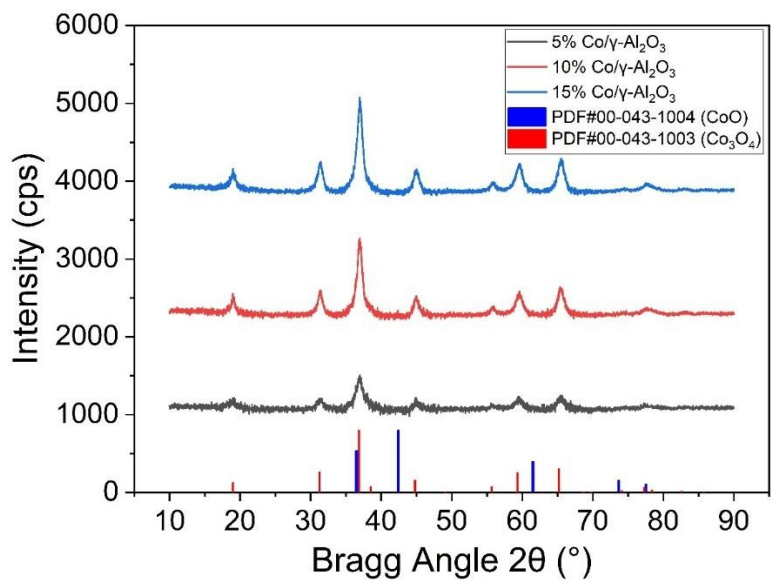
### C.1. ANALYSIS

In order to correctly subtract the baseline, the most intense peak of the support was selected as reference in each diffractogram. Afterwards, the hole diffractogram support was normalized using the peak intensity prior to use it as a baseline. Results are shown in Figure C.1.

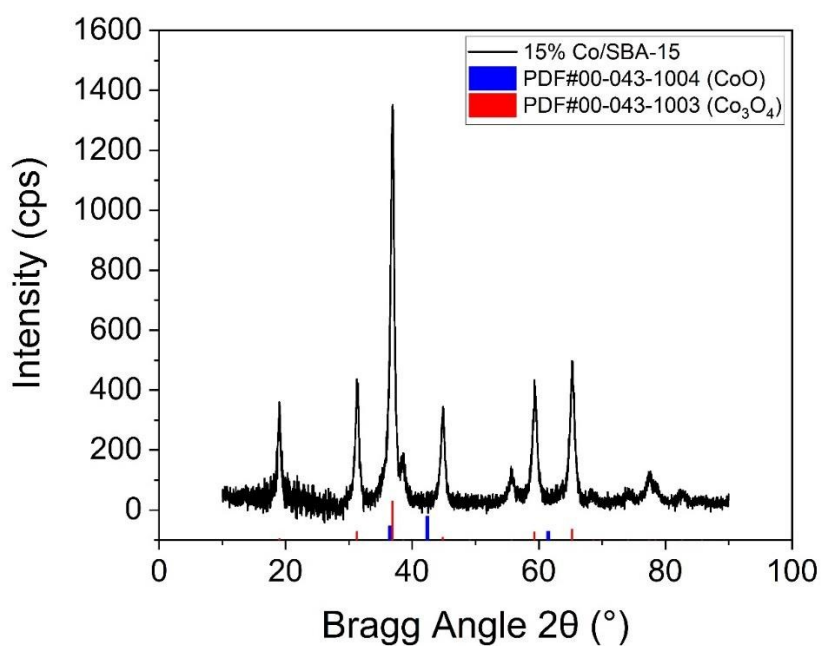
After detection of each peak, the crystallite sizes were calculated using Pseudo-Voigt fitting. The PsdVoigt1 fitting function, selected for fitting, is a linear combination of Gaussian function and Lorentzian function (Figure C.2).

The data is showed next in different tables, respectively to each catalyst prepared in this study (Tables C.1-C.4). Hence, fitting results provided both  $2\theta$  and FWHM as  $x_c$  and  $w$ , respectively, for each catalyst XRD peak, in order to calculate  $d_{hkl}$  and  $L_{hkl}$ . Fitting quality was measured through Squared Pearson Correlation,  $R^2$ . Error was calculated based on  $d_{hkl}$  (crystallographic data was used as reference, while experimental data provided  $d_{hkl}$  by Bragg's Law).

Figure C.1 – X-Ray Diffractogram of (a)  $\gamma$ -Al<sub>2</sub>O<sub>3</sub>-supported and (b) SBA-15-supported catalysts

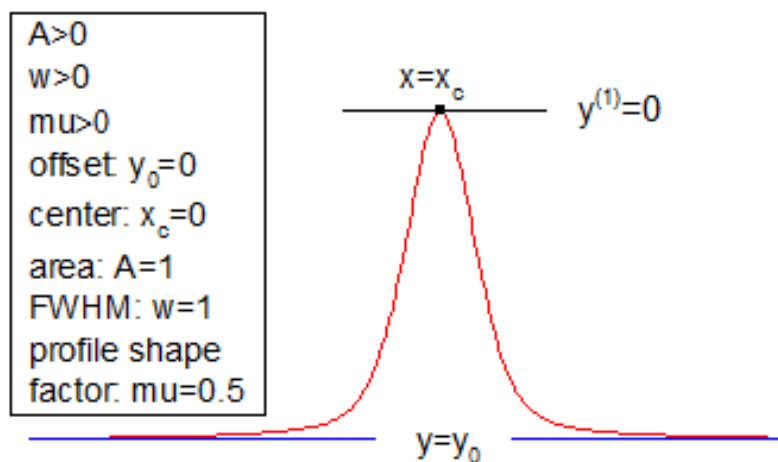


(a)



(b)

Figure C.2 – PsdVoigt1 fitting function example, with specification of the parameters



Source: Origin Lab (2020).

Note:  $y_0$  is the offset,  $x_c$  is the center,  $A$  is the peak area,  $w$  is the FWHM,  $\mu$  is the profile shape factor.

Table C.1 – Crystallite sizes calculated using the Scherrer equation based on 5% Co/ $\gamma$ -Al<sub>2</sub>O<sub>3</sub> diffractogram with subtracted baseline

Crystallographic Sheet Data			Calculated from Subtracted Diffractogram						
Co <sub>3</sub> O <sub>4</sub> (PDF#00-043-1003)			5% Co/ $\gamma$ -Al <sub>2</sub> O <sub>3</sub>						
$2\theta$ (deg)	$d_{hkl}$ (nm)	(hkl)	FWHM (deg)	$\beta$ (rad)	$2\theta$ (deg)	L (nm)	$d_{hkl}$ (nm)	Error (%)*	R <sup>2</sup>
19.00	4.667	(111)	1.05	0.018	18.99	7.6	4.674	0.15	0.4464
31.27	2.858	(220)	0.96	0.017	31.38	8.5	2.850	0.27	0.7316
36.85	2.437	(311)	1.67	0.029	36.93	5.0	2.434	0.13	0.9215
38.55	2.334	(222)	-	-	-	-	-	-	-
44.81	2.021	(400)	1.25	0.022	45.02	6.8	2.013	0.38	0.6041
49.08	1.855	(331)	-	-	-	-	-	-	-
55.66	1.65	(422)	0.52	0.009	56.36	17.0	1.632	1.07	0.1557
59.35	1.556	(511)	1.28	0.022	59.52	7.1	1.553	0.18	0.7120
65.23	1.429	(440)	1.94	0.034	65.45	4.8	1.426	0.21	0.6939
68.63	1.366	(531)	-	-	-	-	-	-	-
69.74	1.347	(442)	-	-	-	-	-	-	-
74.12	1.278	(620)	-	-	-	-	-	-	-
77.34	1.233	(533)	0.74	0.013	77.60	13.7	1.230	0.22	0.1894
78.41	1.219	(622)	-	-	-	-	-	-	-
82.63	1.167	(444)	-	-	-	-	-	-	-
85.76	1.132	(551)	-	-	-	-	-	-	-

Note: Error was calculated using experimental and crystallographic sheet-derived  $d_{hkl}$  values.

Table C.2 – Crystallite sizes calculated using the Scherrer equation based on 10% Co/ $\gamma$ -Al<sub>2</sub>O<sub>3</sub> diffractogram with subtracted baseline

Crystallographic Sheet Data			Calculated from Subtracted Diffractogram						
Co <sub>3</sub> O <sub>4</sub> (PDF#00-043-1003)			10% Co/ $\gamma$ -Al <sub>2</sub> O <sub>3</sub>						
2 $\theta$ (deg)	d <sub>hkl</sub> (nm)	(hkl)	FWHM (deg)	$\beta$ (rad)	2 $\theta$ (deg)	L (nm)	d <sub>hkl</sub> (nm)	Error* (%)	R <sup>2</sup>
19.00	4.667	(111)	0.59	0.010	19.01	13.6	4.668	0.02%	0.8399
31.27	2.858	(220)	0.77	0.013	31.36	10.6	2.852	0.20%	0.9570
36.85	2.437	(311)	0.86	0.015	36.96	9.6	2.432	0.21%	0.9882
38.55	2.334	(222)	-	-	-	-	-	-	-
44.81	2.021	(400)	0.89	0.015	45.00	9.6	2.014	0.32%	0.9038
49.08	1.855	(331)	-	-	-	-	-	-	-
55.66	1.65	(422)	1.03	0.018	55.85	8.7	1.646	0.23%	0.7474
59.35	1.556	(511)	1.28	0.022	59.56	7.1	1.552	0.24%	0.9575
65.23	1.429	(440)	1.05	0.018	65.48	8.9	1.425	0.25%	0.9553
68.63	1.366	(531)	-	-	-	-	-	-	-
69.74	1.347	(442)	-	-	-	-	-	-	-
74.12	1.278	(620)	-	-	-	-	-	-	-
77.34	1.233	(533)	1.64	0.029	77.89	6.2	1.226	0.53%	0.7691
78.41	1.219	(622)	-	-	-	-	-	-	-
82.63	1.167	(444)	-	-	-	-	-	-	-
85.76	1.132	(551)	-	-	-	-	-	-	-

Note: Error was calculated using experimental and crystallographic sheet-derived d<sub>hkl</sub> values.

Table C.3 – Crystallite sizes calculated using the Scherrer equation based on 15% Co/ $\gamma$ -Al<sub>2</sub>O<sub>3</sub> diffractogram with subtracted baseline

Crystallographic Sheet Data			Calculated from Subtracted Diffractogram						
Co <sub>3</sub> O <sub>4</sub> (PDF#00-043-1003)			15% Co/ $\gamma$ -Al <sub>2</sub> O <sub>3</sub>						
2 $\theta$ (deg)	d <sub>hkl</sub> (nm)	(hkl)	FWHM (deg)	$\beta$ (rad)	2 $\theta$ (deg)	L (nm)	d <sub>hkl</sub> (nm)	Error* (%)	R <sup>2</sup>
19.00	4.667	(111)	0.82	0.014	19.00	9.8	4.671	0.08%	0.8652
31.27	2.858	(220)	0.91	0.016	31.36	9.0	2.852	0.20%	0.9703
36.85	2.437	(311)	0.96	0.017	36.98	8.7	2.431	0.25%	0.9914
38.55	2.334	(222)	-	-	-	-	-	-	-
44.81	2.021	(400)	1.01	0.018	45.00	8.5	2.014	0.32%	0.9485
49.08	1.855	(331)	-	-	-	-	-	-	-
55.66	1.65	(422)	1.38	0.024	55.86	6.5	1.646	0.25%	0.7927
59.35	1.556	(511)	1.11	0.019	59.56	8.2	1.552	0.24%	0.9697
65.23	1.429	(440)	1.20	0.021	65.49	7.8	1.425	0.26%	0.9726
68.63	1.366	(531)	-	-	-	-	-	-	-
69.74	1.347	(442)	-	-	-	-	-	-	-
74.12	1.278	(620)	1.87	0.033	74.48	5.3	1.274	0.33%	0.3309
77.34	1.233	(533)	2.38	0.042	77.84	4.3	1.227	0.48%	0.8645
78.41	1.219	(622)	-	-	-	-	-	-	-
82.63	1.167	(444)	-	-	-	-	-	-	-
85.76	1.132	(551)	-	-	-	-	-	-	-

Note: Error was calculated using experimental and crystallographic sheet-derived d<sub>hkl</sub> values.

Table C.4 – Crystallite sizes calculated using the Scherrer equation based on 15% Co/SBA-15 diffractogram with subtracted baseline

Crystallographic Sheet Data			Calculated from Subtracted Diffractogram						
Co <sub>3</sub> O <sub>4</sub> (PDF#00-043-1003)			15% Co/SBA-15						
2θ (deg)	d <sub>hkl</sub> (nm)	(hkl)	FWHM (deg)	β (rad)	2θ (deg)	L (nm)	d <sub>hkl</sub> (nm)	Error* (%)	R <sup>2</sup>
19.00	4.667	(111)	0.63	0.011	18.97	12.6	4.677	0.21%	0.8994
31.27	2.858	(220)	0.70	0.012	31.29	11.7	2.858	0.02%	0.9776
36.85	2.437	(311)	0.68	0.012	36.86	12.2	2.439	0.06%	0.9949
38.55	2.334	(222)	0.93	0.016	38.44	9.0	2.342	0.33%	0.8065
44.81	2.021	(400)	0.76	0.013	44.83	11.2	2.022	0.04%	0.9777
49.08	1.855	(331)	-	-	-	-	-	-	-
55.66	1.65	(422)	0.92	0.016	55.70	9.7	1.650	0.02%	0.8098
59.35	1.556	(511)	0.89	0.015	59.37	10.2	1.557	0.04%	0.9749
65.23	1.429	(440)	0.86	0.015	65.29	10.9	1.429	0.01%	0.9818
68.63	1.366	(531)	1.49	0.026	68.53	6.4	1.369	0.24%	0.3001
69.74	1.347	(442)	-	-	-	-	-	-	-
74.12	1.278	(620)	1.95	0.034	74.25	5.1	1.277	0.06%	0.3288
77.34	1.233	(533)	1.56	0.027	77.46	6.5	1.232	0.07%	0.8512
78.41	1.219	(622)	1.49	0.026	79.82	6.9	1.202	1.43%	0.7418
82.63	1.167	(444)	1.16	0.020	82.64	9.0	1.168	0.05%	0.4923
85.76	1.132	(551)	-	-	-	-	-	-	-

Note: Error was calculated using experimental and crystallographic sheet-derived d<sub>hkl</sub> values.

## REFERENCES

HEREIN, D. **Structure and Morphology: X-Ray Powder Diffraction**. Handbook of Heterogeneous Catalysis, 2008.

ORIGIN LAB, O. **29.1.139 PsdVoigt1**. In: <https://www.originlab.com/doc/origin-help/psdvoigt1-fitfunc>



## APPENDIX D – TEMPERATURE PROGRAMMED METHODS

The following sections details the temperature programmed methods used in the study, including calibration, methods and supplementary results.

### D.1. H<sub>2</sub> TEMPERATURE PROGRAMMED DESORPTION

The catalysts submitted to H<sub>2</sub>-TPD analysis were first submitted to H<sub>2</sub> reduction. The reduction profile, along with dispersion (D), cobalt surface area (S) and particle size<sub>p</sub>(d) calculation method are given next. Geyer *et al.* (2012) evaluated different methods TPD (CO and H<sub>2</sub>), chemisorption (CO and H<sub>2</sub>) and XRD to assess Ni particle size, in which almost all techniques showed similar results to the impregnated Ni/Al<sub>2</sub>O<sub>3</sub> catalyst. Noteworthy is that the XRD, followed by H<sub>2</sub>-TPD, presented the highest standard deviations. Therefore, it seems that both TPD and chemisorption, given its differences, can give direct measurement of the number of surface atoms. At last, by considering spherical particles, dispersion can be calculated by the specific surface area or by the mean particle size calculated by volume-area (d<sub>VA</sub>).

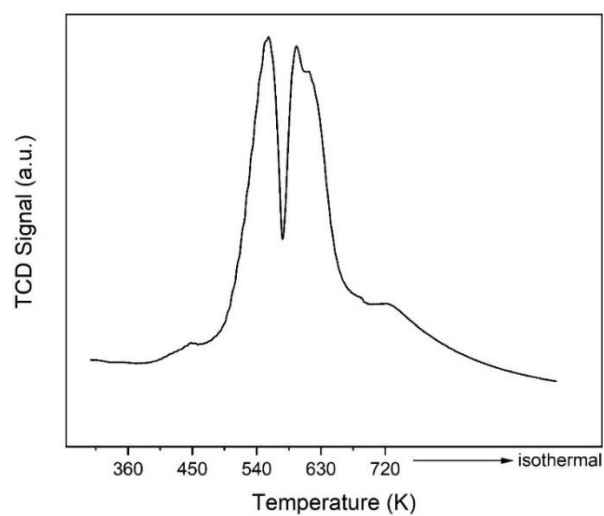
### D.2. H<sub>2</sub> REDUCTION PROFILE OF CATALYSTS PRIOR TO TPD ANALYSIS

The H<sub>2</sub>-TPR profile is given in Figure D.1. The reduction temperature (K) and mass (g) used on the analysis is displayed in Table D.1.

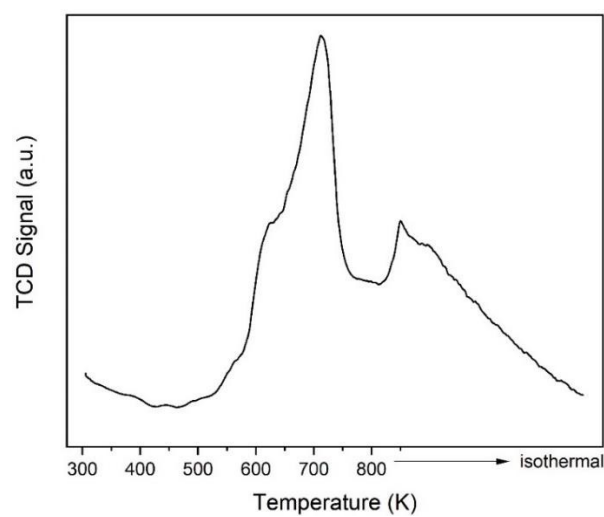
Table D.1 – Catalysts reduction temperature (K) and mass (g) used for H<sub>2</sub>-TPD analysis

Catalyst	Reduction Temperature (K)	Mass (g)
15%Co/SBA-15	723	0.2029
15% Co/ $\gamma$ -Al <sub>2</sub> O <sub>3</sub>	823	0.2012
10% Co/ $\gamma$ -Al <sub>2</sub> O <sub>3</sub>	823	0.2010

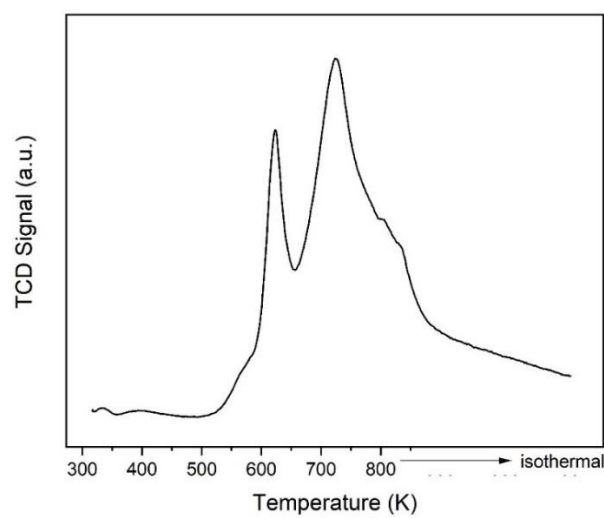
Figure D.1 – Temperature Programmed Reduction ( $H_2$ -TPR) profile (TCD signal versus temperature) for (a) 15%Co/SBA-15, (b) 15%Co/ $\gamma$ - $Al_2O_3$  and (c) 10%Co/ $\gamma$ - $Al_2O_3$  catalysts



(a)



(b)



(c)

### D.3. CALIBRATION

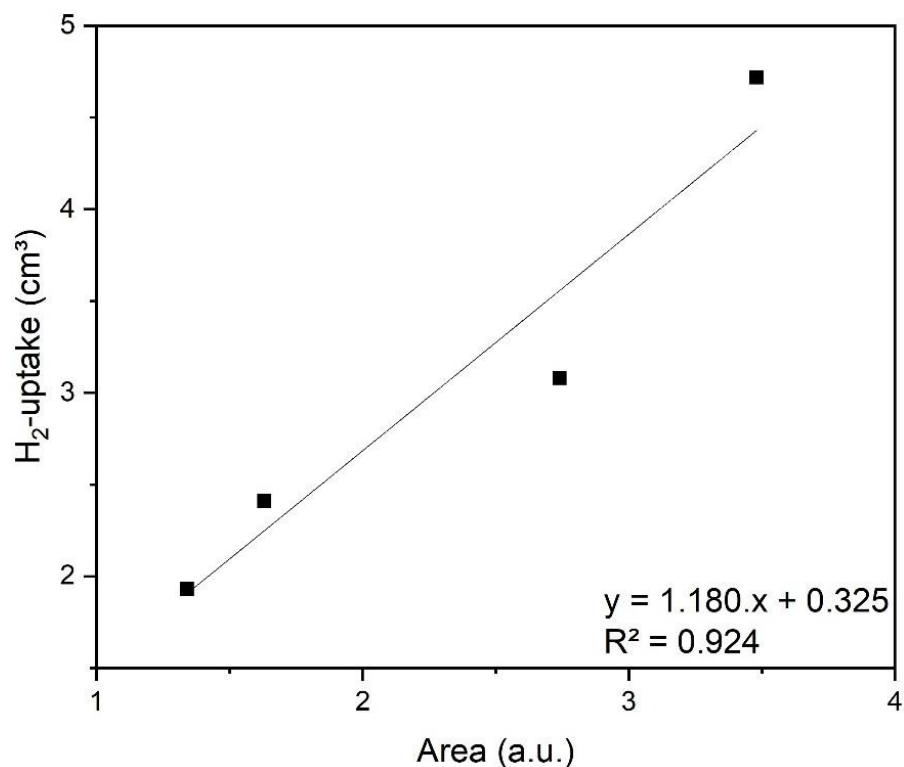
The quantification was performed using Ag<sub>2</sub>O as the standard. The calibration was obtained by varying the standard mass inside the reactor and determining the corresponding H<sub>2</sub> consumption area. Ag<sub>2</sub>O is a well known standard in the literature and is provided by Micromeritics. The Ag<sub>2</sub>O H<sub>2</sub> uptake is of 96.4 cm<sup>3</sup>/g (MICROMERITICS, 2020). The calibration performed is given at Table D.2.

Table D.2 – Calibration of H<sub>2</sub>-TPD analysis using various Ag<sub>2</sub>O masses (g) and the respective Area (a.u.) obtained from the TCD signal

Mass (g)	Area (a.u.)	H <sub>2</sub> -uptake (cm <sup>3</sup> )
0.02	1.34	1.93
0.025	1.63	2.41
0.032	2.74	3.08
0.049	3.48	4.72

A plot of H<sub>2</sub>-uptake (cm<sup>3</sup>) versus Area (a.u.) leads to a relationship between the read Area for each catalyst (calculated using Origin) and the H<sub>2</sub> consumed at TPR or desorbed at TPD analysis (Figure D.2).

Figure D.2 – H<sub>2</sub>-TPD calibration curve [H<sub>2</sub>-uptake (cm<sup>3</sup>) versus Area (a.u.) of standard Ag<sub>2</sub>O] for catalyst's consumption (TPR) and desorption (TPD) quantification



The relationship between H<sub>2</sub>-uptake (cm<sup>3</sup>) and area were, therefore:

$$\text{H}_2 \text{ - uptake (cm}^3\text{)} = 1.180 \times \text{Area(a.u.)} + 0.325$$

#### D.4. QUANTIFICATION

The quantification performed from H<sub>2</sub>-TPR prior to analysis was the degree of reduction, which was important to calculate the number of active sites and, therefore, dispersion, metallic surface area and particle size. The degree of reduction ( $DR$ ), dispersion ( $D$ , %), metallic surface area ( $S_m$ , m<sup>2</sup>/gCo), and the mean particle size ( $d_p$ , nm) were calculated following the literature (BERGERET; GALLEZOT, 2008; SCHMAL, 2011).

##### D.4.1. DEGREE OF REDUCTION

The degree of reduction definition as given by Schmal (2011) is a relationship between the number of mols of H consumed during reduction ( $n_{exp}$  obtained by the TCD signal area integration using Origin<sup>®</sup>) and the total number of mols of H required to achieve a total

reduction of the catalyst ( $n_{teo}$ ), known the catalyst mass ( $m_{cat}$ ) and the catalyst load ( $\chi$ ), as described by Equation . Here, the catalyst load must be analytically obtained using any of the available techniques, such as ICP-OES performed in this study, in order to provide an accurate result.

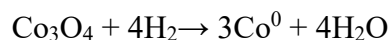
$$DR (\%) = 100 \cdot \frac{n_{exp}}{n_{teo}} \quad (D.1)$$

After the reduction, the TCD area was converted to volume of  $H_2$  uptake. Afterwards, the volume was converted to mols, considering the Ideal-Gas equation at STP.

$$n_{exp} = P \cdot \frac{V_{H_2\text{-uptake}}}{R \cdot T}$$

Where  $n_{exp}$  is the number of mols at STP ( $P = 10^5$  Pa,  $T = 273.15$  K,  $R = 8.314472$  Pa.m<sup>3</sup>.mol<sup>-1</sup>.K<sup>-1</sup>) (IUPAC, 1997a).

The  $n_{teo}$  is obtained by considering the reduction reaction of the oxide. For instance, given the  $Co_3O_4$  reduction to  $Co^0$  global reaction



It is possible to notice that 4 mols of  $H_2$  is required to reduce 1 mol of  $Co_3O_4$ . Deriving the equation for  $n_{teo}$  calculation, which is used to determine the number of mols of  $H_2$  required to reduce the amount of  $Co_3O_4$  of the catalyst, is straightforward.

$$n_{teo} = n \cdot \frac{m_{Co_3O_4}}{MM_{Co_3O_4}} = n \cdot \frac{\left(\frac{\chi}{y}\right) \cdot m_{cat}}{MM_{Co_3O_4}}$$

Where  $n$  is the  $H_2$ -to- $Co_3O_4$  stoichiometric ratio,  $m_{Co_3O_4}$  is the mass of cobalt oxide in the catalyst,  $MM_{Co_3O_4}$  is the molar mass of the cobalt oxide (240.8 g.mol<sup>-1</sup>),  $\chi$  is the mass fraction of cobalt in the catalyst determined by ICP-OES (in our study) and  $y$  is the fraction of cobalt in the respective cobalt oxide [see Equation (A.3)].

Therefore:

$$DR (\%) = 100 \cdot P \cdot \frac{V_{H_2\text{-uptake}}}{R \cdot T} \cdot \frac{3 \cdot MM_{Co}}{n \cdot \chi \cdot m_{cat}} \quad (D.2)$$

Where  $M_{Co}$  is the cobalt molar mass (58.9 g.mol<sup>-1</sup>). Table D.3 shows the DR% results.

Table D.3 – Catalysts DR (%) for further calculations

Catalyst	DR (%)
15%Co/SBA-15	72.27
15% Co/ $\gamma$ -Al <sub>2</sub> O <sub>3</sub>	38.58
10% Co/ $\gamma$ -Al <sub>2</sub> O <sub>3</sub>	36.12

#### D.4.2. DISPERSION

The dispersion is a useful parameter for metal catalysts. Considering  $N_S$  as the total number of metal atoms present on the surface and  $N_T$  as the total number of metal atoms (surface and bulk), the metal dispersion D is given by Equation (D.3).

$$D = \frac{N_S}{N_T} \quad (D.3)$$

This value is usually between 0 and 1 (0 or 100%), since it represents the fraction of surface atoms. By considering spherical particles, useful relationships can be established by making assumptions on the nature of the superficial crystal planes. Assuming equal proportions of the three low-index planes of a given metallic polycrystalline surface (e.g., fcc), calculating the number of atoms per unit area and the mean number of atoms,  $n_S$  from crystal data is straightforward. The surface area occupied by an atom  $m$  on a polycrystalline surface is the inverse of the mean number of atoms,  $a_m$ , and the volume occupied by an atom  $m$  in the bulk of metal is  $v_m$ . The values of  $n_S$ ,  $a_m$  and  $\rho$  for the most common metals are listed in Table D.4.

Table D.4 – Useful data on different metals to obtain dispersion ( $D$ , %), metallic surface area ( $S_m$ , m<sup>2</sup>/g<sub>Co</sub>), and the particle size ( $d_p$ , nm)

Metal	Structure	$n_s$	$a_m$ (Å <sup>2</sup> )	M (g.mol <sup>-1</sup> )	$\rho$ (g.cm <sup>-3</sup> )
Ag	fcc	1.14	8.75	107.87	10.50
Au	fcc	1.15	8.75	196.97	19.31
Co	fcc	1.52	6.59	58.93	8.90
	hcp	1.84	5.43		
Cr	bcc	1.62	6.16	52.00	7.20
Cu	fcc	1.46	6.85	63.55	8.92
Fe	bcc	1.64	6.09	55.85	7.86
Ir	fcc	1.29	7.73	192.22	22.42
Mo	bcc	1.36	7.34	95.94	10.20
Ni	fcc	1.54	6.51	58.69	8.90
Os	hcp	1.54	6.47	190.20	22.48
Pd	fcc	1.26	7.93	106.42	12.02
Pt	fcc	1.24	8.07	195.08	21.45
Re	hcp	1.52	6.60	186.21	20.53
Rh	fcc	1.32	7.58	102.91	12.40
Ru	hcp	1.57	6.35	101.07	12.30
W	bcc	1.35	7.42	183.85	19.32

Source: Bergeret and Gallezot (2008).

Notes:  $n_s$  is the number of surface atoms per 10<sup>-19</sup> m<sup>2</sup> calculated using the following proportion of index planes: fcc (111):(100):(110) = 1:1:1; bcc (110):(100):(211) = 1:1:2; hcp (001);  $a_m$  is the area occupied by a surface atom; M is the atomic mass;  $\rho$  is the mass density;  $v_m$  is the volume occupied by an atom in bulk metal.

The cited data is valuable to calculate the dispersion, surface area and particle size. Using the chemisorption data, the metal dispersion is directly obtained. Consider the following definitions: the active surface is defined as sites or superficial atoms accessible to molecules. The total number of atoms ( $N_T$ ), which is the total amount of loaded cobalt over the support in this study, is different from total number of active sites ( $N_S$ ).  $N_S$  vary depending on the efficiency of the pre-treatment, i.e. the degree of reduction for a reaction catalyzed by metallic particles.  $N_S'$ , on the other hand, is the number of superficial sites, i.e. the number of molecules chemically adsorbed over the active phase surface, per gram of catalyst.

$$N_S' = \frac{V_{ads}}{V_M} \cdot \frac{N_A}{m_{cat}} \cdot n_{cs} = \frac{V_{STP}}{V_{IG}} \cdot \frac{N_A}{m_{cat}} \cdot n_{cs} \left[ \frac{\text{atoms}}{\text{g}_{cat}} \right] \quad (D.4)$$

$$N_S = N_S' \cdot m_{cat} = \frac{V_{STP}}{V_{IG}} \cdot N_A \cdot n_{cs} [\text{atoms}]$$

$$N_T = n_T \cdot N_A = x \cdot \frac{m_{cat}}{M} \cdot N_A \text{ [atoms]}$$

Therefore, the dispersion can be calculated by Equation D.5.

$$D (\%) = \frac{100 \cdot \left( \frac{V_{STP} \cdot n_{cs}}{V_{IG}} \right)}{\frac{x \cdot m_{cat}}{MM}} \quad (D.5)$$

Where  $V_{STP}$  is the volume of molecules adsorbed over the catalyst, forming the monolayer and expressed in  $\text{cm}^3$  (STP),  $n_{cs}$  is the chemisorption stoichiometry,  $V_{IG}$  is the volume occupied by a mol of atoms at STP conditions, i.e.  $22,710.98 \text{ cm}^3 \cdot \text{mol}^{-1}$  at 273.15 K and  $10^5$  Pa, as depicted at IUPAC's gold book (IUPAC, 1997a),  $N_A$  is the Avogadro number, representing the molar number of entities,  $6.022 \ 141 \ 79(30) \times 10^{23} \ \text{mol}^{-1}$  (IUPAC, 1997b),  $m_{cat}$  is the mass of the catalyst sample (g),  $x$  is the metal loading (obtained by ICP-OES) and  $MM$  the atomic mass of metal. The chemisorption stoichiometry represents the average number of surface metal atoms associated with the adsorption of each gas molecule at monolayer coverage (BERGERET; GALLEZOT, 2008). The stoichiometric factor is directly related to the adsorption type, as depicted in Table D.5. For this study,  $n_{cs} = 2$  (hydrogen) due to its dissociative adsorption type (SCHMAL, 2011).

Table D.5 – Stoichiometric factor values for different types of adsorption over the metallic surface

Type		$n_{cs}$
	Dissociative – H <sub>2</sub>	2
Associative – CO	Linear	1
	Bridge	2
Oxygen	O <sub>2</sub> + 2MS → 2MsO	2
	O <sub>2</sub> + MS → ½ MsO	0.5
Titration	O <sub>2</sub> and H <sub>2</sub>	3

Source: Schmal (2011).

#### D.4.3. RELATIONSHIPS BETWEEN PARTICLE SIZE, SURFACE AREA AND DISPERSION

The relationship between specific surface area ( $S_m$ ) and dispersion (D) is:

$$S_m = a_m \cdot \left( \frac{N_A}{MM} \right) \cdot D$$

The relationship between specific surface area ( $S_m$ ) and mean particle size ( $d_p$ ) is:

$$S_m = \frac{6000}{\rho \cdot d_p}$$

With  $d_p$  in nm,  $\rho$  in  $\text{g}\cdot\text{cm}^{-3}$  and  $S_m$  in  $\text{m}^2\cdot\text{g}^{-1}$ .

The relationship between metal dispersion (D) and mean particle size is:

$$d_p = 6 \cdot \left(\frac{v_m}{a_m}\right) \cdot \frac{1}{D}$$

Noteworthy is that, here, the sphere model was considered. For very small particles, representative geometric of the particle morphology should be considered. The equations should not be used for particles smaller than 1.2 nm (BERGERET; GALLEZOT, 2008).

Knowing that the catalyst does not totally reduce during pretreatment, it is relevant to consider the degree of reduction effect on calculations. The corrected dispersion, as given by Equation D.6, reflects over the surface area and particle size (TORSHIZI et al., 2021):

$$D_{\text{cor}} (\%) = 100 \cdot \frac{D (\%)}{DR (\%)} \quad (\text{D.6})$$

Therefore:

$$S_m = a_m \cdot \left(\frac{N_A}{MM}\right) \cdot D_{\text{cor}} (\%)$$

$$d_p = 6 \cdot \left(\frac{v_m}{a_m}\right) \cdot \frac{1}{D_{\text{cor}} (\%)}$$

## REFERENCES

BERGERET, G.; GALLEZOT, P. **Particle Size and Dispersion Measurements. In: Handbook of Heterogeneous Catalysis.** Weinheim, Germany: Wiley-VCH Verlag GmbH & Co. KGaA, 2008. p. 738–765.

GEYER, R.; HUNOLD, J.; KECK, M.; KRAAK, P.; PACHULSKI, A.; SCHÖDEL, R. **Methods for determining the metal crystallite size of Ni supported catalysts.** Chemie-Ingenieur-Technik, v. 84, n. 1–2, p. 160–164, 2012.

IUPAC. **Compendium of Chemical Terminology, 2nd ed. (the “Gold Book”)**. Disponível em: <<http://goldbook.iupac.org/S06036.html>>. Acesso em: 21 jan. 2020a.

IUPAC. **Compendium of Chemical Terminology, 2nd ed. (the “Gold Book”)**. Disponível em: <<http://goldbook.iupac.org/A00543.html>>. Acesso em: 21 jan. 2020b.

MICROMERITICS. **Chemisorption Reference Material**. Disponível em: <<https://www.micromeritics.com/product-Showcase/ChemiSorb-2720-2750/Chemisorption-Reference-Material.aspx>>. Acesso em: 28 jul. 2020.

SCHMAL, M. **Catálise heterogênea**. Rio de Janeiro: Synergia, 2011.

TORSHIZI, H. O.; NAKHAEI POUR, A.; MOHAMMADI, A.; ZAMANI, Y.; KAMALI SHAHRI, S. M. **Fischer-Tropsch synthesis by reduced graphene oxide nanosheets supported cobalt catalysts: Role of support and metal nanoparticle size on catalyst activity and products selectivity**. *Frontiers of Chemical Science and Engineering*, v. 15, n. 2, p. 299–309, 2021.

## APPENDIX E – CATALYTIC TESTS

The following sections details supplementary results obtained for the catalytic tests.

### E.1. TABLES

The catalytic tests generated a large amount of data. Herein, summarized results for each catalyst in each tested condition are reported in Table E.1 and Table E.2 for the for the 15% Co/SBA-15 and 15% Co/ $\gamma$ -Al<sub>2</sub>O<sub>3</sub> catalysts, respectively.

Table E.1 – Summarized performance assessment for the 15% Co/SBA-15 catalyst at different reaction conditions. The TOS was of 98.6 h

T (K)	WHSV (L.g <sup>cat</sup> <sup>-1</sup> .h <sup>-1</sup> )	X <sub>CO</sub> (%)	S <sub>CO<sub>2</sub></sub> (wt. %)	S <sub>H<sub>2</sub></sub> (wt. %)	H <sub>2</sub> /CO mol ratio	Selectivities (wt. %)										Carbon Mass Balance (%)	Productivity					
						CH <sub>4</sub>	C <sub>2</sub> -C <sub>4</sub>	C <sub>2</sub> =C <sub>4</sub>	C <sub>5</sub> -C <sub>10</sub>	C <sub>10</sub> -C <sub>20</sub>	C <sub>5</sub> <sup>+</sup>	CO <sub>2</sub>	m <sub>OP</sub>	H <sub>2</sub> O (g.g <sup>cat</sup> <sup>-1</sup> .h <sup>-1</sup> )	HC (g.g <sup>cat</sup> <sup>-1</sup> .h <sup>-1</sup> )		CT	HT				
	7.67	74.7	9.4	14.6	1.98																	
	8.77	59.4	4.5	14.8	2.07																	
	10.11	53.1	4.5	15.7	2.09																	
543.15	10.82	53.7	5.8	19.2	2.21	24.02	7.56	4.14	6.46	5.12	64.28	5.73	0.55	100.19	1.152	0.294						
	13.96	43.9	4.9	20.2	2.29																	0.003
	17.11	39.2	4.7	22.0	2.26																	
	17.11	39.7	5.7	26.0	2.34																	
523.15	17.11	22.5	2.5	19.5	2.24	19.05	5.70	5.73	10.28	6.30	69.52	2.89	1.00	106.10	0.411	0.069						
493.15	17.11	7.3	0.0	19.7	2.10	16.57	2.80	6.62	9.31	10.63	74.01	0.00	2.36	109.46	0.110	0.014						
543.15	7.67	48.3	3.4	17.4	2.14	14.91	4.76	3.97	9.04	4.31	76.36	3.39	0.83	93.86	1.041	0.094						

Notes: X<sub>CO</sub> stands for CO conversion; S<sub>CO<sub>2</sub></sub> and S<sub>CH<sub>4</sub></sub> stands for CO<sub>2</sub> and CH<sub>4</sub> selectivities (wt. %), respectively; H<sub>2</sub>/CO mol ratio stands for the consumed molar ratio, which was given by the molar ratio between the consumed hydrogen and the consumed CO; C<sub>2</sub>-C<sub>4</sub> stands for paraffins in the C<sub>2</sub> to C<sub>4</sub> range; C<sub>2</sub>=C<sub>4</sub> stands for olefins in the C<sub>2</sub> to C<sub>4</sub> range; C<sub>5</sub>-C<sub>10</sub> stands for paraffins in the C<sub>5</sub> to C<sub>10</sub> range; C<sub>10</sub>-C<sub>20</sub> stands for paraffins in the C<sub>10</sub> to C<sub>20</sub> range; C<sub>5</sub><sup>+</sup> stands for selectivity for hydrocarbons equal or higher than C<sub>5</sub>. m<sub>OP</sub> stands for the olefin-to-paraffin ratio. The CO<sub>2</sub> selectivity displayed here was calculated considering the CO converted, while the selectivity to any of the hydrocarbons was calculated by discounting the CO<sub>2</sub> contribution; Carbon Mass Balance (%) was calculated by evaluating the inlet and outlet carbon balance; differences occurs due to uncertainties in the outlet mass flowmeter measurement, along with any contribution of hydrocarbons inline while transitioning from one reaction conditions to another; Productivity stands for the amount of collected liquid products (water or hydrocarbons – H<sub>2</sub>O or HC) per gram of catalyst per hour of reaction at a given reaction condition. The hydrocarbons were collected by the Cold Trap (CT) or by the Wax Trap (WT) and quantified using an analytical and semi-analytical scale, respectively.

Table E.2 – Summarized performance assessment for the 15% Co/ $\gamma$ -Al<sub>2</sub>O<sub>3</sub> catalyst at different reaction conditions. The TOS was of 96.3 h

T (K)	WHSV (L.g <sub>cat</sub> <sup>-1</sup> .h <sup>-1</sup> )	X <sub>CO</sub> (%)	S <sub>CO<sub>2</sub></sub> (wt. %)	S <sub>CH<sub>4</sub></sub> (wt. %)	H <sub>2</sub> /CO mol ratio	Selectivities (wt. %)						CO <sub>2</sub> m <sub>O/P</sub>	Carbon Mass Balance (%)	Productivity				
						CH <sub>4</sub>	C <sub>2</sub> -C <sub>4</sub>	C <sub>2</sub> =C <sub>4</sub> =	C <sub>5</sub> -C <sub>10</sub>	C <sub>10</sub> -C <sub>20</sub>	C <sub>5+</sub>			H <sub>2</sub> O (g.g <sub>cat</sub> <sup>-1</sup> .h <sup>-1</sup> )	HC (g.g <sub>cat</sub> <sup>-1</sup> .h <sup>-1</sup> )	CT	HT	
	8.79	52.8	7.7	11.7	1.97													
	7.68	54.0	5.7	10.2	1.98													
543.15	10.84	42.0	5.9	14.3	2.12	17.14	6.25	4.32	7.17	3.89	72.28	5.75	0.69	91.09	1.233	0.315		
	17.15	32.8	6.0	16.8	2.26													
	17.16	34.0	6.1	18.9	2.19													0.003
523.15	17.16	15.5	2.0	18.2	2.21	11.08	3.19	5.45	7.42	7.00	80.28	2.10	1.71	95.53	0.430	0.072		
493.15	17.16	3.71	0.0	37.4	2.18	8.99	1.45	5.63	4.57	9.16	83.93	0.00	3.88	102.06	0.129	0.016		
543.15	7.68	48.2	4.6	11.2	2.02	9.25	4.12	2.53	8.24	3.74	84.09	4.32	0.61	80.88	0.790	0.071		

Notes: X<sub>CO</sub> stands for CO conversion; S<sub>CO<sub>2</sub></sub> and S<sub>CH<sub>4</sub></sub> stands for CO<sub>2</sub> and CH<sub>4</sub> selectivities (wt. %), respectively; H<sub>2</sub>/CO mol ratio stands for the consumed molar ratio, which was given by the molar ratio between the consumed hydrogen and the consumed CO; C<sub>2</sub>-C<sub>4</sub> stands for paraffins in the C<sub>2</sub> to C<sub>4</sub> range; C<sub>2</sub>=C<sub>4</sub>= stands for olefins in the C<sub>2</sub> to C<sub>4</sub> range; C<sub>5</sub>-C<sub>10</sub> stands for paraffins in the C<sub>5</sub> to C<sub>10</sub> range; C<sub>10</sub>-C<sub>20</sub> stands for paraffins in the C<sub>10</sub> to C<sub>20</sub> range; C<sub>5+</sub> stands for selectivity for hydrocarbons equal or higher than C<sub>5</sub>. m<sub>O/P</sub> stands for the olefin-to-paraffin ratio. The CO<sub>2</sub> selectivity displayed here was calculated considering the CO converted, while the selectivity to any of the hydrocarbons was calculated by discounting the CO<sub>2</sub> contribution; Carbon Mass Balance (%) was calculated by evaluating the inlet and outlet carbon balance; differences occurs due to uncertainties in the outlet mass flowmeter measurement, along with any contribution of hydrocarbons inline while transitioning from one reaction conditions to another; Productivity stands for the amount of collected liquid products (water or hydrocarbons – H<sub>2</sub>O or HC) per gram of catalyst per hour of reaction at a given reaction condition. The hydrocarbons were collected by the Cold Trap (CT) or by the Wax Trap (WT) and quantified using an analytical and semi-analytical scale, respectively.



## APPENDIX F – BLANK REACTOR TEST

To understand if any part of the system could possibly affect the reaction, a run was carried out with an empty reactor. For the test, similar conditions to the study performed as follows was selected and an empty SS316 reactor was used for the test. No pre-treatment was performed. Table G.1 shows the conditions for the test, while Table G.2 shows the calculated conversion values.

Table G.1 – Operating conditions for the blank reactor test

Condition	Value	
Pressure	20	bar
Temperature (Reactor)	543	K
Temperature (Hot Box)	463	K
Temperature (Wax Trap)	423	K
N <sub>2</sub> Flow	4.9	mL/min
H <sub>2</sub> Flow	29.3	mL/min
CO Flow	14.6	mL/min
TOS	8.3	h
Injections	7	

Table G.2 – H<sub>2</sub> and CO conversions ( $X_{H_2}$  and  $X_{CO}$ , respectively) attained after 7 injections

Injection #	$X_{H_2}$ (%)	$X_{CO}$ (%)
001 <sup>a</sup>	6.22	4.45
002 <sup>a</sup>	5.68	3.24
003 <sup>a</sup>	4.06	1.30
004 <sup>a</sup>	3.77	0.47
005 <sup>c</sup>	6.60	3.74
006 <sup>c</sup>	2.69	2.98

Notes: (a) – injection results using only the TCD method; (b) – injection results using the TCD + FID method.

It is clear that the selected conditions would result in the highest conversion, and even in this case, values obtained were very low. In fact, CO conversion almost reaches zero in the 4<sup>th</sup> injection. Injections 005 and 006 follows the same trend. Variation between runs might be due to inline gas stabilization. Before the beginning of the runs, the system was purged using pure N<sub>2</sub> (50 mL/min). Differences between injections using only TCD method and using TCD + FID are based on the analysis method and process differences.

#### Analysis Method:

- Solely TCD runs takes only 30 min (including cooling time)
- TCD +FID runs takes much more time, ~3h per run (including cooling time);

#### Process (Data Acquisition):

- Solely TCD runs considers a system in which the reactor output is connected to the liquid-liquid-gas separator and to a three-way valve that connects the outlet gases to a cold line with a mass flowmeter and to the gas chromatograph TCD injection loop;
- TCD + FID runs considers a system in which the reactor output bypasses the liquid-liquid-gas separator and goes directly to a three-way valve that connects the outlet gases to a heated line (temperature set to Hot Box values), bypassing also the mass flowmeter and being directed to the gas chromatograph injection loops, providing a solution to the hydrocarbon online assessment. In this study, both FID and TCD injection loops are connected in series. The sample that exits FID loop passes through an ambient pressure liquid-liquid-gas separator. Resultant gases are directed to TCD injection loop.

## APPENDIX G – RAMAN ANALYSIS

The Raman analysis performed for the SBA-15 support is shown in Figure G.1. Figure G.2 shows the used 15% Co/ $\gamma$ -Al<sub>2</sub>O<sub>3</sub> Raman spectrum at low laser power. Figure G.3 displays the used 15% Co/ $\gamma$ -Al<sub>2</sub>O<sub>3</sub> Raman spectrum at high laser power.

Figure G.1 – Pure SBA-15 Raman spectrum

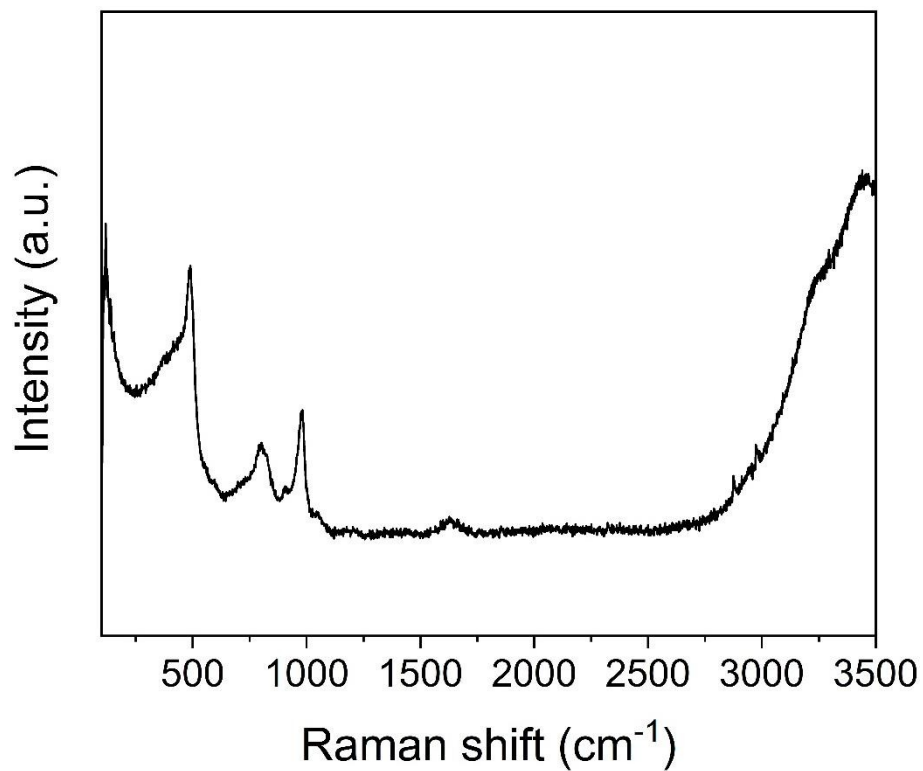


Figure G.2 – Low power laser Raman spectrum (1%) for the 15% Co/SBA-15 (post-reaction). D and G bands are detected even in this condition

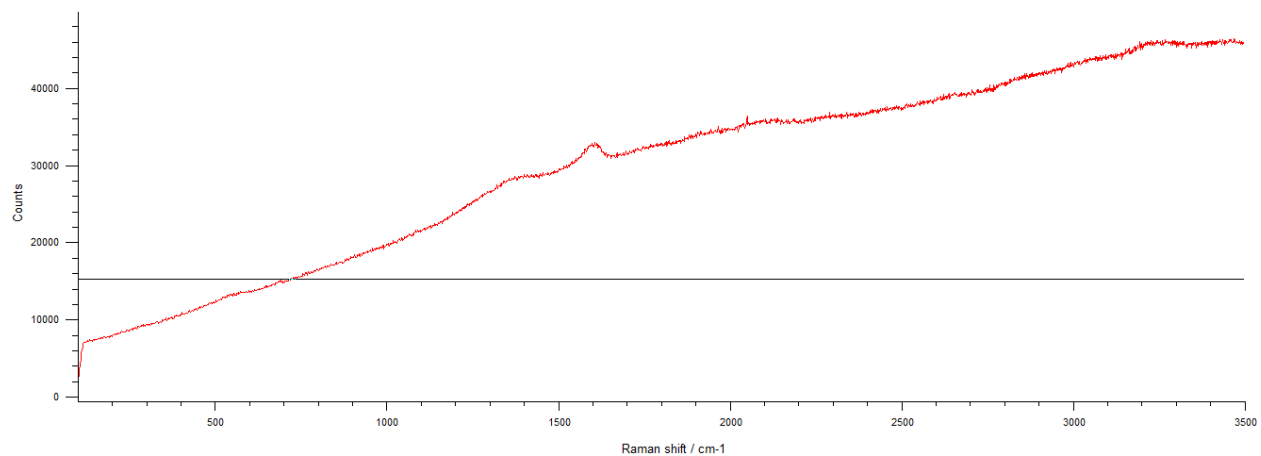


Figure G.3 – High power laser Raman spectrum (10%) for the 15% Co/ $\gamma$ - $\text{Al}_2\text{O}_3$  (post-reaction). After 2000  $\text{cm}^{-1}$ , fluorescence was too high. D and G bands are detected even in this condition

